

# **The role of chromatin remodeling in H3K27M-mutant gliomas**

Brian Krug

Department of Human Genetics  
Faculty of Medicine and Health Science  
McGill University, Montreal, Canada  
April 2022

A thesis submitted to McGill University in partial fulfillment of the requirements of the degree  
of Doctor of Philosophy Human Genetics

© Brian Krug 2022

## **Abstract**

Deregulation of the epigenome underlies oncogenesis in numerous primary brain tumours. The Histone H3 Lys-27-Met (H3K27M) mutation is the driver event of a distinct subgroup of high-grade gliomas in young children. This mutant ‘oncohistone’ poisons the catalytic activity of polycomb repressive complex 2 (PRC2), that is required to establish H3K27me<sub>2/3</sub> and initiate repression of chromatin. This work seeks to characterize the mechanisms and consequences of H3K27M-mediated chromatin remodeling in a disease relevant context. My work creates pairs of tumour-derived H3K27M-mutant cell cultures and isogenic CRISPR-edited knockout lines that delineate specific effects of the mutation. The charting of repressive and active chromatin landscapes identifies global redistribution of H3K27me<sub>2</sub>, H3K27me<sub>3</sub> and H3K27ac. Mapping of chromatin alterations with transcriptional changes contributes understanding to mechanisms of tumour initiation and progression, and therapeutic strategies to target tumour cells, namely a sensitivity to PRC2 inhibitors, DNA demethylating agents and histone deacetylase inhibitors. This work serves to describe how H3K27M mutations contribute to impaired differentiation that associates with tumour development, and parallels with converging driver events altering chromatin in several brain tumour entities.

## Résumé

Les altérations de l'épigénome causent le développement de plusieurs types de tumeurs cérébrales. La substitution d'acides aminés sur la région N-terminale de l'histone H3 telles que la lysine 27 en méthionine (K27M), est associée à des gliomes de haut grade chez les jeunes enfants. L'oncohistone H3K27M inhibe l'activité catalytique répressive du complexe polycomb 2 (PRC2), qui est requis pour établir la di/triméthylation de la lysine 27 de l'histone H3 (H3K27me<sub>2/3</sub>) et permettre ainsi de limiter l'accessibilité à la chromatine. Cette thèse porte sur la caractérisation des mécanismes et les conséquences du remodelage de la chromatine causés par la mutation H3K27M. Mon projet de recherche combine à la fois l'utilisation de lignées cellulaires dérivées à partir de tumeurs de patients, et sur la génération de modèles isogéniques portant la mutation H3K27M endogène à l'aide de la technologie CRISPR-Cas9, ceci pour définir précisément les effets de la mutation. Dans un premier temps je compte identifier l'impact de la mutation sur la redistribution des marques d'histones tels que H3K27me<sub>2</sub>, H3K27me<sub>3</sub> and H3K27ac. Puis je compte évaluer les changements en termes d'expression géniques, qui me permettront d'évaluer les mécanismes d'initiation et de développement des tumeurs. Ces informations serviront dans la mise en place de stratégies thérapeutique pour cibler les cellules tumorales, tels que le développement d'inhibiteurs contre PRC2, la méthylation de l'ADN, et la deacetylation des histones. Cette recherche a pour objectif de décrire les effets de la mutation H3K27M qui rassemble plusieurs événements tels que la perturbation du remodelage de la chromatine et par conséquent l'impact sur la différenciation cellulaire causant la formation de tumeurs cérébrales.

## Table of Contents

|  |    |
|--|----|
| <b>Abstract:</b> .....   | 2  |
| <b>Résumé:</b> .....   | 3  |
| <b>List of Abbreviations:</b> .....  | 8  |
| <b>List of Figures:</b> .....  | 12 |
| <b>List of Tables:</b> .....   | 15 |
| <b>Acknowledgements:</b> .....   | 16 |
| <b>Contribution to original knowledge:</b> .....   | 17 |
| <b>Format of the thesis:</b> .....   | 19 |
| <b>Contribution of Authors:</b> .....  | 20 |
| <b>Chapter 1: Introduction:</b> .....  | 22 |
| • Figure 1. Brain tumour subgroups associated with epigenetic remodeling: .....  | 32 |
| • Figure 2. Epigenetic drivers potentiate tumour development in murine models: .....   | 35 |
| <b>Chapter 2: <i>H3K27M induces defective chromatin spread of PRC2-mediated repressive H3K27me2/me3 and is essential for glioma tumorigenesis:</i></b> ..... | 37 |
| • Figure 1. H3K27M-mutant pediatric high-grade gliomas (pHGGs) exhibit distinct distribution of H3K27me3 and H3K27me2: .....                                 | 42 |
| • Figure 2. H3K27M reversibly induces global redistribution of H3K27me2 and H3K27me3: .....  | 44 |
| • Figure 3. EZH2 inhibition does not completely mimic H3K27M effects and EZH2-Y641N partly overcomes H3K27M-induced effects: .....                           | 48 |
| • Figure 4. Transcriptome and H3K27me3 loci implicate H3K27M in neural differentiation: .....  | 50 |
| • Figure 5. H3K27M confers tumorigenicity in vivo: .....   | 52 |
| • Supplementary Figure 1.: .....   | 74 |

|  |           |
|--|-----------|
| • Supplementary Figure 2.: .....   | 75        |
| • Supplementary Figure 3.: .....   | 76        |
| • Supplementary Figure 4.: .....   | 77        |
| • Supplementary Figure 5.: .....   | 78        |
| • Supplementary Figure 6.: .....   | 79        |
| • Supplementary Figure 7.: .....   | 80        |
| • Supplementary Figure 8.: .....   | 81        |
| • Supplementary Figure 9.: .....   | 82        |
| • Supplementary Figure 10.: .....  | 83        |
| • Supplementary Figure 11.: .....  | 84        |
| • Supplementary Figure 12.: .....  | 85        |
| • Supplementary Figure 13.: .....  | 86        |
| • Supplementary Figure 14.: .....  | 87        |
| • Supplementary Figure 15.: .....  | 88        |
| • Supplementary Figure 16.: .....  | 89        |
| • Supplementary Figure 17.: .....  | 90        |
| • Supplementary Figure 18.: .....  | 91        |
| • Supplementary Figure 19.: .....  | 92        |
| • Supplementary Figure 20.: .....  | 93        |
| <b>Preface to Chapter 3:.....</b>  | <b>94</b> |
| <b>Chapter 3: <i>Pervasive H3K27 acetylation leads to ERV expression and a therapeutic vulnerability in H3K27M gliomas:</i>.....</b> | <b>95</b> |
| • Figure 1. Active Regulatory Chromatin Landscape of Pediatric HGG :.....  | 99        |

- Figure 2. Core Regulatory SE and TF Programs Delineate H3.3K27M and H3K27WT HGG : ..... 101
- Figure 3. Mapping of H3K27ac in Isogenic Models of H3K27M Reveal Minimal Alterations of Gene Transcriptional Programs : ..... 106
- Figure 4. H3K27ac Deposits Pervasively across Intergenic Genome and Is Enriched at Repetitive Elements: ..... 109
- Figure 5. H3.3K27M Tumors Exhibit Increased Deposition of H3K27ac and Transcription at Repetitive Elements: ..... 110
- Figure 6. Repeat Element Primed K27M Cells Are Vulnerable to DNA Methylation and Histone Deacetylase Inhibitors: ..... 113
- Figure 7. Epigenetic Therapies Activate Interferon Response Genes and dsRNA Sensing Pathways: ..... 117
- Figure 8. Schematic Summary of Findings Resulting from this Study: ..... 121
- Key Resources Table: ..... 131
- Figure S1. Related to Figure 1.: ..... 145
- Figure S2. Related to Figure 3.: ..... 146
- Figure S3. Related to Figure 3.: ..... 148
- Figure S4. Related to Figure 4.: ..... 149
- Figure S5. Related to Figure 6.: ..... 151
- Figure S6. Related to Figure 6.: ..... 153
- Figure S7. Related to Figure 7.: ..... 154
- Chapter 4: General Discussion: ..... 156**
- Figure 1. Summary of the chromatin consequences of the H3K27M mutation learned from isogenic modeling.: ..... 158
- Figure 2. Manipulation of driver events determines reversibility of tumour epigenomes.: ..... 161

- Figure 3. Chromatin modifiers in normal and altered development among brain tumours.:  
..... 163
- Chapter 5: Conclusions and Future Directions: ..... 165**
- Chapter 6: References: Master Reference List:..... 167**
- Appendices: ..... 196**
  - Copyright permissions:..... 196
  - Ethics certificate: ..... 197

## List of Abbreviations

2-HG: 2-hydroxyglutarate

5mC: 5-methyl cytosine

ACTB: Actin Beta

ACVR1: Activin A receptor type I

ADARB2: Adenosine Deaminase RNA Specific B2

ANOVA: Analysis of variance

ARID1A: AT-rich interactive domain-containing protein 1A

ATAC-seq: Assay of Transposase accessible chromatin sequencing

ATCC: American Type Culture Collection

ATRT: Atypical teratoid rhabdoid tumour

ATRX: Alpha-thalassemia/mental retardation, X-linked

BAF: BRG1/BRM-Associated Factor

BAM: Binary Alignment Map

BET: Bromodomain and Extra-Terminal motif

bFGF: basic fibroblast growth factor

BT: brain tumour

BWA: Burrows-Wheeler Aligner

Cas9: CRISPR-Associated protein 9

CBX: chromobox

CDKN2A: Cyclin dependent kinase inhibitor 2A

CGI: CpG island

ChIP-Rx: Chromatin

Immunoprecipitation with Reference

Exogenous genome

ChIP: Chromatin Immunoprecipitation

CIMP: CpG Island Methylator

Phenotype

COMPASS: Complex of Proteins Associated with Set1

cPRC1: Canonical PRC1

CREBBP/EP300: E1A binding protein p300 and CREB-binding protein

CRISPR: Clustered Regularly

Interspaced Short Palindromic Repeats

CUT&RUN: Cleavage Under Target and Release Under Nuclease

CUT&Tag: Cleavage Under Targets and Tagmentation

DAAM1: Dishevelled Associated Activator Of Morphogenesis 1

DAXX: Death Domain Associated Protein

ddPCR: Droplet Digital Polymerase Chain Reaction

DIPG: Diffuse Intrinsic Pontine Glioma

DMEM: Dulbecco's Modified Eagle Medium

DMSO: Dimethyl Sulfoxide

DNA: Deoxyribonucleic Acid

DNMT3A/B: DNA Methyltransferases A/B

dsRNA: double-stranded RNA  
 ECL: Enhanced Chemiluminescence  
 EED: Embryonic Ectoderm  
 Development  
 EGFR: Epidermal Growth Factor  
 Receptor  
 eIF2a: Eukaryotic Initiation Factor alpha  
 EN1/2: Engrailed Homeobox 1/2  
 ENCODE: Encyclopedia of DNA  
 Elements  
 EPHB2: Ephrin type-B receptor 2  
 precursor  
 ERV: Endogenous Retrovirus  
 ETMR: Embryonal Tumour with  
 Multilayered Rosettes  
 EZH1/2: Enhancer of Zester Homolog  
 1/2  
 EZH2i: EZH2 inhibitor  
 EZHIP: EZH Inhibiting Protein  
 FBS: Fetal Bovine Serum  
 FDA: Federal Drug Administration  
 FDR: False Discovery Rate  
 FGFR1: Fibroblast Growth Factor  
 Receptor 1  
 FOXO3: Forkhead box O-3  
 GAPDH: Glyceraldehyde 3-phosphate  
 dehydrogenase  
 GFP: Green Fluorescent Protein  
 GO: Gene Ontology  
 H3: Histone 3  
 H3.3G34R/V: Histone H3.3 Glycine-34-  
 Arginine/Valine  
 H3K27M: Histone H3 Lysine-27-  
 Methionine  
 H3K36M: Histone H3 Lysine-36-  
 Methionine  
 HAT: Histone Acetyltransferase  
 HDAC: Histone Deacetylase  
 HDACi: Histone Deacetylase inhibitor  
 HGG: High-grade glioma  
 HOMER: Hypergeometric Optimization  
 of Motif EnRichment  
 HOX: Homeobox  
 HPLC: High-Performance Liquid  
 Chromatography  
 IC50: Half-maximal Inhibitory  
 Concentration  
 ICHANGE: International CHildhood  
 Astrocytoma INtegrated Genomic and  
 Epigenomic consortium  
 ID1-4: Inhibitor of DNA binding 1-4  
 IDH: Isocitrate Dehydrogenase  
 IFN-g: Interferon Gamma  
 IgG: Immunoglobulin G  
 IRX2: Iroquois Homeobox 2  
 ISG: Interferon-Stimulated Gene  
 KDM: Lysine Demethylase  
 KDM4: Lysine Demethylase 4  
 KDM6A/B: Lysine Demethylase 6A/B  
 KO: Knockout

LEDGF: Lens Epithelium-Derived Growth Factor  
LFC: Log2 Fold-Change  
LHX2: Lim Homeobox 2  
LIN28B: Lin-28 Homolog B  
LINE: Long Interspersed Nuclear Element  
LTR: Long Terminal Repeat  
MACS2: Model based Analysis of ChIP-seq S2  
MAVS: Mitochondrial Antiviral Signaling protein  
MB: Medulloblastoma  
MDA5: Melanoma Differentiation-Associated protein  
MLL: Mixed Lineage Leukemia  
mM: Millimolar  
MRI: Magnetic Resonance Imaging  
NFIB: Nuclear Factor I B  
nLC-MS: Nano Liquid Chromatography Mass Spectrometry  
nM: Nanomolar  
NOD-SCID: non-obese diabetic-severe combined immunodeficiency  
NPC: Neural Progenitor Cell  
NR4A2: Nuclear Receptor Subfamily 4 Group A Member 2  
NSG: NOD-SCID interleukin-2g (IL-2Rg)-chain-deficient

p300-CBP: E1A binding protein p300 and CREB-binding protein coactivator family  
PAGE: Polyacrylamide Gel Electrophoresis  
PAX3: Paired Box 3  
PCA: Principal Component Analysis  
PCGF1-6: Polycomb group Ring Finger Domain Proteins  
PCR: Polymerase Chain Reaction  
PDGFRA: Platelet Derived Growth Factor Receptor Alpha  
PDOX: Patient-Derived Orthotopic Xenograft  
PFA-EPN: Posterior-Fossa group A Ependymoma  
PKR: Protein Kinase R  
PLAG1: Pleomorphic adenoma gene 1  
PMD: Partially methylated Domain  
PPM1D: Protein Phosphatase, Mg<sup>2+</sup>/Mn<sup>2+</sup> Dependent 1D  
PRC1: Polycomb Repressive Complex 1  
PRC2: Polycomb Repressive Complex 2  
PTEN: Phosphatase and Tensin homolog  
PTM: Post-Translational Modification  
RBBP4/7: Retinoblastoma Binding Protein 4/7  
RELA: REL-Associated protein  
rhEGF: Recombinant human Epidermal Growth Factor  
RING1A/B: Ring finger protein 1A/B

RIPA: Radioimmunoprecipitation assay buffer  
RNA: Ribonucleic Acid  
PCR: Polymerase Chain Reaction  
RPKM: Reads Per Kilobase of transcript per Million mapped reads  
SE: Super Enhancer  
SETD2: SET Domain Containing 2  
shRNA: short hairpin RNA  
SINE: Short Interspersed Nuclear Element  
SMARCA4: SWI/SNF Related, Matrix Associated, Actin Dependent Regulator Of Chromatin, Subfamily A, Member 4  
SMARCB1: SWI/SNF Related, Matrix Associated, Actin Dependent Regulator Of Chromatin, Subfamily B, Member 1  
SNP: Single Nucleotide Polymorphism  
SOX2: SRY-Box Transcription Factor 2  
SOX4: SRY-Box Transcription Factor 4  
STAR: Spliced Transcripts Alignment to a Reference  
STR: Short Tandem Repeats  
SUZ12: Suppressor of Zester 12 Protein Homolog  
*t*-SNE: *t*-stochastic neighbor embedding  
TBST: Tris-Buffered Saline Tween  
TET1/2: Ten-Eleven Translocation 1/2  
TF: Transcription Factor  
TP53: Tumour Protein P53

TRANSFAC: TRANScriptioN FACtor database  
TSS: Transcription Start Site  
TTYH1-C19MC: Tweety Family Member 1- chromosome 19 microRNA cluster  
uM: Micromolar  
UNCX: UNC Homeobox  
WGBS: Whole Genome Bisulfite Sequencing  
WT: Wild Type  
ZMYND11: Zinc Finger MYND-Type Containing

# List of Figures

## Chapter 1

- Figure 1. Brain tumour subgroups associated with epigenetic remodeling.
- Figure 2. Epigenetic drivers potentiate tumour development in murine models.

## Chapter 2

- Figure 1. H3K27M-mutant pediatric high-grade gliomas (pHGGs) exhibit distinct distribution of H3K27me3 and H3K27me2.
- Figure 2. H3K27M reversibly induces global redistribution of H3K27me2 and H3K27me3.
- Figure 3. EZH2 inhibition does not completely mimic H3K27M effects and EZH2-Y641N partly overcomes H3K27M-induced effects.
- Figure 4. Transcriptome and H3K27me3 loci implicate H3K27M in neural differentiation
- Figure 5. H3K27M confers tumorigenicity in vivo.
- Supplementary Figure 1.
- Supplementary Figure 2.
- Supplementary Figure 3.
- Supplementary Figure 4.
- Supplementary Figure 5.
- Supplementary Figure 6.
- Supplementary Figure 7.
- Supplementary Figure 8.
- Supplementary Figure 9.
- Supplementary Figure 10.
- Supplementary Figure 11.
- Supplementary Figure 12.
- Supplementary Figure 13.
- Supplementary Figure 14.
- Supplementary Figure 15.
- Supplementary Figure 16.

- Supplementary Figure 17.
- Supplementary Figure 18.
- Supplementary Figure 19.
- Supplementary Figure 20.

### **Chapter 3**

- Figure 1. Active Regulatory Chromatin Landscape of Pediatric HGG.
- Figure 2. Core Regulatory SE and TF Programs Delineate H3.3K27M and H3K27WT HGG.
- Figure 3. Mapping of H3K27ac in Isogenic Models of H3K27M Reveal Minimal Alterations of Gene Transcriptional Programs.
- Figure 4. H3K27ac Deposits Pervasively across Intergenic Genome and Is Enriched at Repetitive Elements.
- Figure 5. H3.3K27M Tumors Exhibit Increased Deposition of H3K27ac and Transcription at Repetitive Elements.
- Figure 6. Repeat Element Primed K27M Cells Are Vulnerable to DNA Methylation and Histone Deacetylase Inhibitors.
- Figure 7. Epigenetic Therapies Activate Interferon Response Genes and dsRNA Sensing Pathways.
- Figure 8. Schematic Summary of Findings Resulting from this Study.
- Figure S1. Related to Figure 1.
- Figure S2. Related to Figure 3.
- Figure S3. Related to Figure 3.
- Figure S4. Related to Figure 4.
- Figure S5. Related to Figure 6.
- Figure S6. Related to Figure 6.
- Figure S7. Related to Figure 7.

### **Chapter 4**

- Figure 1. Summary of the chromatin consequences of the H3K27M mutation learned from isogenic modeling.
- Figure 2. Manipulation of driver events determines reversibility of tumour epigenomes.
- Figure 3. Chromatin modifiers in normal and altered development among brain tumours.

## List of Tables

Supplementary tables of Chapters 2 and 3 can be found through online links in each chapter.

### Chapter 3

- Key Resources Table

## Acknowledgements

I would like to thank my supervisor Dr. Nada Jabado for all the leadership and insight she has taught me over the years I have had the opportunity of working in her group. As both scientist and mentor she has inspired intellectual pursuit of big ideas across disciplines, original and creative thinking on problems ranging from fundamental science to clinical work, and taking on high-risk, high-reward science thanks to the resources she has built in her team of colleagues and collaborators. I am fortunate to have the privilege of many doors opened to advance my pursuit of academic research, thanks to her generosity and advice.

Our close collaborators Dr. Jacek Majewski, Dr. Claudia Kleinman, Dr. Stephen C. Mack have provided extensive mentorship on our research projects. Their contributions have built the work I present in Chapters 2 and 3, and I am grateful for all the insight they have provided our teams.

Dr. Ashot Harutyunyan and Dr. Nicolas De Jay as co-authors of chapters 2 and 3. I have learned a great amount of science from them and thank them for the collaborative effort that went into Chapters 2 and 3. I thank other members of the Nada Jabado laboratory, Damien Faury, Caterina Russo, Leonie Mikhael, Eef Harmsen, Nikoleta Juretic, Emily Nakada, Shriya Deshmukh, Shakour Mohammadnia, Andrea Bajic, Sima Khazaei, Maud Hulswit, Michele Zeinieh, Melissa McConechy, Carol Chen, Augusto Faria Andrade, Tenzin Gayden, Alexander Weil, Denise Bechet, Yelu Zhang, Jonathan Pratt, Amira Ouanouki, Katya Rossokhata, Elias Jabbour, Wajih Jawhar, Veronique Lisi, Josiane Franca, Gayathri Yogarajah, Chloe Dubuc-Landry, Jihane Adelon, Elvis Valera, Ricardo Santiago Gomez, Carolina Gomes, Adam Ptack and others.

I would like to acknowledge the contributions of many people to assist this research; the patients and their families for enabling research with use of their tissue, Dr. Michelle Monje, Dr. Keith Ligon and Dr. Peter Dirks for sharing tumour-derived cell cultures on which this work is based, and colleagues Dr. Peter Lewis and Dr. Chao Lu for sharing reagents and resources.

## **Contribution to original knowledge**

### **Chapter 2: H3K27M induces defective chromatin spread of PRC2-mediated repressive H3K27me2/me3 and is essential for glioma tumorigenesis. *Nature Communications* (2019)**

My work describes the effects of Histone 3 Lys-27-Met (H3K27M) mutations that define a subgroup of glioma brain tumours. This advance stems from our novel development and characterization of matched pairs of patient tumour-derived cell lines, created through CRISPR editing and removal of the H3K27M mutation. I establish a mechanistic understanding of how H3K27M affects chromatin by decreasing histone chemical modifications deposited polycomb repressive complex 2 (PRC2). My findings refute previous speculations that H3K27M physically sequesters PRC2 on chromatin, and instead show H3K27M's transient interaction with PRC2 results in altered enzyme kinetics. I gain further insight into the application of therapeutic strategies to treat patients, as the H3K27M mutation causes tumour cells to be sensitive to pharmacological inhibitors of PRC2. Finally, the potential of cells to form tumours when engrafted in mice is lost when H3K27M is removed. This demonstrates the mutation is continually required to preserve growth potential in the brain, despite other cancer-promoting mutations.

### **Chapter 3: Pervasive H3K27 acetylation leads to ERV expression and a therapeutic vulnerability in H3K27M gliomas. *Cancer Cell* (2019)**

This work characterizes the patterns and functions of histone 3 lysine 27 acetylation (H3K27ac), a representative feature of active chromatin, in H3K27M gliomas. I profile the landscape of enhancers and promoters of a large cohort of tumour tissue and cell lines, helping to delineate the tumours' precise and unique origins in development. My isogenic tumour lines further show that the H3K27M mutation elevates H3K27ac through pervasive distribution across chromatin. This invalidates previous reports proposing H3K27M creates a new enhancer landscape due to a rise in H3K27ac. My findings orient the field towards a model of how chromatin may generate a therapeutic vulnerability in this disease. I determined that H3K27M mutations render tumours vulnerable to histone deacetylase inhibitors and DNA demethylating agents through activation of a viral mimicry state, contributing to anti-tumour innate immune responses. This provides insight for understanding effects of the drug panobinostat that is in clinical use to treat patients. By

dissecting the effects of epigenetic therapies on this unique tumour type, this work informs the broader field of contexts in which targeted agents may achieve the most therapeutic success.

## Format of the Thesis

This thesis is written in accordance with the guidelines of McGill University Department of Human Genetics. I present a manuscript-based format using two publications as co-first author. In Chapter 1 I introduce chromatin biology in development and its dysregulation underlying brain tumorigenesis. In Chapter 2 I present the manuscript Harutyunyan & Krug, et al. (2019); *“H3K27M induces defective chromatin spread of PRC2-mediated repressive H3K27me2/me3 and is essential for glioma tumorigenesis.”* In Chapter 3 I present the manuscript Krug et al. (2019); *“Pervasive H3K27 acetylation leads to ERV expression and a therapeutic vulnerability in H3K27M gliomas.”* I summarize findings and discuss their relevance to the field in Chapter 4. Final conclusions and future directions are discussed in Chapter 5.

## **Contribution of Authors**

### **Introduction and Discussion**

Components of the introduction and discussion relate to content from the review Krug et al. (2021) in *Trends and Cell Biology*, co-authored with Ashot Harutyunyan, Shriya Deshmukh and Nada Jabado. I thank them for valuable discussion and help with literature review and figure preparation, as well as colleagues in the Nada Jabado laboratory and elsewhere for discussions on ideas and presentation.

### **Chapter 2**

Ashot Harutyunyan generated much of the ChIP-seq data and assisted in study design, data interpretation and manuscript preparation. Haifen Chen, Simon Papillon-Cavanagh, Nicolas De Jay, Rui Li, Hamid Nikbaht, Bo Hu, Gael Cagnon and Warren Cheung contributed to bioinformatic analysis of the data and interpretation of the results. Michele Zeinieh, Shriya Deshmukh, Carol Chen, Jad Belle, Abdulshakour Mohammadnia, Denise Bechet, Damien Faury, Melissa K. McConechy and Sid Jain contributed to data generation and analysis. Dylan Marchione and Benjamin Garcia led the histone proteomics experiments and analysis. Leonie G. Mikhael contributed to study design, data interpretation, and manuscript preparation. Benjamin Ellezam and Alexander G. Weil assisted with the collection of patient samples, study design and data interpretation. Manav Pathania and Paolo Salomoni generated the mouse model used for some ChIP-seq experiments, Alexander Montpetit., Tomi Pastinen, Chao Lu, Peter W. Lewis, Benjamin Garcia, Claudia L. Kleinman, Nada Jabado and Jacek Majewski contributed to study design, data interpretation, and manuscript preparation. I thank Alexey Soshnev for providing the comprehensive schema for the H3K27M mechanism of action.

### **Chapter 3**

Ashot Harutyunyan assisted in the generation of ChIP-seq data, study design, data analysis, interpretation, and manuscript preparation. Nicolas. De Jay led the bioinformatics analysis and assisted in study design, data analysis, interpretation, and manuscript preparation. Shriya Deshmukh and Damien Faury contributed to data collection, analysis and study design. Dylan Marchione and Benjamin Garcia led the histone proteomics experiments and analysis. Paul

Guilhamon and Mathieu Lupien led the ATAC-seq analysis. Kelsey C. Bertrand contributed to enhancer analysis, figure preparation, and data processing. Leonie G. Mikhael contributed to study design, data interpretation, and manuscript preparation. Benjamin Ellezam and Alexander G. Weil assisted with the collection of patient samples, study design and data interpretation. Daniel De Carvalho assisted the analysis and data interpretation regarding repeat element and ERV analysis. Paolo Salomoni generated the mouse model used for cross-species validation of repeat element expression. Claudia L. Kleinman, Nada Jabado and Stephen C. Mack contributed to study design, data interpretation, and manuscript preparation. Claudia L. Kleinman, Nada Jabado and Stephen C. Mack co-led and supervised the project. We thank Jacek Majewski for invaluable guidance in experimental design and critical reading of manuscript. I thank Alexey Soshnev for creating Figure 8.

# Chapter 1: Introduction

## Altered development at the core of pediatric and young adult brain tumours

Primary brain tumours (BT) are a significant cause of morbidity and mortality among children and young adults. These neoplasms are traditionally classified by their presumed cell of origin using histopathological features, into high-grade (grades 3 and 4) or low-grade (grades 1 and 2) tumours, and into specific prognostic subgroups by distinctive protein markers (Sturm et al., 2018). Tumours of presumed glial origin include gliomas, the most frequent malignant BT (~80%), and ependymomas (EPN). Gliomas display glial histological features and encompass a variety of heterogeneous biological subgroups, that are further subdivided in low-grade or high-grade tumours based on morphology, proliferation index, and the level of angiogenesis and necrosis in the tumour. Ependymomas are a type of glioma located in the brain or spinal cord occurring predominantly in children and are thought to arise from ependymal cells. Tumours of neuronal origin include embryonal tumours such as medulloblastomas (MB), atypical teratoid/rhabdoid tumours (ATRT) and embryonal tumours with multilayered rosettes (ETMR). Genomic analysis and molecular profiling helped refine their categorization into prognostic subgroups based on molecular profiles and DNA methylation patterns (Capper et al., 2018; Louis et al., 2021; Sturm et al., 2012, 2014a). A central trend emerging from these studies is the deregulation of the epigenome during development at the core of BT pathogenesis. Many driver events display tight spatiotemporal patterns in the brain, promote altered epigenetic states, and associate with specific lineages of origin as shown in recent single-cell transcriptomic studies (Jessa et al., 2019; Vladioiu et al., 2019). I will review herein the main epigenetic alterations identified in subgroups of high-grade gliomas (HGG) and posterior fossa group A EPN (PFA-EPN). Accumulating evidence shows these alterations can promote tumorigenesis in experimental model systems. Among driver events, the deregulation of Polycomb Repressive Complex 2 (PRC2) targets is a shared outcome among several brain tumour entities. The Histone H3 Lys-27-Met (H3K27M) mutation of pediatric HGGs provides a window of insight into chromatin remodeling at the core of brain tumorigenesis that will be the focus of this thesis.

## **The epigenome and chromatin remodeling in development**

Cytosine DNA methylation (5mC) and histone post-translational modifications (PTMs) form a reversible code that regulates processes acting on DNA, including replication, repair, gene expression and maintenance of chromosome structure (Jenuwein & Allis, 2001). Histone H3 proteins are a core component of the nucleosome, the fundamental unit of chromatin, which can be modulated by a large variety of PTMs which associate with repressive (heterochromatin) or active (euchromatin) states. Here I focus on methylation and acetylation of specific lysine (K) residues on the H3 N-terminal tail, that are the primary targets altered by H3K27M mutations. The trimethylation of either H3K9 or H3K27 (H3K9me<sub>3</sub>/H3K27me<sub>3</sub>) establish heterochromatin and silence transcription, viewed as either constitutive (permanent, regardless of cell state; H3K9me<sub>3</sub>) or facultative (context-dependent; H3K27me<sub>3</sub>). The dimethylated states of these residues; H3K9me<sub>2</sub>/H3K27me<sub>2</sub>, are deposited in distinct areas of chromatin from H3K27me<sub>3</sub>/H3K9me<sub>3</sub> and appear to favour repression, but not as strongly as what is observed in trimethylated domains (Ferrari et al., 2014; Jih et al., 2017). H3K27 is uniquely methylated by PRC2 through either catalytic subunit; Enhancer of Zester Homolog 1 or 2 (EZH1/2), in complex with other core subunits Embryonic Ectoderm Development (EED), Suppressor of Zeste Homolog 12 (SUZ12) and Retinoblastoma Binding Protein 4 or 7 (RBBP4/7) (Laugesen et al., 2019; Schuettengruber et al., 2017; Yu et al., 2019). H3K27 lysine demethylases 6A and 6B (KDM6A/B) oppose the methylation of H3K27 through active removal. Polycomb Repressive Complex 1 (PRC1) is a related group of subcomplexes that serve both repressive chromatin compaction and activating functions on gene expression. All PRC1 complexes share core subunits; RING1A or RING1B that ubiquitylate histone 2A K119 (H2AK119ub), and one of the six Polycomb group ring-finger domain proteins (PCGF1–PCGF6), while accessory subunits distinguish either canonical or variant complexes. Canonical PRC1 (cPRC1) is the main reader protein of H3K27me<sub>3</sub> through chromobox (CBX) subunits and contributes to chromatin compaction (Piunti & Shilatifard, 2021). In mammalian cells, PRC2 is recruited to cell-type specific nucleation sites, often corresponding to CpG islands (CGIs) devoid of 5mC. Upon nucleation, the complex deposits and spreads the H3K27me<sub>2</sub>/me<sub>3</sub> marks throughout adjacent domains. Several other mechanisms, including interaction with RNA and reciprocal interplay with PRC1, can influence PRC2 recruitment to chromatin and its localization (Laugesen et al., 2019; Yu et al., 2019). PRC1 and PRC2 cooperatively regulate diverse cellular processes, including X-chromosome inactivation, genomic

imprinting, the cell cycle, stem cell self-renewal or differentiation, and oncogenic transformation. This functional diversity is achieved by PRC1/2 subunit heterogeneity, as complexes are assembled in a developmental-stage- and cell-specific manner to establish PTMs at target genes, and modify higher-order chromatin structure (Chan & Morey, 2019).

As heterochromatin is maintained and inherited across cell divisions, activation of repressed promoters requires the demethylation of H3K27me<sub>3</sub>, eviction of PRC2 and occupancy by transcription-favouring complexes. These transitions involve complexes belonging to the Trithorax Group, including Complex Proteins Associated with Set1 (COMPASS) and BRG1/BRM Associated Factors (BAF) complexes that compete with PRC2/1 for occupancy and activation of target genes (Schuettengruber et al., 2017). Within COMPASS complexes, lysine methyltransferases of the Mixed Lineage Leukemia family (MLL, also known as KMT2 family) deposit H3K4me<sub>3</sub> at sites of transcription initiation and H3K4me<sub>1</sub> at sites primed for enhancer-promoter activity. Active cis-regulatory elements and promoters also acquire H3K27 acetylation (H3K27ac), deposited by the E1A binding protein p300 and CREB-binding protein (p300-CBP) coactivator family of acetyltransferases. While H3K27ac is the most characterized acetyl PTM, numerous other histone lysine residues are modified to serve regulatory functions. Acetylation of lysine residues weakens electrostatic charge-based affinity of DNA for histones and promote an accessible state for transcription (Chang & Takada, 2016). Various acetyl PTMs are also recognized, or 'read' by bromodomain-containing proteins that localize complexes favouring transcriptional activation (Marmorstein & Zhou, 2014). Genome-wide distributions of histone acetylation are controlled by the countering effects of histone deacetylases (HDACs) when these enzymes are located in the nucleus. The profiling of H3K27ac has served as an approach to catalog the landscape of active enhancers and promoters in particular biological contexts. The top-ranked cis-regulatory elements by H3K27ac abundance, termed 'super enhancers', have shown associations with important oncogenes and cell identity markers (Blobel et al., 2021). Maps of super enhancers have helped refine the classification of cancer subgroups informed by epigenetic states (Mack et al., 2018). Active gene bodies and intergenic euchromatin are marked by H3K36me<sub>2</sub>. Genic regions acquire H3K36me<sub>3</sub> uniquely via SET Domain containing 2 (SETD2) recruitment after splicing of genes' first intron sequences. The recognition of H3K36me<sub>2</sub> and H3K36me<sub>3</sub> by DNA Methyltransferases 3A and 3B (DNMT3A and DNMT3B), respectively,

result in 5mC deposition throughout euchromatin, while promoter DNA methylation is generally associated with gene silencing (Baubec et al., 2015; Weinberg et al., 2019). H3K36me<sub>2/3</sub> and 5mC can limit the spread of H3K27me<sub>2/3</sub> through hindrance of PRC2 activity (Niessen et al., 2009; Streubel et al., 2018; Yu et al., 2019). Mutual exclusivity of active and repressive marks (H3K27ac and H3K27me<sub>2/3</sub>) and indirect antagonism by regulation of methyltransferases (PRC2 and H3K36me<sub>2/3</sub>) help establish and preserve distinct domains of active and repressive chromatin. The antagonism between PRC2/PRC1 and Trithorax Group complexes are part of an evolutionarily conserved epigenetic memory system that maintains active and repressed promoter states (Schuettengruber et al., 2017). The transition from pluripotent stem cells to neural progenitors and further differentiation into neuronal and glial lineages is characterized by major epigenetic changes, wherein redistribution of H3K27me<sub>3</sub> plays a major role (Albert & Huttner, 2018). Deregulation of PRC2 is an oncogenic mechanism shared by numerous drivers in the development of brain tumours that will be described below.

The complexity of eukaryotic genomes is marked by a major contribution of repetitive DNA elements, that are estimated to represent approximately 70% of the human genome (de Koning et al., 2011). These sequences are broadly classified into families of RNA-transcribed retroelements; Long Interspersed Nuclear Elements (LINES), Short Interspersed Nuclear Elements (SINEs) and Long Terminal Repeats (LTRs), or DNA-based elements; transposons and tandem repeats (Wells & Feschotte, 2020). Heterochromatin states marked by H3K27me<sub>3</sub>, H3K9me<sub>3</sub> or H4K20me<sub>3</sub> contribute to preventing transcription of repetitive elements and the structural integrity of chromosome architecture, such as centromeres and telomeres (Almeida et al., 2022). Cells depend on this repression to prevent deleterious outcomes of repeat element transcription, yet we are also gaining appreciation of adaptive relationships between cell physiology and repeat element-derived RNA. 5mC is another central mechanism for preserving the fidelity of active transcription in genic regions through H3K36me<sub>3</sub>-recruited DNMT3B, and H3K36me<sub>2</sub>-recruited DNMT3A. 5mC is linked with prevention of spurious transcription initiation through obstructing stable transcription factor binding to DNA and by reader protein interactions that bridge complexes driving repressive chromatin (Jansz, 2019).

## **Epigenetic events underlie pediatric and young adult HGGs**

***IDH-mutant gliomas.*** Recurrent somatic heterozygous mutations in isocitrate dehydrogenase (*IDH*) 1 and 2 are found in young adult gliomas. They affect specific residues of these enzymes, mainly R132 of *IDH1* and R172 of *IDH2*, and result in loss of native function of the wild-type enzyme. *IDH1/2* mutations are early events in gliomas and are maintained in recurrences after treatment and in progression to HGG (Juratli et al., 2012; Watanabe et al., 2009). *IDH*-mutant tumours occur mainly in the frontal brain and are uniformly deadly when they associate with *TP53* alterations and loss-of-function alterations in the chromatin remodeler and H3.3 chaperone, alpha-thalassemia/mental retardation-X-linked (*ATRX*) (Figure 1) (Liu et al., 2012). *IDH*-mutants show neomorphic activity and generate an oncometabolite 2-hydroxyglutarate (2-HG) that competitively inhibits Ten-Eleven Translocation (*TET1/2*) DNA demethylases as well as Jumonji-domain histone lysine demethylases (*KDMs*) (Lu et al., 2012). *TET1/2* inhibition by *IDH* mutants produces a CpG island methylator phenotype (*CIMP*) characterized by DNA hypermethylation in tumours (Noushmehr et al., 2010). However, exogenous introduction of *IDH* mutations into cells does not consistently induce *CIMP* (Bardella et al., 2016), suggesting a time-dependent clonal evolutionary process in tumours. *IDH* mutants can also variably induce gain of H3K4me<sub>3</sub>, H3K9me<sub>3</sub>, H3K27me<sub>3</sub> and H3K36me<sub>3</sub> through *KDM* inhibition (Lu et al., 2012; M. Gagné et al., 2017; Turcan et al., 2018). Recent data suggests that H3K27me<sub>3</sub> dysregulation through *KDM6A/B* demethylase silencing may potentially play a greater role in transcriptional silencing of *PRC2* target genes than the 5mC-based *CIMP* in *IDH*-mutant tumours (Court et al., 2019). Nonetheless, the specific epigenetic mechanisms by which *IDH* mutants favour the acquisition of *CIMP* and alter gene expression associated with proliferation and stemness remain the subject of active investigations.

***H3-mutant gliomas.*** Disruptions to tumour chromatin states are caused by recurrent somatic mutations at specific residues of H3 variants in HGG affecting children and young adults (Figure 1) (Fontebasso, Schwartzentruber, et al., 2013; Schwartzentruber et al., 2012; Sturm et al., 2012; Wu et al., 2014). H3 mutations, termed oncohistones, show neuroanatomical specificity and associate with distinct DNA methylation patterns, age distributions and partnering genetic alterations. Lysine 27 to methionine amino acid substitutions occur in any H3 variant (*H3K27M*) in gliomas located in the thalamus, midbrain and occasionally the spinal cord (Sturm et al., 2012).

These mutations predominate in children and young adults and very rarely target older patients (Mackay et al., 2017). Glycine 34 to arginine or valine substitutions specifically target noncanonical H3.3 (H3.3G34R/V) and are identified in adolescent/young adult HGG located in the temporo-parietal cortex. These mutations are mutually exclusive with each other and with IDH-mutant tumours and define unique biological subgroups of gliomas (Sturm et al., 2012). They highlight how changing selective pressures can drive gliomagenesis in different developmental contexts.

**H3K27M mutations.** H3K27M mutations are the presumed initiating genetic lesion observed in a high proportion of midline gliomas, as they are clonal among tumour cells (Mackay et al., 2017; Nikbakht et al., 2016). Rare case reports identify H3K27M as the sole initial genetic alteration in low-grade tumours which subsequently transform to HGG upon acquisition of other genetic alterations (Joyon et al., 2017). Early cooperating partner mutations with this subgroup include somatic loss of p53 function or related pathway members (*PPM1D*), and mutually exclusive gain-of-function mutations or genetic amplification of growth factor receptors involved in brain development, namely *ACVR1/ALK2* in the pons, *FGFR1* and *EGFR* in the thalamus and cerebellum, and *PDGFRA* across all brain regions (Fontebasso, Papillon-Cavanagh, et al., 2014; Khuong-Quang et al., 2012; Mackay et al., 2017).

H3K27M mutant histones are dominant negative inhibitors of PRC2 activity, and Chapter 2 will discuss the contribution of this thesis to the field. Even though mutant histones account for only small minority of all H3, they diminish PRC2 activity in the majority of the H3 pool, across models spanning from *C. elegans* to human tumours (Bender et al., 2013; Chan et al., 2013; Delaney et al., 2019; Funato et al., 2014; Lewis et al., 2013; Mohammad et al., 2017; Piunti et al., 2017). Indeed, lysine-to-methionine and lysine-to-isoleucine mutants of H3 impair the catalytic activities of methyltransferases acting on the respective mutant residue, including H3K4, K9, K27 and K36 (Lewis et al., 2013). H3K27M affects PRC2 deposition of K27me<sub>2/3</sub> and diminishes EZH2 automethylation that normally enhances its catalytic activity (Lee et al., 2019). Structural resemblance of K-M and K-I mutants to suitable substrates of lysine methyltransferase catalytic domains plausibly accounts for their inhibitory effects. In this scenario, the H3K27M mutant residue acts as suicide substrate interacting with EZH2, as the catalytic cycle of transferring a methyl group from s-adenosyl methionine to the K27M residue cannot be completed (Justin et al.,

2016). However, the nature of the physical interaction between these oncohistones and target methyltransferases in the context of chromatin remains unclear. There is residual H3K27me3 deposition on chromatin of H3K27M-expressing cells (Bender et al., 2013; Chan et al., 2013; Mohammad et al., 2017), indicating that the mutant does not result in complete loss of PRC2 function. Some models propose that H3K27M physically sequesters PRC2 on mutant nucleosomes on chromatin based on increased binding of the complex to H3K27M, while others suggest the reverse and no increased affinity of this complex to H3K27M-mutant nucleosomes compared to wild-type (Herz et al., 2014; Wang et al., 2017). Regardless, the strength of associations between PRC2 and mutant peptides, mutant histones, or native chromatin substrates largely depends on the experimental context across these biochemical studies. Other hypotheses of H3K27M mode of action favour residual recruitment of PRC2 mainly to its strong affinity sites (Mohammad et al., 2017), or suggest its exclusion from its nucleation sites by heterotypic H3K27M-K27ac nucleosomes that may create new active enhancer landscapes due to increased H3K27ac levels in H3.3K27M mutant cells (Piunti et al., 2017). I will further elaborate on the role of H3K27M in chromatin remodeling in Chapters 2 and 3.

**H3.3G34R/V mutations.** H3.3G34R/V account for 30% of HGGs in adolescents and young adults. These tumours almost invariably carry partner mutations in *ATRX* and *TP53*, and cluster distinctly from other glioma entities based on DNA methylation (Figure 1) (Sturm et al., 2012). Transcriptomic analysis of G34R/V HGGs reveals these mutations occur in interneuron progenitors during early development and that G34R/V or W mutations may affect splicing (Bressan et al., 2021; Chen et al., 2020; Funato et al., 2021). Activation of the MAPK pathway, largely through *PDGFRA* overexpression and gain-of-function mutations, is a major promoter of tumorigenic growth and endows abnormal characteristics of astrocytes that contributes to them being labeled as gliomas. The lineage of origin may facilitate *PDGFRA* co-option through a chromatin loop connecting *PDGFRA* to regulatory elements of the interneuron progenitor core transcription factor *GSX2*, thereby facilitating *PDGFRA* overexpression and possible subsequent mutation of this gene (Chen et al., 2020).

In contrast to H3K27M that affects both canonical H3.1/2 and H3.3 variants, G34R/V mutations occur exclusively on non-canonical H3.3 and appear to act *in cis*, with the mutation affecting PTMs solely on the mutant peptide and not WT histones (Lewis et al., 2013). Substituting glycine 34 for

a variety of larger sized residues hinders the trimethylation of the adjacent K36 residue, as well as reader protein recognition of H3.3K36me3 (Fang et al., 2018; Wen et al., 2014; Yadav et al., 2017). H3.3G34R/V can also inhibit the KDM4 family of demethylases, thus indirectly altering H3K9 and H3K36 methylation (Voon et al., 2018). On H3.3G34 mutant histones, decreased H3K36me3 correlates with the gain of the antagonistic mark, H3K27me3, and decreased expression of genes enriched for this PTM in tumour cells (Chen et al., 2020; Jain et al., 2020). In HGGs, this effect appears to cooperatively impair interneuron differentiation. Other recent studies identify forebrain progenitors as the lineage amenable to H3.3G34R/V oncogenic effects, compared to other lineages and brain locations (Funato et al., 2021, Bressan et al., 2021). The creation of new focal H3K27me3 domains by H3.3G34 mutations parallels patterns of chromatin in giant cell tumours of the bone (Khazaei et al., 2020), which universally carry H3.3G34W/R/L mutations (Behjati et al., 2013). The contribution of PRC2 in the oncogenic process is further substantiated by experiments in which H3.3G34W-K27R double mutants, which are unable to acquire H3K27me3, are less effective in promoting tumour development in mouse mesenchymal cells (Jain, et al., 2020).

The HIRA chaperone deposits H3.3 in the bodies of actively transcribed genes, while the ATRX/DAXX chaperone complex facilitates its deposition in pericentromeric and telomeric heterochromatin (Hammond et al., 2017). These selective deposition patterns likely restrict potential cis-regulatory elements amenable to be repressed by H3.3G34 mutations. ATRX loss-of-function in H3.3G34R/V HGGs may thus drive enhanced remodeling of histone methylation, through increased amounts of H3.3, including mutant H3.3, deposited in euchromatin by HIRA. Collectively, a key role for PRC2 emerges in mediating tumorigenesis. H3.3G34R/V can lead to PRC2 redistribution and the creation of ectopic H3K27me3 domains, which are likely an initial requirement for transformation in H3.3G34 mutants.

**H3 and IDH wild-type HGGs.** In the brain midline, rare H3 wild-type HGGs have carried *IDH* hotspot mutations (L. Zhang et al., 2014), or *MYCN* amplification (Buczkwicz et al., 2014), or ectopic expression of the oncohistone mimic EZH Inhibiting Protein (EZHIP), which is normally seen in PFA-EPN (Sievers et al., 2020). In hemispheric pediatric and young adult HGGs, loss-of-function mutations in the H3K36 methyltransferase *SETD2* and in rare cases in the H3.3K36me3 reader *ZMYND11* have been identified and occur in association to *TP53* and *ATRX* loss

(Fontebasso, Schwartzentruber, et al., 2013; Salloum et al., 2017). This suggests that the loss of H3K36 methylation may parallel the effects of mutually exclusive H3.3G34R/V mutations (Figure 1).

In summary, midline HGG are primarily defined by decreased H3K27me<sub>2/3</sub>, due to H3K27M (~85%) or aberrant expression of EZHIP (10%), while hemispheric HGGs show genetic alterations affecting the methylation of H3K36 and frequent loss-of-function alterations in *ATRX*. More work is needed to better understand the role of cooperating partner mutations shared between oncohistones and IDH mutations and how they promote tumour formation in gliomas.

### **PFA-EPN**

Ependymomas are classified into subgroups by DNA methylation profiles (Pajtler et al., 2015). Among these subgroups, PFA-EPN occur in the hindbrain, affect mainly younger children and show similar dismal prognosis as H3K27M-mutant HGGs. Tumours display CIMP characteristics but lack recurrent genetic alterations, which have exemplified a context of chromatin-driven cancer development (Mack et al., 2014). Recently, abnormal expression of *EZH1P* was shown to occur in ~95% of PFA-EPN and to induce decreased H3K27me<sub>3</sub> levels, while mutually exclusive H3K27M mutations were found in the remaining ~5% (Figure 1) (Pajtler et al., 2018; Ryall et al., 2017). *EZH1P* was subsequently characterized as a factor associating with PRC2 and acts as allosteric inhibitor (Hübner et al., 2019; Jain et al., 2019; Piunti et al., 2019). The sole region of sequence conservation across species in this gene encodes a 12 amino acid peptide sequence, which mimics the H3 tail with a methionine in the site analogous to lysine 27, mirroring H3K27M. This domain potently impairs catalysis of H3K27me<sub>2/3</sub> when *EZH1P* associates in complex with PRC2, and correlates with significant loss of H3K27me<sub>3</sub> previously noted in PFA-EPN tumours, as well as oocytes where *EZH1P* is normally expressed (Bayliss et al., 2016; Jain et al., 2019; Jain, Rashoff, et al., 2020; Ragazzini et al., 2019). *EZH1P* is not incorporated into chromatin but acts similarly to H3K27M and inhibits PRC2, globally reducing H3K27me<sub>3</sub> levels. This finding strengthens the hypothesis that transient association of the oncohistone with PRC2 is sufficient for inhibition of the complex. Functionally interchangeable effects are presumed from rare cases of PFA-EPNs carrying H3K27M mutations, and histone-WT midline HGGs displaying *EZH1P* expression. However, PFA-EPNs arise in a unique context of early brain development linked with hypoxia,

and tumour cells resemble prenatal gliogenic progenitors (Michealraj et al., 2020). Their growth and epigenetic states depend on low oxygen conditions. The dependence of PFA-EPN tumour cells on residual PRC2 activity parallels that of H3K27M-HGGs, as cells likely require the repression of specific H3K27me<sub>3</sub>-marked promoters (Michealraj et al., 2020). EZHIP is a requirement of PFA-EPN cells to maintain loss of H3K27me<sub>2/3</sub>, and in some contexts, proliferative fitness (Piunti et al., 2019). Mechanisms by which tumours abnormally co-opt its expression remain unclear, and likely involve loss of promoter 5mC and responses to hypoxia (Michealraj et al., 2020; Pajtler et al., 2018; Piunti et al., 2019). In all, PFA-EPNs present a unique case of tumour progression involving metabolic-epigenetic crosstalk hinging on abnormal EZHIP expression and leading to the restraint of PRC2 activity.

### **Embryonal brain tumours with epigenetic drivers dysregulate PRC2 targets**

Subunits of BAF complexes are frequently mutated in diverse cancers including ATRTs. In these embryonal BTs, homozygous loss of *SMARCB1* (also known as *SNF5*, *BAF47* or *INI1*) or rarely of *SMARCA4*, are the sole recurrent genetic alterations identified in tumours (Figure 1). In close to 30% of ATRTs, and mainly in younger children, *de novo* germline heterozygous *SMARCB1* mutations predispose patients to these rhabdoid tumours. Integrated expression and DNA methylation further partition ATRTs into 3 molecular entities (Johann et al., 2016; Torchia et al., 2016). *SMARCB1* loss disrupts the antagonism between BAF and PRC2 complexes, leading to widespread gain of H3K27me<sub>3</sub> at PRC2 target genes (Wilson et al., 2010). H3K27me<sub>3</sub>-mediated repression at neuronal differentiation genes reflects the inability of cells to evict PRC2 in the absence of SMARCB1, likely favouring self-renewal (Erkek et al., 2019). Preliminary clinical data in rhabdoid tumours indicate sensitivity to pharmacological inhibition of EZH2, supporting the importance of H3K27me<sub>3</sub> in the maintenance of tumorigenesis (Knutson et al., 2013).

In the cerebellum, recurrent mutations in chromatin modifiers have been identified in the 4 major MB subgroups (Figure 1). These include *MLL2/3*, *SMARCA4*, *ARID1A*, and *KDM6A*, highlighting alterations of COMPASS, PRC2 and BAF complexes in these tumours (Northcott et al., 2017). Mutation of *MLL2/3* methyltransferases results in loss of H3K4me<sub>3</sub>, while *KDM6A* alterations increase H3K27me<sub>3</sub> levels. Given that *KDM6A* can be a component of COMPASS and can also associate with BAF complexes that compete with PRC2 on target promoters (Narayanan et al., 2015), tumours with these mutations may fail to transition repressed polycomb targets to an active

state, thus promoting progenitor cell self-renewal. In mouse models, the overexpression of the PRC1 subunit *Bmi1* combined by *Trp53* loss (Behesti et al., 2013), or deletion of COMPASS subunit *Mll4* can induce medulloblastoma development (Dhar et al., 2018), which implicate the importance of polycomb target regulation in tumour initiation. In ETMR, a fusion between *TTHY1* and the C19MC microRNA cluster leads to expression of this microRNA cluster, which is normally restricted to the trophoblast (Figure 1) (Kleinman et al., 2014). These microRNAs promote overexpression of fetal brain-specific isoforms of the *de novo* DNA methyltransferases DNMT3B and DNMT3A. This leads to abnormal DNA methylation patterns, including gain of methylation at PRC2 target promoters, resulting in an oncogenic state that recapitulates early neurogenesis. Single-cell transcriptomics describe ETMR cells in self-renewing states that are unable to progress along their programmed differentiation path, helping explain their histology that resembles undifferentiated neural tubes (Jessa et al., 2019). These tumours thus represent another context where disrupted expression of PRC2 target genes is connected to cellular transformation.

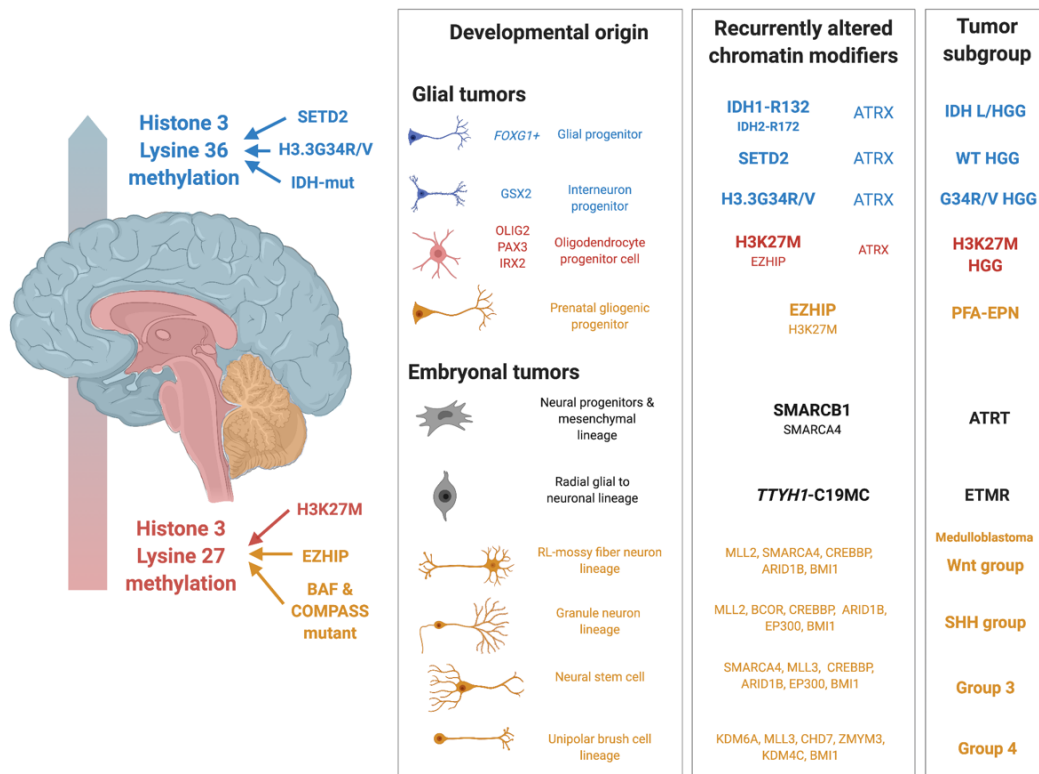


**Figure 1. Brain tumour subgroups associated with epigenetic remodeling.**

Brain tumours are broadly stratified as glial or embryonal, and by regions of occurrence in the forebrain (blue), midbrain and pons (red) or cerebellum (yellow). Tumours arising in early development are located in the midbrain, pons and cerebellum events and are characterized by events altering the methylation of histone 3 lysine 27 (H3K27). H3 lysine 27-methione (H3K27M) mutations and EZH Inhibiting Protein (EZHIP) are likely functionally interchangeable yet associate with either oligodendroglial fates in midline high-grade glioma (HGGs) or radial glial progenitors in posterior fossa group A ependymomas (PFA-EPN). Low and High-Grade Glioma (L/HGG) subgroups of later childhood and young adults target the cortical hemispheres, and carry H3.3G34R/V, isocitrate dehydrogenase 1 or 2 mutations (*IDH1*-R132/*IDH2*-R172) and/or loss of SET domain containing 2 (SETD2) function. These events converge on altering higher methylation states at H3K36, with implications for altered polycomb complex distribution. Subgroup-specific lineage markers demarcate driver mutation associations with glial cell types. Atypical teratoid/rhabdoid tumours (ATRT) driven by *SMARCB1* or occasionally *SMARCA4* loss arise from early neural or mesenchymal progenitors in the brain. Embryonal tumours with multilayered rosettes (ETMR) present unique DNA methylation landscape likely tied to the *TTYH1*-C19MC fusion event, with their transcriptomes recapitulating a neuronal lineage. Four MB subgroups match different neuronal lineages from the cerebellum and carry a variety of mutations in epigenetic targets. The figure is reproduced from Krug et al. (2021) and created with Biorender.com.

### **Modeling of brain tumour epigenomes and their therapeutic targeting**

Mouse models have facilitated appreciation of the contexts in which IDH, H3K27M and SMARCB1 mutations can promote brain tumour development (Figure 2). Introduction of *IDH1*-R132H establishes proliferative and infiltrative progenitors of the subventricular zone and metabolic changes favoring glioma initiation (Bardella et al., 2016; Sasaki et al., 2012). In cooperation with *PDGFRA* overexpression and *CDKN2A*, *PTEN* and *ATRX* loss, IDH mutants accelerate glioma progression and establish tumour expression and 5mC profiles resembling human IDH-mutant tumours. Targeted expression of H3K27M cannot drive HGG development alone and requires cooperation with p53 loss in specific developmental windows (Pathania et al., 2017). This is shown by the embryonic brain being more amenable to transformation than the postnatal brain. *PDGFRA* overexpression and activating mutations accelerate tumour onset, high-

grade features and glial histology (Figure 2) (Larson et al., 2019). These 3 events also impair astrocytic differentiation of neural progenitor cells *in vitro* (Funato et al., 2014). H3K27M can also cooperate with *Acvr1* and *Pik3ca* signaling that help establish a glial progenitor state and resultant tumour formation (Fortin et al., 2020). The restricted developmental windows for H3K27M tumorigenesis may thus relate to chromatin states in the progenitor of origin and its responsiveness to sustained mitogenic signaling. In preclinical models, efforts to target H3K27M HGGs have included inhibition of PRC1 (Balakrishnan et al., 2020), PRC2 (Mohammad et al., 2017), reversal of H3K27me3 loss by inhibition of KDM6B (Hashizume et al., 2014), HDACs (Grasso et al., 2015), or bromodomains (Piunti et al., 2017), or combination therapies of the above pathways (Lin et al., 2019). I will expand on HDAC inhibitors (HDACi) and DNA demethylating agents targeting H3K27M gliomas in Chapter 3. Current clinical trials targeting the epigenome are still in early development. They include the use of HDACi or DNA demethylating agents, and local delivery of EZH2 inhibitors as there are no brain-penetrant compounds currently available (Sasaki et al., 2020). The DNA demethylating agent 5-azacytidine is also in clinical testing for PFA-EPNs (Sandberg et al., 2019). In embryonal tumours, epigenetic models are mainly available for ATRTs (Figure 2). Targeted loss of *Smarchb1* in combination to *Tp53* loss in astrocytic lineages (Ng et al., 2015), or ubiquitous loss of the gene only between E6 and E10 led to tumours resembling human ATRT (Han et al., 2016). The narrow temporal window for oncogenic manifestations of *Smarchb1* loss was further emphasized when loss of this gene in the neural crest lineage prior to E12.5 also led to rhabdoid tumours (Vitte et al., 2017). SMARCB1 absence is required for the continued fitness of ATRT cells. Its restoration favors gain of H3K27ac and diminished proliferation, impaired growth and increased cell cycle arrest (Erkek et al., 2019). Loss of BAF complex function thus likely overcomes barriers to transformation beyond lineage differentiation.

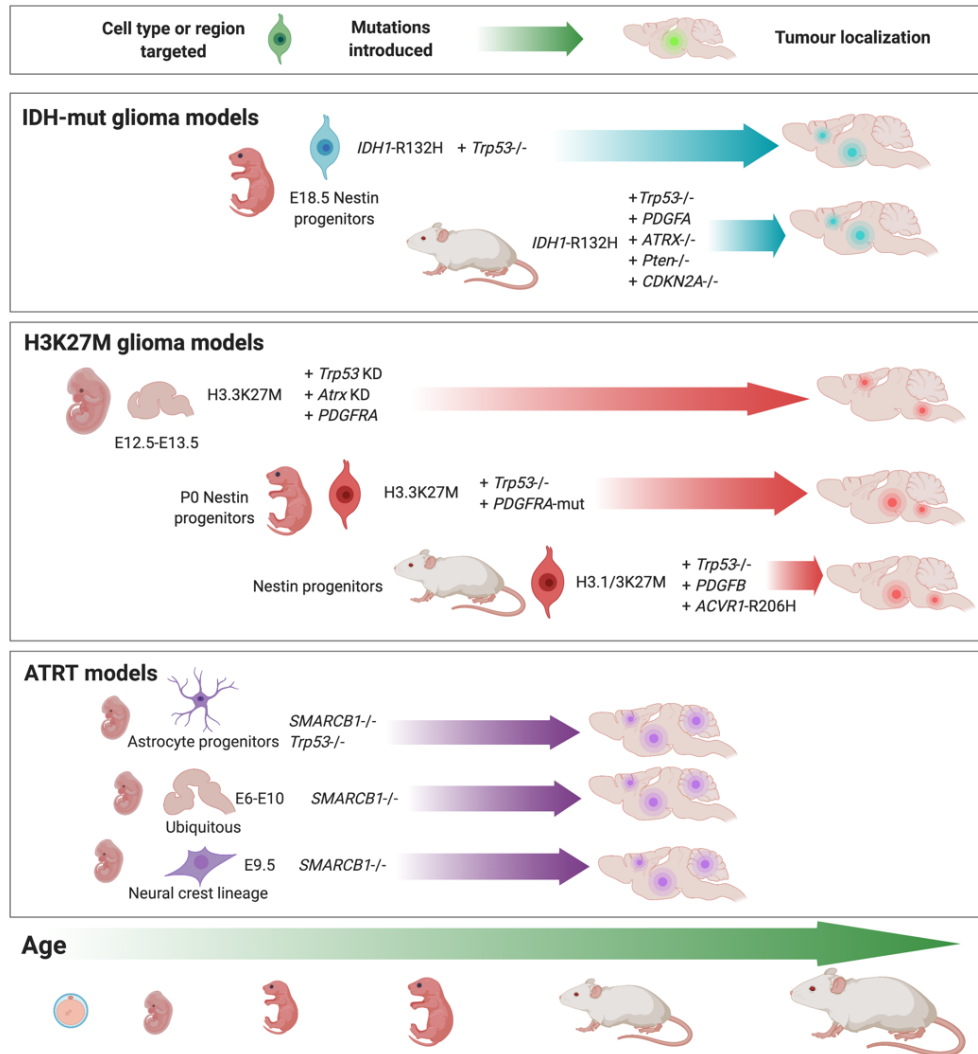


**Figure 2. Epigenetic drivers potentiate tumour development in murine models**

The introduction of epigenetic driver events in mice has revealed the dependencies of tumour formation on time windows, combinations of cooperating oncogenic stimuli, and cell type, lineage or brain region in which they are introduced. In H3K27M, added *Trp53* loss is sufficient to induce HGGs. In other H3K27M mouse models, in addition to loss of p53 function, additional *PDGFRA*/*PDGFB* overexpression or activating mutations, or *ACVR1-R206H* appear needed to accelerate disease onset and induce features of human HGG. *IDH1-R132H* mutant cells also requires *Trp53* loss for tumorigenicity and can promote tumours resembling human disease from late embryonic development to adulthood. Loss of *Smarcb1* transforms neural progenitors either in combination with *Trp53* loss, or on its own between embryonic development days 6-10. The figure is reproduced from Krug et al. (2021) and created with Biorender.com.

## **Hypothesis and Objectives**

The H3K27M oncohistone has been established to be a dominant negative inhibitor of PRC2 catalytic activity towards depositing H3K27me2 and H3K27me3. However, early studies have nonetheless observed residual deposition of H3K27me3 peaks in tumour models (Chan et al., 2013; Mohammad et al., 2017). The role of elevated H3K27ac is also unclear based on weak evidence of altered enhancer landscapes in H3K27M tumours. Introduction of the mutation into mice using various techniques clearly show it can potentiate tumour development, in cooperation with other genetic drivers (Larson et al., 2019; Pathania et al., 2017). *In vitro* cell culture models implicate H3K27M, PDGFRA gain of function and p53 loss with impaired differentiation potential (Funato et al., 2014). These findings link remodeling of chromatin with the basis for cellular transformation. However, we lack an understanding of the role of altered PRC2 activity plays in driving the human disease. Given that H3K27M pHGGs have precise spatiotemporal origins and mouse models require distinctive targeting of oncogenic drivers to produce tumours, this raises questions of how faithfully murine tumours or neural stem cell cultures can recapitulate the human disease context. To develop a better understanding of the H3K27M disease mechanism, I propose that CRISPR editing of endogenous H3K27M mutations in tumour-derived cell cultures will create model systems to specifically delineate the effects of H3K27M. This approach will serve to understand how changes to the distribution of H3K27me2/3 and H3K27ac will affect transcription and cellular phenotypes. Our secondary objective is to understand how chromatin states of H3K27M pHGGs may render them vulnerable to therapeutic strategies that perturb the fitness of tumour cells. I predict my approach will contribute knowledge of fundamental disease biology and serve as the rationale for application of epigenetic therapies for treatment strategies.

## Chapter 2

**H3K27M induces defective chromatin spread of PRC2-mediated repressive H3K27me2/me3 and is essential for glioma tumorigenesis. *Nature Communications*. 2019 Mar 19;10(1):1262.**

Ashot S. Harutyunyan<sup>1\*</sup>, Brian Krug<sup>1\*</sup>, Haifen Chen<sup>1</sup>, Simon Papillon-Cavanagh<sup>1</sup>, Michele Zeinieh<sup>1</sup>, Nicolas De Jay<sup>1,2</sup>, Shriya Deshmukh<sup>1</sup>, Carol CL Chen<sup>1</sup>, Jad Belle<sup>1</sup>, Leonie G. Mikael<sup>3</sup>, Dylan M. Marchione<sup>4</sup>, Rui Li<sup>1</sup>, Hamid Nikbakht<sup>1</sup>, Bo Hu<sup>1</sup>, Gael Cagnone<sup>1</sup>, Warren A. Cheung<sup>1,5</sup>, Abdulshakour Mohammadnia<sup>1</sup>, Denise Bechet<sup>1</sup>, Damien Faury<sup>1</sup>, Melissa K McConechy<sup>1</sup>, Manav Pathania<sup>6</sup>, Siddhant U. Jain<sup>7</sup>, Benjamin Ellezam<sup>8</sup>, Alexander G. Weil<sup>9</sup>, Alexandre Montpetit<sup>10</sup>, Paolo Salomoni<sup>11,6</sup>, Tomi Pastinen<sup>1,5</sup>, Chao Lu<sup>12</sup>, Peter W. Lewis<sup>7</sup>, Benjamin A. Garcia<sup>4</sup>, Claudia L. Kleinman<sup>1,2</sup>, Nada Jabado<sup>1,3†</sup>, Jacek Majewski<sup>1,10†</sup>

<sup>1</sup> Department of Human Genetics, McGill University, Montreal, QC, H3A 1B1, Canada

<sup>2</sup> Lady Davis Research Institute, Jewish General Hospital, Montreal, QC H3T 1E2, Canada

<sup>3</sup> Department of Pediatrics, McGill University, and The Research Institute of the McGill University Health Center, Montreal, QC, H4A 3J1, Canada

<sup>4</sup> Department of Biochemistry and Biophysics, and Penn Epigenetics Institute, Perelman School of Medicine, University of Pennsylvania, Philadelphia, PA, 19104 USA

<sup>5</sup> Center for Pediatric Genomic Medicine, Children's Mercy Kansas City, Kansas City, MO 64108, USA

<sup>6</sup> Samantha Dickson Brain Cancer Unit, University College London Cancer Institute, London, WCE1 6DD, United Kingdom

<sup>7</sup> Department of Biomolecular Chemistry, School of Medicine and Public Health and Wisconsin Institute for Discovery, University of Wisconsin, Madison, WI 53715, USA.

<sup>8</sup> Department of Pathology, Centre Hospitalier Universitaire Sainte-Justine, Université de Montréal, Montréal, QC, H3T 1C5, Canada

<sup>9</sup> Department of Pediatric Neurosurgery, Centre Hospitalier Universitaire Sainte-Justine, Université de Montréal, Montréal, QC, H3T 1C5, Canada

<sup>10</sup> McGill University and Genome Quebec Innovation Centre, Montreal, QC, H3A 0G1, Canada

<sup>11</sup> Nuclear Function in CNS pathophysiology, German Center for Neurodegenerative Diseases, 53127 Bonn, Germany

<sup>12</sup> Department of Genetics and Development, Columbia University Irving Medical Center, New York, NY 10032, USA.

\*These authors contributed equally to this work

† Corresponding authors [nada.jabado@mcgill.ca](mailto:nada.jabado@mcgill.ca); [jacek.majewski@mcgill.ca](mailto:jacek.majewski@mcgill.ca)

## Abstract

Lys-27-Met mutations in histone 3 genes (H3K27M) characterize a subgroup of deadly gliomas and decrease genome-wide H3K27 trimethylation. Here we use primary H3K27M tumor lines and isogenic CRISPR-edited controls to assess H3K27M effects in vitro and in vivo. We find that whereas H3K27me3 and H3K27me2 are normally deposited by PRC2 across broad regions, their deposition is severely reduced in H3K27M cells. H3K27me3 is unable to spread from large unmethylated CpG islands, while H3K27me2 can be deposited outside these PRC2 high-affinity sites but to levels corresponding to H3K27me3 deposition in wild-type cells. Our findings indicate that PRC2 recruitment and propagation on chromatin are seemingly unaffected by K27M, which mostly impairs spread of the repressive marks it catalyzes, especially H3K27me3. Genome-wide loss of H3K27me3 and me2 deposition has limited transcriptomic consequences, preferentially affecting lowly-expressed genes regulating neurogenesis. Removal of H3K27M restores H3K27me2/me3 spread, impairs cell proliferation, and completely abolishes their capacity to form tumors in mice.

## Introduction

High-Grade Gliomas (HGG) are devastating brain tumors and a major cause of cancer-related mortality<sup>1</sup>. Pediatric HGG have molecular signatures distinct from those of adult HGG<sup>2-4</sup>. Specifically, they frequently harbor somatic mutations in histone 3 (H3) genes<sup>5-7</sup>. These mutations primarily impact the epigenome and show neuroanatomical and age specificity, suggesting that they occur during brain development<sup>1,5,6,8-10</sup>. The most frequent oncohistone, H3K27M, specifies diffuse midline gliomas, which include deadly diffuse intrinsic pontine gliomas (DIPG) and represents a newly recognized molecular HGG entity in the 2016 World Health Organization classification<sup>11</sup>. This somatic heterozygous mutation<sup>11</sup> is present in all tumor cells at diagnosis, tumor spread, and in autopsy samples, and is recognized to be the major oncogenic driver in these HGGs<sup>1,6,10,12,13</sup>.

The mechanism of H3K27M action remains unclear. Mutant H3K27M, which can occur in both the canonical (H3.1 or H3.2) and non-canonical (H3.3) histone variants, contributes to only a fraction of the total H3 pool (3–17%)<sup>14</sup>. However, it has a dominant effect as it drastically reduces overall levels of the repressive H3K27me3 mark in cells<sup>14–16</sup>. In vitro, H3K27M has been shown to severely affect the enzymatic activity of EZH2, a core component of the Polycomb Repressive Complex2 (PRC2), which normally catalyzes H3K27 methylation (reviewed in ref. 17), possibly through strong binding of the enzyme to H3K27M-containing nucleosomes, which sequesters and inactivates the complex<sup>18,19</sup>. How the resulting in vivo loss of H3K27me3 induces tumorigenesis remains the subject of active investigations. Several contradictory hypotheses have been proposed, namely preferential recruitment and/or sequestration of PRC2 on chromatin by K27M mutant nucleosomes<sup>14,19–21</sup>, preferential recruitment of PRC2 to its strong affinity sites<sup>22</sup>, or exclusion of this complex by mutant nucleosomes from its normal sites in mutant cells<sup>23</sup>. Indeed, studies using H3K27M-DIPG lines and mouse neural progenitor cells (NPCs) manipulated to overexpress H3K27M argue that H3K27me3 loss in large genomic areas leads to increased gene expression at bivalent promoters (marked, in the normal state, by both H3K27me3 and H3K4me3)<sup>20,24</sup>, while residual H3K27me3 deposition still occurs at several genomic loci and mediates oncogenesis<sup>22</sup>. Varying levels of PRC2 activity across sites have been suggested to account for these differential effects of H3K27M on distinct genomic loci, with those strongly binding PRC2 retaining the mark, and the weaker binding sites losing it in the presence of the mutation<sup>22</sup>. Another study suggested that the specific enrichment of H3.3K27M-carrying nucleosomes in actively transcribed genomic regions where H3.3 is preferentially deposited precludes PRC2 recruitment and subsequent H3K27me3 deposition<sup>23</sup>. In all, despite many enticing hypotheses, a unified view on downstream effects of H3K27M is lacking. One notable limitation of all studies to date<sup>15,20,22,23</sup> is the lack of an isogenic tumor-relevant context for studying the effects of the mutation. The precise cell of origin for these tumors remains unknown. Given that H3K27M is tumorigenic only when introduced in specific neurodevelopmental windows<sup>22,23,25,26</sup>, and that H3K27me3 deposition varies with cellular context and differentiation stage<sup>27</sup>, it follows that the absence of an appropriate isogenic background would likely represent a major confounder. In addition, no data exists on the more abundant repressive mark H3K27me2, whose production by PRC2 is similarly affected by H3K27M<sup>14</sup>, and which may contribute to K27M tumorigenesis. Moreover, while there is evidence that H3K27M mutation is the initiating oncogenic event<sup>12</sup>, there is a clear requirement for

additional specific oncogenic partners to drive tumor formation<sup>6,9,12,13,28–30</sup>. Whether H3K27M is necessary for tumor progression and/or maintenance is not yet known.

To address how decreased H3K27me3/me2 levels lead to tumorigenesis and to examine the requirement of K27M for tumor maintenance, here we use multiple human primary pediatric HGG cell lines as a controlled tumor-relevant setting for the H3K27M mutation in this study. We directly manipulate H3K27M by overexpressing it in wild-type lines or using CRISPR editing to remove it from mutant cell lines. We further alter PRC2 by overexpression or pharmacological inhibition. We use epigenome and transcriptome analysis to study the molecular consequences, cell assays to profile proliferation, and a mouse orthotopic xenograft model to determine the final effect of the mutation on tumorigenicity (Supplementary Fig. 1, Supplementary Table 1). Our data show that PRC2 deposition and propagation on the chromatin are unaffected by K27M. The main effect of the mutation is in preventing the spread of H3K27me3, and to a lesser level H3K27me2, from PRC2 binding sites to larger silencing domains. This epigenetic defect is reversible upon removal of the H3K27M mutation, suggesting possible reversibility of its functional consequences. Importantly, we show H3K27M is essential for tumor maintenance as removal of this mutation in HGG is sufficient to mitigate tumor growth *in vivo*.

## Results

**H3K27me2 loss is less marked than H3K27me3 in H3.3K27M.** We used mass spectrometry to assess H3K27 methylation levels in primary HGG cell lines carrying H3.3K27M (n = 3) or wild-type (n = 3) for this mutation. Massive loss of H3K27me3 was observed as expected, while a significant but less drastic loss of H3K27me2, and a modest increase in H3.1/H3.2K27me1 were seen in H3.3K27M cell lines (Fig. 1a). We then used chromatin immunoprecipitation combined with sequencing (ChIP-seq) to profile H3K27me3 and H3K27me2 distribution in these cell lines. Exogenous chromatin spike-in (ChIP-Rx, see methods), used to quantitate signal intensity, confirmed overall decrease in H3K27me3/me2 methylation levels in H3K27M cells compared to wild-type HGGs (Supplementary Fig. 1–2, Supplementary Table 2). Analyzing genome-wide distribution of both marks showed striking differences between K27M and wild-type HGG lines (Fig. 1b, Supplementary Fig. 3a). While H3K27me3 was distributed in broad domains in wild-type cells, H3K27M cells showed sharp peaks of H3K27me3 coinciding with loss of the mark in

the broad domains where it is normally found and resembling the pattern of embryonic stem cells (ESC) (Supplementary Fig. 3a). Notably, H3K27me3 distribution was highly consistent across six H3K27M cell lines tested and comparable to that of the primary tumors from which the cell lines were derived (Supplementary Fig. 3b-d). In contrast, the H3K27me2 mark showed a broader distribution in K27M, resembling the distribution of H3K27me3 in wild-type HGGs, while in these cells not carrying the mutation this mark spread as expected genome-wide largely outside H3K27me3 domains (Fig. 1b, c). We further profiled PRC2 distribution by ChIP-seq of the core PRC2 component SUZ12. In H3K27M-mutant cells, H3K27me3 deposition showed near-complete co-occupancy with SUZ12, suggesting that H3K27me3 is restricted in these cells to PRC2 binding sites (Fig. 1b, c, Supplementary Fig. 4–5). Wild-type HGGs, in turn, showed additional deposition of H3K27me3 in broad domains with limited SUZ12 occupancy (Fig. 1b, c, Supplementary Fig. 4–5). Our data indicate that, in the presence of K27M, H3K27me2 production by PRC2 is decreased but to a lesser magnitude than H3K27me3. Accordingly, a level of spread on chromatin is seemingly achieved for this mark while H3K27me3 deposition appears confined to specific genomic loci.

H3K27me3 is retained at unmethylated CGIs. To obtain a quantitative characteristic of H3K27me3 distribution, we divided the genome into 1 kb bins and calculated the average normalized read counts in top 1% of the most enriched bins (Fig. 1d). H3K27M cells had significantly higher enrichment in top bins, reflecting focused distribution of H3K27me3 mark in those cells in contrast to broad distribution in wild-type cells. Large unmethylated CpG islands (CGIs) are known high-affinity recruitment sites for PRC2. We subsequently quantified the proportion of H3K27me3 reads within CGIs and SUZ12 peaks and observed a significantly higher percentage of the H3K27me3 signal within those features for H3K27M cells compared to wild-type (Fig. 1d). While H3K27me3 was preserved at unmethylated CGIs (Fig. 1b, c), we noticed that broad domains of H3K27me3 in wild-type cells, generally coinciding with partially methylated DNA domains (PMD), were greatly depleted in K27M cells (Fig. 1e, Supplementary Fig. 6). Accordingly, we observed a shift in a proportion of H3K27me3 from intergenic to promoter regions between wild-type and H3K27M cells (Fig. 1d, Supplementary Fig. 7).

We next investigated the distribution of the H3K27me3 writer (PRC2) and reader (PRC1) complexes. In all cell lines, PRC2 (SUZ12) was largely localized to unmethylated CGIs (Fig. 1b,

c). However, a visibly broader pattern of SUZ12 around CGIs was observed in H3K27M cells, contrasting with its narrow deposition in wild-type lines (Fig. 1c, Supplementary Fig. 4) and consistent with an increased retention of PRC2 around its binding sites. The PRC1 complex can recognize H3K27me3 and mediate transcriptional repression but, depending on subunit composition, it can also bind and regulate active promoters<sup>31</sup>. We observed that the core PRC1 subunit RING1B showed increased overlap with H3K27me3/SUZ12 occupancy at CGIs in H3K27M lines compared to wild-type (Supplementary Fig. 5).

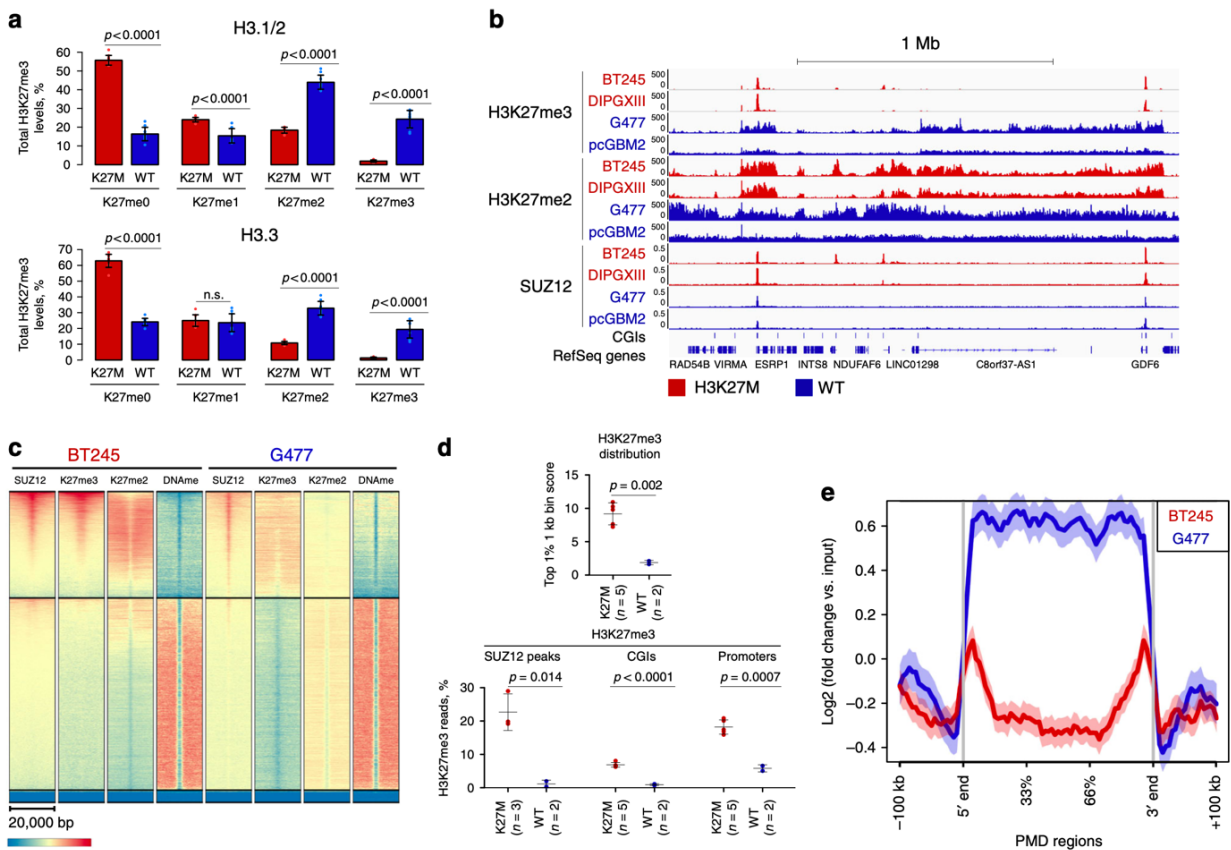


**Fig. 1. H3K27M-mutant pediatric high-grade gliomas (pHGGs) exhibit distinct distribution of H3K27me3 and H3K27me2**

**a.** H3K27me1/2/3 abundance quantified by mass spectrometry, primary cells (WT n=3 cell lines, K27M n=3 cell lines, 3 replicates for each cell line, mean  $\pm$  standard deviation, Student's t-test).

**b.** Example of normalized H3K27me3 and H3K27me2 chromatin immunoprecipitation sequencing (ChIP-seq) tracks of H3K27M and WT pHGG lines, showing qualitative differences

in distribution of these marks. For comparison, SUZ12 ChIP-seq tracks, and CpG islands (CGIs) are shown.

**c.** Heatmap plots of ChIP-seq signal intensity for SUZ12, H3K27me2/3 and DNA methylation (whole genome bisulphite sequencing (WGBS)) over CGIs for BT245 (H3K27M) and G477 (WT). CGIs are separated by kmeans clustering (k=3).

**d.** Top: Average enrichment at the top 1% of 1kb bins for H3K27me3. Bottom: Proportion of H3K27me3 reads in SUZ12 peaks, CGIs, promoters. H3K27M cells show higher enrichment for H3K27me3 in top 1% 1kb bins, SUZ12 peaks, CGIs and promoters compared to wild-type cells (mean  $\pm$  standard deviation, Student's t-test).

**e.** H3K27me3 signal intensity over partially methylated domain (PMD) regions in BT245 (H3K27M) and G477 (WT) cells, aggregate plot.

Source data are provided as a Source Data file.

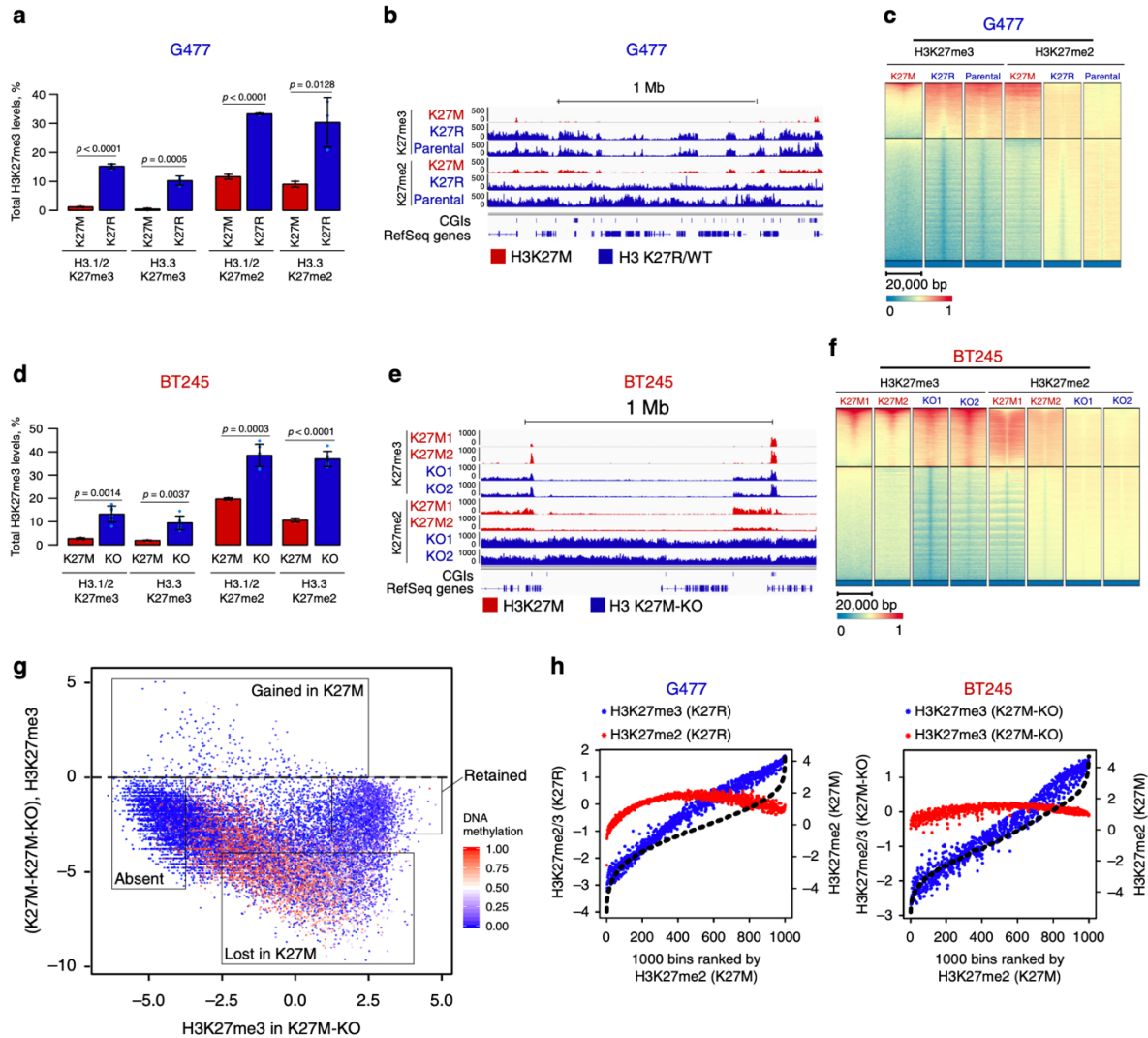


**Fig. 2. H3K27M reversibly induces global redistribution of H3K27me2 and H3K27me3**

(a-c). G477 wild-type cell line with H3.3-K27M overexpression.

a. H3K27me2/3 abundance by histone mass spectrometry (n=3 in each group, mean  $\pm$  standard deviation, Student's t-test).

b. Example ChIP-seq tracks of H3K27me2/3 distribution, normalized by drosophila spike-in (ChIP-Rx).

c. Heatmap plots of ChIP-seq signal intensity for H3K27me2 and H3K27me3 over CGIs for parental G477 (wild-type) and G477 overexpressing K27R and K27M. CGIs are separated by kmeans clustering (k=3).

(d-f). BT245 with H3K27M knockout (KO) by CRISPR/Cas9.

d. H3K27me3 abundance by histone mass spectrometry (K27M n=3, KO n=6, mean  $\pm$  standard deviation, Student's t-test). Whiskers represent standard deviation.

e. Example ChIP-seq tracks of H3K27me2/3 distribution, ChIP-Rx normalized.

f. Heatmap plots of ChIP-seq signal intensity for H3K27me2 and H3K27me3 over CGIs for parental BT245 (H3K27M) and K27M knockout (K27M-KO) by CRISPR. CGIs are separated by kmeans clustering (k=3).

g. H3K27me3 signal change at CGIs of BT245, K27M-KO vs. K27M, color coded for DNA methylation. y axis shows the difference in normalized H3K27me3 levels at CGIs in K27M vs. K27M-KO ( $\log_2$ ), while x axis shows normalized H3K27me3 levels in non-K27M state (K27M-KO,  $\log_2$ ). Four categories of CGIs based on H3K27me3 levels and difference are depicted by squares.

h. Strong correlation of H3K27me2 in H3K27M with H3K27me3 in respective isogenic non-K27M state (K27R in G477, K27M-KO in BT245). 1000 aggregate bins are ranked on x axis based on H3K27me2 in H3K27M state (black dotted line). H3K27me3 levels in each bin for non-K27M sample are shown in blue, H3K27me2 levels in non-K27M in red (normalized,  $\log_2$ ).

Source data are provided as a Source Data file.

**H3K27M directly affects H3K27me3/me2 spread.** We derived H3K27M mutants by CRISPR-Cas9 in HEK293T (Supplementary Fig. 8) and overexpression of H3.3K27M in a wild-type HGG line (G477, Fig. 2a–c, Supplementary Fig. 9). In both lines, we observed significant loss of H3K27me3 (Fig. 2a–c, Supplementary Fig. 8–9) and conversion of broad domains to narrow peaks, resembling patterns seen in primary H3K27M-HGG lines (Fig. 2b, c, Supplementary Fig. 8–9). Accordingly, the proportion of H3K27me3 increased in CGIs and promoters (Supplementary Fig. 8–9). Impaired spreading of methylated H3K27 upon K27M expression is consistent both in wild-type HGG cells and HEK293T, an unrelated differentiated cell type, demonstrating this effect is independent of cell context and is directly linked to the mutation. Interestingly, when assessing H3K27me2 deposition in H3.3K27M-expressing G477, this mark showed significantly less broad deposition, while its genome-wide distribution was strikingly similar to that of H3K27me3 in the parental G477 line (Fig. 2b, c). This further supports our observation that the effect of K27M appears more pronounced on H3K27me3 deposition than on H3K27me2.

To study the mutation in a controlled, tumor-relevant context, we removed the K27M mutant allele from two HGG lines, BT245 and DIPGXIII (SU-DIPGXIII), using the CRISPR/Cas9 system (Supplementary Fig. 10–11). Edited clones (H3K27M-KO) showed an average five-fold increase in H3K27me3 and a 2–3-fold increase in H3K27me2 levels (Fig. 2d, Supplementary Fig. 10–11). This was accompanied by spread of H3K27me3 and H3K27me2 signals into broad domains, resembling those of wild-type HGG cell lines (Fig. 2e, f, Supplementary Fig. 10–11), and subsequent decrease in the proportion of H3K27me3 reads in promoters and CGIs (Supplementary Fig. 10–11). A number of unmethylated CGIs (Fig. 2g, Supplementary Fig. 10, 12–13) had low to absent H3K27me3 levels both in the original mutant cell lines and in isogenic H3K27M-KO, which generally corresponded to active promoters marked by H3K27ac (absent). Also, a number of unmethylated CGIs with no H3K27me3 in H3K27M cells (lost) showed deposition of the mark in H3K27M-KO. Notably, the degree of loss in H3K27M cells was positively correlated with the levels of the mark on that site in H3K27M-KO edited cells. Importantly, the large unmethylated CGIs enriched for SUZ12, where most of H3K27me3 is deposited in H3K27M cells, retained the mark (retained), which spread from these sites in H3K27M-KO cells (Fig. 2g, Supplementary Fig. 10, 12–13). The relatively broad enrichment of SUZ12 in these regions in H3K27M became more focused in H3K27M-KO cells, similar to the SUZ12 pattern observed in wild-type HGG (Supplementary Fig. 12, 14). Very few CGIs acquired higher H3K27me3 levels in the presence of H3K27M (gained); these gained regions were distinct in each edited line (Supplementary Table 3), and thus likely represent secondary downstream effects of unclear significance. Interestingly, the CDKN2A (p16) locus, a candidate driver gene in K27M gliomas<sup>22</sup>, retained high levels of H3K27me3, regardless of the presence of the H3K27M mutation (Supplementary Fig. 15). Finally, H3K27me3 retention has been proposed to correspond to regions of H3K27M deposition<sup>19</sup>. However, levels of H3K27me3 and H3K27M did not positively correlate in our cell lines or in a mouse model<sup>26</sup> of H3K27M tumorigenesis (Supplementary Fig. 16). Thus, H3K27M redistributes H3K27me3 to follow PRC2 recruitment, but not H3.3/K27M deposition. In addition, the H3K27me2 mark spreads outside CGIs in H3.3K27M mutant cells. Notably, when comparing H3K27M lines to their isogenic CRISPR-edited lines, we observe that it is confined in mutant cells to regions of H3K27me3 spread in H3.3K27M-KO lines (Fig. 2e, f, Supplementary Fig. 11) similar to what we observed in H3.3K27M G477 cells (Fig. 2b, c). Indeed, a strong correlation between H3K27me2 in K27M and H3K27me3 in wild-type isogenic cells is seen (Fig. 2h). Overall, these

findings, together with our data on H3K27M-KO or H3.3K27M-expressing wild-type HGG, indicate that H3K27M decreases H3K27me3 and to a lower extent K27me2 levels and deposition. Importantly, while H3K27me3 is confined to specific and narrow regions corresponding to large unmethylated CGIs marked with PRC2, H3K27me2 is able to spread outside these domains in the presence of the mutation. Unlike H3K27me3, di-methylation of H3K27 is enzymatically easier for the PRC2 complex and can be produced by transient interactions with the chromatin<sup>32,33</sup>, possibly accounting for the differential effects we observe for both marks in our model systems.

**H3K27M does not sequester PRC2 on chromatin.** Pediatric HGG have no known mutations in PRC2 components<sup>6,9,34</sup>, suggesting the effect of H3K27M may be distinct from complete loss of PRC2 function. Moreover, small molecule PRC2 inhibitors impair the growth of H3K27M lines<sup>22</sup>. We replicated this in our model system where we treated H3K27M-HGG and isogenic H3K27M-KO cell lines using two EZH2 inhibitors and found significantly more growth inhibition in the presence of K27M (Supplementary Fig. 17). Pharmacological EZH2 inhibition drastically decreases H3K27me3 and H3K27me2 marks and uniformly affects their deposition and spread in both lines (Fig. 3a, b, Supplementary Fig. 17). In contrast, the effect of H3K27M is more pronounced on H3K27me3 deposition, which is then restricted to CGIs, therefore suggesting that the mutation does not fully phenocopy PRC2 inhibition. Next, we tested whether we could rescue H3K27M-induced effects by over-expressing either: (1) wild-type EZH2 or (2) EZH2-Y641N, a preferential di- to tri-methylase mutant<sup>35</sup> shown to be less sensitive to inhibition by H3K27M<sup>14</sup>. Overexpression of wild-type EZH2 had minor effects on H3K27me3 and H3K27me2 (~1.5-fold gain) suggesting that increased EZH2 levels are unable to overcome K27M-induced confinement of both marks (Supplementary Fig. 18). Strikingly, EZH2-Y641N induced a large gain of H3K27me3 (~7-fold). Notably, this was achieved by the spread of H3K27me3 from sites retaining the mark in H3K27M cells on corresponding domains showing H3K27me2 spread in H3.3K27M mutant cells (Fig. 3c–e, Supplementary Fig. 18). Accordingly, a drastic depletion of H3K27me2 in H3.3K27M mutant cells overexpressing EZH2-Y641N was observed in these regions (Fig. 3c, Supplementary Fig. 18). As no new PRC2 nucleation sites were generated, our overall data further support that H3K27M induces defective spread of H3K27me3/me2, which is more pronounced for H3K27me3. Importantly, H3.3K27M does not appear to retain the PRC2 complex at CGIs, as we

observe spread of H3K27me2 despite the presence of the mutation, while spread of the H3K27me3 mark is possible in this setting when overexpressing EZH2-Y641N.

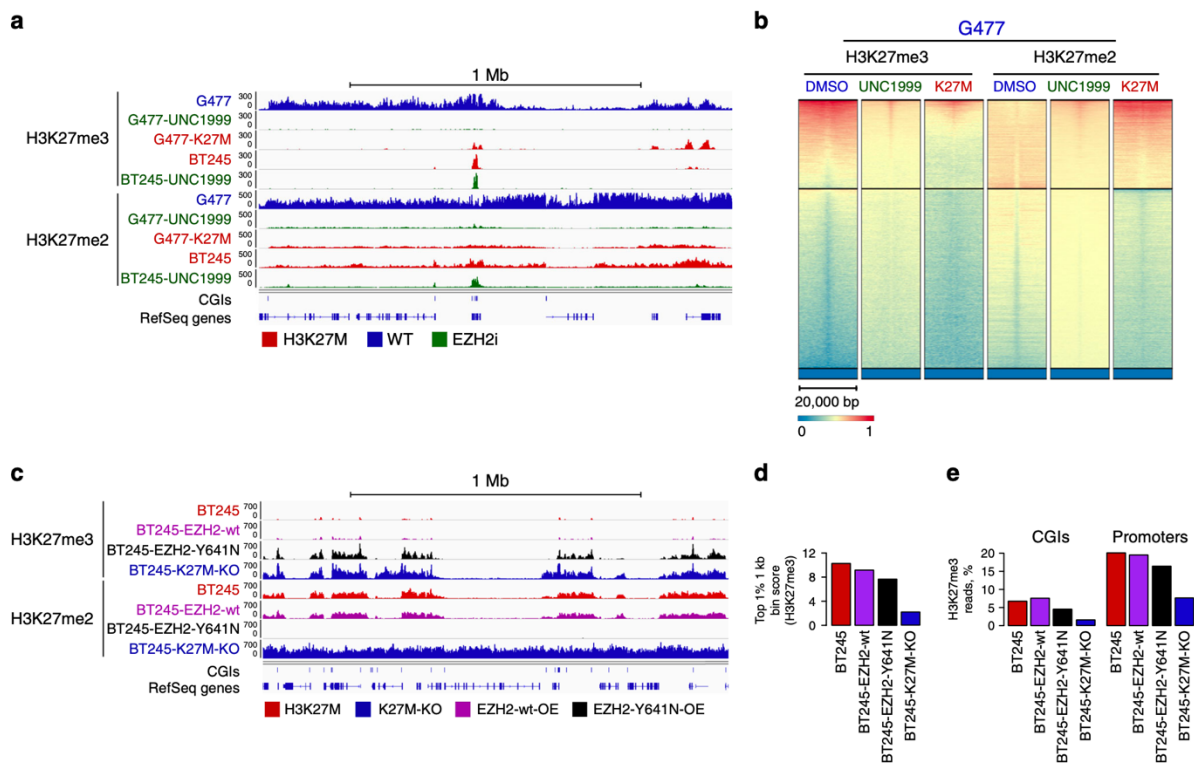


**Fig. 3. EZH2 inhibition does not completely mimic H3K27M effects and EZH2-Y641N partly overcomes H3K27M-induced effects.**

(a-b). Changes in H3K27me2/3 levels and distribution upon EZH2 inhibition.

**a.** Example ChIP-seq tracks of H3K27me2/3 distribution in G477 (wild-type) and BT245 (H3K27M) cell lines treated and not treated with UNC1999 (EZH1/2 inhibitor), ChIP-Rx normalized. For comparison, G477 cell line with H3.3-K27M overexpression is also included.

**b.** Heatmap plots of ChIP-seq signal intensity for H3K27me2 and H3K27me3 over CGIs for G477 cell line (wild-type) treated and not treated with UNC1999, as well as with H3.3-K27M overexpression. CGIs are separated by kmeans clustering (k=3).

(c-e). Changes in H3K27me2/3 levels and distribution upon overexpression of EZH2-wt and EZH2-Y641N.

**c.** Example ChIP-seq tracks (ChIP-Rx normalized) of H3K27me2/3 distribution in BT245 cell line (H3K27M) overexpressing wild-type or Y641N mutant forms of EZH2. Parental BT245 and CRISPR edited K27M-KO clone are included for comparison.

**d** Average enrichment at the top 1% of 1kb bins for H3K27me3.

e. Proportion of H3K27me3 reads in CGIs and promoters upon EZH2 overexpression.

Source data are provided as a Source Data file.

**H3K27M induces limited transcriptomic changes.** To assess specific effects of H3K27M mutation on gene expression, we compared the transcriptomes of isogenic lines in the presence or absence of H3K27M (G477, HEK293T, BT245, DIPGXIII). We correlated changes in gene expression with promoter H3K27me3 levels. Although H3K27me3 is lost in wide genomic areas, the resulting effect on transcription in H3K27M-mutant cells is relatively modest. Indeed, most genes had no H3K27me3 (Absent) or no change in H3K27me3 levels (Retained) on their promoter regardless of H3K27M (Fig. 4a). As expected, we observed limited changes in their expression. Despite the loss of H3K27me3 on a large number of promoters in the context of H3K27M (Lost), only a modest fraction of associated genes showed differential expression, mainly upregulation. Moreover, very few genes had a gain of promoter H3K27me3 (Gained) in H3K27M-expressing cells, only a small fraction of which were downregulated (Fig. 4b). In all our model systems—irrespective of whether H3K27M was introduced or removed—the presence of H3K27M resulted in overall transcriptional derepression characterized by an excess of upregulated genes (Fig. 4b, c). Interestingly, the number of upregulated genes was highest within the low-expression range (Fig. 4c), suggesting that one of the effects of H3K27M on the transcriptome is to disable proper H3K27me3 repression and permit low levels of aberrant transcription. To identify potential driver targets/pathways in H3K27M mutagenesis, we investigated the genes that were significantly affected by knockout of H3K27M in both BT245 and DIPGXIII cells (Supplementary Table 4). In the presence of H3K27M, we found more upregulated (102) than downregulated (12) genes, reflecting the overall trend of gene derepression. Pathway analysis on the downregulated set did not identify any Gene Ontology (GO) enrichment, but the upregulated set showed overrepresentation of genes involved in neural differentiation and developmental pathways, consistent with previous observations in other systems<sup>22,25,26</sup> (Fig. 4d). Notably, across all three HGG lines, the presence of H3K27M-induced upregulation of ID1-ID4 genes (Supplementary Fig. 19). These ID (inhibitors of DNA binding/ differentiation) genes are broadly implicated in developmental processes, inhibition of differentiation, maintenance of self-renewal, and multipotency in stem cells. ID genes have been shown to be upregulated in response to growth factor receptor stimulation, including ACVR1, a receptor activated in 20% of DIPGs<sup>9,28–30</sup>. Thus,

H3K27M-HGG can promote an undifferentiated cellular state through aberrant expression of ID genes due to both K27M or ACVR1 mutations.

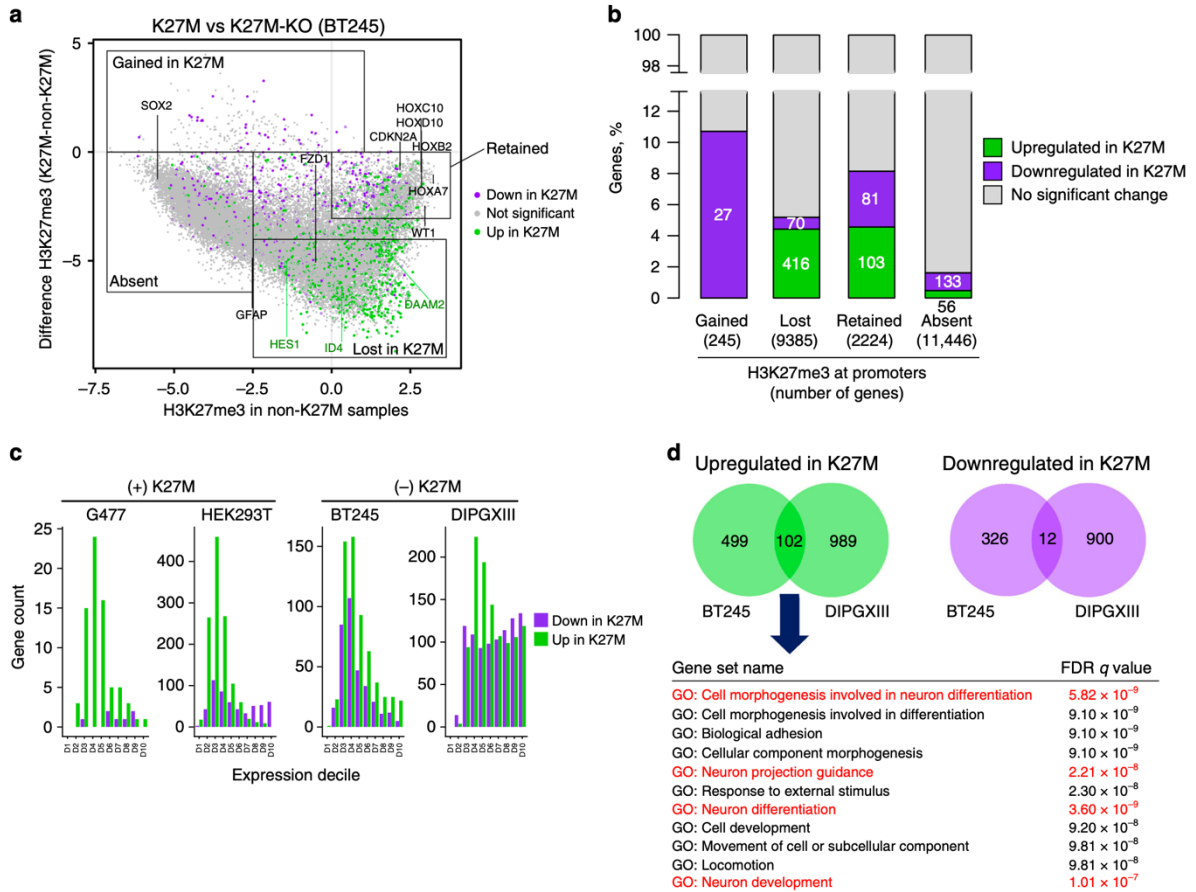


**Fig 4. Transcriptome and H3K27me3 loci implicate H3K27M in neural differentiation**

**a.** H3K27me3 level difference plot in BT245 dataset, color coded by gene expression changes (green for upregulated in K27M state, purple – downregulated, grey – no significant change in expression). y axis shows the difference in normalized H3K27me3 levels at promoters in K27M vs. K27M-KO (log2), while x axis shows normalized H3K27me3 levels in non-K27M state (K27M-KO, log2). Four categories of promoters based on H3K27me3 levels and difference are depicted by squares.

**b.** Number and proportion (x axis) of significantly up- or downregulated genes in each selected region from plot 4A (gained in K27M, lost in K27M, retained, absent). Numbers inside the columns show the number of genes up- or downregulated in each category, while the number in brackets below column labels shows the total number of genes in that category.

c. Gene expression changes by deciles in different experimental datasets. The genes were assigned to deciles according to their expression in the original cell line, before manipulation. Most of differentially expressed genes (and upregulated in K27M) are among lower expressed deciles in all 4 datasets.

d. Overlap of differentially expressed genes in BT245 and DIPGXIII datasets. Gene set enrichment analysis of differentially expressed genes (genes upregulated in K27M state in both cell lines).

**H3K27M is required for tumorigenesis.** We examined the consequences of the introduction and removal of the H3K27M mutation on cell proliferation in vitro, as well as on tumor growth in orthotopic xenograft models (PDOX). In vitro, across the three tumor cell lines, we observed a consistent trend of H3K27M conferring a proliferative advantage (Supplementary Fig. 20a). In BT245, where H3K27M removal has the strongest effect, we were able to rescue the decrease in growth rate when we re-expressed the mutation (Supplementary Fig. 20b). To investigate the requirement of H3K27M for tumor growth in vivo, we injected independently edited BT245 and DIPGXIII (H3K27M-KO) clonal lines in the brains of NSG mice. As positive controls, for both BT245 and DIPGXIII, we performed parallel injections with two H3K27M-mutant lines (one parental and one unedited). We have previously successfully propagated BT245 and DIPGXIII as PDOX in numerous experiments and, as expected, mice injected with the positive control H3K27M lines progressively developed tumors resembling HGG. However, none of the mice injected with H3K27M-KO cells developed tumors during follow-up of over 1 year for BT245 and 6 months for DIPGXIII (Fig. 5a, Supplementary Fig. 20c), despite the presence of other highly oncogenic mutations in the injected cells (TP53 in both parental lines, TERT promoter mutation and C-MYC amplification present in the BT245 parental line, N-MYC amplification in DIPGXIII line). Our data strongly indicate that the H3K27M mutation is not only necessary for initial stages of tumor establishment but also continuously needed to preserve the proliferative and tumorigenic potential of these tumors.

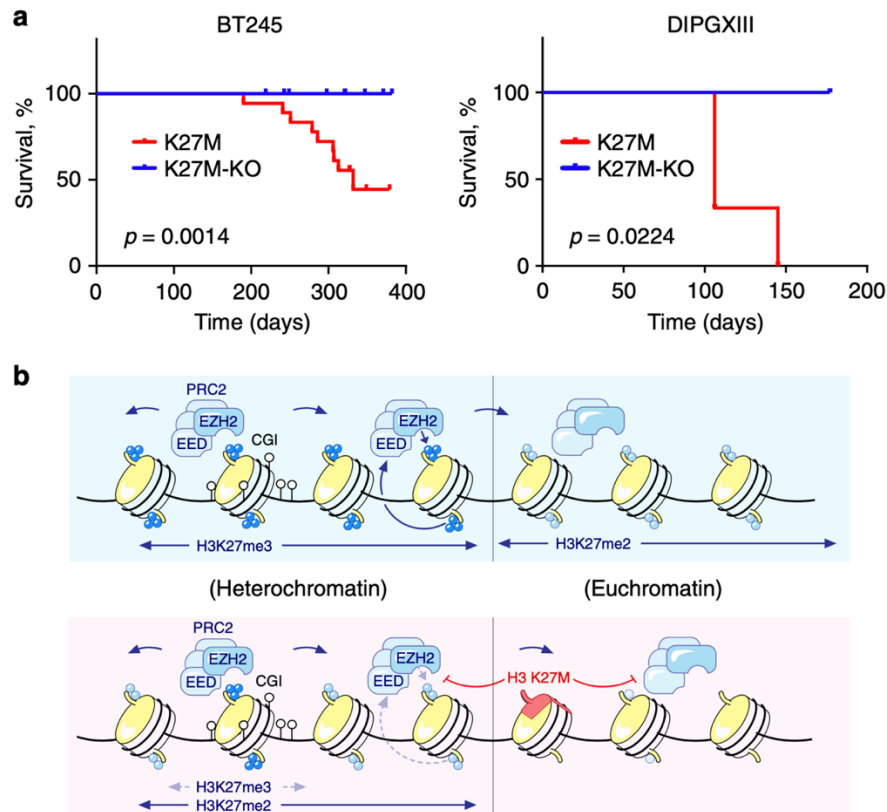


**Fig. 5. H3K27M confers tumorigenicity in vivo**

**a.** Survival of mouse orthotopic xenograft cohorts injected with BT245 (K27M; n=18 mice, K27M-KO; n=19 mice, log-rank test) and DIPGXIII lines (K27M; n=3 mice, K27M-KO; n=3 mice, log-rank test).

**b.** A model of H3K27M reversibly inhibiting the spread of H3K27me2 and H3K27me3 deposition by PRC2 from initial recruitment sites. Note that while in H3K27M H3K27me3 mark is restricted to unmethylated CGIs, H3K27me2 is found in domains where there is H3K27me3 in non-K27M condition.

Source data are provided as a Source Data file.

## Discussion

We provide evidence that H3K27M impairs the production and the spread of the repressive H3K27me3 mark from PRC2 high-affinity sites (Fig. 5d). We observe non-random decrease of H3K27me3 in the presence of the mutation, with residual deposition confined to large unmethylated CGIs enriched for PRC2. Notably, we show that the production and the distribution

of H3K27me<sub>2</sub>, a repressive mark that is abundantly deposited by PRC2 across the silent euchromatin and the basis from which this complex synthesizes H3K27me<sub>3</sub><sup>32,33</sup>, are also affected by H3.3K27M, albeit at a lower magnitude than H3K27me<sub>3</sub>. Importantly, in H3.3K27M mutant cells, H3K27me<sub>2</sub> spreads outside unmethylated CGIs, mirroring H3K27me<sub>3</sub> distribution in wild-type cells, indicative that the PRC2 complex is not retained at these CGIs. Introducing H3K27M in HGG cell lines wild-type for this mutation and in HEK293T cells reproduces decreased production and confinement of both marks (H3K27me<sub>3</sub> to CGIs, H3K27me<sub>2</sub> to spread of H3K27me<sub>3</sub> in wild-type cells). We further show that defective H3K27me<sub>3</sub>/me<sub>2</sub> spread induced by K27M is reversible. When the mutation is removed, uninhibited PRC2 restores deposition of H3K27me<sub>3</sub> from these large CGIs to sites that had lost it, mainly intergenic sites and PMDs with poor PRC2 recruitment, while H3K27me<sub>2</sub> distribution becomes comparable to that seen in wild-type HGGs. Additionally, Y641N-EZH2, an EZH2 mutant less sensitive to H3K27M inhibition which catalyzes me<sub>2</sub>/me<sub>3</sub><sup>14</sup>, restores deposition of H3K27me<sub>3</sub> by extending it from existing PRC2 recruitment sites, without creating new sites, similar to what we observe in H3K27M-KO isogenic cells. This further argues against retention of the PRC2 complex at given genomic loci and supports a K27M-induced defective spread of both H3K27me<sub>2</sub> and H3K27me<sub>3</sub> repressive marks.

Several recent reports on PRC2 function support our findings that decreased catalysis of K27me<sub>3</sub>/me<sub>2</sub> due to K27M results in a defective spread on chromatin of these repressive marks from PRC2 high-affinity sites. In one study, newly deposited H3K27me<sub>3</sub> and me<sub>2</sub> progress from PRC2 high-affinity sites recruiting the complex following total erasure<sup>36</sup>. This observation is in keeping with our findings that most of the retained H3K27me<sub>3</sub> peaks in H3K27M cells correspond to unmethylated CGIs, while H3K27me<sub>2</sub> spreads from these sites, even though at lower magnitude compared to wild-type cells. This indicates that the PRC2 complex is not retained by the mutation and can still spread on chromatin. The differential effects observed for K27me<sub>2</sub> and K27me<sub>3</sub> are probably due to differential catalytic constraints for PRC2 when depositing these marks. Indeed, production of H3K27me<sub>2</sub> is enzymatically easier and seems to require transient interactions on the chromatin for the complex as compared to H3K27me<sub>3</sub>, which is produced from H3K27me<sub>2</sub> and requires a more stable association with PRC2<sup>19,37</sup>. This may also account for the broader distribution of SUZ12 in H3K27M-mutant cells and the near-complete overlap with H3K27me<sub>3</sub> we observe at unmethylated CGIs. Lack of distribution of H3K27me<sub>3</sub> from PRC2 recruitment

high-affinity sites, may also be partly due to poor allosteric activation of EZH2 following decreased production of H3K27me3 in the presence of K27M, which would further preclude the spread of the repressive mark. Indeed, EED is an essential subunit of PRC2 that recognizes initial H3K27me3 and allosterically activates the complex, promoting further deposition of the mark<sup>38</sup>. Also, an EED cage mutant that prevents H3K27me3 recognition by PRC2 was shown to induce similar confinement of H3K27me3<sup>39</sup>, indicating a potential effect of K27M in impairing allosteric activation of PRC2. Further experiments are needed to support decreased allosteric activation of EED as a consequence of K27M mutagenesis. In addition, the lack of H3K27me2 deposition in H3K27M cells outside typical H3K27me3 domains could be due to the presence of other histone marks such as H3K36me2 in those regions. This defect in spread of the marks, but not recruitment or spread of PRC2, is further supported by the dynamic deposition of H3K27me3 at novel loci in response to external stimuli that we (Supplementary Fig. 15 and<sup>26</sup>) and others<sup>22</sup> observe, despite the presence of the mutation. These suggest that in H3K27M cells, PRC2 could be recruited to locally as needed to deposit H3K27me3 as the effect required does not involve spread of the mark.

Experimental results obtained with the pharmacological inhibition of EZH2 indicates that the mutation does not fully reproduce pharmacological EZH2 inhibition in K27M wild-type HGG lines. In addition, specific retention of H3K27me3 in H3K27M lines suggests regional functional requirement for H3K27me3, and may explain their sensitivity to these EZH2 inhibitors that we and others<sup>22</sup> observe, as these cells may not be able to tolerate further loss of the mark. Interestingly, while K27M induces widespread loss of H3K27me3, only a modest proportion of genes that lose the mark at their promoters are dysregulated. One explanation of such modest transcriptional dysregulation could be the observation that in H3K27M cells, H3K27me2 occupies the regions that lost H3K27me3 and it might maintain certain level of gene silencing. We propose that the changes observed in the presence of H3K27M consist predominantly of low-level transcriptional derepression that results from incomplete silencing. Dysregulated genes showed over-representation of functions involved in stemness and neurogenesis, in keeping with recent results suggesting that K-M mutations on H3K27 or K36 induce transcriptional deregulation affecting cell differentiation<sup>40</sup>. In normally developing cells, lineage commitment and further cell differentiation is mediated by a multitude of epigenetic changes, including an interplay of acquisition or loss of H3K27me3 and me2 at multiple sites, with increased H3K27me3 deposition

needed upon cellular differentiation<sup>24,27,41</sup>. While normal cells can dynamically regulate this mark to differentiate, H3K27M-HGG have severely impaired H3K27me3 production and show its confinement to specific CGIs, not allowing the mark to fully silence neighboring regions and thus possibly stalling further differentiation. The CGIs retaining H3K27me3, from which the mark would have spread in the absence of H3K27M, may thus represent original binding sites in committed NPCs, as suggested by the blockade in neurogenesis and brain developmental pathways we observe in K27M HGG and in keeping with recent data indicating an oligodendroglial progenitor cell as a potential cell of origin for these HGG<sup>25,26,37,42</sup>. Notably, our results mirror findings in ES cells, which show similar restriction of H3K27me3 to CGIs, and where loss of PRC2 does not promote major transcriptional changes but stalls further differentiation and lineage specification.

There is an ongoing debate regarding the requirement of H3K27M in maintaining tumorigenesis. Our data show that the removal of K27M is sufficient to abolish tumor formation in an *in vivo* orthotopic mouse model. Indeed, despite the presence of other oncogenic lesions, including TERT promoter mutation, TP53 alterations, and C-MYC or N-MYC amplification, no tumors formed in the brain of mice injected with HGG cells rendered wild-type for the H3K27M mutation. The mice were followed for over 6 months to one year to exclude the possibility of delayed tumor onset. The K27M mutation is thus not simply a remnant of initial stages of tumorigenesis, it seems to be continuously required for both tumor formation and maintenance.

In summary, we propose a model where the K27M mutation affects H3K27me3 and H3K27me2 production and the relative spread of both these repressive marks from initial PRC2 binding sites in the cell of origin. Neither the recruitment of PRC2 to its nucleation sites nor the deposition of the H3K27me3 mark in the proximity of those sites is affected by the mutation. However, as the marks cannot spread to establish the proper silencing landscape, further lineage specification, a major role of PRC2, is not possible, and the cell is stalled in an early epigenetic and progenitor state, indefinitely multiplying without being able to further differentiate. Over time, this will allow acquisition of other genetic alterations ultimately leading to tumor formation. We propose that H3K27M has a vital role for maintaining this specific epigenomic landscape that prevents further cell differentiation. This in turn allows for tumor formation and is necessary for tumor

maintenance, making H3K27M an important therapeutic target in HGG. Compounds targeting this mutation, when available, have the potential to greatly improve survival in this deadly cancer.

## Methods

**Patient samples and clinical information.** This study was approved by the Institutional Review Board of the respective institutions from which the samples were collected. We thank Keith Ligon and Michelle Monje for generously sharing primary tumor cell lines established from patients with high-grade glioma.

**Cell culture.** Tumor-derived cell lines were maintained in Neurocult NS-A proliferation media (StemCell Technologies) supplemented with bFGF (10 ng/mL) (StemCell Technologies), rhEGF (20 ng/mL) (StemCell Technologies), and heparin (0.0002%) (StemCell Technologies) on plates coated in poly-L-ornithine (0.01%) (Sigma) and laminin (0.01 mg/mL) (Sigma). HEK293T cells (ATCC) were cultured in DMEM containing 4.5 g/L glucose, L-glutamine, phenol red, and 10% FBS (Wisent). All lines tested negative for mycoplasma contamination, checked monthly using the MycoAlert Mycoplasma Detection Kit (Lonza). Tumor-derived cell lines (Supplementary Table 1) were confirmed to match original samples by STR fingerprinting.

**CRISPR/Cas9 genome editing.** pSpCas9(BB)-2A-GFP (PX458) was a gift from Feng Zhang (Addgene plasmid # 48138). pSpCas9n(BB)-2A-GFP (PX461) was a gift from Feng Zhang (Addgene plasmid # 48140). CRISPR-Cas9 editing was carried out as described in ref. <sup>43</sup>. Constructs were transfected with lipofectamine 2000 (Thermo Fischer Scientific) according to the manufacturer's protocol. Flow cytometry sorted single GFP + cells in 96-well plates, 72-h post-transfection. A summary of the FACS gating strategy is provided in the Source Data File. Clones were expanded and the target locus sequenced by Sanger sequencing. Selected clones were screened by Illumina MiSeq system for the target exon to confirm complete mutation of the K27M allele. Mass spectrometry confirmed the absence of K27M mutant peptide in these clones. In HEK293T cells, clones heterozygous for HIST1H3B-K27M were derived through use of PX461 with the guide sequence and repair template in Supplementary Table 5. In primary HGG lines heterozygous for H3F3A-K27M, clones were derived with the mutant allele edited using PX458 and the guide sequence in Supplementary Table 5.

**Lentiviral transduction.** Lentiviruses were gifts from Dr. Peter Lewis. EZH2-WT and EZH2-Y641N constructs were applied to cells for 24 h, and puromycin (Wisent) selection (2 ug/mL) was maintained for the duration of growth. Lentiviruses expressing H3.3-K27R and H3.3-K27M were applied for 24 h and G418 (Wisent) selection (500 ng/mL) was maintained for the duration of growth.

**Western blotting.** Cells were lysed using RIPA buffer with added protease inhibitors (Roche). Whole lysate protein concentration was determined with the Bradford assay reagent (Bio-Rad). Ten micrograms of protein was separated on NuPAGE 3–8% Tris Acetate Protein gels (ThermoFischer Scientific) and wet-transferred to a nitrocellulose membrane (Bio-Rad). Membrane blocking was performed with 5% skim milk in tris buffered saline (50 mM Tris, 150 mM NaCl, 0.1% Tween 20, pH 7.4) (TBST) for 1 h. Membranes were incubated overnight with primary antibody solutions in 1% skim milk in TBST: anti-EZH2 ((1:1000, CST 5246), anti-H3K27M (1:200, Millipore ABE419), anti-H3K27me3 (1:1000, Millipore ABE44), anti-total H3 (1:2000, Abcam 1791), and anti-beta-actin (1:1000, CST 4970), also listed in Supplementary Table 6. Membranes were washed three times in TBST, and the ECL anti-rabbit IgG Horseradish Peroxidase linked whole antibody (GE Healthcare) was applied for 1 h, at 1:1000 dilution in 1% skim milk in TBST. Membranes were washed three times and the signal was resolved with Amersham ECL Prime Western Blotting Detection Reagent (GE Healthcare) and imaged on a ChemiDoc MP Imaging System (Bio-Rad). Uncropped versions of all blots are provided in Source Data file.

**Histone modification identification and quantification with nLC-MS.** The complete workflow for histone extraction, LC/MS, and data analysis was recently described in detail<sup>44</sup>. Briefly, cell pellets (~1 × 10<sup>6</sup> cells) were lysed on ice in nuclear isolation buffer supplemented with 0.3% NP-40 alternative. Isolated nuclei were incubated with 0.4 N H<sub>2</sub>SO<sub>4</sub> for 3 h at 4 °C with agitation. Hundred percent trichloroacetic acid (w/v) was added to the acid extract to a final concentration of 20% and samples were incubated on ice overnight to precipitate histones. The resulting histone pellets were rinsed with ice cold acetone + 0.1% HCl and then with ice cold acetone before resuspension in water and protein estimation by Bradford assay. Approximately 20 µg of histone extract was then resuspended in 100 mM ammonium bicarbonate and derivatized with propionic anhydride. One microgram of trypsin was added and samples were incubated overnight at 37 °C.

After tryptic digestion, a cocktail of isotopically-labeled synthetic histone peptides was spiked in at a final concentration of 250 fmol/ $\mu$ g and propionic anhydride derivatization was performed for second time. The resulting histone peptides were desalted using C18 Stage Tips, dried using a centrifugal evaporator, and reconstituted using 0.1% formic acid in preparation for nanoLC-MS analysis. nanoLC was performed using a Thermo Scientific™ Easy nLCTM 1000 equipped with a 75  $\mu$ m  $\times$  20 cm in-house packed column using Reprisil-Pur C18-AQ (3  $\mu$ m; Dr. Maisch GmbH, Germany). Buffer A was 0.1% formic acid and Buffer B was 0.1% formic acid in 80% acetonitrile. Peptides were resolved using a two-step linear gradient from 5 to 33% B over 45 min, then from 33 to 90% B over 10 min at a flow rate of 300 nL/min. The HPLC was coupled online to an Orbitrap Elite mass spectrometer operating in the positive mode using a Nanospray Flex™ Ion Source (Thermo Scientific) at 2.3 kV. Two full MS scans (m/z 300–1100) were acquired in the orbitrap mass analyzer with a resolution of 120,000 (at 200 m/z) every 8 DIA MS/MS events using isolation windows of 50 m/z each (e.g., 300–350, 350–400, ..., 650–700). MS/MS spectra were acquired in the ion trap operating in normal mode. Fragmentation was performed using collision-induced dissociation (CID) in the ion trap mass analyzer with a normalized collision energy of 35. AGC target and maximum injection time were 10e6 and 50 ms for the full MS scan, and 10e4 and 150 ms for the MS/MS scan, respectively. Raw files were analyzed using EpiProfile.

**Cell proliferation assays.** Cell lines were plated at low confluency in either 12- or 24-well plates. Cell number was counted every 7 days using a Cellometer Auto T4 bright field cell counter (Nexcelom Bioscience). Cell index is reported as an average cell count of at least three biological replicates, normalized to a control group. For CRISPR-edited lines, a minimum of two distinct clones per group were included in experiments.

**Drug sensitivity assay.** Cells were plated at a density of 7000 cells per well in 96 well plate. They were treated with an increasing dose of EZH2 inhibitors, GSK343 and UNC1999, obtained from the Structural Genomic Consortium, ranging from 0.5 $\mu$ M to 10 $\mu$ M. DMSO was used as a vehicle control. Cells were incubated with the drugs for 7 days and media was changed every 3 days. In order to assess cell viability, Alamar blue was added on cells on the 7th day for 6 hours and absorbance at 570nm and 600nm was determined using i-Control microplate reader software by Tecan. Ratio of cell viability was calculated according to the following formula for measuring cytotoxicity and proliferation:

Percentage difference between treated and control cells

$$\frac{(O2*A1)-(O1*A2)}{(O2*P1)-(O1*P2)} * 100 \text{ where:}$$

O1 = molar extinction coefficient (E) of oxidized Alamar Blue (Blue) at 570 nm (80586)

O2= E of oxidized Alamar Blue at 600 nm (117216)

A1 = absorbance of test wells at 570 nm

A2 = absorbance of test wells at 600 nm

P1 = absorbance of positive growth control well (cells plus Alamar Blue but no test agent) at 570 nm

P2 = absorbance of positive growth control well (cells plus Alamar Blue but no test agent at 600 nm

Graphs were plotted using Graphpad software using mean of three different replicates. Bars represent standard error of means.

**Mouse orthotopic xenograft.** All mice were housed, bred and subjected to listed procedures according to the McGill University Health Center Animal Care Committee and were in compliance with the guidelines of the Canadian Council on Animal Care. Female NOD SCID mice (4-6 weeks) were used for xenograft experiments. Mice were injected with the following cell lines at a density of  $10^5$  cells in the caudate putamen for BT245: 1) BT245 parental cells (n=9), 2) BT245 Clone C1 (unedited cells, n=9), 3) BT245 Clone C4 (K27M KO clone, n=9), 4) BT245 Clone D2 (K27M KO clone, n=10), and  $7.10^5$  cells in the pons for DIPG-XIII: 1) DIPG XIII parental cells (n=3), 2) DIPG XIII K27M KO (n=3). The Robot Stereotaxic machine from Neurostar was used for stereotaxic injections. Mice were monitored daily for over a year, for neurological symptoms of brain tumors: weight loss, epilepsy, altered gait, lethargy. Mice brains were imaged by MRI when symptoms appeared. They were euthanized immediately when clinical endpoint is reached. The brains were removed and put in formalin for histology. Kaplan-Meier curve for mice survival was generated using the Graphpad software. Mice that died due to a tumor are considered as 1. Those that were still surviving at the end of the experiment, or those that were euthanized for non-tumor related reasons were considered as 0.

**Droplet Digital PCR.** RNA was extracted from cells using the Aurum Total RNA Mini Kit (Bio-Rad) and concentration was quantified on the BioDrop uLite (Montreal Biotech). cDNA was generated using iScript Reverse Transcription Supermix (Bio-Rad). Target concentration

was determined using the QX200 ddPCR EvaGreen Supermix assay (Bio-Rad) using 20 uL per reaction containing 0.5 ng of cDNA, using manufacturer's protocol cycling conditions with a 58 degrees annealing temperature and 40 cycles. Droplets were assayed using the QX200 Droplet Reader (Bio-Rad) and manually scored for positive signal using QuantaSoft Software (Bio-Rad). The concentration of positive droplets per target was normalized to the concentration of GAPDH. The relative mRNA abundance is shown as the average of three biological replicates (distinct passages of each cell line) determined by a single technical replicate. Primer sequences for each target are found in Supplementary Table 7.

**ChIP-sequencing.** Cells (cell lines or dissociated tumor cells) were fixed with 1% formaldehyde (Sigma). Fixed cell preparations were washed, pelleted and stored at -80°C. Sonication of lysed nuclei (lysed in a buffer containing 1% SDS) was performed on a BioRuptor UCD-300 for 60 cycles, 10s on 20s off, centrifuged every 15 cycles, chilled by 4°C water cooler. Samples were checked for sonication efficiency using the criteria of 150-500bp by gel electrophoresis. After the sonication, the chromatin was diluted to reduce SDS level to 0.1% and before ChIP reaction 2% of sonicated drosophila S2 cell chromatin was spiked-in the samples for quantification of total levels of histone mark after the sequencing (see below).

ChIP reaction for histone modifications was performed on a Diagenode SX-8G IP-Star Compact using Diagenode automated Ideal ChIP-seq Kit. 25ul Protein A beads (Invitrogen) were washed and then incubated with antibodies (anti-H3K27M (1:66, Millipore ABE419), anti-H3K27me3 (1:40, CST 9733), anti-H3K27me3 (1:100, Active Motif 61017), anti-H3K27me2 (1:50, CST 9728), anti-H3.3 (1:66, Millipore 09-838), anti-HA(1:100, CST 3724)) as listed in Supplementary Table 6, and 2 million cells of sonicated cell lysate combined with protease inhibitors for 10 hr, followed by 20 min wash cycle with provided wash buffers.

ChIP reaction for SUZ12 and RING1B was performed as follows: antibodies (anti-SUZ12 (1:150, CST 3737), anti-RING1B (1:200, Active Motif 39663)), also listed in Supplementary Table 6) were conjugated by incubating with 40ul protein A or G beads at 4°C for 6 hours, then chromatin from ~4 million cells was added in RIPA buffer, incubated at 4°C o/n, washed using buffers from Ideal ChIP-seq Kit (1 wash with each buffer, corresponding to RIPA, RIPA+500mM NaCl, LiCl, TE), eluted from beads by incubating with Elution buffer for 30 minutes at room temperature.

Reverse cross linking took place on a heat block at 65°C for 4 hr. ChIP samples were then treated with 2ul RNase Cocktail at 65°C for 30 min followed by 2ul Proteinase K at 65°C for 30 min.

Samples were then purified with QIAGEN MiniElute PCR purification kit as per manufacturers' protocol. In parallel, input samples (chromatin from about 50,000 cells) were reverse crosslinked and DNA was isolated following the same protocol.

Library preparation was carried out using Kapa HTP Illumina library preparation reagents. Briefly, 25ul of ChIP sample was incubated with 45ul end repair mix at 20°C for 30 min followed by Ampure XP bead purification. A tailing: bead bound sample was incubated with 50ul buffer enzyme mix for 30°C 30 min, followed by PEG/NaCl purification. Adaptor ligation: bead bound sample was incubated with 45ul buffer enzyme mix and 5ul of different TruSeq DNA adapters (Illumina) for each sample, for 20°C 15 min, followed by PEG/NaCl purification (twice). Library enrichment: 12 cycles of PCR amplification. Size selection was performed after PCR using a 0.6x/0.8x ratio of Ampure XP beads (double size selection) set to collect 250-450bp fragments. ChIP libraries were sequenced using Illumina HiSeq 2000, 2500 or 4000 at 50bp single reads.

**RNA-seq.** Total RNA was extracted from cell pellets and mouse tumors using the AllPrep DNA/RNA/miRNA Universal Kit (Qiagen) according to instructions from the manufacturer. Library preparation was performed with ribosomal RNA (rRNA) depletion according to instructions from the manufacturer (Epicentre) to achieve greater coverage of mRNA and other long non-coding transcripts. Paired-end sequencing (100 bp) was performed on the Illumina HiSeq 2500 or 4000 platform.

**Whole genome bisulphite sequencing.** Whole-genome sequencing libraries were generated from 700 to 1000 ng of genomic DNA spiked with 0.1% (w/w) unmethylated  $\lambda$  DNA (Promega) previously fragmented to 300–400 bp peak sizes using the Covaris focused-ultrasonicator E210. Fragment size was controlled on a Bioanalyzer DNA 1000 Chip (Agilent) and the KAPA High Throughput Library Preparation Kit (KAPA Biosystems) was applied. End repair of the generated dsDNA with 3' or 5' overhangs, adenylation of 3' ends, adaptor ligation, and clean-up steps were carried out as per KAPA Biosystems' recommendations. The cleaned-up ligation product was then analyzed on a Bioanalyzer High Sensitivity DNA Chip (Agilent) and quantified by PicoGreen (Life Technologies). Samples were then bisulfite converted using the Epiect Fast DNA Bisulfite Kit (Qiagen) according to the manufacturer's protocol. Bisulfite-converted DNA was quantified using OliGreen (Life Technologies) and, based on quantity, amplified by 9–12 cycles of PCR using the Kapa Hifi Uracil + DNA polymerase (KAPA Biosystems) according to the manufacturer's protocol. The amplified libraries were purified using Ampure XP Beads (Beckman Coulter),

validated on Bioanalyzer High Sensitivity DNA Chips, and quantified by PicoGreen. Sequencing of the WGBS libraries was performed on the Illumina HiSeq2500/HiSeqX system using 125 or 150-bp paired-end sequencing.

**Analysis of ChIP-seq data.** Raw reads were aligned to human (UCSC hg19) or mouse (UCSC mm10) and drosophila (UCSC dm6) genome build using BWA<sup>45</sup> version 0.7.17 with default parameters. We divided genome into three different types of bins: 1kb, 10kb and 100kb, and counted number of reads from ChIP-seq experiments in those bins. We also counted reads in CpG islands (CGIs), promoters and genic regions. All the read counting was done using bedtools<sup>46</sup> version 2.22.1. The annotations of CGIs, promoters and RefSeq transcripts for hg19 and mm10 genomes were downloaded from UCSC Table Browser. Promoters were defined as 5kb regions centered on RefSeq TSS. For genic regions, we took the region with the longest length of (TES-TSS) if multiple TSS and/or TES exist. Top 1% bin scores were calculated as follows. After alignment, genome was divided into 1kb bins. Then ChIP-seq RPKM values were calculated for each bin (for H3K27me3 and input), and input was subtracted (i.e. H3K27me3 - input). The bins were sorted by these values, and average value of top 1% bins was taken. The data manipulation was performed in R. As known, ChIP-seq enrichments are qualitative measures and cannot be directly used to compare signal strength across samples. This is particularly problematic where the overall level of the bound protein varies across conditions, as is the case for most of the histone modifications in this study. To address this issue, we quantified the ChIP enrichments for each sample using a technique called ChIP with reference exogenous genome (ChIP-Rx), which applies spike-in Drosophila chromatin as internal control<sup>47</sup>. For each ChIP-seq profile, we calculated the ChIP-Rx ratio (denoted as Rx) as follows:

$$Rx = \frac{s/s\_dmel}{i/i\_dmel}$$

where  $s$  is the percentage of reads mapped to human or mouse genome in the target sample,  $s\_dmel$  is the percentage of spike-in Drosophila genome in the sample, and similarly  $i$  and  $i\_dmel$  are defined for the input sample. To compare the genome-wide H3K27me3 distribution between H3K27M and H3WT cells, we normalized the tracks using ChIP-Rx ratios as follows: for each sample, the read counts in the genomic compartments (e.g. bins) were first divide by the total number of reads, then multiplied by ChIP-Rx ratio of the sample, and then multiplied by a normalization factor (which is the same for all samples, set as  $10^{10}$  here) to avoid very small values. We also normalized the ChIP-seq enrichments of target samples by their input data. Let  $S_i$

and  $N_i$  be the read counts in the  $i$ -th genomic compartment of the sample and input respectively, and TS and TN be the total read counts of the two samples, the normalization on  $S_i$  was done as follows:

$$S_{i\_norm} = \log_2 \frac{S_i/TS}{N_i/TN}.$$

To avoid 0 in denominator or logarithm, we added a pseudo count (denoted as  $c$ , here we set  $c=1$ ) during input normalization, as follows:

$$S_{i\_norm} = \log_2 \frac{(S_i+c)/TS}{(N_i+c)/TN}.$$

ChIP-sequencing coverage tracks were visualized using IGV 2.3 software<sup>48,49</sup>. To call narrow peaks, we used “macs2 callpeak -t  $\{\text{CHIP}\}$  -c  $\{\text{INPUT}\}$  -f BAM -g hs -n  $\{\text{NAME}\}$  -q 0.01 --outdir  $\{\text{OUTDIR}\}$ ”. For broad histone marks, we call peaks using “macs2 callpeak -t  $\{\text{CHIP}\}$  -c  $\{\text{INPUT}\}$  -f BAM --broad -g hs --broad-cutoff 0.1 -n  $\{\text{NAME}\}$  --outdir  $\{\text{OUTDIR}\}$ ”.

Peak-calling was done using MACS2<sup>50</sup> version 2.1.1.

The SUZ12 peak-centered H3K27me2, H3K27me3 enrichment plots and PMD plot were generated using ngs.plot.r package<sup>51</sup>. The signal around SUZ12 peak centers ( $\pm$  50 kb) was normalized by input and by ChIP-Rx ratio. The signal around PMD regions was extended by 100 kb on each side. The following command was used to generate the plots: “./ngs.plot.r -G hg19 -R bed -C  $\{\text{Config file}\}$  -O  $\{\text{output file}\}$  -L  $\{\text{extend by number of bases}\}$ ”. The config file contains the names of H3K27me3/H3K27me2 and input BAM files and BED file name of SUZ12 peaks for SUZ12-centered plot. For PMD plot, the config file contains the BED file of PMD regions instead.

The aggregate plots of SUZ12, H3K27me2 and H3K27me3 for primary cell lines were generated using deepTools v3.1.0<sup>52</sup>. The signals were normalized by both input and ChIP-Rx ratios as follows:

$$S_{i\_norm} = \log_2 \frac{(Rx*(S_i+c))/TS}{(N_i+c)/TN},$$

where Rx is the ChIP-Rx ratio, the rest variables have the same meanings as in the input-normalization equation. The normalization was done using deepTools' bamCompare, where the bin size and fragment length were set to 500bp and 200bp respectively. After normalization, the signals were aggregated around ( $\pm$  50 kb) the centres of the top CGIs (for SUZ12) or TSS of repressed genes (for H3K27me3) using deepTools' computeMatrix and visualized by averaging the score in bins equidistant from the mid-point (with NaN values discarded).

Heat map plots for comparing H3K27me3, SUZ12, RING1B, and DNA methylation were generated using ChAsE v.1.0.11 software<sup>53</sup>. The regions were centered on CGIs, extending 5kb, 10kb or 50kb upstream and downstream.

We characterized the variations of H3K27me3 at CGIs in H3WT (or H3K27M-KO) versus H3K27M cells by plotting the differential enrichment of H3K27me3 between the two conditions against the H3K27me3 enrichment in H3WT (or H3K27M-KO) cells. Accordingly, the x and y axes are defined as follows:

$$X = \log_2 \left( \frac{H3WT}{INPUT} \right), Y = \log_2 \left( \frac{H3K27M}{H3WT} \right),$$

where H3WT, H3K27M and INPUT represent the processed read counts at CGIs in the three types of samples, i.e. WT, K27M and input ChIP-seq libraries. The “processed read counts” here means the number of mapped reads at CGIs divided by total read counts of the genome. Note that for H3WT and H3K27M, we also multiplied the processed read counts by their ChIP-Rx ratios. We filtered out the CGIs which overlap with the ENCODE DAC blacklisted regions<sup>54</sup>. To reduce stochasticity in low coverage regions, we took the average of H3K27me3 enrichment in two available WT samples. Therefore, the x and y axes are modified to:

$$X = \frac{1}{2}(\log_2 \left( \frac{H3WT_1}{INPUT_1} \right) + \log_2 \left( \frac{H3WT_2}{INPUT_2} \right)), Y = \log_2 \left( \frac{H3K27M}{\frac{1}{2}(H3WT_1 + H3WT_2)} \right).$$

The plot of H3K27me3 variations at promoters is similar to the one at CGIs. The dots were colored based on the differential analysis of gene expression (see Analysis of RNA-seq data for details). The H3K27me3 variations at promoters are categorized into four groups: Gained in K27M, Absent, Lost in K27M and Retained. The categorization was based on H3K27me3 values in WT (x axis) and H3K27me3 difference (y axis) as follows: for CGI/DNA methylation plot (Fig. 2g, Supplementary Fig. 10g-h, 13a-c): Gained in K27M (BT245:  $y > 0$ ; DIPGXIII:  $y > 2.6$ ), Absent (BT245:  $y < 0$ ,  $x < -3.75$ ; DIPGXIII:  $y < 2.5$ ,  $x < -5$ ), Lost in K27M (BT245:  $y < -4$ ,  $x > -2.5$ ; DIPGXIII:  $y < -2.5$ ,  $x > -2.5$ ), Retained (BT245:  $-3 < y < 0$ ,  $x > 1.25$ ; DIPGXIII:  $y > -2$ ,  $x > 0.5$ ); for promoter/differential expression plot (Fig. 4a): Gained in K27M (BT245:  $y > 0$ ), Absent (BT245:  $y < 0$ ,  $x < -2.5$ ), Lost in K27M (BT245:  $y < -4$ ,  $x > -2.5$ ), Retained (BT245:  $-3 < y < 0$ ,  $x > 0$ ).

To show the correlation between H3K27me2 in K27M and H3K27me3 in wild-type isogenic cells, we first sorted the 1kb non-overlapping bins based on the H3K27me2 enrichment (after input normalization) in K27M cells, then grouped the sorted bins into 1000 windows, and plot the mean values of ChIP enrichment (WT-H3K27me3 and WT-H3K27me2) in the 1000 windows. We used

the dashed line to indicate the K27M-H3K27me2 enrichment per window. The procedure was adapted from<sup>55</sup>.

**Analysis of RNA-seq data.** Raw reads were aligned to human genome build (UCSC hg19) using STAR<sup>56</sup> version 2.5.3a. For each sample, we counted the mapped reads for each gene from annotation files in GTF format (downloaded from UCSC Table Browser) using featureCounts program (version 1.5.3). Read counts from RNA-seq alignment were transformed (regularized log transformation) using the rlog function from R package DESeq2. Differential expressed (DE) genes between H3WT and H3K27M were defined as genes with log2FoldChange larger (Up genes) or smaller (Down genes) than 1 and with adjusted p-value smaller than 0.05. To make Decile plot of DE genes, first we categorized the DE genes into ten groups based on their expression levels in parental samples (i.e. before CRISPR-editing or overexpression). Then we counted the number of genes (including Up genes and Down genes) in each category, and plotted the gene counts using geom\_bar in R Package ggplot2. Gene set enrichment analysis (GSEA) was performed using the GSEA tool from Broad Institute (<https://software.broadinstitute.org/gsea/index.jsp>)<sup>57,58</sup>.

**Analysis of WGBS data.** Raw reads were aligned to human genome build (UCSC hg19) using BWA (version 0.6.1)<sup>59</sup> after converting the reference genome to bisulfite mode. Low-quality sequence at the 3' ends were trimmed. And for the overlapping paired-end reads, we clipped the 3' end of one of them to avoid double counting. This was done on both forward and reverse strand. After alignment, we filtered reads that were duplicate, or were poorly mapped (with more than 2% mismatches), or not mapped at the expected distance based on the library insert size. To call methylation of individual CpGs, Samtools<sup>59</sup> (version 0.1.18) in mpileup mode was applied. CpGs covered by less than five reads were removed. We also discarded the CpGs that were overlapped with SNPs from dbSNPs (137) or were located within the ENCODE DAC blacklisted regions or Duke excluded regions<sup>54</sup>. To call partially methylated domains (PMDs), we used a window size of 10 kb and slid the window on the measurements of methylation level at each CpG. For each 10 kb window where the average methylation level of mCGs was less than 70% (with each CpG covered by at least 5 MethylC-Seq reads), we extended the region with increments of 10 kb until the average methylation level of the region was greater than 70%. After that, we reported the regions with size larger than 1 Mb as PMDs.

**Code availability**

Custom R scripts used to generate the top 1% bin scores, the plots of H3K27me3 variations, the correlation plots of K27M-K27me2 and WT-K27me3 and the Decile plots, are available upon request.

### Data availability

The sequencing data reported in this paper are available for download through the GenAP portal at <https://datahub-jv6f4mbl.udes.genap.ca/>

The source data underlying Figs 1a, 1d, 2a, 2d, 3d-e, 5a and Supplementary Figs 2, 4a, 7a, 8b-c, 8e-f, 9a-d, 10b-e, 11b-e, 13d, 16c-d, 17a-e, 18a-b, 19b and 20a-c are provided as a Source Data file.

### References

- 1 Sturm, D. *et al.* Paediatric and adult glioblastoma: multifactorial (epi)genomic culprits emerge. *Nature reviews. Cancer* **14**, 92-107, doi:10.1038/nrc3655 (2014).
- 2 Faury, D. *et al.* Molecular profiling identifies prognostic subgroups of pediatric glioblastoma and shows increased YB-1 expression in tumors. *Journal of clinical oncology : official journal of the American Society of Clinical Oncology* **25**, 1196-1208, doi:10.1200/JCO.2006.07.8626 (2007).
- 3 Haque, T. *et al.* Gene expression profiling from formalin-fixed paraffin-embedded tumors of pediatric glioblastoma. *Clinical cancer research : an official journal of the American Association for Cancer Research* **13**, 6284-6292, doi:10.1158/1078-0432.CCR-07-0525 (2007).
- 4 Qu, H. Q. *et al.* Genome-wide profiling using single-nucleotide polymorphism arrays identifies novel chromosomal imbalances in pediatric glioblastomas. *Neuro-oncology* **12**, 153-163, doi:10.1093/neuonc/nop001 (2010).
- 5 Khuong-Quang, D. A. *et al.* K27M mutation in histone H3.3 defines clinically and biologically distinct subgroups of pediatric diffuse intrinsic pontine gliomas. *Acta neuropathologica* **124**, 439-447, doi:10.1007/s00401-012-0998-0 (2012).
- 6 Schwartzenuber, J. *et al.* Driver mutations in histone H3.3 and chromatin remodelling genes in paediatric glioblastoma. *Nature* **482**, 226-231, doi:10.1038/nature10833 (2012).

- 7 Wu, G. *et al.* Somatic histone H3 alterations in pediatric diffuse intrinsic pontine gliomas and non-brainstem glioblastomas. *Nature genetics* **44**, 251-253, doi:10.1038/ng.1102 (2012).
- 8 Fontebasso, A. M., Liu, X. Y., Sturm, D. & Jabado, N. Chromatin remodeling defects in pediatric and young adult glioblastoma: a tale of a variant histone 3 tail. *Brain pathology* **23**, 210-216, doi:10.1111/bpa.12023 (2013).
- 9 Fontebasso, A. M. *et al.* Recurrent somatic mutations in ACVR1 in pediatric midline high-grade astrocytoma. *Nature genetics* **46**, 462-466, doi:10.1038/ng.2950 (2014).
- 10 Sturm, D. *et al.* Hotspot mutations in H3F3A and IDH1 define distinct epigenetic and biological subgroups of glioblastoma. *Cancer cell* **22**, 425-437, doi:10.1016/j.ccr.2012.08.024 (2012).
- 11 Louis, D. N. *et al.* The 2016 World Health Organization Classification of Tumors of the Central Nervous System: a summary. *Acta neuropathologica* **131**, 803-820, doi:10.1007/s00401-016-1545-1 (2016).
- 12 Nikbakht, H. *et al.* Spatial and temporal homogeneity of driver mutations in diffuse intrinsic pontine glioma. *Nature communications* **7**, 11185, doi:10.1038/ncomms11185 (2016).
- 13 Fontebasso, A. M. *et al.* Epigenetic dysregulation: a novel pathway of oncogenesis in pediatric brain tumors. *Acta neuropathologica* **128**, 615-627, doi:10.1007/s00401-014-1325-8 (2014).
- 14 Lewis, P. W. *et al.* Inhibition of PRC2 activity by a gain-of-function H3 mutation found in pediatric glioblastoma. *Science* **340**, 857-861, doi:10.1126/science.1232245 (2013).
- 15 Bender, S. *et al.* Reduced H3K27me3 and DNA hypomethylation are major drivers of gene expression in K27M mutant pediatric high-grade gliomas. *Cancer cell* **24**, 660-672, doi:10.1016/j.ccr.2013.10.006 (2013).
- 16 Bechet, D. *et al.* Specific detection of methionine 27 mutation in histone 3 variants (H3K27M) in fixed tissue from high-grade astrocytomas. *Acta neuropathologica* **128**, 733-741, doi:10.1007/s00401-014-1337-4 (2014).
- 17 Margueron, R. & Reinberg, D. The Polycomb complex PRC2 and its mark in life. *Nature* **469**, 343-349, doi:10.1038/nature09784 (2011).

- 18 Jiao, L. & Liu, X. Structural basis of histone H3K27 trimethylation by an active polycomb repressive complex 2. *Science* **350**, aac4383, doi:10.1126/science.aac4383 (2015).
- 19 Justin, N. *et al.* Structural basis of oncogenic histone H3K27M inhibition of human polycomb repressive complex 2. *Nature communications* **7**, 11316, doi:10.1038/ncomms11316 (2016).
- 20 Chan, K. M. *et al.* The histone H3.3K27M mutation in pediatric glioma reprograms H3K27 methylation and gene expression. *Genes Dev* **27**, 985-990, doi:10.1101/gad.217778.113 (2013).
- 21 Fang, D. *et al.* H3.3K27M mutant proteins reprogram epigenome by sequestering the PRC2 complex to poised enhancers. *Elife* **7**, doi:10.7554/eLife.36696 (2018).
- 22 Mohammad, F. *et al.* EZH2 is a potential therapeutic target for H3K27M-mutant pediatric gliomas. *Nature medicine* **23**, 483-492, doi:10.1038/nm.4293 (2017).
- 23 Piunti, A. *et al.* Therapeutic targeting of polycomb and BET bromodomain proteins in diffuse intrinsic pontine gliomas. *Nat Med* **23**, 493-500, doi:10.1038/nm.4296 (2017).
- 24 Bernstein, B. E. *et al.* A bivalent chromatin structure marks key developmental genes in embryonic stem cells. *Cell* **125**, 315-326, doi:10.1016/j.cell.2006.02.041 (2006).
- 25 Funato, K., Major, T., Lewis, P. W., Allis, C. D. & Tabar, V. Use of human embryonic stem cells to model pediatric gliomas with H3.3K27M histone mutation. *Science* **346**, 1529-1533, doi:10.1126/science.1253799 (2014).
- 26 Pathania, M. *et al.* H3.3(K27M) Cooperates with Trp53 Loss and PDGFRA Gain in Mouse Embryonic Neural Progenitor Cells to Induce Invasive High-Grade Gliomas. *Cancer cell* **32**, 684-700 e689, doi:10.1016/j.ccell.2017.09.014 (2017).
- 27 Mikkelsen, T. S. *et al.* Genome-wide maps of chromatin state in pluripotent and lineage-committed cells. *Nature* **448**, 553-560, doi:10.1038/nature06008 (2007).
- 28 Buczkowicz, P. *et al.* Genomic analysis of diffuse intrinsic pontine gliomas identifies three molecular subgroups and recurrent activating ACVR1 mutations. *Nature genetics* **46**, 451-456, doi:10.1038/ng.2936 (2014).
- 29 Taylor, K. R. *et al.* Recurrent activating ACVR1 mutations in diffuse intrinsic pontine glioma. *Nature genetics* **46**, 457-461, doi:10.1038/ng.2925 (2014).
- 30 Wu, G. *et al.* The genomic landscape of diffuse intrinsic pontine glioma and pediatric non-brainstem high-grade glioma. *Nature genetics* **46**, 444-450, doi:10.1038/ng.2938 (2014).

- 31 van den Boom, V. *et al.* Non-canonical PRC1.1 Targets Active Genes Independent of H3K27me3 and Is Essential for Leukemogenesis. *Cell Rep* **14**, 332-346, doi:10.1016/j.celrep.2015.12.034 (2016).
- 32 Ferrari, K. J. *et al.* Polycomb-dependent H3K27me1 and H3K27me2 regulate active transcription and enhancer fidelity. *Mol Cell* **53**, 49-62, doi:10.1016/j.molcel.2013.10.030 (2014).
- 33 Sneeringer, C. J. *et al.* Coordinated activities of wild-type plus mutant EZH2 drive tumor-associated hypertrimethylation of lysine 27 on histone H3 (H3K27) in human B-cell lymphomas. *Proc Natl Acad Sci U S A* **107**, 20980-20985, doi:10.1073/pnas.1012525107 (2010).
- 34 Mackay, A. *et al.* Integrated Molecular Meta-Analysis of 1,000 Pediatric High-Grade and Diffuse Intrinsic Pontine Glioma. *Cancer cell* **32**, 520-537 e525, doi:10.1016/j.ccell.2017.08.017 (2017).
- 35 McCabe, M. T. *et al.* Mutation of A677 in histone methyltransferase EZH2 in human B-cell lymphoma promotes hypertrimethylation of histone H3 on lysine 27 (H3K27). *Proc Natl Acad Sci U S A* **109**, 2989-2994, doi:10.1073/pnas.1116418109 (2012).
- 36 Hojfeldt, J. W. *et al.* Accurate H3K27 methylation can be established de novo by SUZ12-directed PRC2. *Nat Struct Mol Biol* **25**, 225-232, doi:10.1038/s41594-018-0036-6 (2018).
- 37 Filbin, M. G. *et al.* Developmental and oncogenic programs in H3K27M gliomas dissected by single-cell RNA-seq. *Science* **360**, 331-335, doi:10.1126/science.aao4750 (2018).
- 38 Margueron, R. *et al.* Role of the polycomb protein EED in the propagation of repressive histone marks. *Nature* **461**, 762-767, doi:10.1038/nature08398 (2009).
- 39 Oksuz, O. *et al.* Capturing the onset of PRC2-mediated repressive domain formation. *bioRxiv*, doi:10.1101/272989 (2018).
- 40 Lu, C. *et al.* Histone H3K36 mutations promote sarcomagenesis through altered histone methylation landscape. *Science* **352**, 844-849, doi:10.1126/science.aac7272 (2016).
- 41 Mohn, F. *et al.* Lineage-specific polycomb targets and de novo DNA methylation define restriction and potential of neuronal progenitors. *Mol Cell* **30**, 755-766, doi:10.1016/j.molcel.2008.05.007 (2008).
- 42 Monje, M. *et al.* Hedgehog-responsive candidate cell of origin for diffuse intrinsic pontine glioma. *Proc Natl Acad Sci U S A* **108**, 4453-4458, doi:10.1073/pnas.1101657108 (2011).

- 43 Ran, F. A. *et al.* Genome engineering using the CRISPR-Cas9 system. *Nature protocols* **8**, 2281-2308, doi:10.1038/nprot.2013.143 (2013).
- 44 Karch, K. R., Sidoli, S. & Garcia, B. A. Identification and Quantification of Histone PTMs Using High-Resolution Mass Spectrometry. *Methods in enzymology* **574**, 3-29, doi:10.1016/bs.mie.2015.12.007 (2016).
- 45 Li, H. & Durbin, R. Fast and accurate short read alignment with Burrows-Wheeler transform. *Bioinformatics* **25**, 1754-1760, doi:10.1093/bioinformatics/btp324 (2009).
- 46 Quinlan, A. R. & Hall, I. M. BEDTools: a flexible suite of utilities for comparing genomic features. *Bioinformatics* **26**, 841-842, doi:10.1093/bioinformatics/btq033 (2010).
- 47 Orlando, D. A. *et al.* Quantitative ChIP-Seq normalization reveals global modulation of the epigenome. *Cell reports* **9**, 1163-1170, doi:10.1016/j.celrep.2014.10.018 (2014).
- 48 Robinson, J. T. *et al.* Integrative genomics viewer. *Nature biotechnology* **29**, 24-26, doi:10.1038/nbt.1754 (2011).
- 49 Thorvaldsdottir, H., Robinson, J. T. & Mesirov, J. P. Integrative Genomics Viewer (IGV): high-performance genomics data visualization and exploration. *Briefings in bioinformatics* **14**, 178-192, doi:10.1093/bib/bbs017 (2013).
- 50 Feng, J., Liu, T., Qin, B., Zhang, Y. & Liu, X. S. Identifying ChIP-seq enrichment using MACS. *Nature protocols* **7**, 1728-1740, doi:10.1038/nprot.2012.101 (2012).
- 51 Shen, L., Shao, N., Liu, X. & Nestler, E. ngs.plot: Quick mining and visualization of next-generation sequencing data by integrating genomic databases. *BMC genomics* **15**, 284, doi:10.1186/1471-2164-15-284 (2014).
- 52 Ramirez, F. *et al.* deepTools2: a next generation web server for deep-sequencing data analysis. *Nucleic acids research* **44**, W160-165, doi:10.1093/nar/gkw257 (2016).
- 53 Younesy, H. *et al.* ChAsE: chromatin analysis and exploration tool. *Bioinformatics* **32**, 3324-3326, doi:10.1093/bioinformatics/btw382 (2016).
- 54 Consortium, E. P. An integrated encyclopedia of DNA elements in the human genome. *Nature* **489**, 57-74, doi:10.1038/nature11247 (2012).
- 55 Baubec, T. *et al.* Genomic profiling of DNA methyltransferases reveals a role for DNMT3B in genic methylation. *Nature* **520**, 243-247, doi:10.1038/nature14176 (2015).
- 56 Dobin, A. *et al.* STAR: ultrafast universal RNA-seq aligner. *Bioinformatics* **29**, 15-21, doi:10.1093/bioinformatics/bts635 (2013).

- 57 Mootha, V. K. *et al.* PGC-1alpha-responsive genes involved in oxidative phosphorylation are coordinately downregulated in human diabetes. *Nature genetics* **34**, 267-273, doi:10.1038/ng1180 (2003).
- 58 Subramanian, A. *et al.* Gene set enrichment analysis: a knowledge-based approach for interpreting genome-wide expression profiles. *Proceedings of the National Academy of Sciences of the United States of America* **102**, 15545-15550, doi:10.1073/pnas.0506580102 (2005).
- 59 Li, H. *et al.* The Sequence Alignment/Map format and SAMtools. *Bioinformatics* **25**, 2078-2079, doi:10.1093/bioinformatics/btp352 (2009).

**Acknowledgements.** This work was supported by funding from: US National Institutes of Health (NIH grant P01- CA196539 to N.J., J.M., P.W.L., B.A.G., T.P.; GM110174 to B.A.G.; T32GM008275 and TL1TR001880 to D.M.M.), the Canadian Institutes for Health Research (CIHR grant MOP-286756 and FDN-154307 to N.J., EP1-120608 to T.P. and P.J.T.-156086 to C.L.K.), the Fonds de Recherche du Québec en Santé (FRQS) salary award to C.L.K. N.J. is a member of the Penny Cole Laboratory and the recipient of a Chercheur Boursier, Chaire de Recherche Award from the FRQS. This work was performed within the context of the International CHildhood Astrocytoma INtegrated Genomic and Epigenomic (ICHANGE) consortium, and the Stand Up to Cancer, Canada Cancer Stem Cell Dream Team initiative, with funding from Genome Canada and Genome Quebec. A.S.H., W.A.C., and N.D.J. are recipients of fellowships from FRQS. D.B. is the recipient of a fellowship from the TD CanadaTrust/ Montreal Children's Hospital Foundation. M.K.M. is funded by a CIHR Banting postdoctoral fellowship. P.W.L. is a Pew Scholar in the Biomedical Sciences. C.L. acknowledges support from Damon Runyon Cancer Research Foundation and Matthew Larson Foundation. P.S. and M.P. are supported by the ERC (H3.3Cancer). We thank Alexey Soshnev for providing the comprehensive schema for the K27M mechanism of action. We are especially grateful for the generous philanthropic donations of Kat D DIPG and We Love You Connie Foundations.

**Author contributions.** A.S.H. and B.K. led and performed a majority of the functional studies, and were actively involved in study design, data analysis, interpretation, and manuscript preparation. H.C., S.P.-C., N.D.J., R.L., H.N., B.H., G.C. and W.A.C. contributed to bioinformatic analysis of the data and interpretation of the results. M.Z., S.D., C.C.L.C., J.B., Ab.M., D.B., D.F.,

M.K.M. and S.U.J. contributed to data collection, analysis, and study design. D.M.M. and B.G. led the histone proteomics experiments and analysis. L.M. contributed to study design, data interpretation, and manuscript preparation. B.E. and A.W. assisted with the collection of patient samples, study design, and data interpretation. M.P. and P.S. generated the mouse model used for some ChIP-seq experiments, A.I.M., T.P., C.L., P.W.L., B.G., C.L.K, N.J. and J.M. contributed to study design, data interpretation, and manuscript preparation.

### **Additional information**

Supplementary Information accompanies this paper at <https://doi.org/10.1038/s41467-019-09140-x>.

Competing interests: The authors declare no competing interests

Reprints and permission information is available online at <http://npg.nature.com/reprintsandpermissions/>

Journal peer review information: Nature Communications thanks the anonymous reviewers for their contribution to the peer review of this work. Peer reviewer reports are available.

Publisher's note: Springer Nature remains neutral with regard to jurisdictional claims in published maps and institutional affiliations.

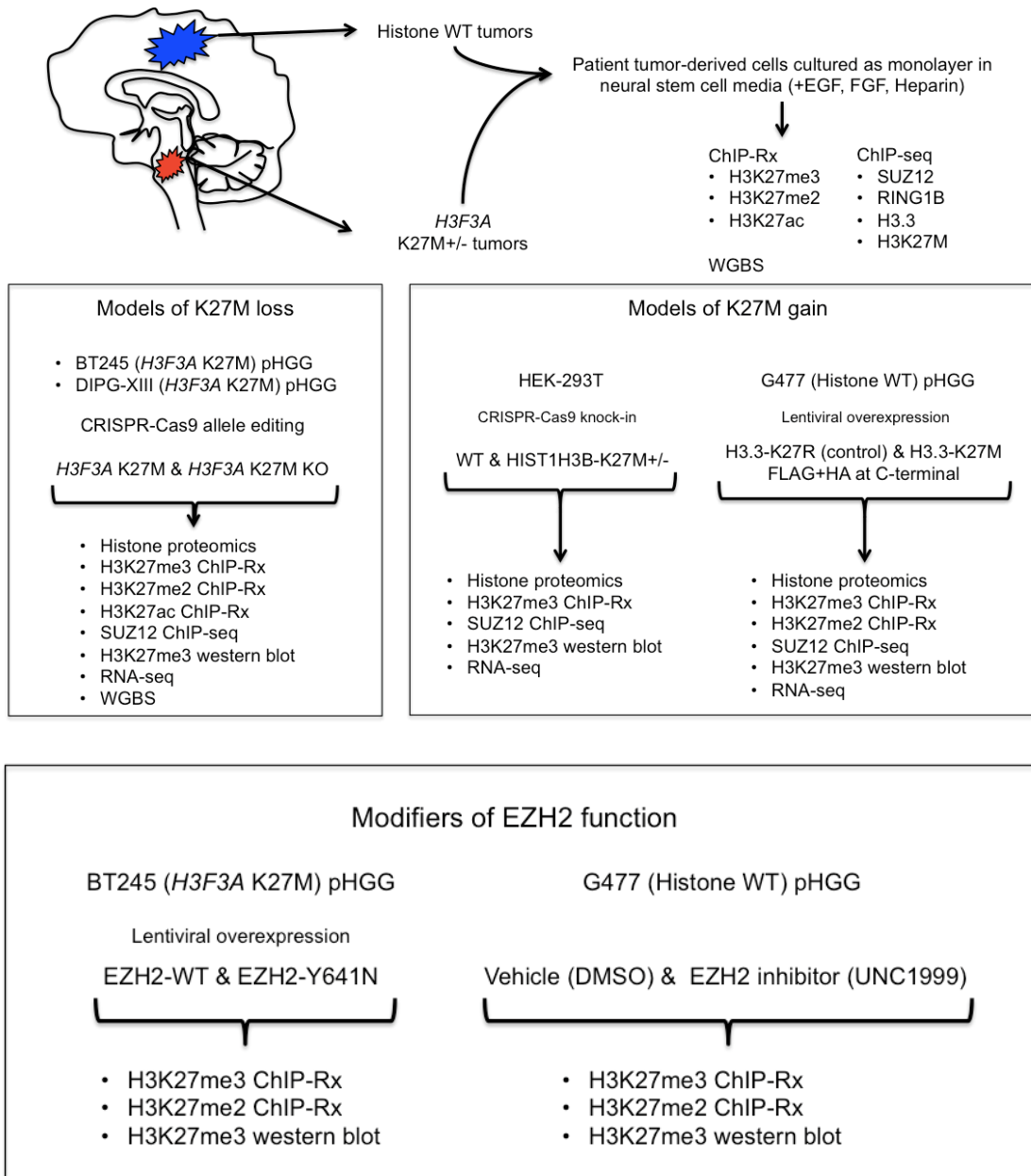
**Open Access** This article is licensed under a Creative Commons

Attribution 4.0 International License, which permits use, sharing, adaptation, distribution and reproduction in any medium or format, as long as you give appropriate credit to the original author(s) and the source, provide a link to the Creative Commons license, and indicate if changes were made. The images or other third party material in this article are included in the article's Creative Commons license, unless indicated otherwise in a credit line to the material. If material is not included in the article's Creative Commons license and your intended use is not permitted by statutory regulation or exceeds the permitted use, you will need to obtain permission directly from the copyright holder. To view a copy of this license, visit <http://creativecommons.org/licenses/by/4.0/>.

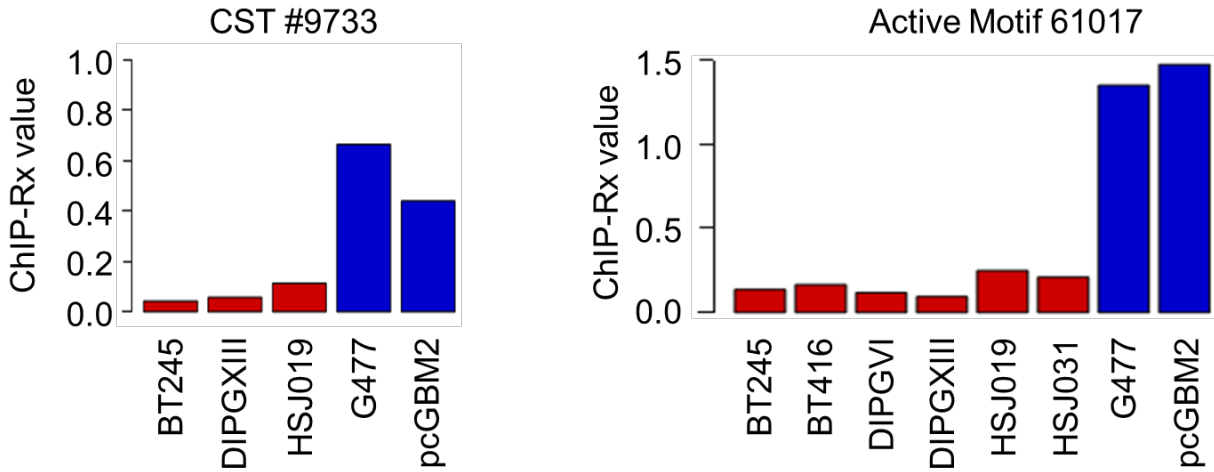
© The Author(s) 2019

### **Supplementary information**

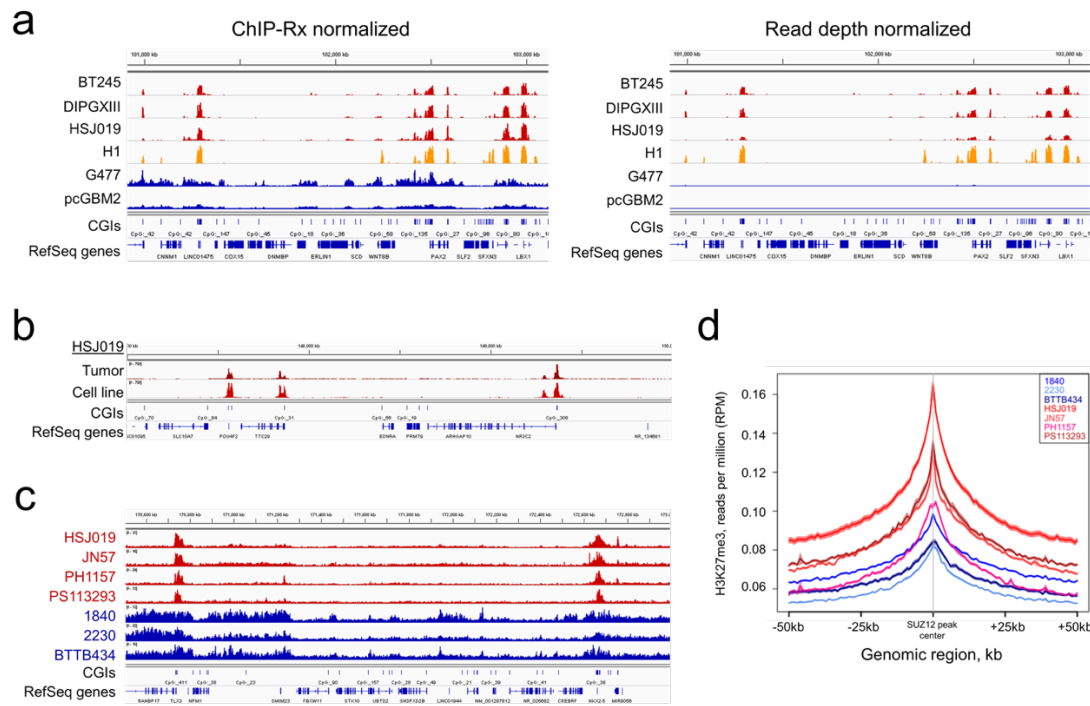
Supplementary Information accompanies this paper at <https://doi.org/10.1038/s41467-019-09140-x>. I have not reproduced supplemental tables S1-7 due to space limitations.



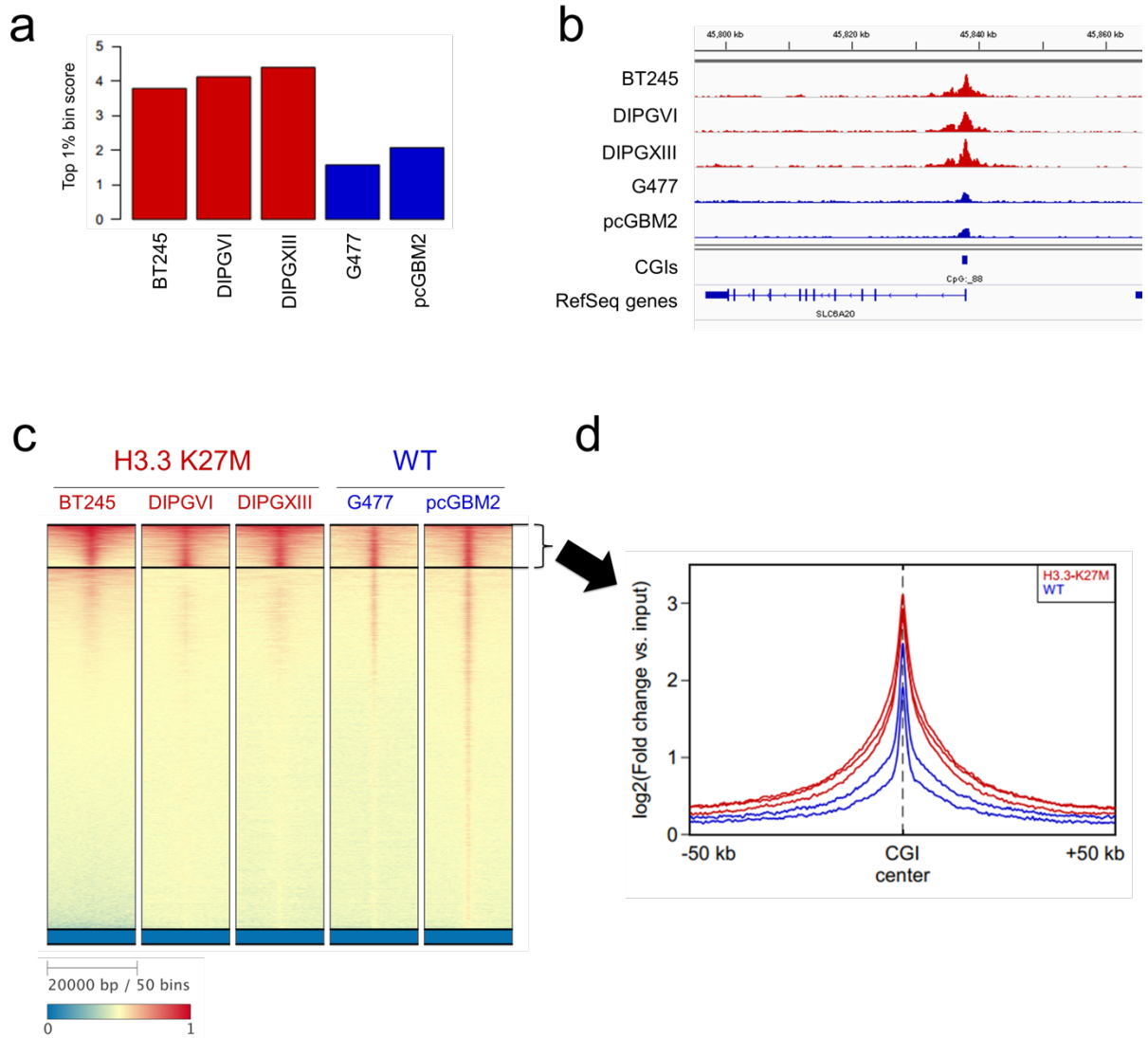
**Supplementary Figure 1.** Scheme of experimental datasets. Please note the color code used throughout the figures for cells: **red** is for cell lines expressing H3K27M mutation (primary pediatric high-grade gliomas (pHGG) lines, gene-edited cell lines, cells overexpressing H3K27M) and **blue** for cell lines wild-type (WT) for this mutation.



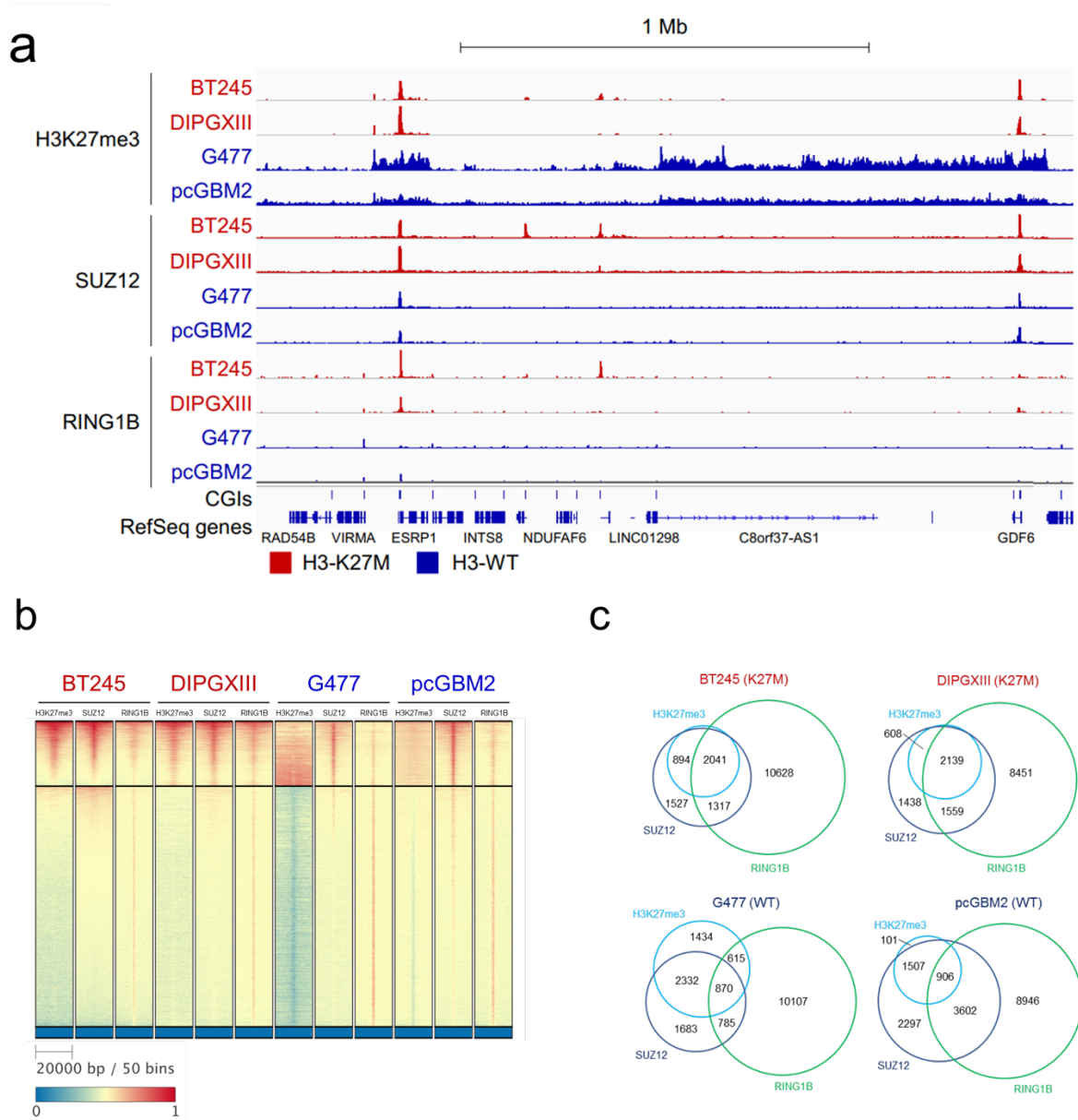
**Supplementary Figure 2.** ChIP-Rx values for H3K27me3 in different primary high-grade glioma (HGG) cell lines, using two different antibodies. Similar drastic decrease of the mark in H3.3K27M HGG cells (red) compared to wild-type HGG (blue) was observed using either anti-H3K27me3 antibody for ChIP-seq. Source data are provided as a Source Data file.



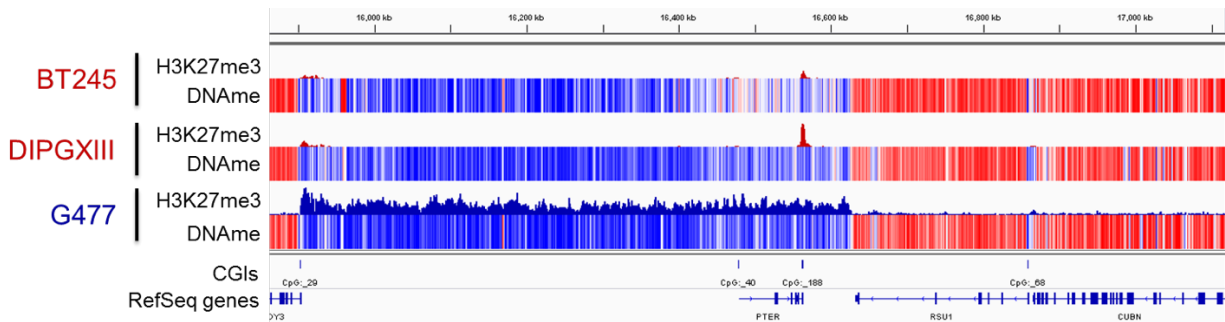
**Supplementary Figure 3. a.** Tracks of H3K27me3 for pediatric high-grade gliomas (pHGG)-derived primary cell lines and H1 human Embryonic Stem Cells (ESC), ChIP-Rx normalized (upper panel) and read depth normalized (lower panel). Note the significant differences that lead to overestimating the amount of H3K27me3 in H3K27M when using read depth (standard) normalization compared to ChIP-Rx. Note the “peaky” distribution of residual H3K27me3 in H3K27M cells (red tracks) which is centered around CpG islands (CGIs) like what is observed in H1 ESCs (orange track). This contrasts with the wide distribution of H3K27me3 in cells WT for this mutation (blue tracks). **b.** This distribution of residual H3K27me3 observed in primary cell lines mirrors the distribution of the mark in the original tumour as shown for the cell line where we had material for both (lower panel). Indeed, tracks of H3K27me3 for a tumor tissue of the primary sample HSJ019 and cell line derived from that tumor, ChIP-Rx normalized indicate that cell line models are reflective of the predominant epigenomic state of tumors *in vivo*. **c.** The distribution of residual H3K27me3 in primary tumors follows the same pattern as in cell lines when comparing H3.3 K27M (n=4) and H3 wild-type (n=3) tumor tissues. Tracks of H3K27me3 from glioblastoma tissue samples are shown, autoscaled due to the absence of drosophila spike-in. **d.** Aggregate plots of H3K27me3 in primary tumor tissue samples over common SUZ12 peaks derived from BT245 (H3.3K27M) and G477 (wild-type) cell lines. H3K27M mutant tumors are represented by shades of red, while wild-type tumors by shades of blue.



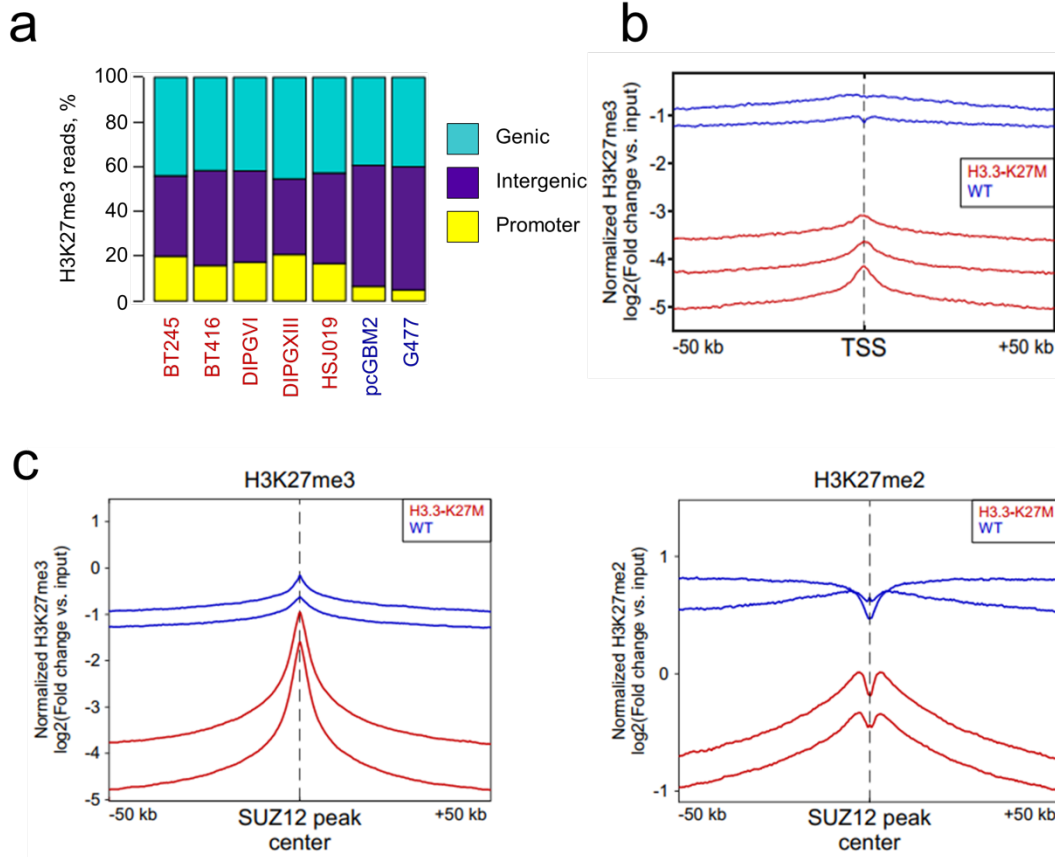
**Supplementary Figure 4.** SUZ12 deposition in H3K27M (red) is broader and enriched in unmethylated CGIs as compared to high-grade gliomas (HGG) lines wild-type (WT) for H3K27M (blue). **a.** SUZ12 top 1% 1kb bin scores and **b.** Representative SUZ12 ChIP-seq tracks, read depth normalized. **c.** heatmap plots at CGIs, primary cells, K27M vs. WT. Clustered by kmeans clustering (k=3). **d.** Aggregate plots of SUZ12 signal over CGIs for the top cluster. Source data are provided as a Source Data file.



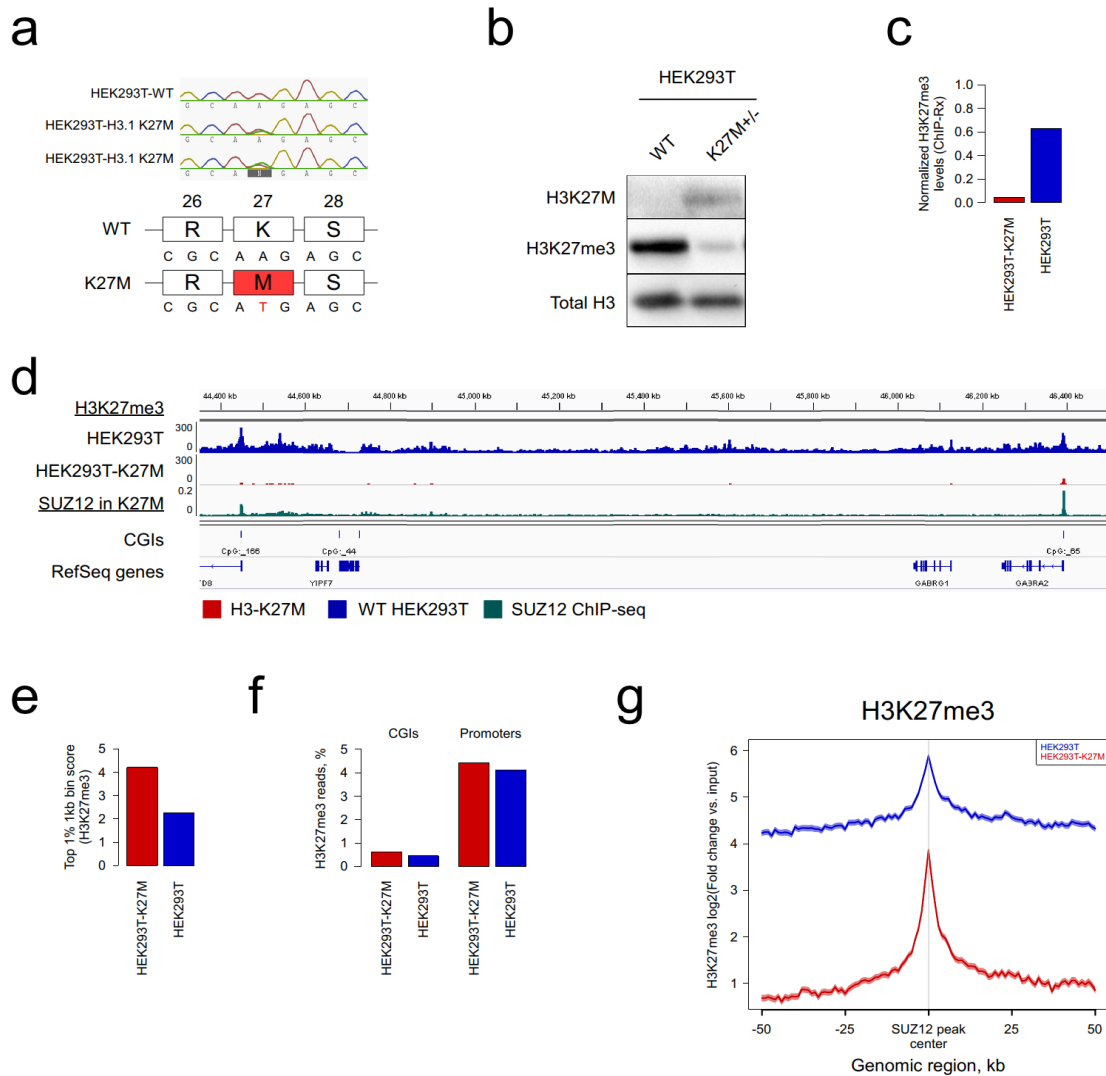
**Supplementary Figure 5. a.** Representative ChIP-seq tracks of H3K27me3, SUZ12 and RING1B for H3K27M and WT pHGG lines, showing differences in distribution of H3K27me3, SUZ12 and RING1B. **b.** Stacked heatmap plots for H3K27me3, SUZ12 and RING1B around CGIs showing stronger enrichment of RING1B in SUZ12/H3K27me3 positive regions in H3K27M cells. **c.** SUZ12/RING1B/H3K27me3 peaks overlap in wild-type (WT, G477, pcGBM2) and H3.3 K27M (BT245, DIPGXIII) high-grade glioma (HGG) lines. H3K27me3 deposition strongly overlaps with SUZ12 sites in H3K27M lines BT245 and DIPGXIII compared to WT lines. Deposition of RING1B on these overlapping H3K27me3/SUZ12 sites shows ~ 2.5-fold enrichment in H3.3 K27M compared to WT.



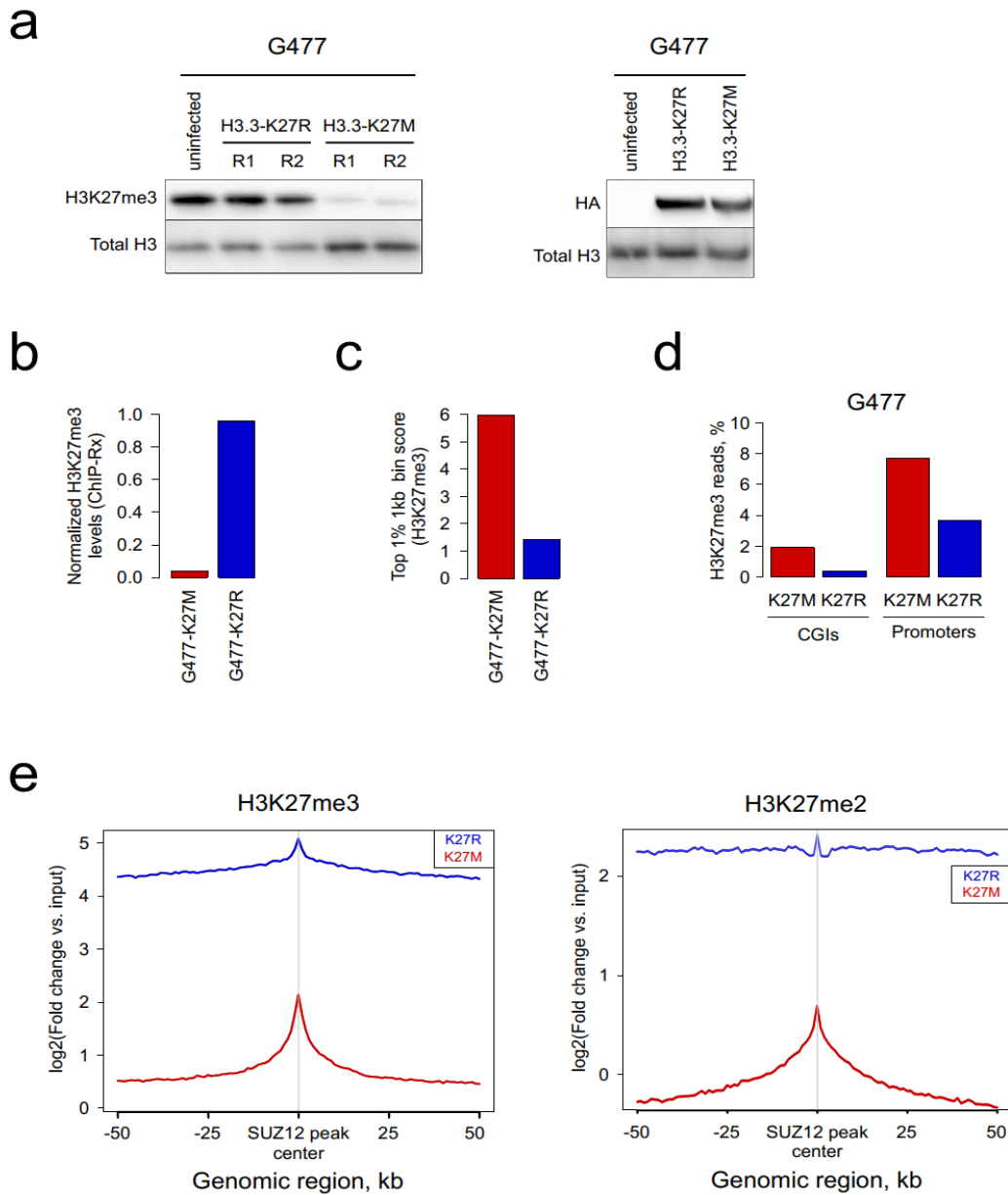
**Supplementary Figure 6.** Normalized ChIP-seq tracks demonstrating loss of H3K27me3 in partially methylated domain (PMD) regions in H3 K27M in pediatric high-grade gliomas (HGG) primary cells. DNA methylation is scaled from blue (0) to red (1) based on methylated base density calculated from whole genome-bisulfite sequencing.



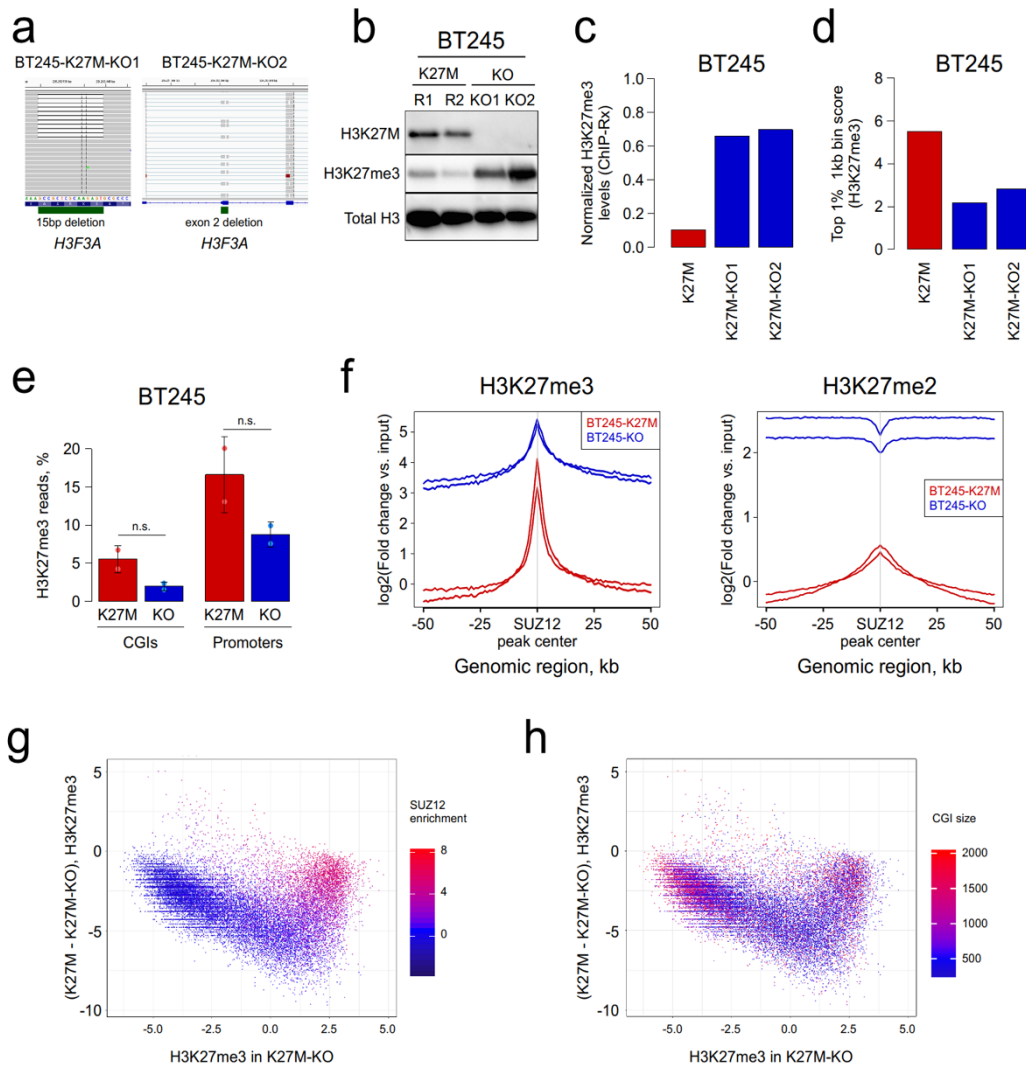
**Supplementary Figure 7.** H3K27me3 distribution in different genomic compartments. **a.** Promoter-genic-intergenic plot, primary cells. Proportion of H3K27me3 reads mapping to different genomic compartments (promoters, gene bodies or intergenic space) in wild-type or H3.3 K27M high-grade gliomas cell lines. **b.** H3K27me3 aggregate plots over TSS of commonly repressed genes in 5 analyzed cell lines (3 H3K27M, 2 WT). **c.** H3K27me2 and H3K27me3 aggregate plots over overlapping SUZ12 peaks in 4 analyzed cell lines (2 H3K27M, 2 WT). Source data are provided as a Source Data file.



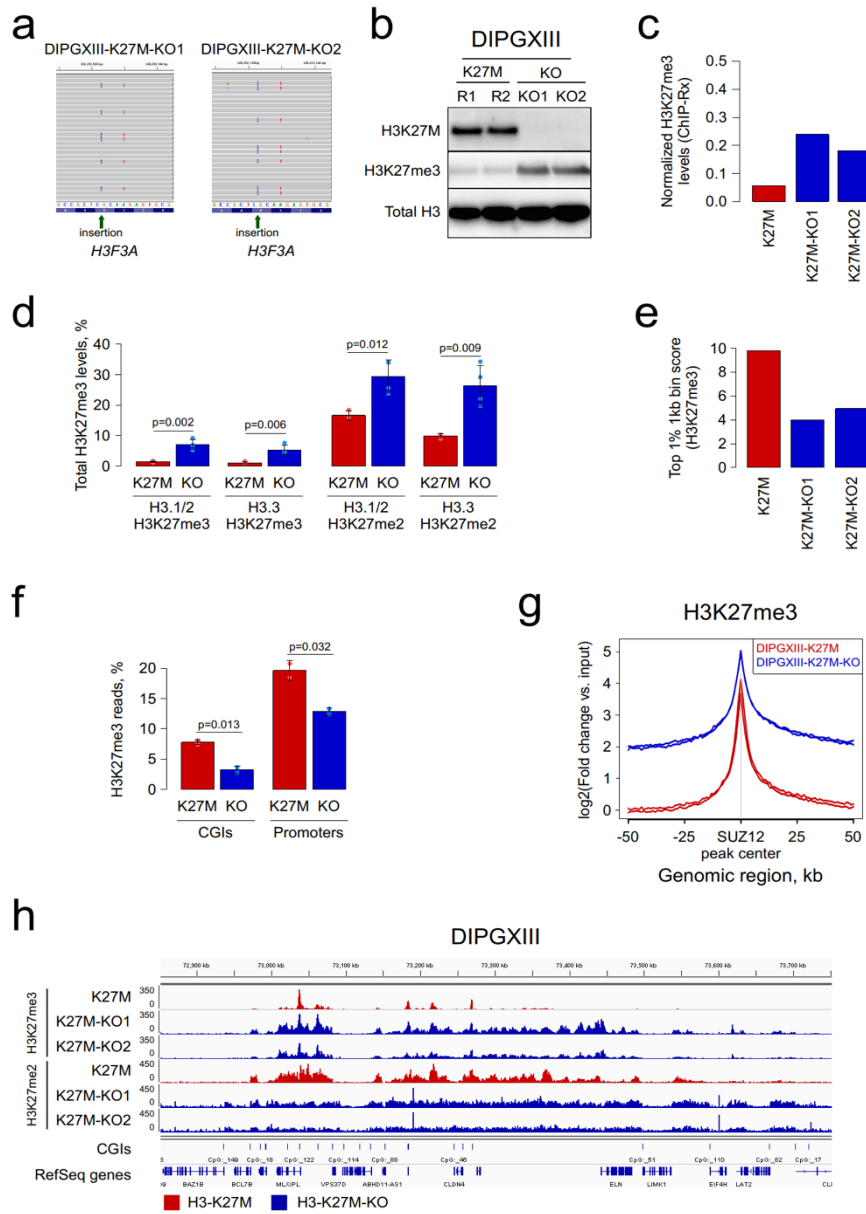
**Supplementary Figure 8.** Experimental introduction of H3.1K27M in HEK293T cell using CRISPR/Cas editing reproduces patterns of H3K27me3 distribution seen in H3K27M mutant high-grade gliomas (HGG). **a.** Sanger sequencing confirmation of CRISPR editing. Introduction of K27M induces a drastic decrease of H3K27me3 in HEK293 as shown using **b.** Western blot analysis or **c.** ChIP-Rx scores. Distribution of the H3K27me3 mark becomes confined to CGIs and mirrors H3K27M high -grade glioma lines as shown on **d.** ChIP-Rx normalized tracks, or using **e.** top 1% 1kb bin scores, **f.** proportion of H3K27me3 reads in CGIs or promoter regions and, **G.** SUZ12 peak centered aggregate plots of H3K27me3. Source data are provided as a Source Data file.



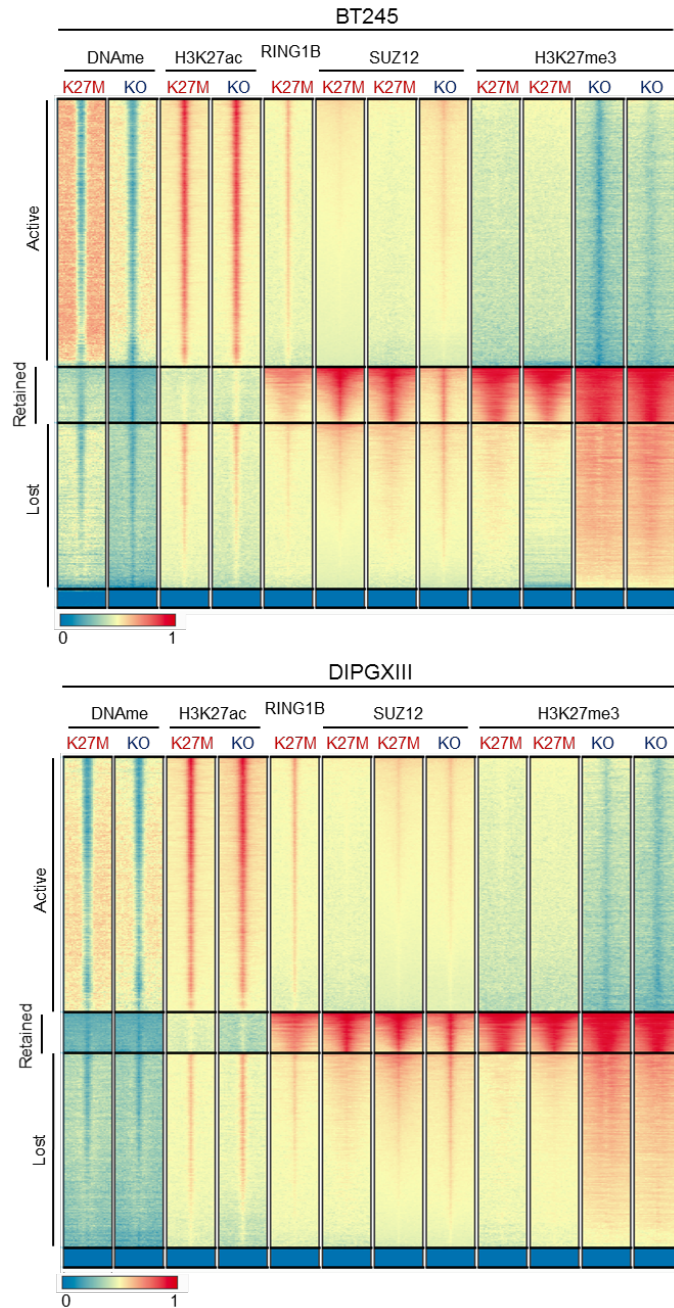
**Supplementary Figure 9.** H3K27me3 levels are drastically decreased in H3.3 K27M overexpressing G477 (red) compared to control G477 high-grade gliomas (HGG) the H3.3K27R mutation (blue), which was shown not to affect H3K27me3 levels<sup>1</sup>. **a.** Western blot showing decreased H3K27me3 levels in H3.3K27M expressing cells. Western blot of HA-tag confirms comparable levels of overexpression. **b.** ChIP-Rx scores and **c.** Top 1% 1kb bin scores further confirming decrease of the mark in H3.3K27M expressing G477 cells. **d.** Proportion of H3K27me3 reads in CGIs or promoter regions and, **e.** SUZ12 peak centered aggregate plots of H3K27me3 and H3K27me2. Source data are provided as a Source Data file.



**Supplementary Figure 10.** CRISPR/Cas9 editing of K27M in BT245 restores increased H3K27me3 levels and spread of the mark from the unmethylated CGIs it is confined to in the presence of the mutation. **a.** MiSeq confirmation of CRISPR editing **b.** Western blot showing removal of H3K27M and increase in H3K27me3 levels **c.** ChIP-Rx scores and **d.** Top 1% 1kb bin scores showing increased H3K27me3 deposition in gene-edited lines (blue). **e.** Proportion of H3K27me3 reads in CGIs and promoters (n=2, mean  $\pm$  standard deviation, Student's t-test). **f.** SUZ12 peak centered H3K27me3 and H3K27me2 aggregate plots. **g-h.** H3K27me3 levels in CGIs in BT245 (please refer to Figure 2G). For each CGI, H3K27me3 levels in K27M-KO state (x axis) are plotted against H3K27me3 change (K27M – K27M-KO) (y axis). Color coding is respectively by: **(g)** SUZ12 enrichment or **(h)** CGI size. Source data are provided as a Source Data file.

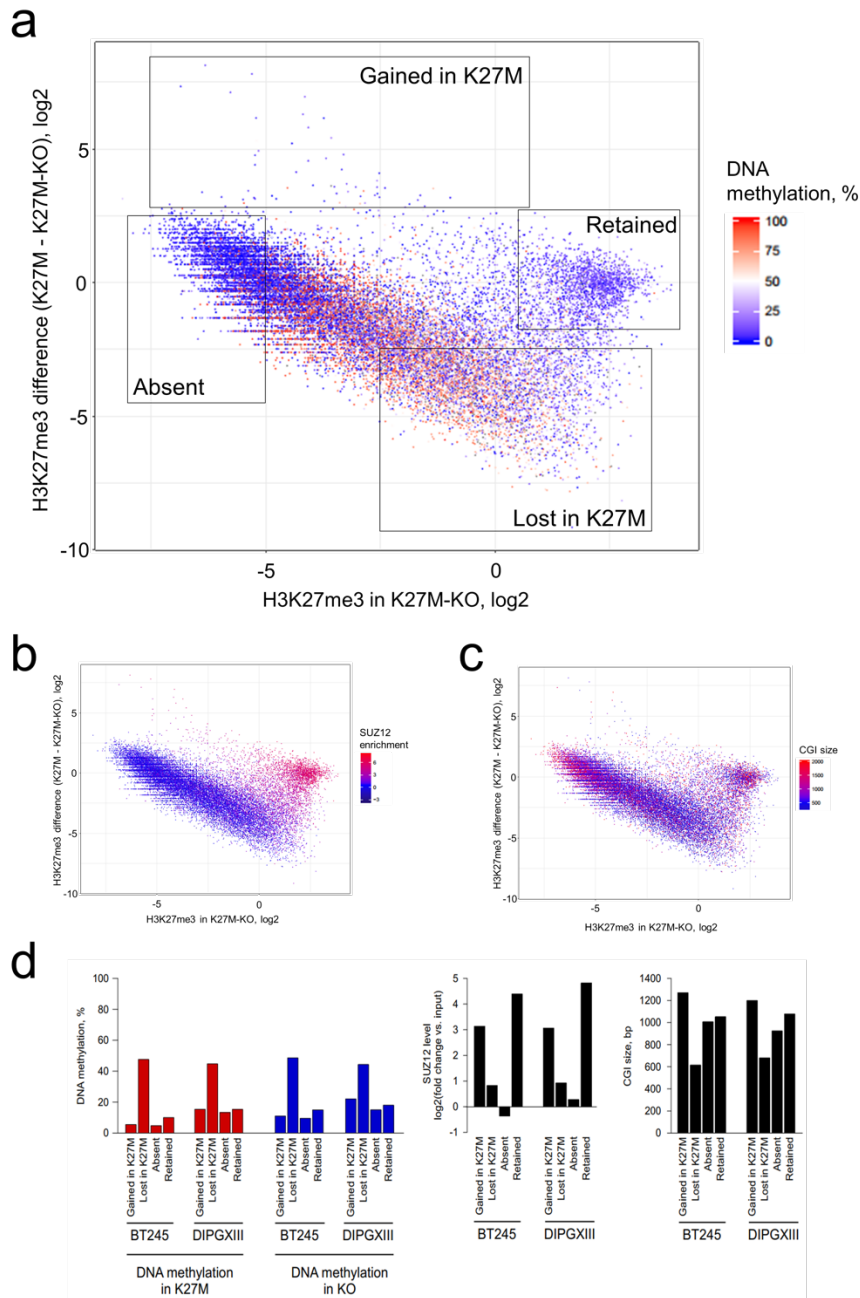


**Supplementary Figure 11.** CRISPR/Cas9 editing of K27M in DIPGXIII. **a.** MiSeq confirmation of CRISPR editing. **b.** Western blot showing removal of H3K27M and increase in H3K27me3 levels **c.** ChIP-Rx scores for H3K27me3. **d.** Mass spectrometry data for H3K27me2 and H3K27me3 (K27M: n=3, KO: n=4, mean  $\pm$  standard deviation, Student's t-test). **e.** Top 1% 1kb bin scores for H3K27me3. **f.** Proportion of H3K27me3 reads in CGIs and promoters (n=2, mean  $\pm$  standard deviation, Student's t-test). **g.** SUZ12 peak centered H3K27me3 aggregate plot for DIPGXIII **h.** ChIP-Rx normalized tracks for DIPGXIII. Source data are provided as a Source Data file.



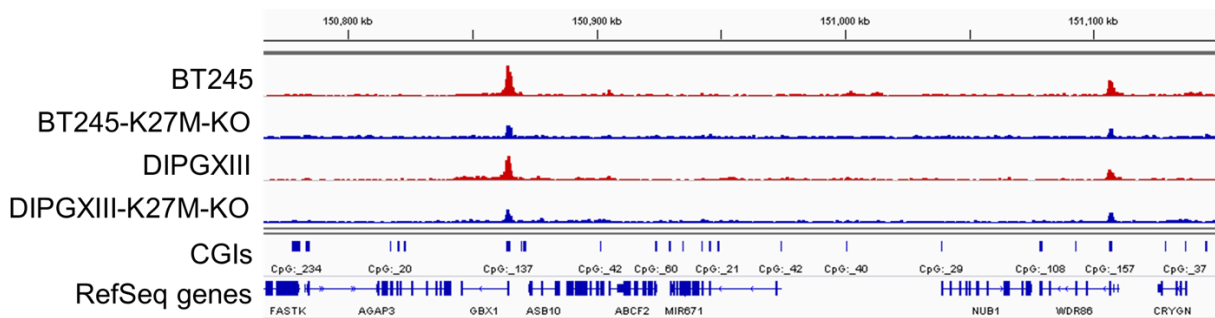
**Supplementary Figure 12.** Stacked heatmap plots of genome wide ChIPseq of H3K27me3, H3K27ac, SUZ12, RING1B and DNA methylation assessed using whole genome bisulfite sequencing. Note that H3K27me3 levels are unchanged in 1) sites that were previously devoid of the mark and that potentially mark active chromatin as shown by enrichment in H3K27ac in both H3K27M and H3K27-KO BT245 or DIPGXIII 2) or sites that had the mark in H3K27M cell lines (retained). Sites that had lost the mark regain it when the mutation is removed (Lost) while limited

sites show de novo gain of the mark in H3K27M cells. Two distinct edited clones are shown for each cell line.

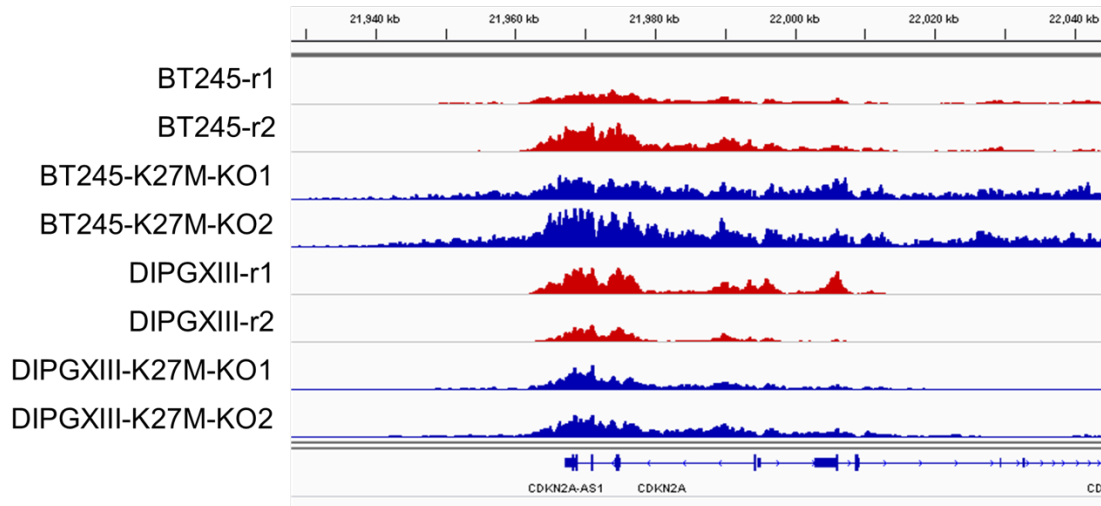
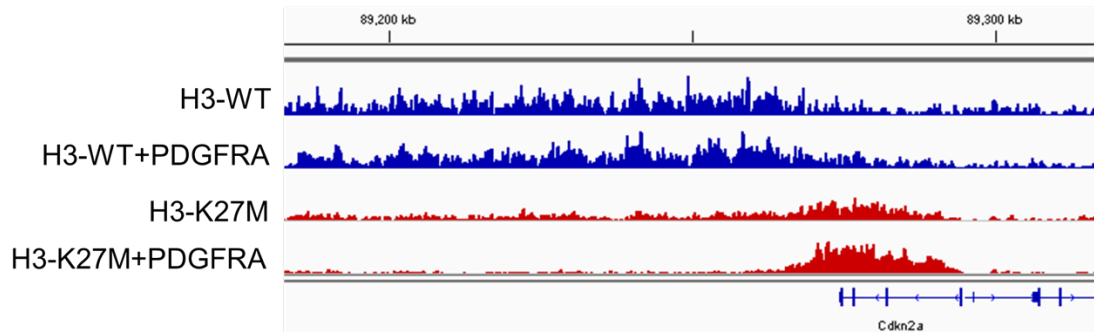


**Supplementary Figure 13.** H3K27me3 levels in CGIs in DIPGXIII showing similar distribution to BT245 (please refer to Fig. 2g). For each CGI, H3K27me3 levels in K27M-KO state (x axis) are plotted against H3K27me3 change (K27M – K27M-KO) (y axis). Color coding is respectively by: **(a)** DNA methylation levels as assessed using whole genome bisulphite sequencing, **(b)** SUZ12

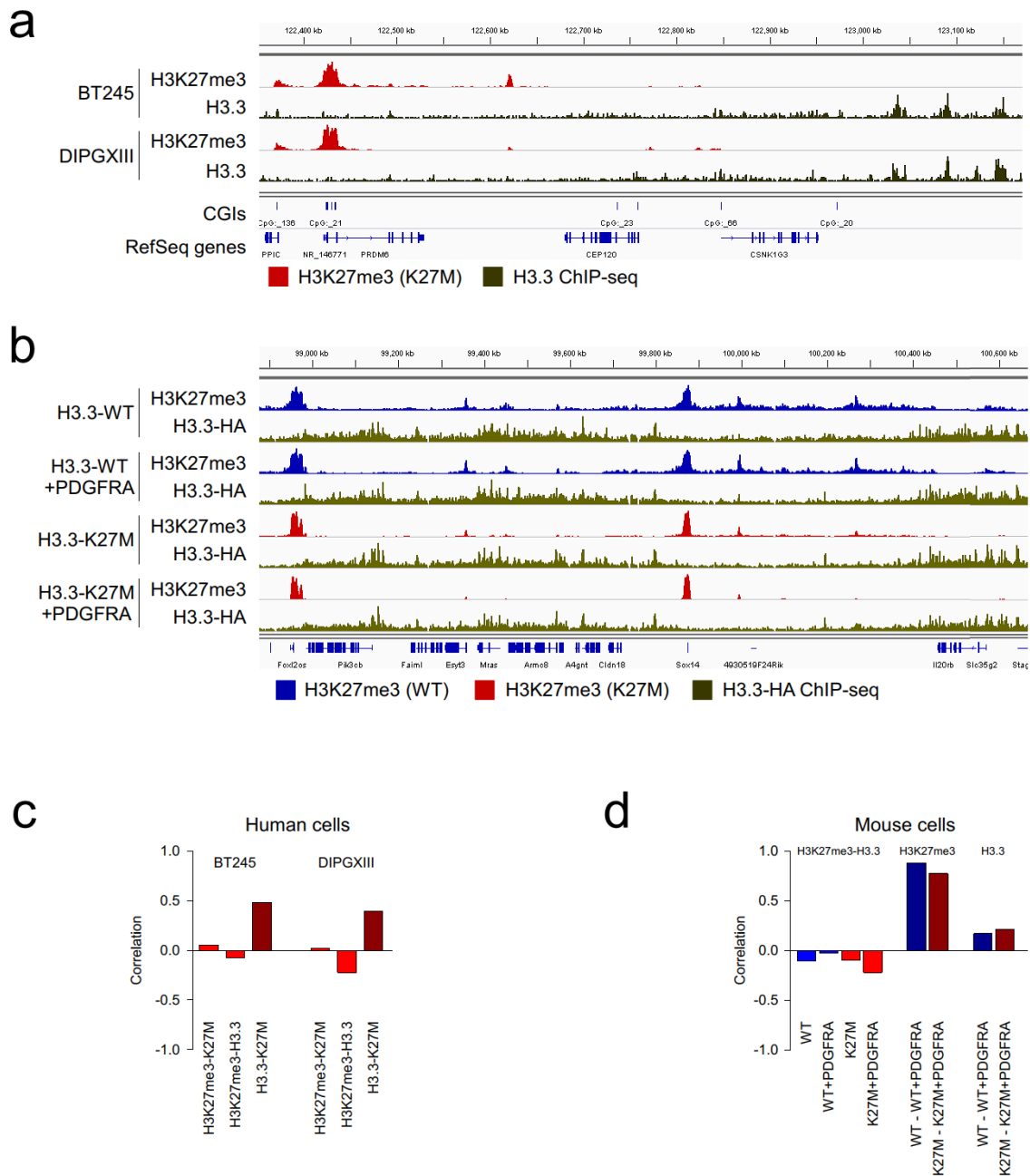
enrichment or (c) CGI size. **d.** Summary statistics for Fig. 2g, Supplementary Fig. 10g-h (BT245) and 13a-c (DIPGXIII). For each category of CGIs, as depicted on Fig. 2g and Supplementary Fig. 13a, average levels of respective factors at those CGIs are shown: DNA methylation in K27M condition (left panel, in red), DNA methylation in K27M-KO condition (left panel, in blue), SUZ12 enrichment (middle panel), CGI size (right panel). In summary, DNA methylation is much higher in CGIs of “Lost in K27M” category, SUZ12 is highly enriched in “Retained” and “Gained in K27M” categories, while CGIs are smaller in “Lost in K27M” category. Source data are provided as a Source Data file.



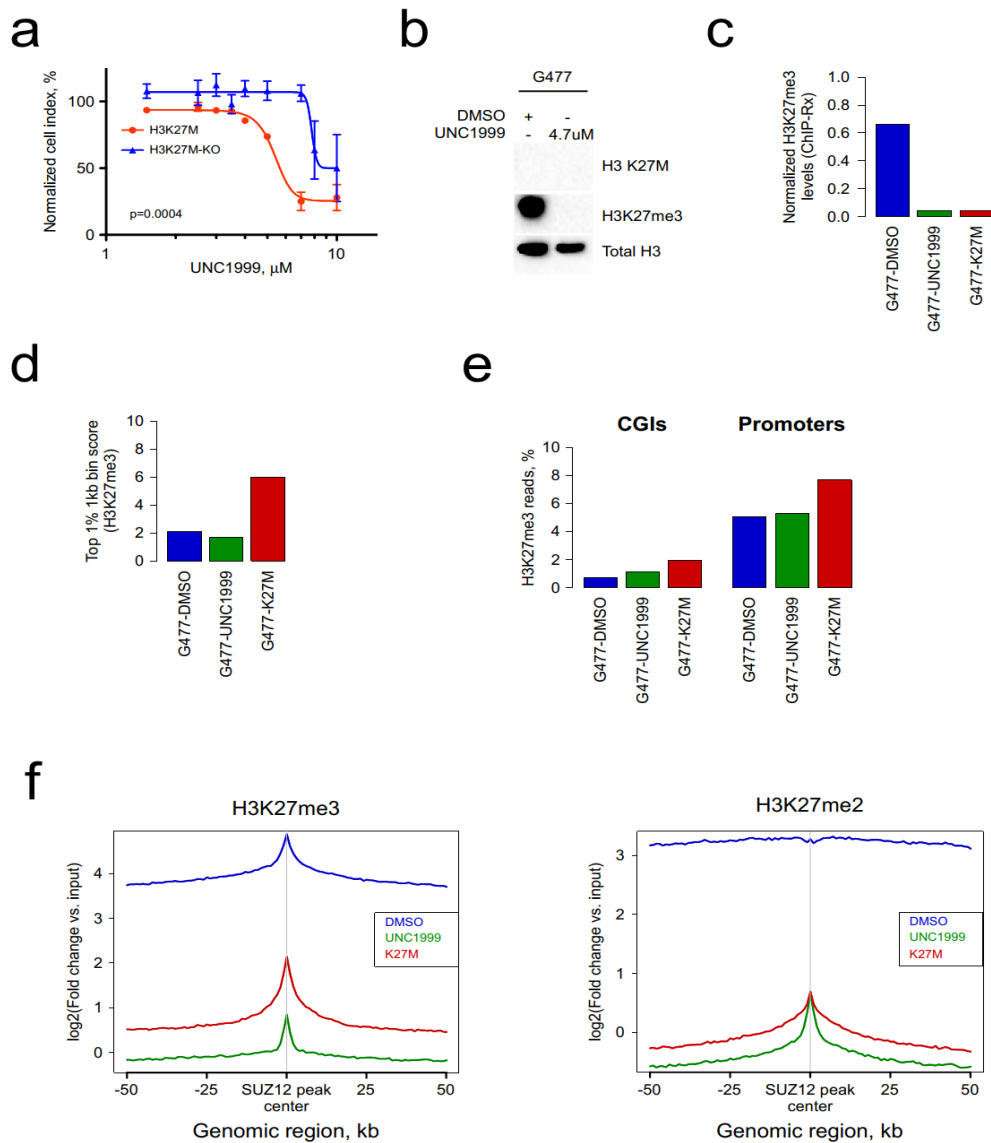
**Supplementary Figure 14.** SUZ12 in CRISPR-KO cells (blue tracks) vs. parental (red tracks), read depth normalized shows decreased deposition of the PRC2 complex member in gene-edited lines compared to the isogenic K27M mutant lines.

**a****b**

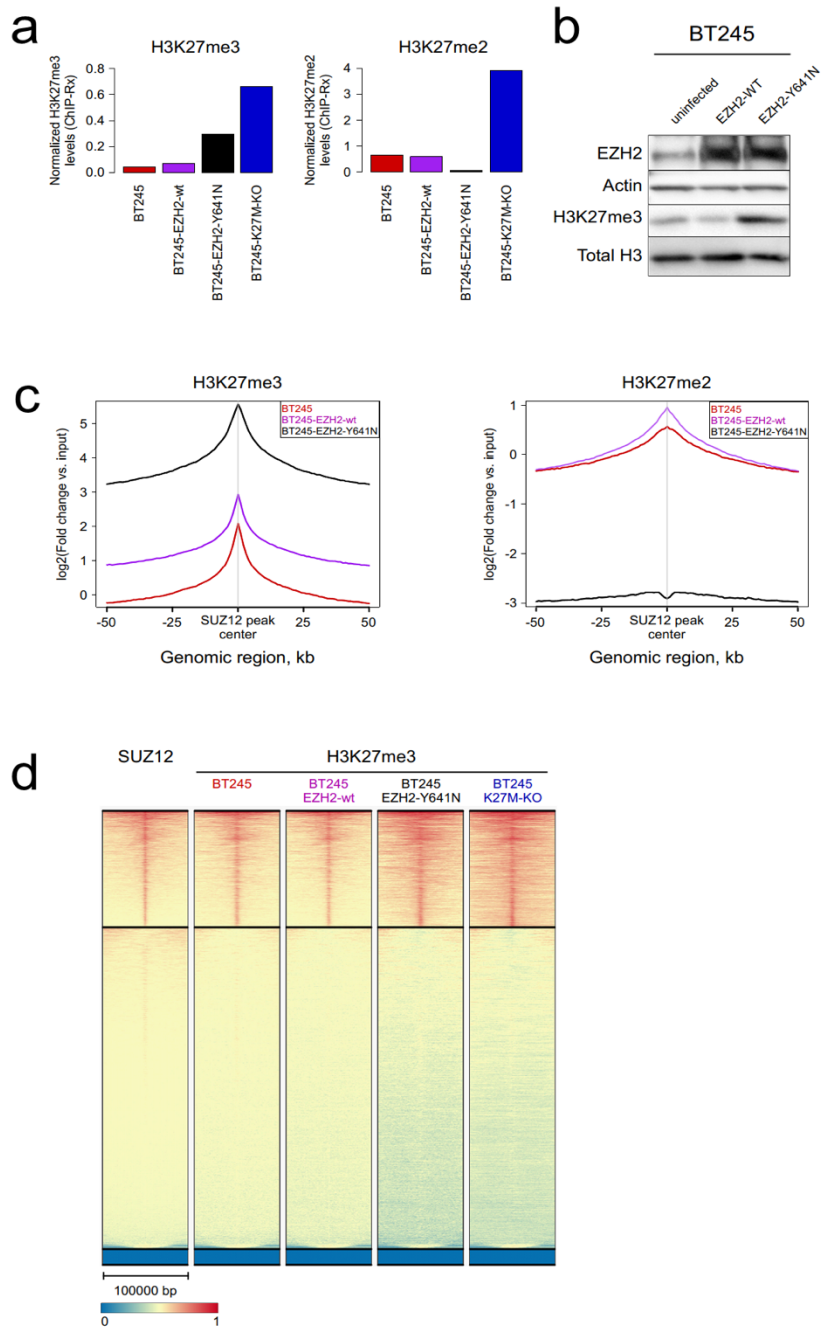
**Supplementary Figure 15. a.** Normalized H3K27me3 tracks for *CDKN2A* locus in BT245 and DIPGXIII (parental, red tracks, CRISPR-KO, blue tracks). HEK293 and G477 tracks are not shown since both cell lines have homozygous deletion of this gene. **b.** Normalized H3K27me3 tracks for mouse H3-WT (blue) and H3-K27M (red) neural progenitor cell lines showing a degree of enrichment of H3K27me3 on the *CDKN2A* promoter. Additionally, these cells have TP53 knockout and ATRX knockdown. Two of the cell lines overexpress PDGFRA, which interestingly increases deposition of the mark on *CDKN2A* promoter in both H3K27M mutant and WT NPC, which may account for the discrepancy with Mohammad et al. (2017)<sup>2</sup>, where mouse NPCs with overexpression of both K27MH3.3 and *Pdgfrb* were studied. Mouse data taken from Pathania et al. (2017)<sup>3</sup>.



**Supplementary Figure 16.** H3K27me3 deposition does not correlate with K27M-H3.3 or WT-H3.3 deposition. **a.** Tracks for GBM cell lines **b.** Tracks for mouse NPC cells used in Pathania et al. (2017)<sup>3</sup> where the K27M-H3.3 mutant was HA-tagged. **c.** Correlation values for human cell lines. **d.** For mouse cell lines. Source data are provided as a Source Data file.



**Supplementary Figure 17.** High-grade glioma cell line treated with an EZH2 inhibitor. **a.** H3K27M mutant cells (BT245, red) are more sensitive to the inhibitor (UNC1999) than CRISPR-edited H3K27M-KO (blue) cells (n=3 passage replicates, mean  $\pm$  standard deviation, Extra sum-of-squares F test). Similar results were observed for another inhibitor (GSK343). **b.** Drastic decrease in H3K27me3 levels in WT HGG line G477 shown by Western blot and **c.** ChIP-Rx normalized levels of H3K27me3. **d.** Top 1% 1kb bin scores for H3K27me3. **e.** Proportion of H3K27me3 reads in CGIs and promoters show global genomic decrease of H3K27me3 in G477 and no redistribution to CGIs in EZH2-inhibited cells when compared to the same line engineered to express H3.3K27M. **f.** SUZ12-centered aggregate plots of H3K27me3 and H3K27me2. Source data are provided as a Source Data file.



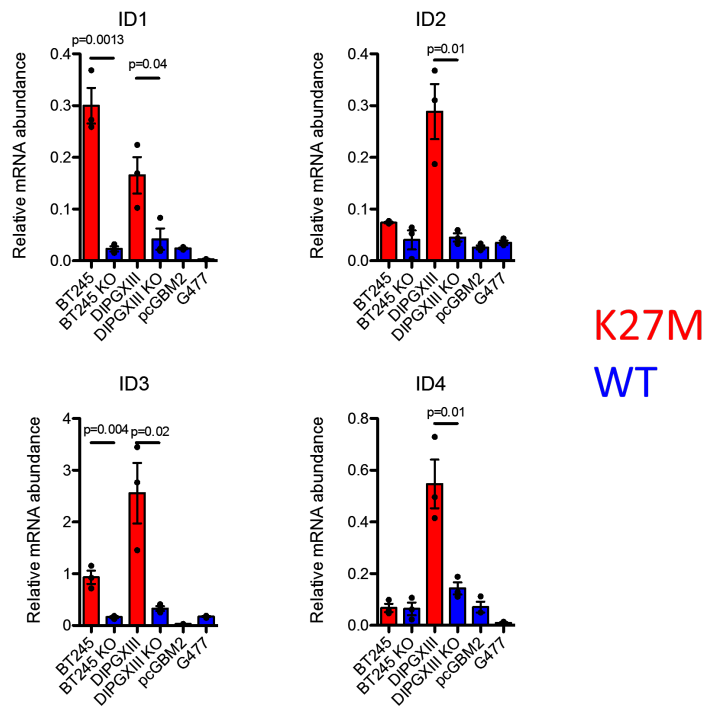
**Supplementary Figure 18.** H3K27me3 levels increase in K27M-mutant BT245 high-grade glioma cell line mainly when overexpressing Y641N EZH2, a mutant EZH2 shown to be less sensitive to K27M inhibition, in contrast to wild-type EZH2. This increase is accompanied in these cells by a partial restoration of the spread of the mark compared to gene-edited BT245-KO lines. Spread occurs downstream from the unmethylated CGIs it was restricted to by the H3K27M mutation. **a.** ChIP-Rx normalized H3K27me2 and H3K27me3 levels. **b.** Western blot. **c.** SUZ12

peak centered aggregate plots of H3K27me2 and H3K27me3. **d.** Heatmap plot of H3K27me3. Source data are provided as a Source Data file.

**a**

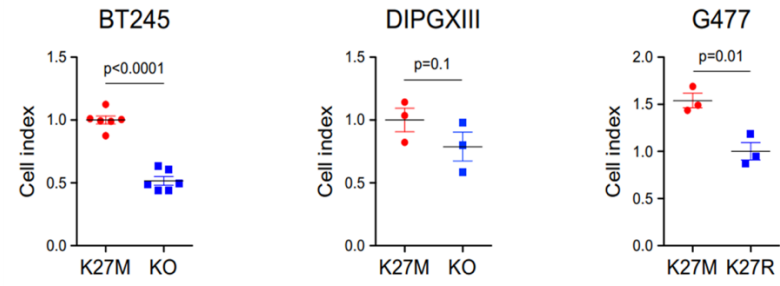
| Gene | G477               |                 | BT245            |                 | DIPGXIII         |                 |
|------|--------------------|-----------------|------------------|-----------------|------------------|-----------------|
|      | LOG2FC (K27M/K27R) | P value         | LOG2FC (K27M/KO) | P value         | LOG2FC (K27M/KO) | P value         |
| ID1  | 0.94               | 2.32E-17        | 0.97             | 1.18E-01        | 0.36             | 4.21E-01        |
| ID2  | 0.68               | <b>7.04E-06</b> | 1.13             | <b>3.34E-02</b> | 1.75             | <b>3.97E-07</b> |
| ID3  | 0.22               | <b>4.30E-02</b> | 1.63             | <b>2.11E-03</b> | 0.79             | <b>2.41E-02</b> |
| ID4  | 0.78               | <b>1.22E-06</b> | 1.71             | <b>2.90E-06</b> | 1.44             | <b>5.61E-05</b> |

**b**

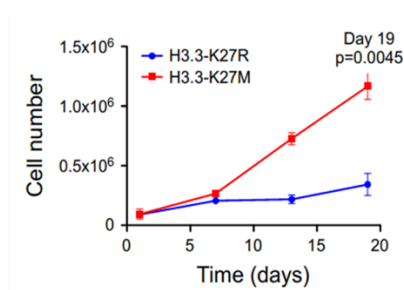


**Supplementary Figure 19.** ID1-4 mRNA expression in K27M high-grade glioma (HGG) mutant lines (n=2 cell lines), K27M-KO controls (n=2 cell lines), and wild-type (WT) lines (n=2 cell lines), measured by **a.** RNA-seq, **b.** droplet digital PCR. ID genes are broadly increased in K27M compared to WT HGG lines (n = 3 passage replicates per cell line, mean  $\pm$  standard error, Student's t-test comparing each K27M vs KO group). Source data are provided as a Source Data file.

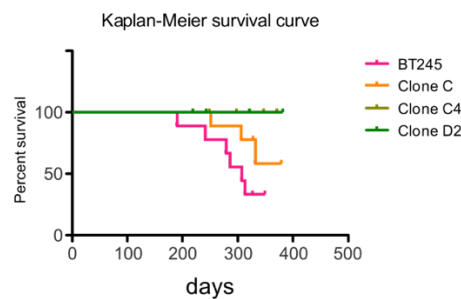
a



b



c



**Supplementary Figure 20. a.** Cell index in a seven-day proliferation assay of two H3K27M mutant cell lines (BT245 n=6 passage replicates of each group, DIPGXIII n=3 passage replicates of each group) upon removal of the mutation, and a wild-type cell line (G477) upon H3.3 K27R and K27M overexpression (n=3 passage replicates each group) (mean  $\pm$  standard error, Student's t-test). **b.** Cell number over time upon rescue of BT245 H3K27M-KO lines by overexpressing H3.3-K27M or H3.3-K27R (n=3 passage replicates of each group, mean  $\pm$  standard error, Student's t-test of Day 19 data). **c.** Kaplan-Meier survival curve of mice bearing orthotopic xenografts of the cell line BT245. The group bearing the parental cell line expressing K27M is shown in pink, a clone derived from CRISPR editing that maintained K27M in orange, and two clonal lines that underwent K27M knockout are shown in shades of green. (9-10 mice were used for each experimental group). Source data are provided as a Source Data file.

## **Preface to Chapter 3**

In Chapter 2, I summarize the effect of H3K27M on PRC2 deposition of H3K27me2 and H3K27me3 using our isogenic tumour-derived cultures. Since the spread of PRC2 can shape both the establishment repressive chromatin and prevention of active chromatin marks, I next sought to examine the role of H3K27ac in H3K27M tumours. Once H3K27me2 is established, it the residue is no longer able to be acetylated (Ferrari et al., 2014). Therefore, the significant loss of both H3K27me2/3 that we describe in Chapter 2 accounts for why H3K27ac can increase in abundance, as previously reported (Lewis et al., 2013). However, the functions of increased H3K27ac have not been addressed. Some published work suggests nucleosomes containing H3.3K27M are amenable to acquisition of H3.3K27ac, which may create a new enhancer landscape driving oncogenic gene expression programs (Piunti et al., 2017). Our group and I aimed to better understand changes to H3K27ac using isogenic model systems, as they retain many features of epigenetic states defining the human disease context.

## Chapter 3

### **Pervasive H3K27 Acetylation Leads to ERV Expression and a Therapeutic Vulnerability in H3K27M Gliomas. *Cancer Cell*. 2019 May 13;35(5):782-797.**

Brian Krug,<sup>1,16</sup> Nicolas De Jay,<sup>1,2,16</sup> Ashot S. Harutyunyan,<sup>1,16</sup> Shriya Deshmukh,<sup>1</sup> Dylan M. Marchione,<sup>3</sup> Paul Guilhamon,<sup>4,5,6</sup> Kelsey C. Bertrand,<sup>7</sup> Leonie G. Mikael,<sup>8</sup> Melissa K. McConechy,<sup>1</sup> Carol C.L. Chen,<sup>1</sup> Sima Khazaei,<sup>1</sup> Robert F. Koncar,<sup>9</sup> Sameer Agnihotri,<sup>9</sup> Damien Faury,<sup>8</sup> Benjamin Ellezam,<sup>10</sup> Alexander G. Weil,<sup>11</sup> Josie Ursini-Siegel,<sup>2</sup> Daniel D. De Carvalho,<sup>4</sup> Peter B. Dirks,<sup>12</sup> Peter W. Lewis,<sup>13</sup> Paolo Salomoni,<sup>14</sup> Mathieu Lupien,<sup>4,5,6</sup> Cheryl Arrowsmith,<sup>5</sup> Paul F. Lasko,<sup>15</sup> Benjamin A. Garcia,<sup>3</sup> Claudia L. Kleinman,<sup>1,2,\*</sup> Nada Jabado,<sup>1,8,17,\*</sup> and Stephen C. Mack<sup>7,\*</sup>

1. Department of Human Genetics, McGill University, Montreal, QC H3A 1B1, Canada
2. Lady Davis Research Institute, Jewish General Hospital, Montreal, QC H3T 1E2, Canada
3. Department of Biochemistry and Biophysics, and Penn Epigenetics Institute, Perelman School of Medicine, University of Pennsylvania, Philadelphia, PA 19104, USA
4. Princess Margaret Cancer Centre, University Health Network, Toronto, ON M5G 1L7, Canada
5. Department of Medical Biophysics, University of Toronto, Toronto, ON M5S 1A8, Canada
6. Ontario Institute for Cancer Research, Toronto, ON M5G 0A3, Canada
7. Department of Pediatrics, Division of Hematology and Oncology, Texas Children's Cancer and Hematology Centers, Dan L Duncan Cancer Center, Baylor College of Medicine, Houston, TX 77030, USA
8. Department of Pediatrics, McGill University, The Research Institute of the McGill University Health Center, Montreal, QC H4A 3J1, Canada
9. Department of Neurological Surgery, Children's Hospital, University of Pittsburgh School of Medicine, Pittsburgh, PA 15232, USA 10
10. Department of Pathology, Centre Hospitalier Universitaire Sainte-Justine, Universite de Montreal, Montreal, QC H3T 1C5, Canada
11. Department of Pediatric Neurosurgery, Centre Hospitalier Universitaire Sainte-Justine, Universite de Montreal, Montreal, QC H3T 1C5, Canada

12. Department of Surgery and Department of Molecular Genetics, University of Toronto, Toronto, ON M5S 1A8, Canada
13. Department of Biomolecular Chemistry, School of Medicine and Public Health and Wisconsin Institute for Discovery, University of Wisconsin, Madison, WI 53715, USA
14. Nuclear Function in CNS Pathophysiology, German Center for Neurodegenerative Diseases, 53127 Bonn, Germany
15. Department of Biology, McGill University, Montreal, QC H3A 1B1, Canada
16. These authors contributed equally
17. Lead Contact

\*Correspondence: [claudia.kleinman@mcgill.ca](mailto:claudia.kleinman@mcgill.ca) (C.L.K.), [nada.jabado@mcgill.ca](mailto:nada.jabado@mcgill.ca) (N.J.), [scmack@bcm.edu](mailto:scmack@bcm.edu) (S.C.M.) <https://doi.org/10.1016/j.ccell.2019.04.004>

## Summary

High-grade gliomas defined by histone 3 K27M driver mutations exhibit global loss of H3K27 trimethylation and reciprocal gain of H3K27 acetylation, respectively shaping repressive and active chromatin landscapes. We generated tumor-derived isogenic models bearing this mutation and show that it leads to pervasive H3K27ac deposition across the genome. In turn, active enhancers and promoters are not created de novo and instead reflect the epigenomic landscape of the cell of origin. H3K27ac is enriched at repeat elements, resulting in their increased expression, which in turn can be further amplified by DNA demethylation and histone deacetylase inhibitors providing an exquisite therapeutic vulnerability. These agents may therefore modulate anti-tumor immune responses as a therapeutic modality for this untreatable disease.

## Significance

Elevated levels of H3K27ac are linked to oncogenesis in H3K27M mutant midline HGGs through altering enhancer landscapes. We find that increased H3K27ac leads to a therapeutic vulnerability in H3K27M tumors. By removing the confounding effects due to the epigenetic landscape of the cell of origin, we show that increased H3K27ac is pervasively distributed across the genome in H3K27M HGGs. This renders repeat elements susceptible to activation by epigenetic therapies, including DNA demethylating agents. Insight into the induction of endogenous retroviruses and activation of innate immune pathways in response to epigenetic therapies in H3K27M tumors

suggests that patients with these intractable tumors may benefit from combining these agents with immune-modulating therapies.

## **Introduction**

High-grade gliomas (HGGs) are a leading cause of cancer-related death in children and young adults. These devastating primary brain tumors have less than 10% survival 2 years following diagnosis, with no targeted therapies currently available. Pediatric HGGs are characterized by epigenetic alterations directly or indirectly affecting the post-translational modification (PTM) of two major opposing chromatin marks, repressive H3K27me3 and active H3K36me3 (Fontebasso et al., 2014; Khuong-Quang et al., 2012; Schwartzenuber et al., 2012; Wu et al., 2012). The most frequent epigenetic modification in pediatric HGGs is a somatic heterozygous mutation in histone 3 (H3) variants leading to lysine-to-methionine substitutions at position 27 (H3K27M). This mutation characterizes more than 80% of midline gliomas, the most common HGGs in children, which include universally lethal diffuse intrinsic pontine gliomas (DIPG) (Khuong-Quang et al., 2012; Sturm et al., 2014; Wu et al., 2012). H3K27M leads to a global decrease in H3K27me3 levels, a PTM marking transcriptionally silent regions of the genome, shown *in vitro* to be due to a disruption of the catalytic activity of the polycomb repressive complex 2 (PRC2) (Bender et al., 2013; Lewis et al., 2013). H3K27M also leads to increased global H3K27 acetylation (H3K27ac) (Lewis et al., 2013), a PTM associated with active transcription (Creyghton et al., 2010). The role of residual H3K27me3 deposition in promoting oncogenesis in H3K27M is currently debated (Chan et al., 2013; Mohammad et al., 2017; Piunti et al., 2017). Increased H3K27ac was recently suggested to associate with aberrant deposition of heterotopic nucleosomes containing H3.3K27M-H3.3K27ac (Piunti et al., 2017). These aberrant nucleosomes are seemingly bound by bromodomain-containing proteins and suggested to act by excluding PRC2 from cellular differentiation genes regulated by Clusters of Regulatory Elements, stretch enhancers, or super enhancers (SEs) (Loven et al., 2013; Piunti et al., 2017; Whyte et al., 2013). This model, however, does not explain why K27M mutations in canonical H3.1 or H3.2, which have broader and distinct deposition patterns from non-canonical H3.3-containing nucleosomes, show exclusion of the PRC2 complex similar to H3.3. Our goal is thus to gain insight into the active *cis*-regulatory programs in H3.3K27M HGGs, delineate the effects of increased H3K27ac on active chromatin loci, their implications for gene expression, and uncover potential therapeutic vulnerabilities.

## Results

**Active Chromatin Landscape of Pediatric HGG.** We performed a comprehensive epigenomic characterization of a large panel of pediatric HGGs wild-type (WT) (denoted H3K27WT) or carrying the H3.3K27M mutation. These included primary tumors, patient-derived xenografts, and cell lines, which were analyzed using quantitative histone mass spectrometry (n = 6), chromatin immunoprecipitation sequencing (ChIP-seq) of H3K27ac (n = 38), assay for transposase accessible chromatin sequencing (ATAC-seq) (n = 4), and RNA sequencing (RNA-seq) (n = 41) (Figure S1A; Tables S1 and S2). To quantify global alterations in histone modifications associated with H3.3K27M mutation, we performed histone mass spectrometry of H3.3K27WT and H3.3K27M samples. We observed that H3.3K27M HGGs displayed a global loss of H3K27me3 and a global increase in H3K27ac, both on H3.3 and H3.1/H3.2 nucleosomes (Figure 1A). We asked whether this global increase in H3K27ac was associated with a distinct landscape of *cis*-regulatory elements, characterized by enhancers (peaks  $\pm 2.5$  kb outside of transcription start sites [TSS]) and promoters (at 2.5kb within TSS) across groups of pediatric HGG samples. Using unsupervised hierarchical clustering of the top 10,000 variant H3K27ac loci (Akhtar-Zaidi et al., 2012) identified by H3K27ac ChIP-seq, we found that patterns of H3K27ac separated H3.3K27M from H3K27WT models (including patient-derived primary cell lines and mouse xenografts) (Figure 1B; Tables S1 and S2). Primary tumors that harbored the H3.3K27M mutation had distinct deposition of H3K27ac compared with *IDH1* mutated and H3K27WT samples (Figure 1C). Despite the global increase in H3K27ac, H3.3K27M, and H3K27WT tumors had comparable numbers of active enhancers and promoters (Figure 1D; K27M, 43,333 and K27WT, 39,946, H3K27ac loci detected in at least three samples), indicating that increased H3K27ac in H3.3K27M results in a relatively modest difference in the total number of regulatory H3K27ac loci. We then defined the regions of gene transcription associated with differential H3K27ac deposition, by integrating RNA-seq with H3K27ac ChIP-seq patterns (Figure 1E; Table S3). H3K27ac-associated gene expression changes specific to H3.3K27M HGGs included increased expression of *LIN28B* and *PLAG1*, two genes shown to be upregulated in H3K27M mutant DIPGs (Funato et al., 2014) (Figure S1B), along with overexpression of additional genes including *ADARB2*. Conversely, H3K27WT HGGs were defined by distinct lineage markers expressed in different brain regions during development such as *EN1*, *HOXD9*, and *HOXA10*. Our findings reveal that H3.3K27M tumors harbor distinct

H3K27ac deposition patterns when compared with H3K27WT HGGs and, unexpectedly, show minimal differences in absolute numbers of active enhancers and promoters despite the global increase in H3K27ac levels.

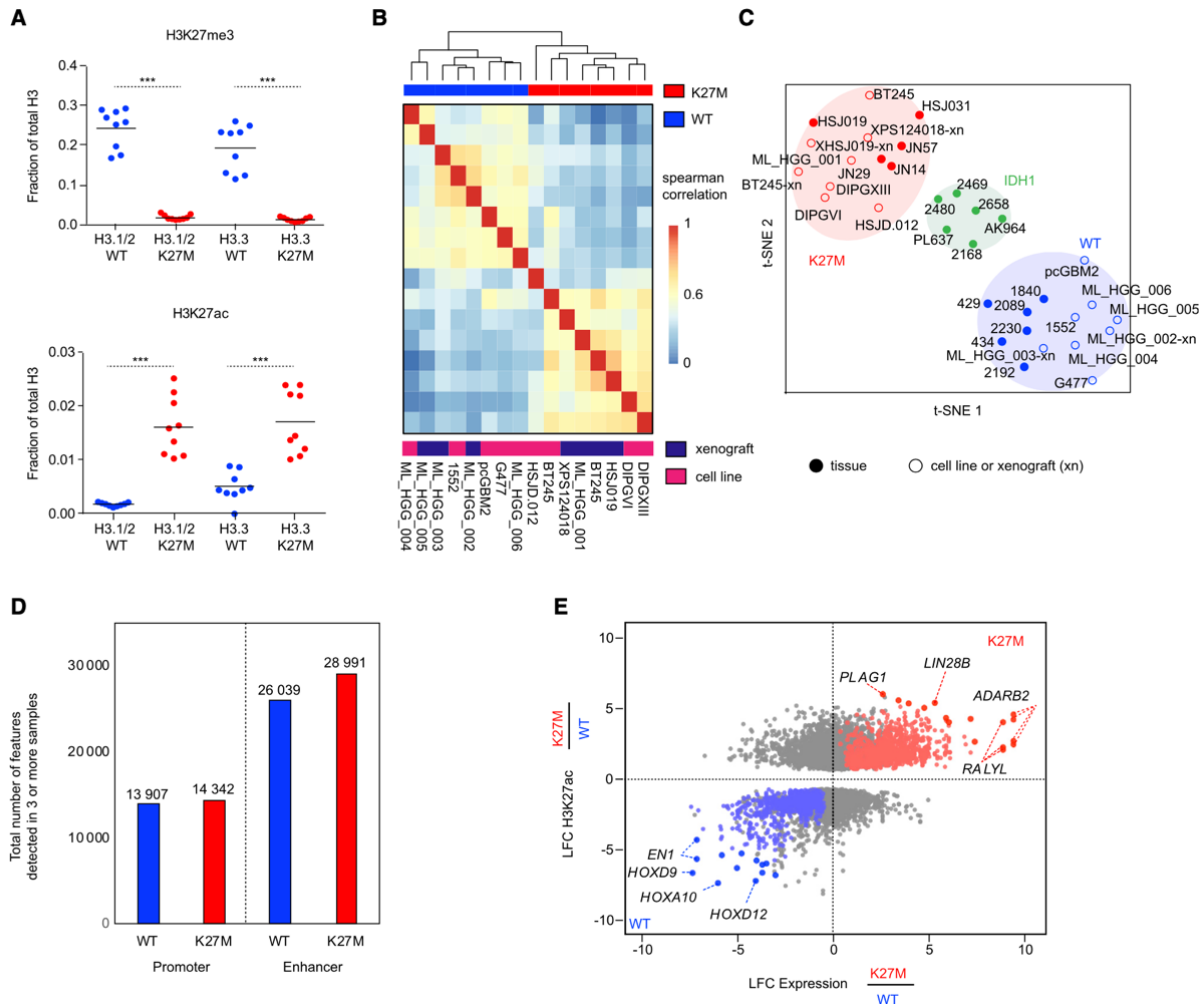


**Figure 1. Active Regulatory Chromatin Landscape of Pediatric HGG**

(A) Quantification of H3K27me3 (top panel) levels and H3K27ac (bottom panel), abundance by mass spectrometry in H3.3-K27M HGG lines compared with WT lines (n = 9; 3 technical replicates of 3 cell lines). Solid horizontal line indicates mean. Two-sided Wilcoxon rank-sum test, \*\*\*p < 0.001.

(B) Unsupervised hierarchical clustering of pairwise Spearman correlations performed between cell K27M and WT culture models based on read density within H3K27ac loci.

(C) t-SNE analysis on HGG cell lines, xenografts (denoted with the suffix -xn), and primary tissues using distinct H3K27ac loci between K27M and WT identified in cell lines.

(D) Number of H3K27ac positive enhancers and promoters detected in at least three samples out of either n = 13 K27M or n = 14 WT HGG samples shown in Figure 1C. Enhancers were defined by MACS1.4 peaks ( $p < 1.3 \times 10^{-9}$ ) called greater than 2.5 kb upstream or downstream of the nearest TSS, and promoters defined by peaks within 2.5 kb.

(E) Identification of subgroup-specific genes with concordant changes in both expression and H3K27ac in patient-derived cell lines. x axis: log<sub>2</sub> fold-change (LFC) of gene expression between H3K27M (n = 7 replicates) and H3K27WT (n = 6 replicates) cell lines. y axis: LFC of H3K27ac at a promoter or enhancer associated with the gene. Genes with significantly differentially acetylated regulatory regions between H3K27M and H3K27WT lines are shown ( $p \leq 0.05$ ). Red: significantly

upregulated in H3K27M. Blue: significantly upregulated in H3K27WT. Gray: no significant changes in expression. Filled circle: genes with the greatest magnitude

of changes in both H3K27ac and expression:  $\sqrt{LFC_{RNA}^2 + LFC_{H3K27ac}^2}$ .

See also Figure S1 and Tables S1, S2 and S3.

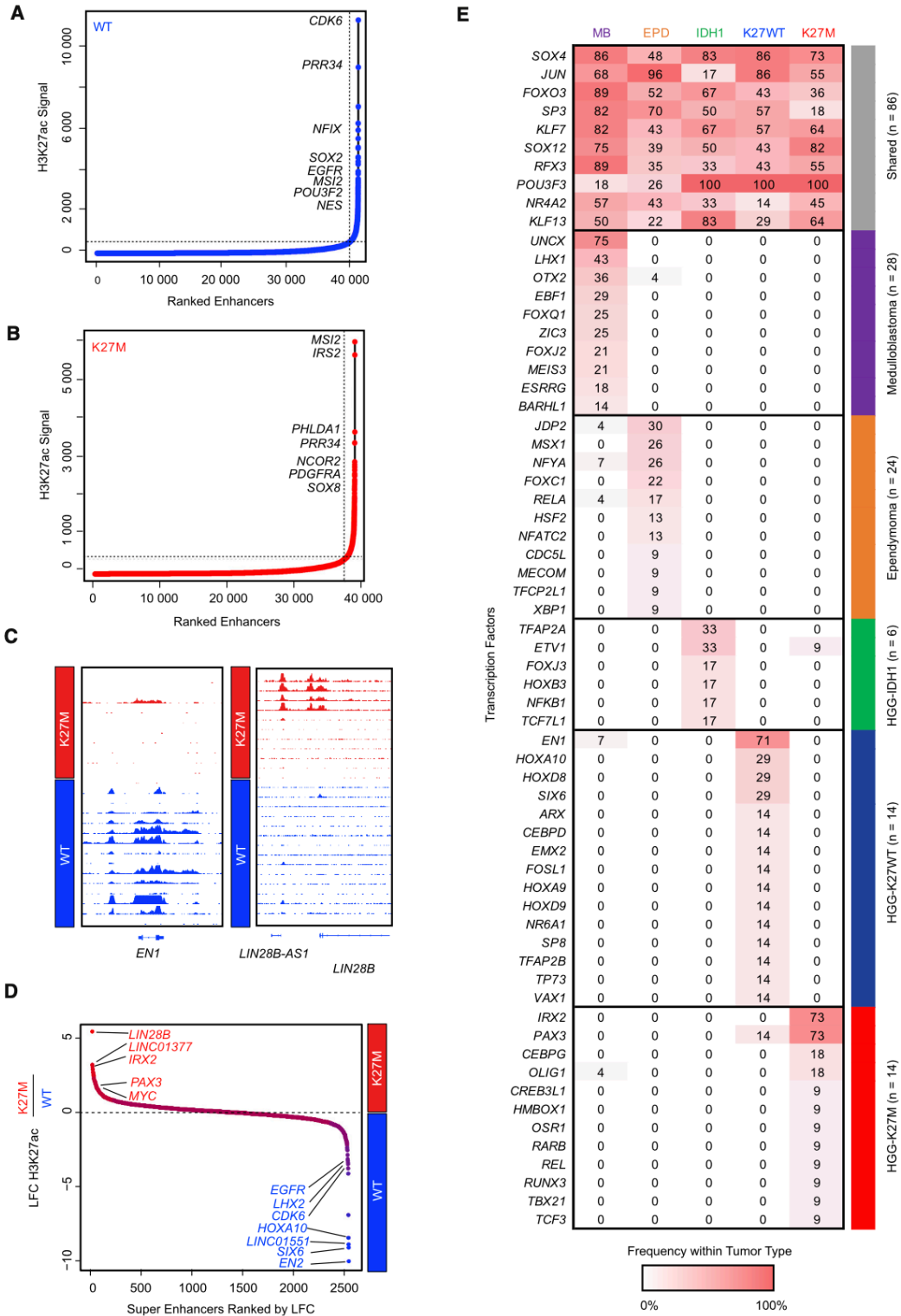


**Figure 2. Core Regulatory SE and TF Programs Delineate H3.3K27M and H3K27WT HGG**  
 (A and B) Super enhancers detected across all H3K27WT HGG samples (n = 8) (A) and H3.3K27M HGG samples (n = 8) (B) using the same samples listed in Figure 1B.

(C) Patterns of H3K27ac shown surrounding the EN1 locus (left panel) and LIN28B (right panel).  
(D) Differential super enhancers restricted to H3K27WT and H3K27M samples as detected by DiffBind in DESeq2 mode.

(E) Core regulatory circuitry transcription factors shared or enriched in medulloblastoma, ependymoma, IDH1-glioma, H3K27WT (n = 8), and H3K27M HGG (n = 11) samples. Score indicates the number of core TFs detected within at least one core regulatory circuit in a given tumor type.

See also Table S4.

**Distinct Core Transcriptional Regulatory Circuitry Programs Define H3K27M- and H3K27WT-Driven HGG.** We next identified SEs within each group (Figures 2A–2D; Table S4) using the Ranking of Super Enhancer algorithm (Loven et al., 2013; Whyte et al., 2013). Differential analysis identified SEs specific to H3.3K27M, including known (*LIN28B* and *MYC*) and additional (*IRX2* and *PAX3*) developmental-associated genes (Figure 2D). Notably, all H3.3K27M cell lines showed either *MYC* amplification (data not shown) or increased LIN28B, *MYC*, or *MYCN* expression (Figure S1C), possibly through potential SE association. H3K27WT-specific SE genes included *EN2*, *HOXA10*, *CDK6*, *LHX2*, and *EGFR* (Figure 2D), consistent with known enrichment of *EGFR* and *CDK6* amplifications in cortex HGGs (Sturm et al., 2014).

We then re-constructed the core transcription factor (TF) circuitry programs that regulate shared and specific H3.3K27M and H3K27WT SE networks, and compared their specificity with other known brain tumor entities (Saint-Andre et al., 2016). Using this approach, we identified core regulatory circuit TFs active in ependymoma, medulloblastoma, IDH1-glioma, HGG-H3.3K27M, or HGG-H3K27WT tumors (Lin et al., 2016; Mack et al., 2018) (Figure 2E). Several core TFs, including *SOX4*, *JUN*, *FOXO3*, *SP3*, and *NR4A2*, were shared across this set of brain tumors while many others were disease specific, possibly acting as potential disease driver genes and/or lineage-associated markers of cellular and developmental origins. Indeed, *LHX1* and *OTX2* have been shown to be drivers of medulloblastoma tumor formation, while *RELA* was identified as a core TF in the context of C11ORF95-*RELA* fusions in ependymoma. *UNCX*, highly expressed during embryonic development at embryonic day 14.5 in the mid-external granule layer (Machold et al., 2011), was in turn shown to be specific to medulloblastoma and to be a potential marker of tumor cellular origins. We identified two specific key core TFs in H3.3K27M HGGs, *IRX2* and

PAX3 (Figure 2E), in keeping with recent data from a study using single-cell profiling of H3K27M HGGs, which demonstrated restricted expression of these TFs to H3K27M cells (Filbin et al., 2018). Interestingly, only a subset of H3K27M tumor-derived cells expressed IRX2. These IRX2-positive cells had no specific association to the described astrocyte, oligodendrocyte, and cell-cycle signatures (Filbin et al., 2018) (Figure S1D). In contrast, H3K27WT cells harbored other candidate lineage-associated core TFs such as EN1, HOXA10, and HOXD8. EN1 expression in development is found within the mid-hindbrain junction coincident with midbrain dopaminergic neuronal development (Alves dos Santos and Smidt, 2011). Altogether, our results on typical enhancer, SE, and core TF networks converge on lineage genes involved in brain development for both H3.3K27M mutant and H3K27WT HGGs, some of which may also represent tumor growth dependencies. In H3K27M tumors, these lineage-associated TF programs may intersect with other oncogenic programs, namely the LIN28B/MYC axis, to promote tumorigenesis. Core TF regulation in pediatric HGGs resembles that observed in other pediatric brain tumors such as ependymoma and medulloblastoma, leading us to hypothesize that they largely reflect cell state programs related to the cell identity and origin of these tumors (Lin et al., 2016; Mack et al., 2018). Thus, we conclude that these SEs and their core TF circuitries, which mark important brain developmental programs, are most likely an indication of cellular states associated with H3K27M tumor cells and may not necessarily be a direct consequence of H3K27M mutagenesis.

**Isogenic H3K27M Models Decouple Lineage and Oncogenic Patterns Associated with H3K27 Acetylation.** To address whether H3.3K27M directly impacts “active” chromatin loci including enhancers, SEs, and associated TF programs, or regulates other uncharacterized genomic loci, we designed an isogenic tumor experimental system to interrogate solely the effect of the mutation. We introduced frameshift deletions/mutations in the *H3F3A*-K27M mutant allele in two tumor-derived primary cell lines, BT245 and DIPG-XIII, using CRISPR-Cas9 engineering (Figures 3A, S2A, and S2B). H3.3K27M knockout (KO) abrogated mutant protein expression and was validated using mass spectrometry, which also confirmed that total H3.3 levels were similar in both edited and unedited clones (Figures 3A–3C and S2B–S2D). CRISPR-mediated editing decreased H3K27ac and increased H3K27me3 levels (Figures 1A, 3D, 3E, S2E, and S2F). Surprisingly, when assessing H3K27ac changes common to both cell lines by ChIP-Rx (a quantitative ChIP-seq assay) (Orlando et al., 2014), the comparison of H3.3K27M mutant cell lines with their parental isogenic clones showed that only a very small proportion of H3K27ac sites

(0.25%) were consistently lost in both lines while the vast majority of H3K27ac sites were unchanged (96.6%) upon H3.3K27M removal (Figures 3F and 3G). This genome-wide finding was also recapitulated when assessing changes occurring specifically in each of the two cell lines compared with its isogenic H3K27WT clone (Figures S2G and S2H). One of the two H3.3K27M cell lines (DIPG-XIII) showed 10% loss of H3K27ac loci when the K27M mutation was removed. However, except for rare genes, including *ADARB2*, these H3K27ac changes did not significantly alter regulatory elements (enhancers or SEs) identified through H3K27ac profiling (Figures 3F–3H and S2G–S2J; Table S5). Surprisingly, upon H3K27M KO, we observed gains of H3K27ac at several loci in cells (Figure 3G). Interestingly, several genes associated with these H3K27ac gains have documented roles in neural differentiation and glial development, and include *DAAMI*, *NFIB*, and *EPHB2* (Table S6) (Kang et al., 2012; Zhu et al., 2017). These results support, at least in part, the hypothesis that distinct cell states associate with H3K27M or H3K27WT mutational status and the premise that H3K27M may lead to a blockade in differentiation which could be reversible upon removal of the mutation, similar to what we previously observed for another mutant histone H3K36M (Lu et al., 2016).

We further examined open chromatin distribution using ATAC-seq in H3.3K27M and H3K27WT HGGs, and in one isogenic HGG line carrying H3.3K27M mutation compared with H3.3K27M-KO. When overlaying open chromatin loci called by ATAC-seq with H3K27ac peaks, we observed that the overlap between both markers of open chromatin was significantly lower in H3.3K27M HGGs compared with H3K27WT lines (Figure S2K). Notably, removal of the mutation increased the overlap between ATAC-seq data and H3K27ac peaks from 53% to 73% (Figure S2K), a level typically observed in a standard ATAC-seq experiment. The lower overlap observed between ATAC-seq and H3K27ac loci in H3K27M HGG compared with H3K27WT HGG cell lines suggests regions of active chromatin outside well-defined H3K27ac peaks in H3.3K27M HGGs. Together with the unchanged number of canonical H3K27ac sites (Figures 1D, 3F, and 3G), these findings suggest that the global increase in H3K27ac in H3K27M cells does not substantially alter or create new sites of focal H3K27ac deposition (including enhancers and promoters). Deposition of this active mark at these sites is largely independent of H3.3K27M, probably marking cell of origin state and lineage genes.

Based on their increased H3K27ac levels, H3.3K27M mutant cells have been suggested to exhibit cell growth dependencies on transcriptional activity mediated by bromodomain and extra-terminal

domain (BET) proteins (Piunti et al., 2017; Nagaraja et al., 2017). However, we did not observe differential sensitivity of H3.3K27M mutants to the BET inhibitors JQ-1 or I-BET762 in any of the H3.3K27M cell lines we tested compared with H3K27WT or isogenic H3K27M KO cells (Figures S3A–S3C). Furthermore, when treating cells with inhibitors of the CREBBP/ EP300 histone acetyltransferases (CBP-30 and C646) we observed a trend of the H3K27WT line being more vulnerable to these agents (Figures S3D–S3I), indicative that the growth of H3.3K27M cells is not dependent on elevated histone acetyltransferase activity. Altogether, these findings support our observation that H3K27M SE landscapes reflect the cell state and/or lineage, and that H3K27ac gain does not create a sensitivity to BET or CREBBP/EP300 histone acetyltransferase inhibitors in K27M mutant cells.

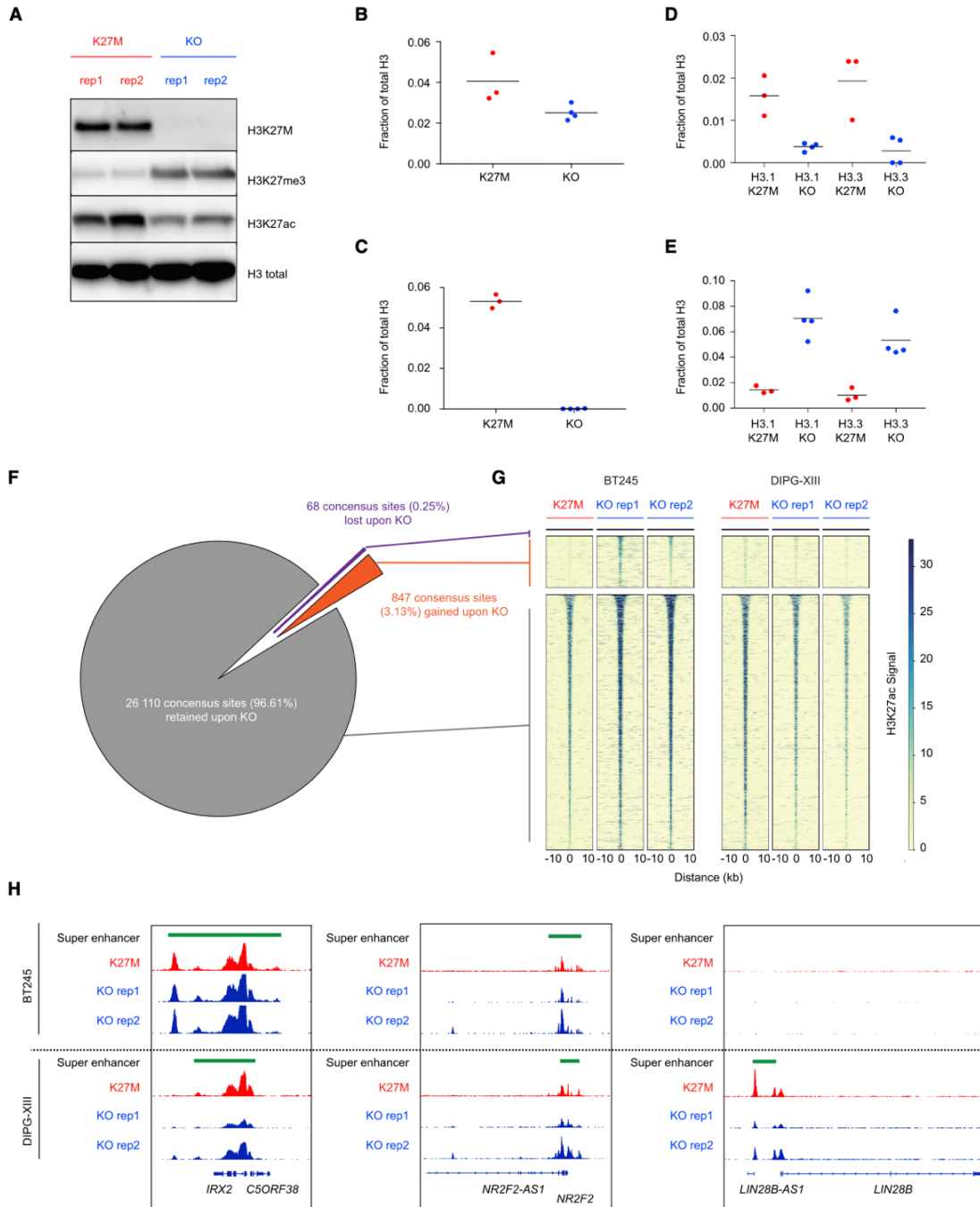


**Figure 3. Mapping of H3K27ac in Isogenic Models of H3K27M Reveal Minimal Alterations of Gene Transcriptional Programs**

(A) Immunoblot in parental and clonal H3K27M KO lines of DIPG-XIII. (B–E) Mass spectrometry analysis in DIPG-XIII for total H3.3 (B), K27M (C), H3K27ac (D), and H3K27me3 (E) peptides among total H3, plot of mean of  $n = 3$  or 4 technical replicates. Solid horizontal lines indicate the mean.

(F and G) Pie graph (F) and heatmap (G) illustrating number and proportion of gained, lost, and retained H3K27ac sites consistent between BT245 and DIPG-XIII K27M expressing models as compared with KO lines.

(H) Gene plot illustrating patterns of H3K27ac and super enhancers between H3.3K27M cell models and isogenic KO clones.

See Figures S2 and S3 and Tables S5 and S6.

### **H3.3K27M Induces Aberrant H3K27ac Deposition at Repetitive Elements in Human and Mouse HGG.**

We investigated whether H3K27ac deposition occurs outside of traditional loci called with standard peak-calling algorithms. Indeed, both DIPG-XIII and BT245 H3.3K27M cell lines harbored, genome-wide, a greater number of domains with increased H3K27ac, including deposition of the mark in intergenic regions (Figures 4A, 4B, S4A, and S4B). The human genome is mainly comprised (70%) of repetitive elements broadly categorized to include LINES, SINES, LTRs, DNA transposons, and other repeat elements (de Koning et al., 2011). Genomic silencing of these repetitive sequences is important for the maintenance of genome integrity, and tightly regulated using several layered mechanisms, which include combinatorial deposition of repressive epigenetic marks, namely H3K9me3 and H4K20me3, H3K27me3, or DNA methylation (Bestor and Bourc'his, 2004; Bourc'his and Bestor, 2004; Walsh et al., 1998). We examined whether this pervasive deposition of an active chromatin mark results in increased baseline expression of large regions of the genome that tend to be normally transcriptionally silent. Cell lines bearing H3.3K27M showed an increase of H3K27ac in unique reads mapping to these repetitive elements when compared with their isogenic H3K27M-KO primary HGG lines (Figures 4C and S4C); consistent with the genome-wide increase in H3K27ac observed by histone mass spectrometry.

We next refined the quantification at repetitive elements by alignment of ChIP-Rx reads to the human database of repetitive regions (Repbase), an approach that has been shown to provide robust quantification of transcriptional abundance at repeat elements (Solovyov et al., 2018). We observed, in both cell lines, increased H3K27ac deposition in H3.3K27M lines compared with isogenic H3K27M-KO controls for most repetitive elements present in the reference (Figures 4D and S4D). Notably, matching RNA-seq analyses showed upregulation of transcription of families of repeat elements in mutant lines (Figures 4E, S4E, and S4F). At the transcriptional level, we observed increased baseline expression of specific families of repeat sequences, including

endogenous retroviruses (ERVs) in H3.3K27M mutant cells when compared with their isogenic counterparts (data not shown). ERVs represent about 10% of the genome and have been associated with viral mimicry in cancer (Chiappinelli et al., 2015; Roulois et al., 2015). We selected ERV families previously implicated in viral mimicry (Chiappinelli et al., 2015; Roulois et al., 2015) and further validated this increase using droplet digital PCR (ddPCR), a highly sensitive technique to quantify changes in lowly expressed transcripts (Figures 4F and S4G).

Finally, we confirmed that this pattern is recapitulated in human tumors. Using ChIP-Rx in H3.3K27M and H3K27WT HGG tumors, we observed increased H3K27ac deposition in the H3.3K27M group genome-wide (Figure 5A) and at repetitive elements (Figures 5B and 5C). Notably, RNA-seq analysis of a large panel of H3.3K27M (n = 17) and H3K27WT (n = 15) HGGs showed increased transcription of these elements in the H3.3K27M group (Figure 5D). Furthermore, analysis of RNA-seq data generated in our recently published H3.3K27M-HGG mouse model (Pathania et al., 2017) provided cross-species validation for these findings. We observed a significant increase in the proportion of reads mapping to the murine repeat genome only in H3.3K27M HGG mouse tumors when compared with experimental controls ( $p < 0.05$ ; Figure 5E). In all, our convergent findings in primary tumors, in primary cell lines derived from patients and in our syngeneic H3.3K27M mouse model indicate that the global increase in H3K27ac induced by H3.3K27M leads to pervasive deposition of the mark throughout the genome, including at normally silent repeat elements, resulting in aberrant transcription in H3.3K27M tumors.

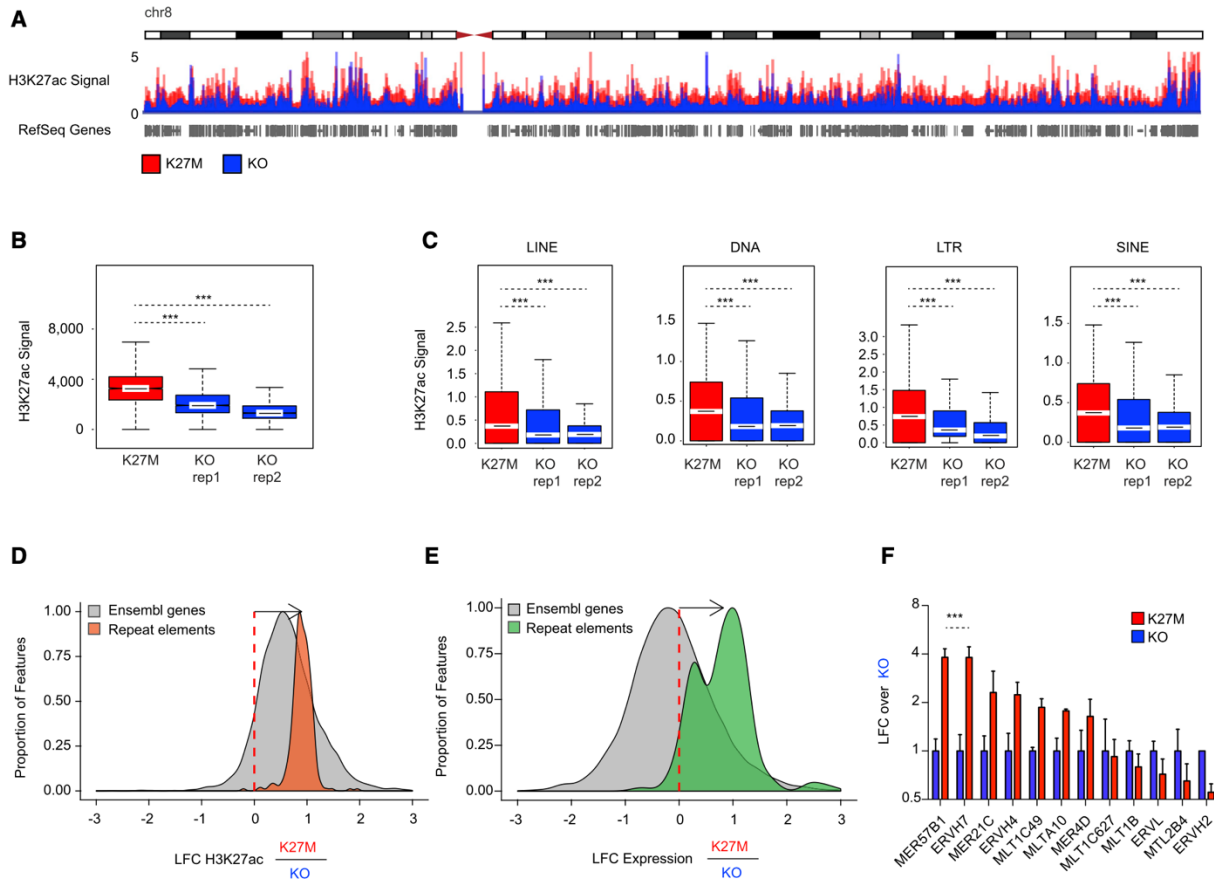


## Figure 4. H3K27ac Deposits Pervasively across Intergenic Genome and Is Enriched at Repetitive Elements

(A) Quantitative H3K27ac ChIP-Rx scaled reads between DIPG-XIII K27M and KO cell cultures across chromosome 8.

(B) Enrichment of H3K27ac across the human genome in 1-MB windows comparing DIPG-XIII H3K27M with KO clones using a Wilcoxon rank-sum test,  $***p < 0.001$ . The horizontal line inside the box corresponds to the median, the lines above and below the box delimit the interquartile range (IQR), and the end of the whiskers delimit values up to 1.5 times the IQR.

(C) Enrichment of H3K27ac across repetitive regions (LINE, DNA, LTR, and SINE) of the human genome annotated by the RepeatMasker database comparing DIPG-XIII K27M versus KO using a Wilcoxon rank-sum test,  $***p < 0.001$ .

(D and E) Changes in deposition of H3K27ac (D) and transcription (E) of repeat elements in DIPG-XIII K27M relative to KO. Histograms show the distributions of the LFC of genomic features in K27M relative to KO. Orange: H3K27ac deposition in repetitive elements (Rebase with ChIP-

seq; DIPG-XIII n = 1; DIPG-XIII-KO n = 2). Green: transcription of repetitive elements (Repbase with RNA-seq; DIPG-XIII n = 2; DIPG-XIII-KO n = 2). Gray: H3K27ac (left) and transcription (right) of Ensembl genes (GRCh37). Elements with sufficiently high expression (baseMean >100) and LFCs in [3, 3] range shown here.

(F) Sensitive measurement of expression of a panel of ERV families by ddPCR in H3K27M lines compared with respective KO DIPG-XIII cells. Plot shows mean + SEM of three experimental replicates. Two-way ANOVA compares H3K27M to KO, with Bonferroni post-test significance shown by\*\*\*p < 0.001. y axis is in log2 scale.

See also Figure S4.

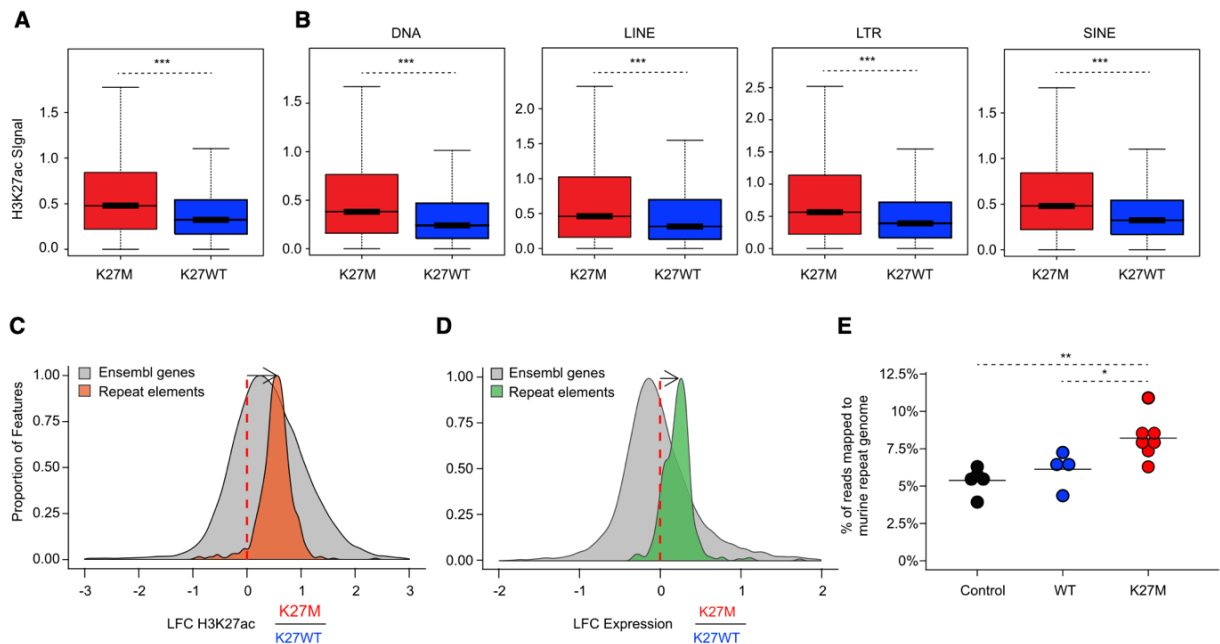


### Figure 5. H3.3K27M Tumors Exhibit Increased Deposition of H3K27ac and Transcription at Repetitive Elements

(A) Enrichment of H3K27ac across the human genome in 1-MB windows comparing 2 H3.3K27M with 3 H3K27WT tumors using a Wilcoxon rank-sum test, \*\*\*p < 0.001. The horizontal line inside the box corresponds to the median, the lines above and below the box delimit the IQR, and the end of the whiskers delimit values up to 1.5 times the IQR.

(B) Enrichment of H3K27ac across repetitive regions (LINE, DNA, LTR, and SINE) of the human genome annotated by the RepeatMasker database comparing two H3.3K27M with three H3K27WT tumors using a Wilcoxon rank-sum test, \*\*\*p < 0.001.

(C and D) Changes in H3K27ac (C) and transcription (D) of repeat elements in H3.3K27M tumors relative to H3K27WT tumors. Histograms show the distributions of the LFC of genomic features in K27M relative to K27WT. Orange: H3K27ac deposition over repetitive elements (ChIP-seq; H3.3K27M n = 2; H3K27WT n = 3). Green: transcription of repetitive elements (RNA-seq; H3.3K27M n = 17; H3K27WT n = 15). Gray: H3K27ac (left) and transcription (right) of Ensembl genes (GRCh37). Elements with sufficiently high expression (baseMean >100) and LFCs in the [-3,3] (C) and [-2,2] (D) ranges shown here.

(E) Proportion of RNA-seq reads that map to the repeat genome in K27M tumors relative to controls in a preclinical K27M mouse model. Black: neural progenitor cell (NPCs) controls (n = 4). Teal: NPCs overexpressing H3.3WT (n = 4). Red: K27M tumors (n = 7). Preclinical K27M mouse model RNA-seq data taken from Pathania et al. (2017). Significance between conditions assessed using a two-sample t test and is shown by \*\*p < 0.01, \*p < 0.05. Solid horizontal lines indicate the mean.

### **Epigenetic Inhibitors Exacerbate Repeat Element Expression in an H3.3K27M HGGs.**

DNA methylation is important in the containment of ERVs, and manipulation of this epigenetic mark is the basis of several therapeutic strategies in cancer (Baylin and Jones, 2016; Chiappinelli et al., 2015; Roulois et al., 2015). Histone deacetylase inhibitors (HDACi), in turn, often used in combination with DNA demethylating agents, have a documented role in promoting ERV expression (Topper et al., 2017). We thus interrogated whether pharmacological modulation of baseline expression of repeat elements is a specific cellular vulnerability in H3.3K27M versus H3K27WT HGGs. We tested the DNA demethylating agent 5-azacytidine and panobinostat, a pan-HDAC inhibitor currently in clinical trials for DIPG (<https://clinicaltrials.gov/ct2/show/NCT02717455>). We observed large transcriptomic changes, with the combination of 5-azacytidine and panobinostat inducing a greater increase in expression of repetitive elements in H3.3K27M lines compared with their H3.3K27M-KO isogenic counterparts (Figures 6A, 6B, and S5A–S5C). This was further confirmed using ddPCR, which identified specific ERVs to be significantly induced by panobinostat or 5-azacytidine in H3.3K27M lines, and showed that this induction was greatly attenuated upon H3.3K27M loss (Figures 6C, 6D, S5D, and S5E). The pharmacologically induced expression shift of repeat elements correlated with drug response, as H3.3K27M cell lines were more sensitive than

H3K27WT HGG lines to DNA demethylation (Figure 6E). Consistent with a causal role of H3.3K27M, this sensitivity was decreased in H3.3K27M KO cells (Figures 6F and S6A).

HDACi have been reported to inhibit the growth of H3K27M DIPG cell lines despite the already high H3K27ac levels observed in this setting (Grasso et al., 2015). Treatment of H3K27M cell lines using panobinostat greatly elevated H3K27ac levels (Figure 6G) at doses that impaired cell viability. No differential cell growth impairment was observed between H3.3K27M and H3K27WT lines (and between isogenic H3.3K27M versus KO cell lines) when treated with panobinostat (Figures S6B–S6D). However, when used in combination, low doses of 5-azacytidine and panobinostat were additively toxic, resulting in a greater effect in H3.3K27M lines compared with their KO counterparts (Figures 6H and S6E) and to H3K27WT HGG lines (Figure S6F). Notably, mass spectrometry revealed that the gain of acetylation induced by panobinostat mostly occurs in cells on non-canonical H3.3 (Figure 6I), which is known to be deposited in active regulatory elements as well as at repeat elements (Elsasser et al., 2015) and may thus lead to a further increase in repeat element expression.

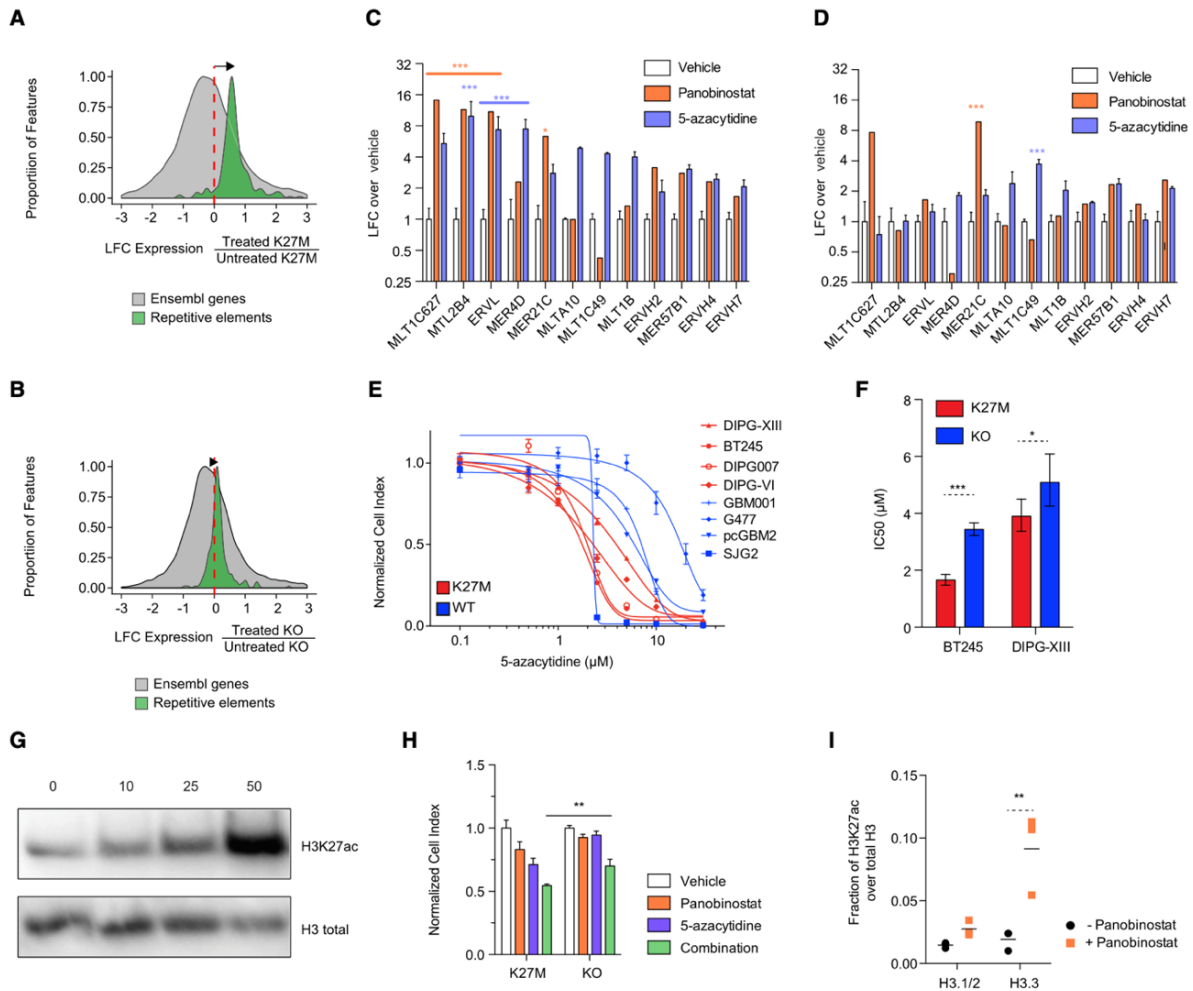


**Figure 6. Repeat Element Primed K27M Cells Are Vulnerable to DNA Methylation and Histone Deacetylase Inhibitors**

(A and B) Induction of expression of repetitive element observed in DIPG-XIII (A) and KO lines (B) after combination treatment (panobinostat and 5-azacytidine). Histograms show the distributions of the LFC of transcription of repetitive elements (green; Rebase) and Ensembl genes (gray; GRCh37) based on RNA-seq in treated compared with untreated cells (DIPG-XIII treated  $n = 3$ , untreated  $n = 3$ ; DIPG-XIII-KO treated  $n = 2$ , untreated  $n = 2$  biological replicates). Elements with sufficiently high expression (baseMean  $> 100$ ) and LFCs in  $[3, 3]$  range shown here.

(C and D) Measurement of ERV family expression by ddPCR upon 48 h treatment with panobinostat (50 nM) or 5-azacytidine 5 mM), normalized to vehicle control, in DIPG-XIII (C) and KO lines (D). Plots show mean + SEM of three experimental replicates of the DIPG-XIII line.

Two-way ANOVA compares vehicle with each drug, with Bonferroni post-test significance shown by \*\*\* $p < 0.001$ , \*\* $p < 0.01$ , \* $p < 0.05$ . y axis is in log<sub>2</sub> scale.

(E) Dose-response curves of a panel of HGG lines to 5-azacytidine in a 7-day growth assay in H3K27M and WT lines. Plots show mean  $\pm$  SEM of three experimental replicates.

(F) The sensitivity of H3K27M and KO lines of BT245 and DIPG-XIII to 5-azacytidine in a 7-day growth assay is portrayed by half maximal inhibitory concentration IC<sub>50</sub> values  $\pm$  95% confidence intervals. \*\*\* $p < 0.001$ , \* $p < 0.05$ .

(G) Western blot of total H3K27ac levels upon panobinostat treatment of DIPG-XIII at various doses (in nM) for 48 h.

(H) Cell viability in a 7-day growth assay under treatment of lines with sub-IC<sub>50</sub> doses of panobinostat (15 nM), 5-azacytidine (1.5 mM) and their combination in DIPG-XIII and isogenic KO lines. Plots show mean + SEM of three experimental replicates. A two-tailed t test compares combination-treated lines, with \*\* $p < 0.01$ . (I) Mass spectrometry measurement of H3K27ac levels on histone H3 variants comparing treated and untreated DIPG-XIII cells with 50 nM panobinostat for 48 h. Plot of mean of three experimental replicates. \*\* $p < 0.01$ .

See also Figures S5 and S6.

**Epigenetic Inhibitors Induce a Cellular Response to Repetitive Elements in Primed H3.3K27M Tumor Cells.** Elevated repeat element expression and formation of double-stranded RNA (dsRNA) stimulate innate immune responses mimicking a viral infectious state (i.e., viral mimicry), through induction of interferon type I signaling and expression of interferon-stimulated genes (ISGs) (Chiappinelli et al., 2015; Roulois et al., 2015; Topper et al., 2017). H3K27M mutant HGGs can have a significant inflammatory infiltrate (Bechet et al., 2014) in keeping with induction of immunogenicity in these tumors. We found no consistent increase in expression of ISGs in H3.3K27M HGG compared with H3K27WT models or in K27M cell lines relative to KO (Figures 7A, S7A, and S7B; Table S7). This is possibly due to the high MYC levels in H3.3K27M mutant cells (Figures 2D and S1C), as MYC expression has been shown to be a potent antagonist of interferon responses (Schlee et al., 2007) and has been shown to promote inhibition of apoptosis and immune evasion in other solid tumors (Topper et al., 2017).

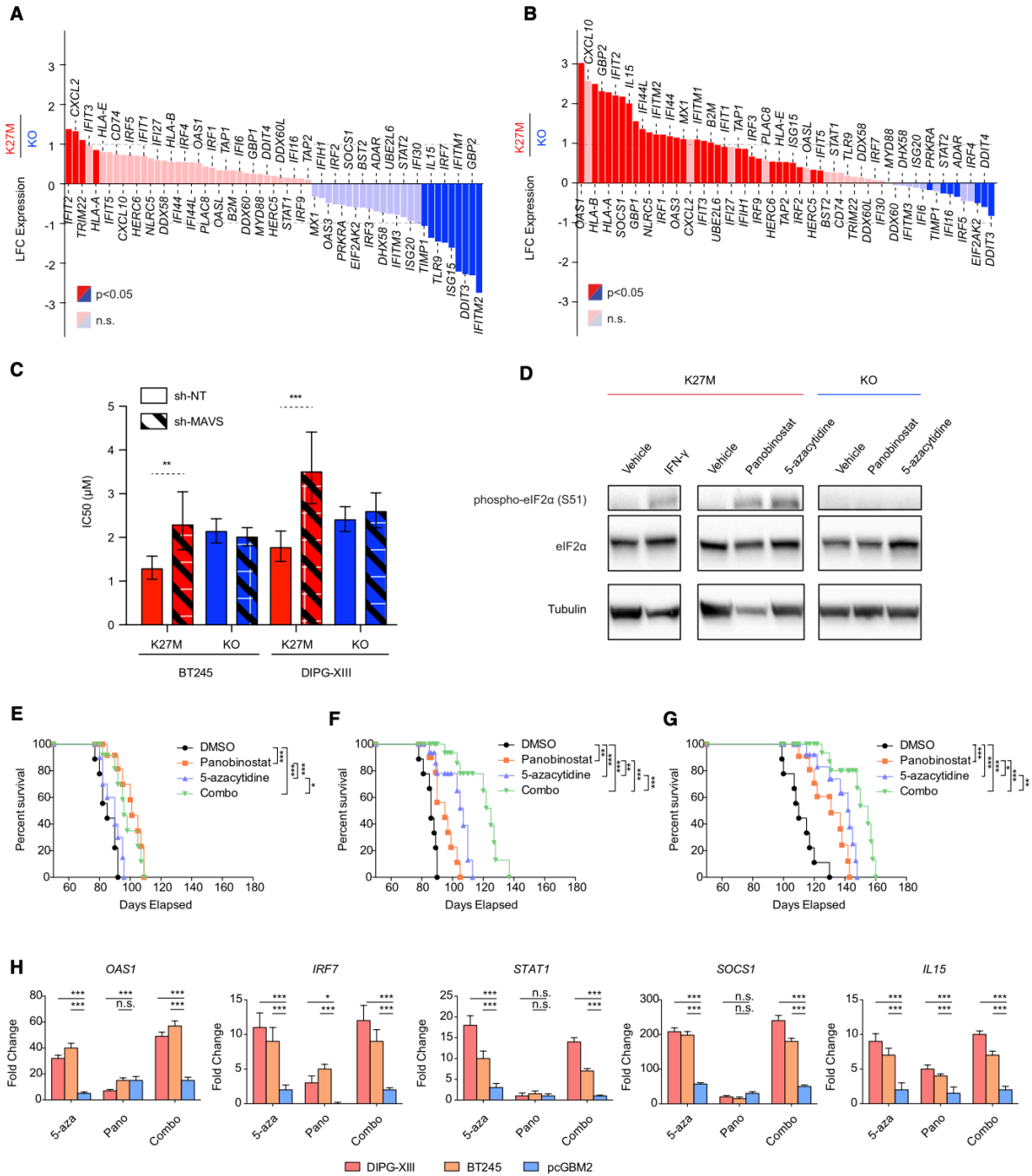
Importantly, 5-azacytidine treatment led to a significantly stronger induction of a large number of ISGs in both H3.3K27M mutant cell lines compared with their isogenic WT clones (Figure 7B;

Table S7), reaching more than 5-fold higher induction for some genes. Notably, relative to KO cells lacking the K27M mutation, 31/61 of the ISGs were significantly overexpressed in K27M mutant cells in response to 5-azacytidine treatment, in line with a stronger ISG response in the presence of the mutation, which seemingly amplifies the ability of the cancer cells to induce an interferon response when exposed to DNA demethylases. Interestingly, a minor increase in ISGs compared with baseline was seen when we used the HDACi panobinostat (Figures S7C and S7D; Table S7). In all, our findings argue that H3.3K27M cells are primed for viral mimicry in a H3K27M-dependent manner, as demonstrated by the baseline ERV expression in mutant cells relative to their WT or KO counterparts and their increased expression following further de-repression of silent repeat elements by epigenetic modulators, with preferential induction of ISGs in K27M mutant cells following the use of DNA demethylating agents.

We then characterized the functional role of dsRNA sensing pathways in the mechanism of epigenetic therapy action in H3.3K27M cell lines. Mitochondrial antiviral-signaling protein (MAVS) is the signaling adaptor common to two known cytoplasmic viral receptors, retinoic acid-inducible gene 1 (RIG-1) and melanoma differentiation-associated protein (MDA5), which recognize dsRNA, and is responsible for activating interferon responses in virally infected cells (Belgnaoui et al., 2011). These proteins have also been implicated in viral mimicry responses to cancer cells treated with DNA demethylating agents. Short hairpin RNA interference-mediated knockdown of MAVS attenuated the sensitivity of H3.3K27M but not H3K27M-KO HGG lines to 5-azacytidine (Figures 7C and S7E–S7I), suggesting the transduction of signals from dsRNA receptors to the interferon pathway is active in the presence of H3.3K27M but not in cells where this mutation was removed. Furthermore, phosphorylation of eukaryotic initiation factor alpha (eIF2a), a key target of the dsRNA sensor protein kinase R (PKR), was induced by panobinostat and 5-azacytidine in H3.3K27M lines but not in H3K27M-KO lines (Figures 7D and S7J). These two responses to dsRNA sensing and adaptation were specific to H3.3K27M HGG cells, further suggesting that H3.3K27M tumors are primed to innate immune responses through global alterations of histone modifications.

Last, we assessed tumor growth following systemic administration of 5-azacytidine, panobinostat, or a combination of these drugs in an orthotopic non-obese diabetic-severe combined immunodeficiency (NOD-SCID)-interleukin-2g (IL-2Rg)-chain-deficient mice (NSG) mouse model. Isogenic lines lacking the H3.3K27M mutation have defective growth *in vivo*. We thus

used parental H3.3K27M DIPG-XIII and BT245 and, as control, an H3.3K27M WT line, pcGBM2. Each group of mice was subjected to one of the four arms: 5-azacytidine, panobinostat as previously described (Borodovsky et al., 2013; Grasso et al., 2015; Yamashita et al., 2018), a combination of both drugs, or control vehicle. Compared to vehicle-treated control mice, we observed extended survival following administration of panobinostat in K27M mutant BT245 and DIPG-XIII-derived tumors, as previously described (Grasso et al., 2015), as well as in K27M-WT tumors derived from the pcGBM2 cell line (Figures 7E–7G). Notably, administration of 5-azacytidine resulted in improved survival in mice carrying H3.3K27M mutant cell lines compared with panobinostat or vehicle alone, while no significant effect of the drug was observed in mice injected with pcGBM2 (Figures 7E–7G and S7K). Moreover, in mice injected with H3.3K27M cell lines, combined administration of 5-azacytidine and panobinostat resulted in further improved survival compared with either drug delivered alone (Figures 7E–7G and S7K). Evaluation of a set of ISGs in the tumors extracted at endpoint from the mouse brain showed their significant induction in tumors carrying the H3.3K27M mutation following the use of 5-azacytidine or the combination therapy (Figure 7H). Limited ISGs induction was observed in tumors WT for H3K27, whereas panobinostat had modest effect on the expression of these genes both in K27M mutant and in K27M WT tumors (Figure 7H). These results confirm our *in vitro* data and further suggest that the use of DNA demethylating agents and this drug combination may be effective in K27M mutant HGGs.



**Figure 7. Epigenetic Therapies Activate Interferon Response Genes and dsRNA Sensing Pathways**

(A and B) Waterfall plots illustrating changes in the expression levels of ISGs in DIPG-XIII H3K27M cells relative to KO at baseline (A) and upon treatment with 5-azacytidine (B). y axis: LFC of expression in K27M relative to KO (baseline DIPG-XIII n = 3, DIPG-XIII-KO n = 2; treated DIPG-XIII n = 3, DIPG-XIII-KO n = 2 biological replicates). Red: upregulated genes in

K27M. Blue: downregulated genes. Significantly deregulated genes highlighted ( $p < 0.05$ ; baseMean  $> 100$ ). (C) The sensitivity of H3K27M and KO lines to 5-azacytidine upon expression of sh-NT (control) or pooled short hairpin RNAs targeting MAVS (sh-MAVS), is portrayed by IC50 values  $\pm$  95% confidence intervals. \*\*\* $p < 0.001$ , \*\* $p < 0.01$ .  $n = 3$ .

(D) Immunoblot of phosphorylated eIF2 $\alpha$  (serine 51) induced by 48-h treatment with panobinostat (50 nM) and 5-azacytidine (5 mM) or interferon gamma (IFN- $\gamma$ ) (1,000 U/mL) in DIPG-XIII H3K27M cells and KO cells.

(E–G) Survival of mice bearing pcGBM2 (E), DIPG-XIII (F), and BT245 (G) xenografts and treated with vehicle, 5-azacytidine, panobinostat, or combination of both drugs. Statistical significance measurements were determined using a log rank test.  $n = 9$  animals per condition.

(H) Induction of interferon signature genes in patient-derived tumor xenografts treated. Mice were treated with vehicle, 5-azacytidine, panobinostat, or combination of both drugs, and tumors were isolated at endpoint and analyzed by qPCR. The fold change of expression compared with DMSO-treated tumors is presented as mean + SD, and statistical significance was determined using a two-way ANOVA test on four distinct biological replicates for each condition. \*\*\* $p < 0.001$ , \*\* $p < 0.01$ .

See also Figure S7 and Table S7.

## Discussion

Our integrative epigenetic analysis of pediatric HGG, including tumors with H3K27M mutations, provides a comprehensive analysis of the specific transcriptional programs associated with H3.3K27M and H3K27WT HGGs, while revealing factors important in defining their respective cellular identity. Specifically, we show that H3.3K27M HGGs have a specific promoter, SE and core TF circuitry program which is indicative of cell lineage and identity, and seemingly independent of the H3K27M mutation. Importantly, analyses of our isogenic models show that the increased H3K27ac in H3K27M HGGs is mainly attributed to pervasive deposition of the H3K27ac mark across the genome following H3K27me3 loss and does not directly activate oncogenic SE programs. This pervasive acetylation induces increased expression of repetitive elements, including ERVs in H3.3K27M cells, which can prime cells for innate immune responses (Figure 8). We show that use of DNA demethylating agents and HDAC inhibitors further increase this baseline expression of ERVs and potentially help overcome possible MYC-driven immune

evasion, allowing robust induction of ISGs following DNA demethylating therapies, while significantly impairing cell growth *in vitro* and *in vivo* in H3.3K27M mutant HGGs. These findings uncover an exquisite vulnerability to available epigenetic therapies in deadly H3.3K27M HGGs. Our refined mapping of the *cis*-regulatory landscape of H3.3K27M and H3K27WT tumors reveals potentially important core regulatory circuitry TFs that will be relevant to developing animal models to study this disease as applied to other pediatric brain tumors (Lin et al., 2016; Mack et al., 2018). In addition to epigenetic mapping by H3K27ac ChIP-seq, ATAC-seq, and RNA-seq, our isogenic models are further validated by histone mass spectrometry to being faithful representations of the disease. While several studies have proposed epigenetic therapies to target H3K27M tumors (Grasso et al., 2015; Mohammad et al., 2017; Piunti et al., 2017), our comparison of isogenic models expressing H3.3K27M is of value to identify those with direct effect on K27M mutant cells while determining their mechanism of action. Thus, in support of our model that H3.3K27M does not create significant *de novo* oncogenic SE features, disruption of transcriptional activity through BET or HAT inhibition is not a specific vulnerability of H3.3K27M mutant lines. This does not exclude the importance of these compounds as agents that may be effective across pediatric HGG; however, they may not be specific to K27M mutagenesis as initially postulated, and their use in the context of priming the immune system may be counterproductive.

Repetitive elements are silenced by epigenetic marks including DNA methylation and H3K9 and H3K27 trimethylation. We show that loss of intergenic H3K27me3 results in pervasive H3K27ac deposition, which induces baseline expression of these normally silenced elements including ERVs. This effect can be further enhanced when manipulating the epigenome using DNA demethylating agents and HDAC inhibitors. Notably, the effects of HDACi in increasing H3K27ac were prominent on H3.3, which is the main H3 variant deposited in nucleosomes on repeat elements (Elsasser et al., 2015), potentially accounting for the further increased ERV expression using these inhibitors. We also show that, despite the high MYC expression resulting from SE regulation in H3.3K27M, DNA demethylating agents could induce a strong ISG response in mutant cells *in vitro* and *in vivo*. Importantly, the use of DNA demethylating agents in combination to HDACi resulted in significant growth inhibition in H3.3K27M mutant cells compared with their isogenic counterpart *in vitro* or to WT cells in *in vivo* orthotopic mouse models. We thus propose a model where pervasive H3K27ac leads to expression of RNA transcripts from repetitive regions and de-repression of ERVs. Repeat element and ERV de-repression may be potentiated by specific

epigenetic therapies, representing a unique vulnerability of H3.3K27M tumors. In line with other solid tumors, modulating the epigenome (with agents such as 5-azacytidine and HDACi) at repeat elements can trigger viral mimicry and induce cellular interferon responses, thus promoting tumor cell death and immune cell activation (Jones et al., 2019). This effect is likely not specific to H3.3K27M HGGs and could be of relevance in a significant number of other cancers exhibiting loss of PRC2 activity and altered H3K27me3 levels, including intractable posterior fossa ependymoma group A and malignant peripheral neural sheath tumors (Lee et al., 2014). In line with our findings of a primed immune state in H3.3K27M mutants, several groups have shown that DIPGs have a level of immune infiltrate of unknown origin and significance, including recent data from single-cell transcriptomic of H3K27M mutant DIPGs (Bechet et al., 2014; Filbin et al., 2018), suggesting that further modulation of interferon signaling could achieve productive anti-tumor responses *in vivo*.

It is also important to consider that treatment of K27M HGG cells with panobinostat or 5-azacytidine have relevant cell-intrinsic effects. We provide support that the release of dsRNA and ERVs normally silenced in midline HGG cells activates a potential viral mimicry response. This occurs through recognition of dsRNAs by intracellular DNA pattern receptors (i.e., RIG-1 and MDA5), activation of MAVS, and induction of interferon response genes (Jones et al., 2019; Roulois et al., 2015). We show that MAVS expression is important for mediating response to 5-azacytidine preferentially in K27M cells. In a K27M-specific context, we show that eIF2a is phosphorylated at the serine 51 position when cells are treated with panobinostat or 5-azacytidine. As a result, eIF2a phosphorylation inhibits translation initiation and therefore protein synthesis, representing one possible mechanism of cell growth inhibition. Another important consideration is that a small subset of genes (such as the p16 tumor suppressor) retain epigenetic silencing in H3K27M cells despite global loss of H3K27me3 and DNA methylation (Cordero et al., 2017). P16 may be re-expressed upon treatment with epigenetic inhibitors and may also negatively impact tumor cell growth.

In summary, our findings identify a potential therapeutic vulnerability in H3.3K27M mutant HGGs. The mutation primes the cells for viral mimicry, a state that we show can be further enhanced by specific epigenetic drugs, which may act by making the tumor “hot” for the immune system. While further work using immune-competent models is warranted, several of these epigenetic therapies are FDA approved and HDACi and immune checkpoint inhibitors are

currently in clinical trials for DIPGs as single agents, as are DNA demethylating agents which are used in combination with cytotoxic agents in several solid tumors including HGGs. It is important to note that, while epigenetic therapies such as nucleoside analogs (5-azacytidine) may incorporate and target actively dividing cells, at higher doses such agents exhibit high levels of cytotoxicity particularly within the bone marrow (Jones et al., 2019). Low-dose combinations of these agents with immunomodulatory compounds could be rapidly tested at the bedside and may represent an effective therapeutic strategy against primed H3.3K27M HGGs, providing a needed alternative in an untreatable deadly disease.

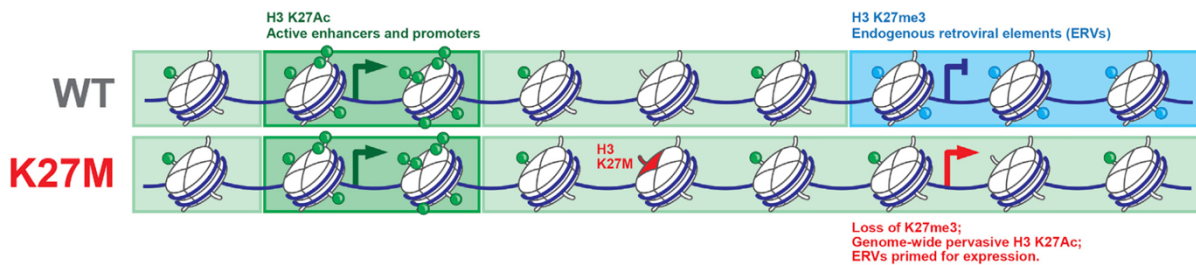


**Figure 8. Schematic Summary of Findings Resulting from this Study**

The global loss of H3K27me3 by H3.3K27M leads to pervasive gain of H3K27ac across broad regions of chromatin, including repeat elements and endogenous retroviruses. This state primes them for activation by DNA demethylation and HDAC inhibition, a therapeutic vulnerability caused by this mutation.

### Acknowledgements

We thank Jacek Majewski for invaluable guidance in experimental design and critical reading of manuscript. We thank Alexey Soshnev for creating Figure 8. This work was supported by funding from: US NIH (grant P01-CA196539 to N.J., P.W.L., and B.A.G.; and T32GM008275 and TL1TR001880 to B.A.G.), the Canadian Institutes of Health Research (CIHR grant MOP-286756 and FDN-154307 to N.J., EP1-120608 to T.P., and PJT-156086 to C.L.K.), the Fonds de Recherche du Quebec en Sante (FRQS) salary award to C.L.K. and fellowships to N.D.J. and A.S.H. N.J. is a member of the Penny Cole Laboratory and the recipient of a Chercheur Boursier, Chaire de Recherche Award from the FRQS. This work was performed within the context of the International CHildhood Astrocytoma INtegrated Genomic and Epigenomic (ICHANGE) consortium with funding from Genome Canada and Genome Quebec. Computational

infrastructure was provided by Compute Canada and Calcul Quebec. M.K.M. is funded by a CIHR Banting postdoctoral fellowship. P.W.L. is a Pew Scholar in the Biomedical Sciences. We are especially grateful for the generous philanthropic donations of Kat D DIPG, Poppies for Irene and We Love You Connie Foundations. S.C.M. is supported by Cancer Prevention Research Institute of Texas (CPRIT) scholar award (RR170023), Alex's Lemonade Stand Foundation (ALSF) A award, and Young investigator award, RALLY research grant, BEAR Necessities Pediatric Cancer Foundation Grant, Children's Cancer Research Fund award, Children's Brain Tumor Foundation Award, and Baylor College of Medicine Junior Faculty Award.

### **Author Contributions**

B.K., and A.S.H. led and performed a majority of the functional studies, and were actively involved in study design, data analysis, interpretation, and manuscript preparation. N.D.J. led the bioinformatics analysis, and also was actively involved in study design, data analysis, interpretation, and manuscript preparation. S.D., M.K.McC., C.C.L.C., and D.F. contributed to data collection, analysis, and study design. D.M.M. and B.G. led the histone proteomics experiments and analysis. P.G. and M.L. led the ATAC-seq analysis. K.C.B. contributed to enhancer analysis, figure preparation, and data processing. L.G.M. contributed to study design, data interpretation, and manuscript preparation. B.E. and A.G.W. assisted with the collection of patient samples, study design and data interpretation. D.D.d.C. led the analysis and data interpretation regarding repeat element and ERV analysis. P.S. generated the mouse model used for cross-species validation of repeat element expression. P.B.D., D.W.P., D.G.P., S.M.P., P.L., M.L., C.A., B.A.G., C.L.K., N.J., and S.C.M. contributed to study design, data interpretation, and manuscript preparation. C.L.K., N.J., and S.C.M. co-led and supervised all aspects the project.

### **DECLARATION OF INTERESTS**

The authors declare no competing interests.

Received: September 25, 2018

Revised: January 16, 2019

Accepted: April 12, 2019

Published: May 13, 2019; corrected online: September 16, 2019

## References

- Akhtar-Zaidi, B., Cowper-Sal-lari, R., Corradin, O., Saiakhova, A., Bartels, C.F., Balasubramanian, D., Myeroff, L., Lutterbaugh, J., Jarrar, A., Kalady, M.F., et al. (2012). Epigenomic enhancer profiling defines a signature of colon cancer. *Science* 336, 736–739.
- Alves dos Santos, M.T., and Smidt, M.P. (2011). En1 and Wnt signaling in midbrain dopaminergic neuronal development. *Neural Dev.* 6, 23.
- Bao, W., Kojima, K.K., and Kohany, O. (2015). Repbase update, a database of repetitive elements in eukaryotic genomes. *Mobile DNA* 6, 11.
- Baylin, S.B., and Jones, P.A. (2016). Epigenetic determinants of cancer. *Cold Spring Harb Perspect. Biol.* 8, <https://doi.org/10.1101/cshperspect.a019505>.
- Bechet, D., Gielen, G.G., Korshunov, A., Pfister, S.M., Rousso, C., Faury, D., Fiset, P.O., Benlimane, N., Lewis, P.W., Lu, C., et al. (2014). Specific detection of methionine 27 mutation in histone 3 variants (H3K27M) in fixed tissue from high-grade astrocytomas. *Acta Neuropathol.* 128, 733–741.
- Belgnaoui, S.M., Paz, S., and Hiscott, J. (2011). Orchestrating the interferon antiviral response through the mitochondrial antiviral signaling (MAVS) adapter. *Curr. Opin. Immunol.* 23, 564–572.
- Bender, S., Tang, Y., Lindroth, A.M., Hovestadt, V., Jones, D.T., Kool, M., Zapatka, M., Northcott, P.A., Sturm, D., Wang, W., et al. (2013). Reduced H3K27me3 and DNA hypomethylation are major drivers of gene expression in K27M mutant pediatric high-grade gliomas. *Cancer Cell* 24, 660–672.
- Bestor, T.H., and Bourc'his, D. (2004). Transposon silencing and imprint establishment in mammalian germ cells. *Cold Spring Harb Symp. Quant Biol.* 69, 381–387.
- Bickel, P., Boley, N., Brown, J., Huang, H., and Zhang, N. (2010). Subsampling methods for genomic inference. *Ann. Appl. Statistics* 4, 1660–1697.

Bolger, A.M., Lohse, M., and Usadel, B. (2014). Trimmomatic: a flexible trimmer for Illumina sequence data. *Bioinformatics* 30, 2114–2120.

Borodovsky, A., Salmasi, V., Turcan, S., Fabius, A.W., Baia, G.S., Eberhart, C.G., Weingart, J.D., Gallia, G.L., Baylin, S.B., Chan, T.A., and Riggins, G.J. (2013). 5-Azacytidine reduces methylation, promotes differentiation and induces tumor regression in a patient-derived IDH1 mutant glioma xenograft. *Oncotarget* 4, 1737–1747.

Bourc'his, D., and Bestor, T.H. (2004). Meiotic catastrophe and retrotransposon reactivation in male germ cells lacking Dnmt3L. *Nature* 431, 96–99.

Carroll, T.S., Liang, Z., Salama, R., Stark, R., and de Santiago, I. (2014). Impact of artifact removal on ChIP quality metrics in ChIP-seq and ChIP-exo data. *Front. Genet.* 5, 75.

Chan, K.M., Fang, D., Gan, H., Hashizume, R., Yu, C., Schroeder, M., Gupta, N., Mueller, S., James, C.D., Jenkins, R., et al. (2013). The histone H3.3K27M mutation in pediatric glioma reprograms H3K27 methylation and gene expression. *Genes Dev.* 27, 985–990.

Chiappinelli, K.B., Strissel, P.L., Desrichard, A., Li, H., Henke, C., Akman, B., Hein, A., Rote, N.S., Cope, L.M., Snyder, A., et al. (2015). Inhibiting DNA methylation causes an interferon response in cancer via dsRNA including endogenous retroviruses. *Cell* 162, 974–986.

Cordero, F.J., Huang, Z., Grenier, C., He, X., Hu, G., McLendon, R.E., Murphy, S.K., Hashizume, R., and Becher, O.J. (2017). Histone H3.3K27M represses p16 to accelerate gliomagenesis in a murine model of DIPG. *Mol. Cancer Res.* 15, 1243–1254.

Creyghton, M.P., Cheng, A.W., Welstead, G.G., Kooistra, T., Carey, B.W., Steine, E.J., Hanna, J., Lodato, M.A., Frampton, G.M., Sharp, P.A., et al. (2010). Histone H3K27ac separates active from poised enhancers and predicts developmental state. *Proc. Natl. Acad. Sci. U S A* 107, 21931–21936.

de Koning, A.P., Gu, W., Castoe, T.A., Batzer, M.A., and Pollock, D.D. (2011). Repetitive elements may comprise over two-thirds of the human genome. *PLoS Genet.* 7, e1002384.

Dobin, A., Davis, C.A., Schlesinger, F., Drenkow, J., Zaleski, C., Jha, S., Batut, P., Chaisson, M., and Gingeras, T.R. (2013). STAR: ultrafast universal RNA-seq aligner. *Bioinformatics* 29, 15–21.

Elsasser, S.J., Noh, K.M., Diaz, N., Allis, C.D., and Banaszynski, L.A. (2015). Histone H3.3 is required for endogenous retroviral element silencing in embryonic stem cells. *Nature* 522, 240–244.

Filbin, M.G., Tirosh, I., Hovestadt, V., Shaw, M.L., Escalante, L.E., Mathewson, N.D., Neftel, C., Frank, N., Pelton, K., Hebert, C.M., et al. (2018). Developmental and oncogenic programs in H3K27M gliomas dissected by single-cell RNA-seq. *Science* 360, 331–335.

Fontebasso, A.M., Papillon-Cavanagh, S., Schwartzenuber, J., Nikbakht, H., Gerges, N., Fiset, P.O., Bechet, D., Faury, D., De Jay, N., Ramkissoon, L.A., et al. (2014). Recurrent somatic mutations in ACVR1 in pediatric midline high-grade astrocytoma. *Nat. Genet.* 46, 462–466.

Funato, K., Major, T., Lewis, P.W., Allis, C.D., and Tabar, V. (2014). Use of human embryonic stem cells to model pediatric gliomas with H3.3K27M histone mutation. *Science* 346, 1529–1533.

Goke, J., Lu, X., Chan, Y.S., Ng, H.H., Ly, L.H., Sachs, F., and Szczerbinska, I. (2015). Dynamic transcription of distinct classes of endogenous retroviral elements marks specific populations of early human embryonic cells. *Cell Stem Cell* 16, 135–141.

Grasso, C.S., Tang, Y., Truffaux, N., Berlow, N.E., Liu, L., Debily, M.A., Quist, M.J., Davis, L.E., Huang, E.C., Woo, P.J., et al. (2015). Functionally defined therapeutic targets in diffuse intrinsic pontine glioma. *Nat. Med.* 21, 555–559.

Heinz, S., Benner, C., Spann, N., Bertolino, E., Lin, Y.C., Laslo, P., Cheng, J.X., Murre, C., Singh, H., and Glass, C.K. (2010). Simple combinations of lineage-determining transcription factors prime cis-regulatory elements required for macrophage and B cell identities. *Mol. Cell* 38, 576–589.

- Jo, H., and Koh, G. (2015). Faster single-end alignment generation utilizing multi-thread for BWA. *Biomed Mater Eng.* 26, S1791–S1796.
- Jones, P.A., Ohtani, H., Chakravarthy, A., and De Carvalho, D.D. (2019). Epigenetic therapy in immune-oncology. *Nat. Rev. Cancer* 19, 151–161.
- Kang, P., Lee, H.K., Glasgow, S.M., Finley, M., Donti, T., Gaber, Z.B., Graham, B.H., Foster, A.E., Novitch, B.G., Gronostajski, R.M., and Deneen, B. (2012). Sox9 and NFIA coordinate a transcriptional regulatory cascade during the initiation of gliogenesis. *Neuron* 74, 79–94.
- Khuong-Quang, D.A., Buczkowicz, P., Rakopoulos, P., Liu, X.Y., Fontebasso, A.M., Bouffet, E., Bartels, U., Albrecht, S., Schwartzentruber, J., Letourneau, L., et al. (2012). K27M mutation in histone H3.3 defines clinically and biologically distinct subgroups of pediatric diffuse intrinsic pontine gliomas. *Acta Neuropathol.* 124, 439–447.
- Langmead, B., and Salzberg, S.L. (2012). Fast gapped-read alignment with Bowtie 2. *Nat. Methods* 9, 357–359.
- Lee, W., Teckie, S., Wiesner, T., Ran, L., Prieto Granada, C.N., Lin, M., Zhu, S., Cao, Z., Liang, Y., et al. (2014). PRC2 is recurrently inactivated through EED or SUZ12 loss in malignant peripheral nerve sheath tumors. *Nat. Genet.* 46, 1227–1232.
- Lewis, P.W., Muller, M.M., Koletsky, M.S., Cordero, F., Lin, S., Banaszynski, L.A., Garcia, B.A., Muir, T.W., Becher, O.J., and Allis, C.D. (2013). Inhibition of PRC2 activity by a gain-of-function H3 mutation found in pediatric glioblastoma. *Science* 340, 857–861.
- Li, H., Handsaker, B., Wysoker, A., Fennell, T., Ruan, J., Homer, N., Marth, G., Abecasis, G., and Durbin, R. (2009). The sequence alignment/map format and SAMtools. *Bioinformatics* 25, 2078–2079.
- Liao, Y., Smyth, G.K., and Shi, W. (2014). featureCounts: an efficient general purpose program for assigning sequence reads to genomic features. *Bioinformatics* 30, 923–930.

- Lin, C.Y., Erkek, S., Tong, Y., Yin, L., Federation, A.J., Zapatka, M., Haldipur, P., Kawauchi, D., Risch, T., Warnatz, H.J., et al. (2016). Active medulloblastoma enhancers reveal subgroup-specific cellular origins. *Nature* *530*, 57–62.
- Love, M.I., Huber, W., and Anders, S. (2014). Moderated estimation of fold change and dispersion for RNA-seq data with DESeq2. *Genome Biol.* *15*, 550.
- Loven, J., Hoke, H.A., Lin, C.Y., Lau, A., Orlando, D.A., Vakoc, C.R., Bradner, J.E., Lee, T.I., and Young, R.A. (2013). Selective inhibition of tumor oncogenes by disruption of super-enhancers. *Cell* *153*, 320–334.
- Lu, C., Jain, S.U., Hoelper, D., Bechet, D., Molden, R.C., Ran, L., Murphy, D., Venneti, S., Hameed, M., Pawel, B.R., et al. (2016). Histone H3K36 mutations promote sarcomagenesis through altered histone methylation landscape. *Science* *352*, 844–849.
- Machold, R., Klein, C., and Fishell, G. (2011). Genes expressed in Atoh1 neuronal lineages arising from the r1/isthmus rhombic lip. *Gene Expr. Patterns* *11*, 349–359.
- Mack, S.C., Pajtler, K.W., Chavez, L., Okonechnikov, K., Bertrand, K.C., Wang, X., Erkek, S., Federation, A., Song, A., Lee, C., et al. (2018). Therapeutic targeting of ependymoma as informed by oncogenic enhancer profiling. *Nature* *553*, 101–105.
- Matys, V., Kel-Margoulis, O.V., Fricke, E., Liebich, I., Land, S., Barre-Dirrie, A., Reuter, I., Chekmenev, D., Krull, M., Hornischer, K., et al. (2006). TRANSFAC and its module TRANSCompel: transcriptional gene regulation in eukaryotes. *Nucleic Acids Res.* *34*, D108–D110.
- Mohammad, F., Weissmann, S., Leblanc, B., Pandey, D.P., Hojfeldt, J.W., Comet, I., Zheng, C., Johansen, J.V., Rapin, N., Porse, B.T., et al. (2017). EZH2 is a potential therapeutic target for H3K27M-mutant pediatric gliomas. *Nat. Med.* *23*, 483–492.
- Nagaraja, S., Vitanza, N.A., Woo, P.J., Taylor, K.R., Liu, F., Zhang, L., Li, M., Meng, W., Ponnuswami, A., Sun, W., et al. (2017). Transcriptional Dependencies in Diffuse Intrinsic Pontine Glioma. *Cancer Cell* *31*, 635–652.e6.

Orlando, D.A., Chen, M.W., Brown, V.E., Solanki, S., Choi, Y.J., Olson, E.R., Fritz, C.C., Bradner, J.E., and Guenther, M.G. (2014). Quantitative ChIP-seq normalization reveals global modulation of the epigenome. *Cell Rep.* *9*, 1163–1170.

Pathania, M., De Jay, N., Maestro, N., Harutyunyan, A.S., Nitarska, J., Pahlavan, P., Henderson, S., Mikael, L.G., Richard-Londt, A., Zhang, Y., et al. (2017). H3.3(K27M) cooperates with Trp53 loss and PDGFRA gain in mouse embryonic neural progenitor cells to induce invasive high-grade gliomas. *Cancer Cell* *32*, 684–700.e9.

Piunti, A., Hashizume, R., Morgan, M.A., Bartom, E.T., Horbinski, C.M., Marshall, S.A., Rendleman, E.J., Ma, Q., Takahashi, Y.H., Woodfin, A.R., et al. (2017). Therapeutic targeting of polycomb and BET bromodomain proteins in diffuse intrinsic pontine gliomas. *Nat. Med.* *23*, 493–500.

Quinlan, A.R., and Hall, I.M. (2010). BEDTools: a flexible suite of utilities for comparing genomic features. *Bioinformatics* *26*, 841–842.

Ramirez, F., Dundar, F., Diehl, S., Gruning, B.A., and Manke, T. (2014). deepTools: a flexible platform for exploring deep-sequencing data. *Nucleic Acids Res.* *42*, W187–W191.

Ramsey, S.A., Knijnenburg, T.A., Kennedy, K.A., Zak, D.E., Gilchrist, M., Gold, E.S., Johnson, C.D., Lampano, A.E., Litvak, V., Navarro, G., et al. (2010). Genome-wide histone acetylation data improve prediction of mammalian transcription factor binding sites. *Bioinformatics* *26*, 2071–2075.

Ran, F.A., Hsu, P.D., Wright, J., Agarwala, V., Scott, D.A., and Zhang, F. (2013). Genome engineering using the CRISPR-Cas9 system. *Nat. Protoc.* *8*, 2281–2308.

Roulois, D., Loo Yau, H., Singhania, R., Wang, Y., Danesh, A., Shen, S.Y., Han, H., Liang, G., Jones, P.A., Pugh, T.J., et al. (2015). DNA-demethylating agents target colorectal cancer cells by inducing viral mimicry by endogenous transcripts. *Cell* *162*, 961–973.

Saint-Andre, V., Federation, A.J., Lin, C.Y., Abraham, B.J., Reddy, J., Lee, T.I., Bradner, J.E., and Young, R.A. (2016). Models of human core transcriptional regulatory circuitries. *Genome Res.* 26, 385–396.

Schlee, M., Schuhmacher, M., Holzel, M., Laux, G., and Bornkamm, G.W. (2007). c-MYC impairs immunogenicity of human B cells. *Adv. Cancer Res.* 97, 167–188.

Schwartzentruber, J., Korshunov, A., Liu, X.Y., Jones, D.T., Pfaff, E., Jacob, K., Sturm, D., Fontebasso, A.M., Quang, D.A., Tonjes, M., et al. (2012). Driver mutations in histone H3.3 and chromatin remodelling genes in paediatric glioblastoma. *Nature* 482, 226–231.

Sidoli, S., Bhanu, N.V., Karch, K.R., Wang, X., and Garcia, B.A. (2016). Complete workflow for analysis of histone post-translational modifications using bottom-up mass spectrometry: from histone extraction to data analysis. *J. Vis. Exp.*

Smit, A., Hubley, R., and Green, P. (2013-2015). RepeatMasker Open-4.0. <http://www.repeatmasker.org>.

Solovyov, A., Vabret, N., Arora, K.S., Snyder, A., Funt, S.A., Bajorin, D.F., Rosenberg, J.E., Bhardwaj, N., Ting, D.T., and Greenbaum, B.D. (2018). Global cancer transcriptome quantifies repeat element polarization between immunotherapy responsive and T cell suppressive classes. *Cell Rep.* 23, 512–521.

Sonoda, E., Takata, M., Yamashita, Y.M., Morrison, C., and Takeda, S. (2001). Homologous DNA recombination in vertebrate cells. *Proc Natl Acad Sci U S A* 98, 8388–8394.

Sturm, D., Bender, S., Jones, D.T., Lichter, P., Grill, J., Becher, O., Hawkins, C., Majewski, J., Jones, C., Costello, J.F., et al. (2014). Paediatric and adult glioblastoma: multiform (epi)genomic culprits emerge. *Nat. Rev. Cancer* 14, 92–107.

Thorvaldsdottir, H., Robinson, J.T., and Mesirov, J.P. (2013). Integrative Genomics Viewer (IGV): high-performance genomics data visualization and exploration. *Brief. Bioinform.* 14, 178–192.

Topper, M.J., Vaz, M., Chiappinelli, K.B., DeStefano Shields, C.E., Niknafs, N., Yen, R.C., Wenzel, A., Hicks, J., Ballew, M., Stone, M., et al. (2017). Epigenetic therapy ties MYC depletion to reversing immune evasion and treating lung cancer. *Cell* *171*, 1284–1300.e21.

van der Maaten, L., and Hinton, G. (2008). Visualizing data using t-SNE. *J. Mach. Learn. Res.* *9*, 2579–2605.

z

Walsh, C.P., Chaillet, J.R., and Bestor, T.H. (1998). Transcription of IAP endogenous retroviruses is constrained by cytosine methylation. *Nat. Genet.* *20*, 116–117.

Whyte, W.A., Orlando, D.A., Hnisz, D., Abraham, B.J., Lin, C.Y., Kagey, M.H., Rahl, P.B., Lee, T.I., and Young, R.A. (2013). Master transcription factors and mediator establish super-enhancers at key cell identity genes. *Cell* *153*, 307–319.

Wu, G., Broniscer, A., McEachron, T.A., Lu, C., Paugh, B.S., Becksfors, J., Qu, C., Ding, L., Huether, R., Parker, M., et al. (2012). Somatic histone H3 alterations in pediatric diffuse intrinsic pontine gliomas and non-brainstem glioblastomas. *Nat. Genet.* *44*, 251–253.

Yamashita, A.S., da Costa Rosa, M., Borodovsky, A., Festuccia, W.T., Chan, T., and Riggins, G.J. (2018). Demethylation and epigenetic modification with 5-azacytidine reduces IDH1 mutant glioma growth in combination with temozolomide. *Neuro Oncol.* 10.1093/neuonc/noy146.

Zhang, Y., Liu, T., Meyer, C.A., Eeckhoute, J., Johnson, D.S., Bernstein, B.E., Nusbaum, C., Myers, R.M., Brown, M., Li, W., and Liu, X.S. (2008). Model-based analysis of ChIP-seq (MACS). *Genome Biol.* *9*, R137.

Zhu, W., Krishna, S., Garcia, C., Lin, C.J., Mitchell, B.D., Scott, K.L., Mohila, C.A., Creighton, C.J., Yoo, S.H., Lee, H.K., and Deneen, B. (2017). Daam2 driven degradation of VHL promotes gliomagenesis. *Elife* *6*, <https://doi.org/10.7554/eLife.31926>.

# STAR METHODS

## KEY RESOURCES TABLE

| REAGENT or RESOURCE   | SOURCE                         | IDENTIFIER                       |
|---|--------------------------------|----------------------------------|
| <b>Antibodies</b>   |                                |                                  |
| Rabbit polyclonal anti-Histone H3 (1 in 1000)                             | Abcam                          | Cat# ab1791; RRID: AB_302613     |
| Rabbit polyclonal anti-H3K27me3 (1 in 1000)                               | Millipore                      | Cat# ABE44; RRID: AB_10563660    |
| Rabbit polyclonal H3K27M (1 in 200)                                       | Millipore                      | Cat# ABE419; RRID: AB_2728728    |
| Rabbit monoclonal H3K27ac (1 in 1000)                                     | Cell Signaling Technology      | Cat# 8173P; RRID: AB_10949887    |
| Rabbit polyclonal anti-beta Tubulin (1 in 1000)                           | Abcam                          | Cat# ab6046; RRID: AB_2210370    |
| Rabbit polyclonal anti-MAVS (1 in 1000)                                   | Abcam                          | Cat# ab31334; RRID: AB_776218    |
| Rabbit polyclonal anti-eIF2 alpha (1 in 1000)                             | Cell Signaling Technology      | Cat# 8722; RRID: AB_2230924      |
| Rabbit polyclonal anti-Phospho-eIF2alpha (Ser51) (1 in 10000)             | Cell Signaling Technology      | Cat# 9721; RRID: AB_330951       |
| Rabbit polyclonal anti-H3K27ac  | Diagenode                      | Cat# C15410196; RRID: AB_2637079 |
| <b>Bacterial and Virus Strains</b>  |                                |                                  |
| MAVS Human shRNA lentiviral particles (Locus ID 57508)                    | OrGene                         | Cat# TL307181V                   |
| H3K27M lentiviral particles   | VectorBuilder                  | Cat# VB171024-1031kuk            |
| <b>Biological Samples</b>   |                                |                                  |
| Pediatric high-grade glioma tumor tissue                                  | This paper                     | N/A                              |
| <b>Chemicals, Peptides, and Recombinant Proteins</b>                      |                                |                                  |
| NeuroCult Proliferation Kit   | STEMCELL Technologies          | Cat # 05751                      |
| EGF   | STEMCELL Technologies          | Cat # 78006.1                    |
| FGF   | STEMCELL Technologies          | Cat # 78003.2                    |
| Poly-L-O-methine  | Sigma Aldrich                  | Cat # A-004-M                    |
| Laminin   | Sigma Aldrich                  | Cat # L2020                      |
| Heparin   | STEMCELL Technologies          | Cat # 07980                      |
| Panobinostat  | Structural Genomics Consortium | N/A                              |
| JQ-1  | Structural Genomics Consortium | N/A                              |
| CBP-30  | Structural Genomics Consortium | N/A                              |
| IBET-762  | Cayman Chemical                | Cat # 1260907-17-2               |
| 5-azacytidine   | Sigma Aldrich                  | Cat # A2385                      |
| Propionic anhydride   | Sigma Aldrich                  | Cat # 240311-50G                 |
| C646  | Sigma Aldrich                  | Cat# SML0002                     |
| <b>Critical Commercial Assays</b>   |                                |                                  |
| Aurum Total RNA Mini Kit  | Bio-Rad                        | Cat # 7306820                    |
| Script Reverse Transcription Supremix                                     | Bio-Rad                        | Cat # 1709841                    |
| QX200 ddPCR EvaGreen Supremix Assay                                       | Bio-Rad                        | Cat # 1709841                    |
| Histone Extraction Kit  | Abcam                          | Cat # ab113476                   |
| RNAeasy mini kit  | Qiagen                         | Cat # 74104                      |
| TruSeq Stranded Total RNA Library Prep Kit with Ribo-Zero Human/Mouse/Rat | illumina                       | Cat # RS-122-2201                |
| Ideal ChIP-seq Kit for Histones   | Diagenode                      | Cat # C01010051                  |
| Kapa HTP Library Preparation Kit Illumina Platforms                       | Roche                          | Cat # 07961901001                |
| Empore Extraction Disk, 3M C18  | Fisher Scientific              | Cat # 143863-2                   |

(Continued on next page)

| REAGENT or RESOURCE              | SOURCE                          | IDENTIFIER  |
|----------------------------------|---------------------------------|---|
| <b>STAR v2.3.0e</b>              |                                 |   |
| STAR v2.3.0e                     | Dobin et al., 2013              | <a href="https://github.com/alexdobin/STAR">https://github.com/alexdobin/STAR</a>   |
| featureCounts v1.4.4             | Liao et al., 2014               | <a href="http://bioinf.wehi.edu.au/featureCounts/">http://bioinf.wehi.edu.au/featureCounts/</a>   |
| DESeq2                           | Love et al., 2014               | <a href="https://bioconductor.org/packages/release/bioc/html/DESeq2.html">https://bioconductor.org/packages/release/bioc/html/DESeq2.html</a>                   |
| t-SNE                            | van der Maaten and Hinton, 2008 | <a href="https://lvdmaaten.github.io/tsne/">https://lvdmaaten.github.io/tsne/</a>   |
| UCSC tools                       | UCSC                            | <a href="https://genome.ucsc.edu/#!/html">https://genome.ucsc.edu/#!/html</a>   |
| Integrative Genomic Viewer       | Thorvaldsdóttir et al., 2013    | <a href="http://software.broadinstitute.org/software/igv/">http://software.broadinstitute.org/software/igv/</a>   |
| bwa v0.7.10-r789                 | Jo and Koh, 2015                | <a href="http://bio-bwa.sourceforge.net/">http://bio-bwa.sourceforge.net/</a>   |
| <b>Other</b>                     |                                 |   |
| Homo sapiens genome build GRCh37 | Illumina iGenomes               | <a href="https://support.illumina.com/sequencing/sequencing_software/igenome.html">https://support.illumina.com/sequencing/sequencing_software/igenome.html</a> |
| Repbase                          | Bao et al., 2015                | <a href="http://www.girinst.org/repbase">http://www.girinst.org/repbase</a>   |

| REAGENT or RESOURCE                           | SOURCE                               | IDENTIFIER   |
|---|--------------------------------------|--|
| <b>Continued</b>                              |                                      |  |
| <b>Deposited Data</b>                         |                                      |  |
| Raw mouse data                                | Puthanla et al., 2017                | GEO: GSE96160  |
| Raw human data                                | This paper                           | GEO: GSE128745   |
| Raw human data                                | This paper                           | EGA: EGA000001003572   |
| <b>Experimental Models: Cell Lines</b>        |                                      |  |
| BT245   | Keith Ligon                          | N/A  |
| SJ-DIPG-XIII                                  | Michelle Morje                       | N/A  |
| SJ-DIPG-VI                                    | Michelle Morje                       | N/A  |
| HSJ-019                                       | This paper                           | N/A  |
| HSJ_ID_DIPG_007                               | Angel Carcaboso                      | N/A  |
| G477  | Peter Dirks                          | N/A  |
| SJ-pcGBM2                                     | Michelle Morje                       | N/A  |
| HSJID-GBM001                                  | Angel Carcaboso                      | N/A  |
| SJ-G2   | COG Cell Line & Xenograft repository | <a href="http://www.cocells.org/d/BrainTumorDataSheets/SJ-GBM2_Cell_Line_Data_Sheet_COGcell.org.pdf">www.cocells.org/d/BrainTumorDataSheets/SJ-GBM2_Cell_Line_Data_Sheet_COGcell.org.pdf</a> |
| BT416   | Keith Ligon                          | N/A  |
| U-251   | Sigma-Aldrich                        | Cat # 09063001   |
| BT35  | This paper                           | N/A  |
| 1834  | This paper                           | N/A  |
| 1953  | This paper                           | N/A  |
| 3752  | This paper                           | N/A  |
| 4121  | This paper                           | N/A  |
| 670   | This paper                           | N/A  |
| JN14  | This paper                           | N/A  |
| Immortalized human astrocytes                 | Soroda et al., 2001                  | <a href="http://www.ncbi.nlm.nih.gov/pubmed/11431323">http://www.ncbi.nlm.nih.gov/pubmed/11431323</a>  |
| <b>Experimental Models: Organisms/Strains</b> |                                      |  |
| Mouse: NSG                                    | Jackson Laboratory                   | Stock No. 005557   |
| <b>Oligonucleotides</b>                       |                                      |  |
| Primers                                       | See Table S8                         | N/A  |
| <b>Recombinant DNA</b>                        |                                      |  |
| hESC-Cas9/BB-2A-GFP (pX458)                   | Feng Zhang                           | Addgene plasmid # 48138  |
| <b>Software and Algorithms</b>                |                                      |  |
| Bowtie2 v2.1.0                                | Langmead and Salzberg, 2012          | <a href="http://bowtie-bio.sourceforge.net/bowtie2/">http://bowtie-bio.sourceforge.net/bowtie2/</a>  |
| PICARD tools                                  | Li et al., 2009                      | <a href="https://broadinstitute.github.io/picard/">https://broadinstitute.github.io/picard/</a>  |
| MACS 1.4                                      | Zhang et al., 2008                   | <a href="https://github.com/taoliu/MACS/wiki">https://github.com/taoliu/MACS/wiki</a>  |
| ADMER v3.12                                   | Hainz et al., 2010                   | <a href="http://home.ucsd.edu/home/mhainz/">http://home.ucsd.edu/home/mhainz/</a>  |
| DeepTools                                     | Ramirez et al., 2014                 | <a href="https://deeptools.readthedocs.io/en/develop/">https://deeptools.readthedocs.io/en/develop/</a>  |
| trim-galore                                   | N/A                                  | <a href="https://www.bioinformatics.babraham.ac.uk/projects/trim_galore/">https://www.bioinformatics.babraham.ac.uk/projects/trim_galore/</a>  |
| MACS2   | Zhang et al., 2008                   | <a href="https://github.com/taoliu/MACS/wiki">https://github.com/taoliu/MACS/wiki</a>  |
| Genome Structure Correction                   | Bickel et al., 2010                  | <a href="https://www.encodeproject.org/software/gsc/">https://www.encodeproject.org/software/gsc/</a>  |
| DiffBind                                      | N/A                                  | <a href="https://bioconductor.org/packages/release/bioc/html/DiffBind.html">https://bioconductor.org/packages/release/bioc/html/DiffBind.html</a>  |
| Samtools v0.1.19                              | Li et al., 2009                      | <a href="https://github.com/samtools/samtools">https://github.com/samtools/samtools</a>  |
| Trimomatic v0.32                              | Bolger et al., 2014                  | <a href="https://www.samtools.com/samtools">https://www.samtools.com/samtools</a>  |
| FASTQC v0.11.2                                | N/A                                  | <a href="http://www.bioinformatics.babraham.ac.uk/projects/fastqc/">http://www.bioinformatics.babraham.ac.uk/projects/fastqc/</a>  |
| BEDtools v2.17.0                              | Quinlan and Hall, 2010               | <a href="http://bedtools.readthedocs.io/en/latest/">http://bedtools.readthedocs.io/en/latest/</a>  |

(Continued on next page)

## CONTACT FOR REAGENT AND RESOURCE SHARING

Further information and requests for resources and reagents should be directed to and will be fulfilled by the Lead Contact Nada Jabado (nada.jabado@mcgill.ca).

## EXPERIMENTAL MODELS AND SUBJECT DETAILS

**Sample Isolation and Processing.** The derivation of tumor cell lines was approved by and procedures conform to the standards of the Institutional Review Boards of McGill University, the University of Toronto, Stanford University, the Dana-Farber Cancer Center and the Hospital San Juan de Deu. Informed consent was obtained from all cases.

**Cell Lines.** Tumor-derived cell lines were maintained in Neurocult NS-A proliferation media (StemCell Technologies) supplemented with bFGF (10 ng/mL) (StemCell Technologies), rhEGF (20 ng/mL) (StemCell Technologies) and heparin (0.0002%) (StemCell Technologies) on plates coated in poly-L-ornithine (0.01%) (Sigma) and laminin (0.01 mg/mL) (Sigma) in an incubator at 37 degrees Celsius and 5% carbon dioxide. All lines tested negative for mycoplasma contamination, checked monthly using the MycoAlert Mycoplasma Detection Kit (Lonza). Tumor-derived cell lines were confirmed to match original tumors by STR fingerprinting, where tumors were available. The sex of all cell lines are reported in Table S1.

**Animals Used in PDOX Studies.** All *in vivo* procedures in mice were approved by and conform to the standards of the Research Animal Care and user committee at McGill University, the Canadian Council of Animal Care, the Animal Welfare and Ethical Review body and institutional and UK Home Office guidelines (Project license 70/8240, 70/7428 and 80/2325). Housing, breeding and procedures performed were in keeping with the US National Institute of Health guide for the care and use of laboratory animals. Both genders were equally used in all experiments. PDOX of two patient-derived H3.3K27M mutant cell lines, DIPGXIII, BT245, and a wild-type high-grade glioma cell line, pcGBM2, were generated as previously described (Grasso et al., 2015). All mice used were NOD SCID-IL2R gamma-chain deficient mice (NSG, Jackson Laboratory) aged 4-6 weeks.

## **METHOD DETAILS**

**Identification and Quantification of Histone Modifications with nLC-MS.** The complete workflow for histone extraction, LC/MS, and data analysis was recently described in detail (Sidoli et al., 2016). Briefly, cell pellets (approx.  $1 \times 10^6$  cells) were lysed on ice in nuclear isolation buffer supplemented with 0.3% NP-40 alternative. Isolated nuclei were incubated with 0.4 N H<sub>2</sub>SO<sub>4</sub> for 3 hr at 4 degrees C with agitation. 100% trichloroacetic acid (w/v) was added to the acid extract to a final concentration of 20% and samples were incubated on ice overnight to precipitate histones. The resulting histone pellets were rinsed with ice cold acetone + 0.1% HCl and then with ice cold acetone before resuspension in water and protein estimation by Bradford assay. Approximately 20 mg of histone extract was then resuspended in 100 mM ammonium bicarbonate and derivatized with propionic anhydride. 1 mg of trypsin was added, and samples were incubated overnight at 37

degrees C. After tryptic digestion, a cocktail of isotopically-labeled synthetic histone peptides was spiked in at a final concentration of 250 fmol/mg and propionic anhydride derivatization was performed a second time. The resulting histone peptides were desalted using C18 Stage Tips, dried using a centrifugal evaporator, and reconstituted using 0.1% formic acid in preparation for nanoLC-MS analysis. nanoLC was performed using a Thermo Scientific™ Easy nLC™ 1000 equipped with a 75 mm x 20 cm in-house packed column using Repronil-Pur C18-AQ (3 mm; Dr. Maisch GmbH, Germany). Buffer A was 0.1% trifluoroacetic acid and Buffer B was 0.1% trifluoroacetic acid in 80% acetonitrile. Peptides were resolved using a two-step linear gradient from 5% to 33% B over 45 min, then from 33% B to 90% B over 10 min at a flow rate of 300 nL/min. The HPLC was coupled online to an Orbitrap Elite mass spectrometer operating in the positive mode using a Nanospray Flex Ion Source (Thermo Scientific) at 2.3 kV. Two full MS scans ( $m/z$  300-1100) were acquired in the orbitrap mass analyzer with a resolution of 120,000 (at 200  $m/z$ ) every 8 DIA MS/MS events using isolation windows of 50  $m/z$  each (e.g. 300-350, 350-400.650-700). MS/MS spectra were acquired in the ion trap operating in normal mode. Fragmentation was performed using collision-induced dissociation (CID) in the ion trap mass analyzer with a normalized collision energy of 35. AGC target and maximum injection time were  $10e6$  and 50 ms for the full MS scan, and  $10e4$  and 150 ms for the MS/MS scan, respectively. Raw files were analyzed using EpiProfile 2.0.

**CRISPR/Cas9 Genome Editing.** pSpCas9(BB)-2A-GFP (PX458v2) was a gift from Feng Zhang (Addgene plasmid # 48138). CRISPR-Cas9 editing was carried out as described in Ran et al (Ran et al., 2013). Constructs were transfected with lipofectamine 2000 (Thermo Fischer Scientific) according to the manufacturer's protocol. Flow cytometry sorted single GFP<sup>+</sup> cells in 96 well plates, 72 hr post-transfection. Clones were expanded, and the target locus sequenced by Sanger sequencing. Select clones were screened by Illumina MiSeq system for the target exon to confirm complete mutation of the K27M allele. Mass spectrometry confirmed the absence of K27M mutant peptide in these clones (Figures 3C and S2D). The guide RNA sequence and the tracks of MiSeq data demonstrating editing of the K27M allele are shown in Figures S2A and S2B.

**Cell Viability Assay.** Cells were plated at a density of 5000 cells per well in 96 well plate, and 24 hr following plating were treated with agents for a 7-day period, with media replaced every 4 days. All agents were dissolved in DMSO (Sigma-Aldrich) which was the vehicle serving as control to

normalize cell indices. We used agents CBP-30, JQ-1, Panobinostat from the Structural Genomics Consortium (Toronto) and 5-aza-cytidine (Sigma-Aldrich). Cell index was measured using Alamar Blue Cell Viability Reagent (ThermoFisher Scientific) according to manufacturer's protocol. Absorbance at 570 nm and 600 nm was determined using i-Control microplate reader software by Tecan. Normalized cell index was calculated by (raw cell index – blank media reading) / (vehicle control index). Cell index response curves were plotted using Graphpad Prism using nonlinear regression of variable slope (four parameters) using least squares (ordinary) fitting method. Differential agent sensitivity was determined by comparing LogIC50 values between cell lines, using the Extra sum-of-squares F test of this parameter. The p value of this comparison is stated in plots. Graphs of IC50 values carry error bars of 95% confidence intervals for pairwise comparisons. Plots of normalized cell index portray mean and SEM of three experimental replicates for each cell line.

**MAVS Knockdown.** MAVS Human shRNA lentiviral particles (TL307181V) were purchased from OriGene. A pool of four shRNAs targeting MAVS were transduced into cell lines at a concentration of 2 TU/cell, alongside a scramble control shRNA particle (sh-NT). Transduced cells were selected with 2 mg/mL puromycin 48 hr post-transduction and puromycin selection was maintained for the duration of the experiment. Loss of MAVS protein was confirmed by western blot at the time of assay for 5-azacytidine sensitivity (Figure S7E).

**Droplet Digital PCR.** RNA was extracted from cells using the Aurum Total RNA Mini Kit (Bio-Rad) and concentration was quantified on the BioDrop uLite (Montreal Biotech). cDNA was generated using iScript Reverse Transcription Supermix (Bio-Rad). Target concentration was determined using the QX200 ddPCR EvaGreen Supermix assay (Bio-Rad) using 20 uL per reaction containing 10 ng of cDNA, using manufacturer's protocol cycling conditions with a 58 degrees annealing temperature and 40 cycles. Droplets were assayed using the QX200 Droplet Reader (Bio-Rad) and manually scored for positive signal using QuantaSoft Software (Bio-Rad). The concentration of positive droplets per target was normalized to the concentration of GAPDH. The relative target abundance is shown as the average of three biological replicates (distinct passages of each cell line) determined by a single technical replicate. Primer sequences are found in Table S8.

**Western Blotting.** Cells were lysed using RIPA buffer with added protease inhibitors (Roche) for non-histone proteins. Histone lysates were extracted using the Histone Extraction Kit (Abcam). Lysate protein concentration was determined with the Bradford assay reagent (Bio-Rad). Ten micrograms of non-histone protein, or 3 micrograms of histone, was separated on NuPAGE Bis-Tris 10% gels (ThermoFischer Scientific) and wet-transferred to a PVDF membrane (GE Healthcare). Membrane blocking was performed with 5% skim milk in tris buffered saline (50 mM Tris, 150 mM NaCl, 0.1% Tween 20, pH 7.4) (TBST) for 1 hr. Membranes were incubated overnight with primary antibody solutions in 1% skim milk in TBST. Membranes were washed 3 times in TBST, and the ECL anti-rabbit IgG Horseradish Peroxidase linked whole antibody (GE Healthcare) was applied for 1 hr, at 1:1000 dilution in 1% skim milk in TBST. Membranes were washed 3 times and the signal was resolved with Amersham ECL Prime Western Blotting Detection Reagent (GE Healthcare) and imaged on a ChemiDoc MP Imaging System (Bio-Rad).

**Chromatin Immunoprecipitation and Sequencing.** Cells were fixed with 1% formaldehyde (Sigma). Fixed cell preparations were washed, pelleted and stored at -80C. Sonication of lysed nuclei (lysed in a buffer containing 1% SDS) was performed on a BioRuptor UCD-300 for 60 cycles, 10 s on 20 s off, centrifuged every 15 cycles, chilled by 4 degrees C water cooler. Samples were checked for sonication efficiency using the criteria of 150-500 bp by gel electrophoresis. After the sonication, the chromatin was diluted to reduce SDS level to 0.1% and before ChIP reaction 5% of sonicated drosophila S2 cell chromatin was spiked-in the samples for quantification of total levels of histone mark after the sequencing (see below). ChIP reaction for histone modifications was performed on a Diagenode SX-8G IP-Star Compact using Diagenode automated Ideal ChIP-seq Kit. 25ul Protein A beads were washed and then incubated with 6 mg of H3K27ac antibody (Diagenode, C15410196), and 2 million cells of sonicated cell lysate combined with protease inhibitors for 10 hr, followed by 20 min wash cycle with provided wash buffers. Reverse cross linking took place on a heat block at 65 degrees C for 4 hr. ChIP samples were then treated with 2ul RNase Cocktail (Life Technologies) at 65 degrees C for 30 min followed by 2 ml Proteinase K (Thermo Fisher Scientific) at 65 degrees C for 30 min. Samples were then purified with QIAGEN MiniElute PCR purification kit as per manufacturers' protocol. In parallel, input samples (chromatin from about 50,000 cells) were reverse crosslinked and DNA was isolated following the same protocol.

Library preparation was carried out using Kapa HTP Illumina library preparation reagents. Briefly, 25 ml of ChIP sample was incubated with 45 ml end repair mix at 20 degrees C for 30 min followed by Ampure XP bead purification. A tailing: bead bound sample was incubated with 50ul buffer enzyme mix for 30 degrees C 30 min, followed by PEG/NaCl purification. Adaptor ligation: bead bound sample was incubated with 45 ml buffer enzyme mix and 5 ml of different TruSeq DNA adapters (Illumina) for each sample, for 20 degrees C 15 min, followed by PEG/NaCl purification (twice). Library enrichment: 12 cycles of PCR amplification. Size selection was performed after PCR using a 0.6x/0.8x ratio of Ampure XP beads (double size selection) set to collect 250-450bp fragments. ChIP libraries were sequenced using Illumina HiSeq 2000, 2500 or 4000 at 50 bp SE reads, and NovaSeq 6000 at 50 bp PE reads.

**RNA-seq Library Preparation and Sequencing.** Total RNA was extracted from cell pellets using the RNeasy mini kit (Qiagen) according to instructions from the manufacturer. Library preparation was performed with ribosomal RNA (rRNA) depletion according to instructions from the manufacturer (Epicentre) to achieve greater coverage of mRNA and other long non-coding transcripts. Paired-end sequencing was performed on the Illumina HiSeq 2000, 2500 and 4000 platforms.

**ATAC-seq Library Preparation and Sequencing.** Adherent cell cultures were dissociated and 100 000 cells were washed twice in cold PBS at 4 degrees C. Cells were resuspended in 100 mL Hypotonic Cell Lysis Buffer (0.1% Sodium Citrate Tribasic Dihydrate, 0.1% Triton X-100) and titrated until cells were dissolved. Samples were incubated on ice 30 minutes, centrifuged at 2000 g for 5 min at 4 degrees C, and pellet resuspended in 100 mL Normal Cell Lysis Buffer (10 mM Tris-HCl, pH 7.4, 10 mM NaCl, 3 mM MgCl<sub>2</sub>, 0.1% IGEPAL CA-630), titrated, incubated on ice 30 min, centrifuged at 2000 g for 5 min at 4 degrees C, and supernatant removed. The transposase reaction was carried out by titrating in 25 mL per sample in TD Buffer (10 mM Tris-HCl, pH 8.00, 5 mM Magnesium Chloride) with 5 mL Transposase (Illumina Nextera Kit), and incubated at 37 degrees C for 30 min, and 8.5 uL of 100 mM EDTA was added, samples transferred to ice, and DNA recovered using MinElute PCR Purification columns (Qiagen). Libraries were generated by PCR in 50 mL reaction (25 mL sample, 10 mL 5x Phusion HF buffer, 0.5 mL Phusion Polymerase, 1 mL 10 mM dNTPs, 0.5 mL of each custom Illumina primers at 12.5 mM). The PCR reaction followed 98 degrees C for 30 s, followed by 12 cycles of 98 degrees C for 10 s, 63 degrees

C for 30 s, 72 degrees C for 1 min, followed by 72C for 5 min. DNA was recovered using GeneRead Purification columns (Qiagen). The libraries were sequenced to 50 million reads per sample on Illumina HiSeq 2500 using Nextera Sequencing Primers.

**PDOX Generation and Treatment.** In single cell suspension, 100,000 cells were stereotactically injected in the fourth ventricle/pons of. Tumor cells were allowed to engraft for 7 days. Mice were then randomly assigned to a control group where only the vehicle control was administered using intra-peritoneal (i.p) injections, or to one of the three therapeutic groups: 5-azacytidine (Sigma Aldrich, MO; 3 mg/kg diluted in sterile water) daily i.p. injections for five days followed by a two-day rest period every 4 weeks as previously described (Borodovsky et al., 2013; Yamashita et al., 2018); panobinostat (Selleck Chemicals, 10 mg/kg diluted in DMSO) five days a week alternating with 5 days rest for 4 weeks as previously described (Grasso et al., 2015); or a combination of both drugs. For each of the three cell lines used to generate PDOX in mice, nine animals were used for each experimental condition. Mice were then observed until they became moribund, at which point they were sacrificed, and the presence of intracranial tumors was confirmed.

**Quantitative PCR for Interferon Signature Genes.** Quantitative PCR (qPCR) was performed to assess for ISGs induction in tumors removed following euthanasia of terminally morbid animals. Total RNA was extracted from tumors derived from H3.3K27M BT245 and DIPG-XIII or pcGBM2 using the miRNeasy mini kit (Qiagen) according to manufacturer's instructions with purity and integrity assessed utilizing Nanodrop (Thermo-Fisher) and Experion Biorad) methodologies. 100 ng of RNA was used for reverse-transcription using the iScript RT Supermix (BioRad) following manufacturer's instructions. Real-time PCR for *OAS1*, *STAT1*, *IL15*, *IRF7* and *SCOS1* was performed on cDNA extracted from 4 biological replicates for each experimental condition (vehicle, 5-azacytidine, panobinostat, combination) using primers described in (Roulois et al., 2015). Samples were run on a Lightcycler 96 (Roche) with the SsoFast Evagreen SuperMix kit (BioRad). Cycling conditions were: 95 degrees C for 30 sec followed by 40 cycles 95 degrees C for 5sec/60 degrees C for 20 sec. Fold change values were calculated utilizing the  $2^{\Delta\Delta Ct}$  method with *ACTB* expression and vehicle treated cells used as the calibrator, comparing each treatment group to the vehicle control group.

## QUANTIFICATION AND STATISTICAL ANALYSIS

The description of statistical details for each experiment can be found in figure legends. Significance was assigned by tests deriving a p value less than 0.05. The largest sample size of tumors and cell lines that were capable of collection were used and no available data was excluded. For functional experiments, two independent cell lines were modeled by CRISPR-Cas9 editing of H3K27M KO, and two independent clones per line were profiled, and followed the same trend in all analyses.

### Analysis of ChIP-seq Data

**Data Processing, Peak Calling and Annotations.** Sequence reads were aligned to the human genome (HG19) using Bowtie2 (v2.1.0) (Langmead and Salzberg, 2012) under default settings. PCR duplicates were removed using PICARD tools generating BAM files (Li et al., 2009). Read processing and alignment for analysis of repeat elements was performed separately (see below for details). Significant peaks were identified using Model Based Analysis for ChIP-seq (MACS 1.4) (Zhang et al., 2008) with a p value cutoff of  $1e^{-9}$ . Peaks were annotated using HOMER (v3.12) (Heinz et al., 2010) with promoter regions classified as any peak within +/- 2.5 kb of a transcriptional start site (TSS), and enhancer region greater than 2.5 kb from a TSS. Peaks were also annotated using ChIP-atlas annotating distal enhancers to genes based upon public CHIA-PET datasets. Super enhancers were identified using the ROSE algorithm with exclusion of peaks within +/- 2.5 kb of a TSS and a stitch distance of 12.5 kb. For visualization of H3K27 acetylation profiles, BAM alignment files were normalized to RPKM values using DeepTools (Ramirez et al., 2014) and visualized in Integrated Genome Viewer (v2.3.40).

**Clustering and Visualization of Samples Based on H3K27ac.** For unsupervised clustering of H3K27ac patterns, a matrix of the normalized H3K27ac density was generated in DiffBind based upon the consensus H3K27ac peaks identified in at least 3 samples. The top 10,000 most variable loci (defined by the variation in H3K27ac signal across all samples used for clustering using Median Absolute Deviation as a distance metric) were selected as features. Unsupervised hierarchical clustering using spearman correlation of samples was then performed on these 10,000 most variant peaks, using Spearman correlation as a distance metric. *t*-stochastic neighbor

embedding (*t*-SNE) (van der Maaten and Hinton, 2008) was also used on consensus H3K27ac peaks to visualize samples based on H3K27ac.

**Differential H3K27ac Enrichment Analysis.** Utilizing the read-depth normalized matrix of H3K27ac signal for all consensus H3K27ac peaks, differential H3K27ac loci between H3K27WT and H3K27M tumors was determined using DiffBind, employing the DESeq2 method. Significant regions were further filtered to events with an FDR < 0.05. The same approach was used to detect differential super enhancer loci between H3K27WT and H3K27M samples.

**Quantitative ChIP-Rx, Sequencing, and Analysis.** The spiked-in drosophila chromatin was used for quantification of histone mark, as described previously (Orlando et al., 2014). After sequencing, the reads were aligned to human (hg19) and drosophila (dm3) genomes, then the number of reads mapping to each genome (from H3K27ac and input samples) were used to compute the relative levels of histone mark using the following formula for each sample:

$$Rx = \frac{ip_{hg}}{ip_{dm}} \bigg/ \frac{input_{hg}}{input_{dm}}$$

where  $ip_{hg}$  is the number of reads in the target sample mapping to the human genome;  $ip_{dm}$ , to the drosophila genome;  $input_{hg}$ , the number of reads in the input sample mapping to the human genome; and  $input_{dm}$ , to the drosophila genome.

**Regulatory Networks for All SE Associated Transcription Factors.** We used core regulatory circuitry (CRC) analysis with default parameters to quantify the interaction network of transcription factor (TF) regulation at super enhancers. Briefly, for all promoters within 100 kb, the most acetylated promoter was assigned as the target of the SE (excluding promoters that overlap SEs, which are automatically assigned the target. If there were no active promoters within 100kb, the SE was assigned to the nearest active promoter. All SE-associated promoters annotated to regulate a TF were considered as the node-list for network construction. For any given TF (TF<sub>i</sub>) The IN degree was defined as the number of TFs with an enriched binding motif at the proximal SE or promoter of TF<sub>i</sub>. The OUT degree was defined as the number of TF associated SEs containing an enriched binding site for TF<sub>i</sub>. Within any given SE, enriched TF binding sites were determined at putative nucleosome free regions (valleys) flanked by high levels of H3K27ac. Valleys were calculated using an algorithm adapted from Ramsey et al., 2010 (Ramsey et al.,

2010). In these regions, we searched for enriched TF binding sites using the FIMO59 algorithm with TF position weight matrices defined in the TRANSFAC database (Matys et al., 2006). An FDR cutoff of 0.01 was used to identify enriched TF binding sites. Group specific core TFs were defined as TFs identified within CRCs present in at least one sample, and statistically assessed between groups using a Wilcoxon Rank Sum test.

### **Analysis of RNA-seq Data**

**Data Processing.** Adaptor sequences and the first four nucleotides of each read were removed from the read sets using Trimmomatic (Bolger et al., 2014) (v0.32). Reads were scanned from start to end and truncated if and when the average quality of a 4-nucleotide sliding window fell too low ( $\text{phred33} < 30$ ). Short reads (<30 bp) were subsequently discarded. Multiple quality control metrics were obtained using FASTQC (v0.11.2), samtools (Li et al., 2009) (v0.1.19), BEDtools (Quinlan and Hall, 2010) (v2.17.0) and custom scripts.

**Gene Expression Analysis.** The remaining clean set of reads were then aligned to the reference genome build hg19 (GRCh37) with STAR (Dobin et al., 2013) (v2.3.0e) using the default parameters. Only primary alignments of reads mapping to 9 or fewer locations in the genome were retained. Analysis of the repeat genome was performed separately (see below for details). Gene expression levels were estimated by quantifying primary alignments of reads mapping to 2 or fewer locations in the genome (MAPQR3) falling into exonic regions defined by the ensGene annotation set from Ensembl (GRCh37;  $N=60234$  genes) using featureCounts (Liao et al., 2014) (v1.4.4). Normalization (mean-of-ratios), variance-stabilized transformations of the data, as well as differential expression analysis, were performed using DESeq2 (Love et al., 2014). Unless otherwise stated, all reported p values have been adjusted for multiple testing using the Benjamini-Hochberg procedure.

**Clustering and Visualization.** Global changes in expression levels were evaluated by hierarchical clustering of samples and principal component analysis (PCA) using normalized expression data coupled with variance-stabilized transformation. For hierarchical clustering, Euclidean distance was used as the distance metric, and complete linkage as the agglomeration method. For visualization, normalized Bigwig tracks were generated using BEDtools (Quinlan and Hall, 2010)

and UCSC tools. Integrative Genomic Viewer (Thorvaldsdottir et al., 2013) was used for data visualization.

### **Analysis of ATAC-Seq Data**

The ATAC-seq libraries were sequenced with 125 bp paired-end reads and trimmed for Nextera sequencing adaptors using trimgalore with default settings. The trimmed reads were then mapped to hg19. Reads were filtered to remove duplicates, unmapped or poor quality (phred33<30) reads, mitochondrial reads, and those overlapping the ENCODE blacklist (Carroll et al., 2014). Following alignment, accessible chromatin regions/peaks were called using MACS2. Default parameters were used, except for the following: `-keep-dup all -B -nomodel -SPMR -q 0.05 -slocal 6250 -llocal 6250`. The signal intensity was calculated as the fold enrichment of the signal per million reads in a sample over a modelled local background using the `bdgcmp` function in MACS2 (Zhang et al., 2008). Custom scripts along with the bedtools suite were used to identify chromatin accessibility peaks unique to specific groups of samples and to identify overlaps with H3K27ac peaks. ENCODE's Genome Structure Correction tool (Bickel et al., 2010) was used to calculate the significance of the change in agreement between the H3K27ac and ATAC-seq signal.

### **Analysis of Repeat Elements**

**Repeat Element H3K27ac Analysis.** Quantifying reads in repetitive regions of the genome is challenging due to the mapping uncertainty induced by sequence similarity and the high number of occurrences in the genome. To obtain a robust quantification, we used several conservative and complementary strategies, by including or excluding multimapping reads, and using either the repeat genome or the complete human genome as reference. Only results consistent across approaches are reported. First, we started with the more conservative approach, as previously described (Goke et al., 2015), where ChIP-rx of H3K27ac experiments were aligned to the human genome (hg19) using Bowtie2 (v2.1.0) (Langmead and Salzberg, 2012). We counted the number of reads over each of the repetitive elements annotated in RepeatMasker using HOMER (v3.12), considering each occurrence of a repetitive elements in the genome to be a distinct entity. In the process, we discarded duplicate reads as well as multimapping reads, and retained only primary alignments with the highest alignment scores. This approach underestimates the true signal since

only uniquely mapped reads are considered. Finally, ChIP-Rx spike-in scaling factors were used to scale read counts. Repetitive elements were subsequently grouped into families (i.e. SINE, LINE, LTR, DNA) using annotations provided by RepeatMasker (Smit et al., 2013-2015). In a second approach, reads were processed as described for RNAseq, and then aligned using the human repeat genome as reference, as previously described (Solovyov et al., 2018). Repbase reference genome was used (Bao et al., 2015) (v23.03) (<http://www.girinst.org/rebase>). Since Repbase largely consists of family consensus sequences, reads are assigned to these sequences regardless of where and how many times they are present in the genome, mitigating mapping uncertainty. We combined humrep.ref and humsub.ref into a single reference of repeat sequences for the human genome, covering a total of 1132 consensus elements, and counted the number of reads mapping into each of these elements using featureCounts (MAPQR3). Differential enrichment of H3K27ac at the consensus sequences were then calculated using DESeq2 (Love et al., 2014). The inverse of ChIP-Rx spike-in scaling factors (i.e. 1/rx) were supplied to DESeq2 as normalization factors (i.e. size factors). We repeated the two approaches with and without discarding multimapping reads for quantification of repeats. Only results robust to inclusion/exclusion or multimapping reads are reported in this work. Results obtained with uniquely mapped reads (i.e. the most conservative approach) are reported in figures and tables.

**Repeat Element Expression Analysis.** The clean set of rRNA-depleted RNA-seq reads were aligned to the human repeat genome (Repbase) using STAR. Normalization (library size) factors derived from canonical genes (Ensembl ensGene annotation) using mean-of-ratios (as described for regular RNA-seq gene expression analysis) were used to normalize the expression of repeat elements. To ensure that the results were robust with respect to the treatment of multimapping reads, we repeated the analysis considering (a) only uniquely mapped reads (MAPQ=255), (b) primary alignments of reads mapping to 2 or fewer locations in the genome (MAPQR3), and (c) primary and secondary alignments of reads mapping up to 1000 locations in the repeat genome (MAPQR0; STAR with "--outFilterMultimapNmax=1000"). Next, we confirmed the findings using a second aligner, BWA (v.7.15), considering only MAPQR3 mapped reads. While all four approaches produced the same results, we report the findings obtained with STAR using approach for the sake of brevity.

**Repeat Element Expression Analysis in K27M Mouse Model.** The rRNA-depleted RNA-seq data was taken from (Pathania et al., 2017) and processed using the same approach as for the human samples. The reference repeat sequences rodrep.ref and rodsub.ref were downloaded from Repbase (Bao et al., 2015) (v23.03) (<http://www.girinst.org/rebase>) and combined into a single reference for the murine repeat genome. We calculated the proportion of reads mapping to the repeat genome using the following formula: # of reads mapped to the repeat genome / # of clean reads.

### **Statistical Analysis of PDOX Studies**

Sample size calculations to detect a 50% difference in tumor growth between two groups with an alpha of 0.05 and power 0.8 indicated a minimum group size of three animals. A log-rank (Mantel-Cox) test was used to compare survival between each pair of treatment groups. A two-way ANOVA was used to compare fold change in expression of ISGs in tumors by qPCR, comparing fold change in pcGBM2 (WT line) to both BT245 and DIPG-XIII (K27M lines).

### **DATA AND SOFTWARE AVAILABILITY**

The accession number for the raw human data are Gene Expression Omnibus (GEO): GSE128745 and European Genome-Phenome Archive (EGA): EGAS00001003572.

## **Supplemental Information**

Supplemental Information and Tables S1-S8 can be found online at <https://doi.org/10.1016/j.ccell.2019.04.004>. I have not reproduced supplemental tables due to space restrictions.



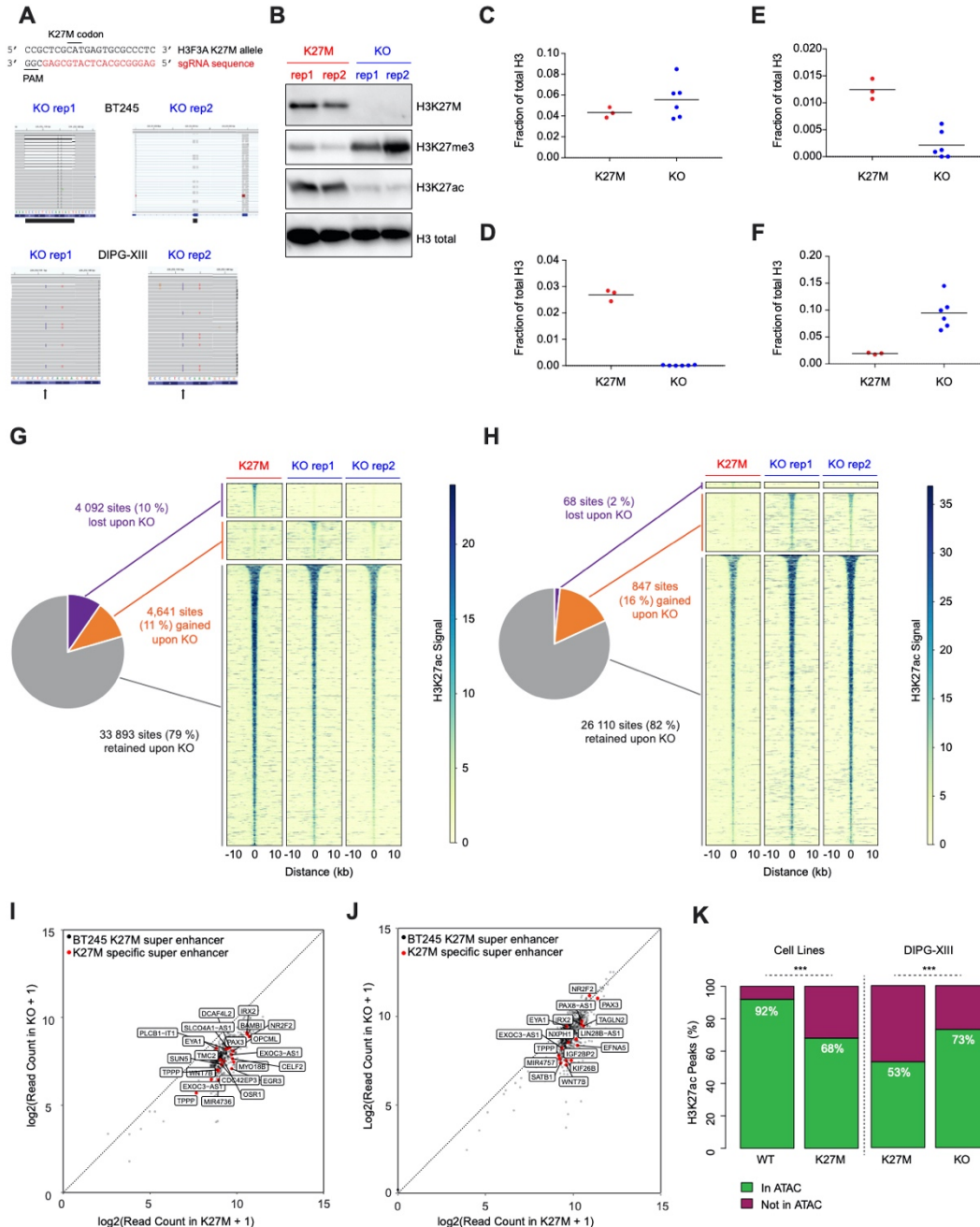


**Figure S2.** Related to Figure 3.

(A) The sequence of the gRNA used to target the K27M mutant allele of *H3F3A* is shown (top). The tracks of MiSeq data at the target locus demonstrate the insertions and deletions present on the mutant allele, while WT reads are not affected (bottom).

(B-F) Western blot (B) and mass spectrometry (C-F) of H3WT (C), H3K27M (D), H3K27ac (E), and H3K27me3 (F) in BT245 and KO.

**(G-H)** Pie graphs and heatmaps illustrating number and proportion of gained, lost, and retained H3K27ac sites within DIPG-XIII **(G)** and BT245 **(H)** H3K27M driven models as compared to isogenic KO lines.

**(I-J)** Dot plot illustrating ChIP-Rx signal (Log<sub>2</sub>) at H3K27M models BT245 **(I)** and DIPG-XIII **(J)** and the minimal to no observable shift in H3K27ac density upon KO.

**(K)** ATAC-seq signal demonstrating loss of coherence with H3K27ac peaks between the K27M and WT

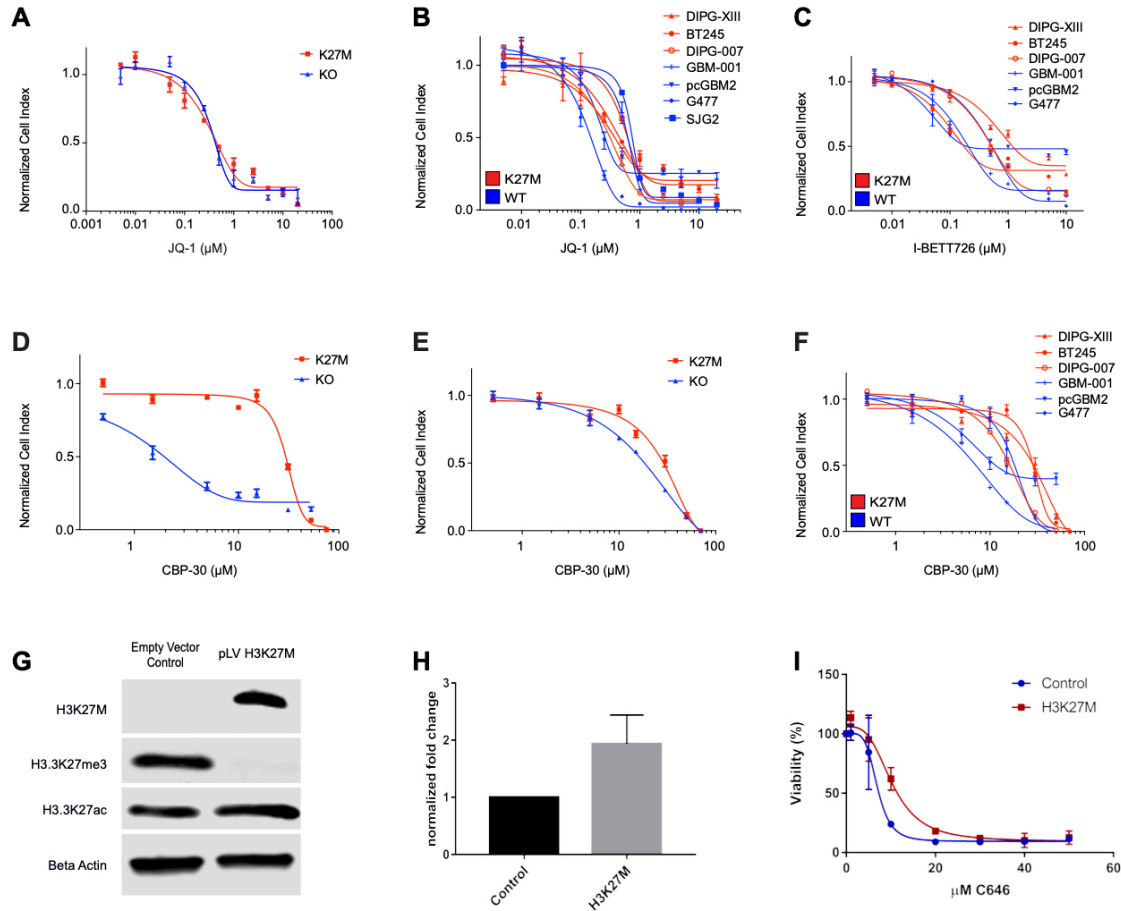


**Figure S3.** Related to Figure 3.

**(A)** Cell viability of BT245 and isogenic KO lines to bromodomain inhibition by JQ-1.

**(B-C)** Cell viability of pHGG lines in a 7-day growth assay under treatment with bromodomain inhibitors JQ-1 and I-BET762.

**(D-E)** Cell viability of BT245 **(D)** and DIPG-XIII **(E)** and corresponding KO control lines to CBP/EP300 inhibitor CBP-30.

**(F)** Viability of pHGG lines in a 7-day growth assay under treatment with the CBP/EP300 inhibitor CBP-30.

**(G)** Immunoblot of an immortalized human astrocyte cell line that over-express H3K27M or empty vector control, along with quantification of H3K27me3 and H3K27ac levels.

**(H)** Quantification of H3K27ac in NSC models that over-express H3K27M as compared to empty vector controls.

**(I)** Cell viability of astrocytes that over-express H3K27M following treatment with C646 as compared to empty vector controls

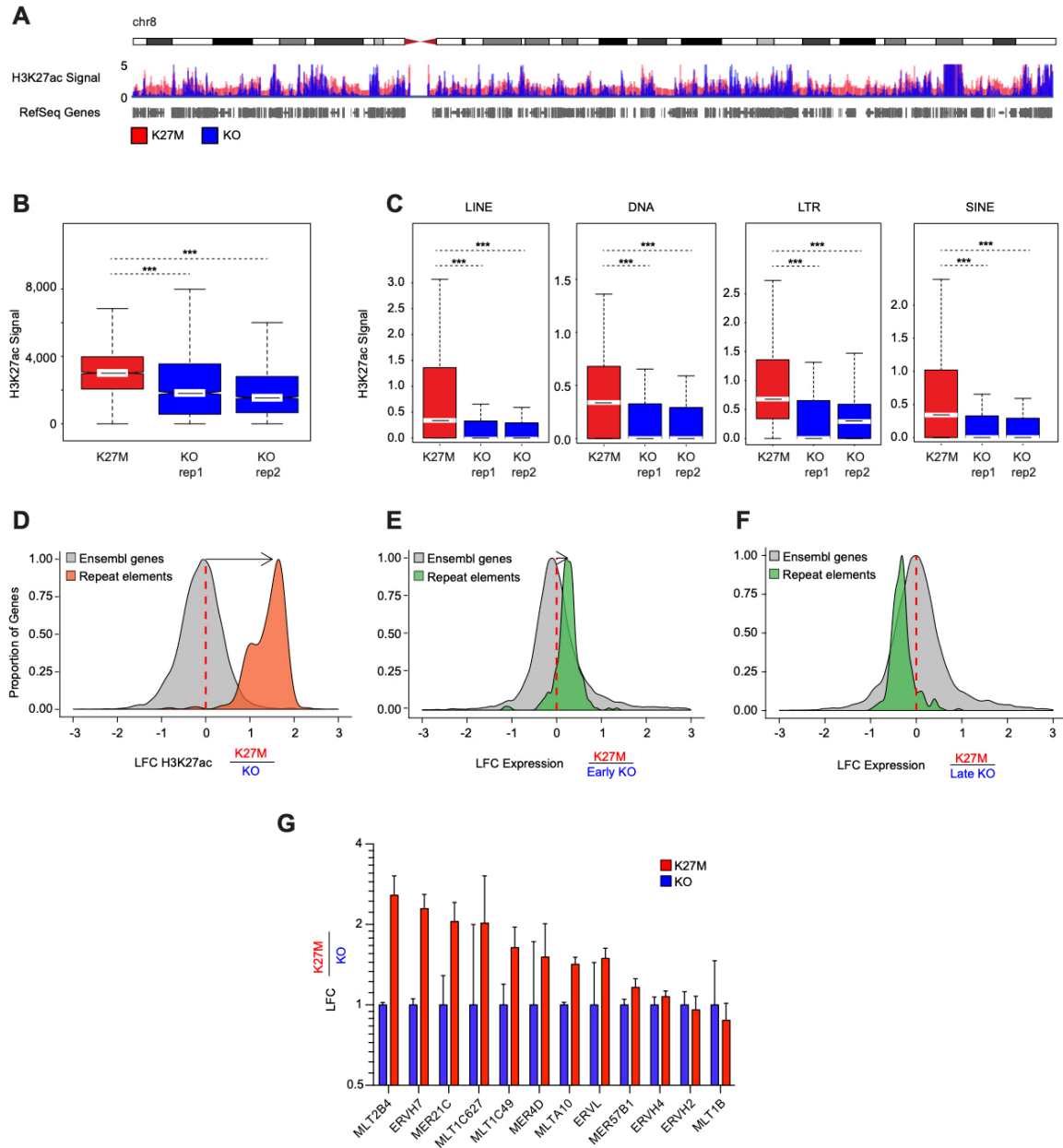


**Figure S4.** Related to Figure 4.

(A) Quantitative ChIP-Rx scaled reads between BT245 K27M (red) and KO (blue) cell cultures across chromosome 8.

(B) Enrichment of H3K27ac across the human genome in one megabase windows comparing BT245 versus KO clones using a Wilcoxon rank sum test.  $p < 0.001 = ***$ . The horizontal line inside the box corresponds to the median, the lines above and below the box delimit the interquartile range (IQR), and the end of the whiskers delimit values up to 1.5 times the IQR.

(C) Enrichment of H3K27ac across repetitive regions (LINE, DNA, LTR, SINE) of the human genome annotated by the RepeatMasker database comparing BT245 vs KO using a Wilcoxon rank sum test.

$p < 0.001 = ***$ .

**(D-F)** Changes in deposition of H3K27ac over repetitive elements in BT245 (n=2) relative to KO (n=1)

**(D)** and in expression of repetitive elements in BT245 (n=5) relative to early-passage KO lines that

represent the effect of K27M-KO (n=3) **(E)** and late-passage KO that may have lost the effect of

H3K27me3 restoration through passaging (n=2) **(F)**. Histograms showing the distributions of the log<sub>2</sub>

fold-change (LFC) of genomic features in K27M relative to KO. Orange: H3K27ac deposition over

repetitive elements (Repbase). Green: transcription of repetitive elements (Repbase). Grey: H3K27ac

(left) and transcription (middle and right) of Ensembl genes (GRCh37). Elements with sufficiently high

expression (baseMean > 100) and LFCs in [-3,3] range shown here.

**(G)** Measurement of expression of a panel of ERV families by droplet digital PCR (ddPCR) in H3K27M

lines compared to respective KO lines. Plots show mean +SEM of 3 experimental replicates, BT245 cell

line. Y-axis is in log<sub>2</sub> scale.

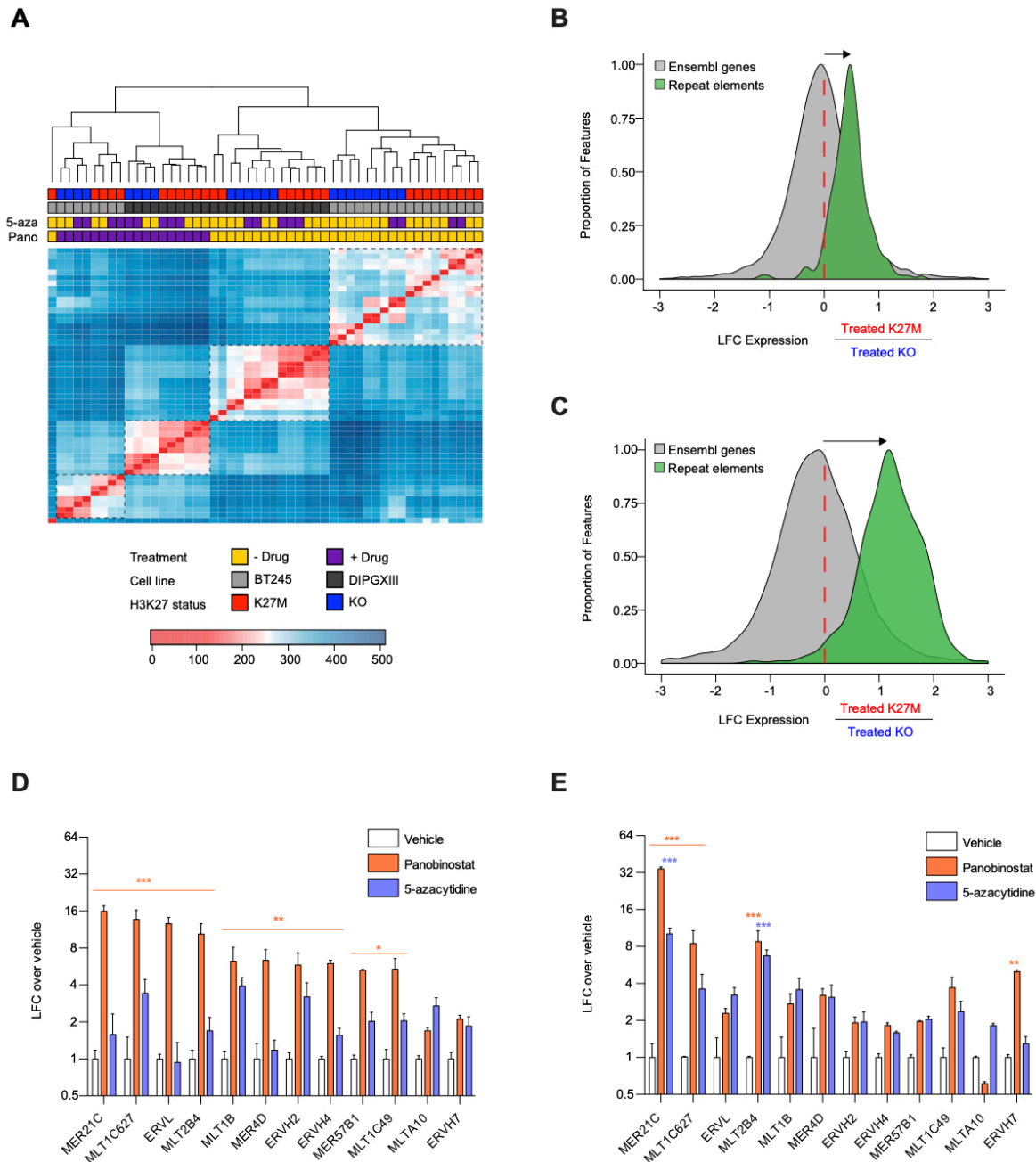


**Figure S5.** Related to Figure 6.

**(A)** Hierarchical clustering of samples based on global transcriptomic profiles. Color key: low (blue) to high (red) similarity between pairs of samples. Similarity between samples is calculated using the Euclidean distance over their variant-stabilizing-transformed transcriptomic profiles.

**(B-C)** Changes in expression of repetitive elements in K27M relative to KO after combination treatment (panobinostat and 5-azacytidine) for both DIPG-XIII (n=3) relative to KO (n=2) **(B)** and BT245 (n=2)

relative to KO (n=2) **(C)**. Histograms showing the distributions of the log<sub>2</sub> fold-change (LFC) of transcription of repetitive elements (green; Repbase) and Ensembl genes (grey; GRCh37) in K27M relative to KO. Elements with sufficiently high expression (baseMean > 100) and LFCs in [-3,3] range shown here. **(D-E)** Measurement of ERV family expression by ddPCR upon 48 hour treatment with panobinostat (50 nM) or 5-azacytine 5 μM), normalized to vehicle control in BT245 **(D)** and corresponding KO lines **(E)**. Plots show mean +SEM of 3 experimental replicates of the BT245 line. Two-way analysis of variance compares vehicle to each drug, with Bonferroni posttest significance shown by p<0.001=\*\*\*, p<0.01=\*\*, p<0.05=\*. Y-axis is in log<sub>2</sub> scale.

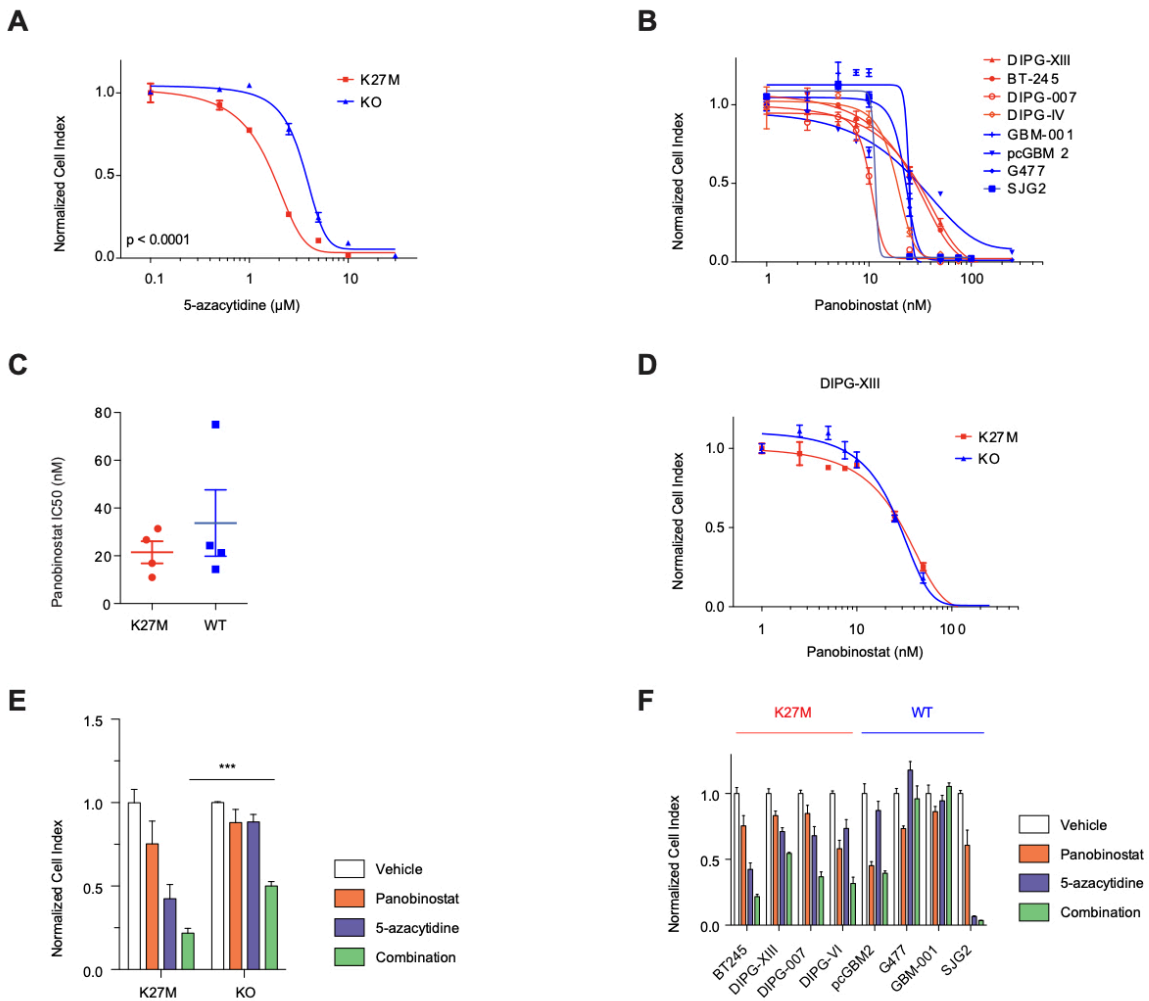


**Figure S6.** Related to Figure 6.

**(A)** Dose response curves of H3K27M and KO lines of BT245 to 5-azacytidine in isogenic context. Plots show mean  $\pm$  SEM of 3 experimental replicates.

**(B-C)** Cell viability of H3.3K27M and WT cells in a 7-day growth assay across a panel of pHGG lines **(B)** and corresponding IC50 values **(C)**.

**(D)** Dose response curves of H3K27M and KO lines of DIPG-XIII to 5-azacytidine in isogenic context. Plots show mean  $\pm$  SEM of 3 experimental replicates.

**(E-F)** Cell viability in 7-day growth assay under treatment of lines with sub-IC50 doses of panobinostat (15 nM), 5-azacytidine (1.5  $\mu\text{M}$ ) and their combination in BT245 versus KO **(E)** and to H3.3K27M compared to WT cell lines **(F)**. Plots show mean  $\pm$  SEM of 3 experimental replicates. A two-tailed t-test compares combination treated lines, with  $p < 0.001 = ***$ .

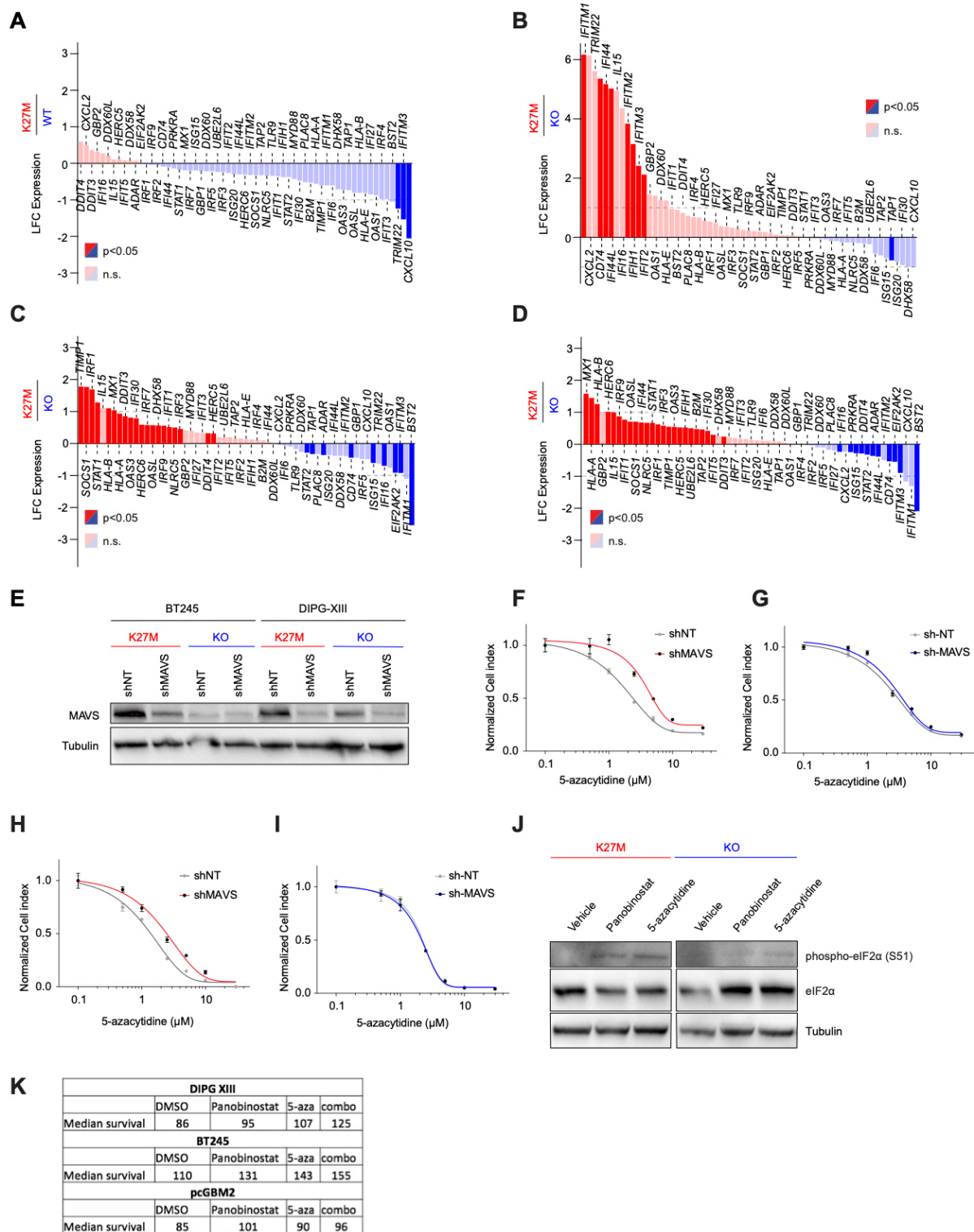


**Figure S7.** Related to Figure 7.

(A-B) Waterfall plot illustrating changes in the expression levels of the interferon response genes in H3.3K27M HGG tumors (n=17) compared to H3K27WT (n=15) (A) and in BT245 cell line (n=5) relative

to KO (n=5) at baseline **(B)**. Y-axis: log<sub>2</sub> fold-change of expression in K27M relative to K27WT or KO. Red: upregulated genes in K27M. Blue: downregulated genes. Significantly deregulated genes highlighted (p<0.05; baseMean>100).

**(C-D)** Waterfall plots illustrating the induction of interferon response genes in DIPG-XIII relative to KO upon treatment with panobinostat and 5-azacytidine **(C)** and panobinostat alone **(D)**. Y-axis: log<sub>2</sub> fold-change of expression in K27M relative to KO (combination DIPG-XIII n=3, DIPG-XIII-KO n=2; panobinostat DIPG-XIII n=3, DIPG-XIII n=2).

**(E)** Western blot demonstrates decreased expression of MAVS protein (57 kD band) by shRNA targeting.

**(F-I)** Dose response curves to 5-azacytidine in a 7-day growth assay of H3.3K27M and KO lines of DIPG-XIII **(F-G)** and BT245 **(H-I)** transduced with lentiviral vectors expressing short hairpin RNA (shRNA) controls (non-targeting, NT) or a pool of 4 shRNAs targeting MAVS. Plots show mean +/-SEM of 3 experimental replicates.

**(J)** Western blot of phosphorylated eIF2-alpha upon 48 hours treatment with panobinostat (50 nM) or 5-azacytidine (5 μM) in BT245 and KO lines.

**(K)** Summary of median survivals of mice bearing PDX models of DIPGXIII, BT245, and pcGBM2 following treatment with DMSO, panobinostat, 5-azacytidine, and combination as related to **Figures 7E-F**.

## Chapter 4: Discussion

Chapters 2 and 3 represent manuscripts published in 2019, within the context of an active field of investigation. I will describe how this work contributes novel findings to the field, corroborates observations of some previously published work, and has since been supported by more recent publications.

### **H3K27M mechanism and tumour chromatin states**

Chapter 2 describes my group's work in which we are the first to knock out the H3K27M mutation using CRISPR. Using quantitative mass spectrometry and ChIP-Rx normalization, this conclusively describes where tumour cells can distribute H3K27me2 and H3K27me3. This confirms earlier reports of impaired H3K27me3 spread and residual PRC2 activity at GCIs (Mohammad et al., 2017; Stafford et al., 2018). Chapter 2 is the first demonstration that H3K27me2 is spread in specific domains that extend more broadly on chromatin than where H3K27me3 is deposited, in H3K27M mutant tumour cells. I further show EZH2-Y641N can extend spatial spread of H3K27me3 over domains normally marked by H3K27me2, even in the presence of H3K27M, and that complete EZH2 inhibition through small molecule application removes both H3K27me2 and H3K27me3 across the epigenome, unlike H3K27M. Together, these findings refute models that the mutant oncohistone sequesters PRC2 on chromatin or elsewhere in the nucleus. More recently, the discovery of the H3K27M-mimic EZH inhibiting protein (EZHIP) also challenges the view that PRC2 is inhibited by its association with a H3K27M-containing chromatin substrate, since EZHIP does not incorporate into chromatin and yet can still affect PRC2's catalytic activity (Jain et al., 2020). Furthermore, incorporation of H3K27M in the nucleosome in various chromatin domains does not preclude the presence of a fraction of labile H3 mutants capable of transient association with PRC2 in the vicinity of H3K27me3-marked domains. Work by the group of Danny Reinberg shows the loss of EZH2 automethylation and may therefore explain the prolonged impairment of EZH2/1 catalysis, in the absence of continual association with H3K27M (Lee et al., 2019).

Chapters 2 and 3 show the loss of distal deposition of H3K27me2/3 results in promoter de-repression, particularly of lowly expressed genes and of repeat elements, that can diversely affect stemness, proliferation and cellular stress responses. These effects are corroborated by more recent isogenic modeling of H3K27M mutations in transgenic mice and cell cultures. Residual

H3K27me3 deposition at specific CGIs plays a role in this oncogenic phenotype. This contributes to explain why complete loss of PRC2 is never observed in gliomas and why pharmacological EZH2 inhibition selectively harms H3K27M mutants. Preserved but restricted occupancy of PRC2 to local nucleation sites contribute to maintaining repression of numerous genes, including developmental regulators (Chapter 2). These loci include Homeobox gene clusters that are repressed in other published H3K27M mouse models and are depleted of strong enhancer features in H3K27M compared to H3 wild-type HGGs (Chapter 3) (Larson et al., 2019; Mohammad et al., 2017). Ultimately, this continuous repression at select CGIs may, in cooperation with H3K27M partner mutations, favour stemness and impair differentiation of tumour cells in an oligodendrocyte progenitor cell state, the presumed lineage of origin inferred from single-cell studies and in enhancer landscape profiles of tumours (Filbin et al., 2018; Jessa et al., 2019). H3K27M has effects that further extend downstream of H3K27 methylation to other chromatin modifications, which may also play a role in transformation (Chapters 2 & 3). Further recent work from our group has demonstrated that intergenic regions of H3K27M mutants, in lacking heterochromatin establishment, acquire H3K27me1, and elevated H3K36me2 in some contexts. Redistribution of H3K27me1 from active genic to intergenic regions suggests that H3K27M-stalled PRC2 is limited in its spatial distribution. Also, the gain of H3K9me3 in regions losing H3K27me2/3 propose alternative forms of heterochromatin compensate for chromatin integrity (Harutyunyan et al., 2020).

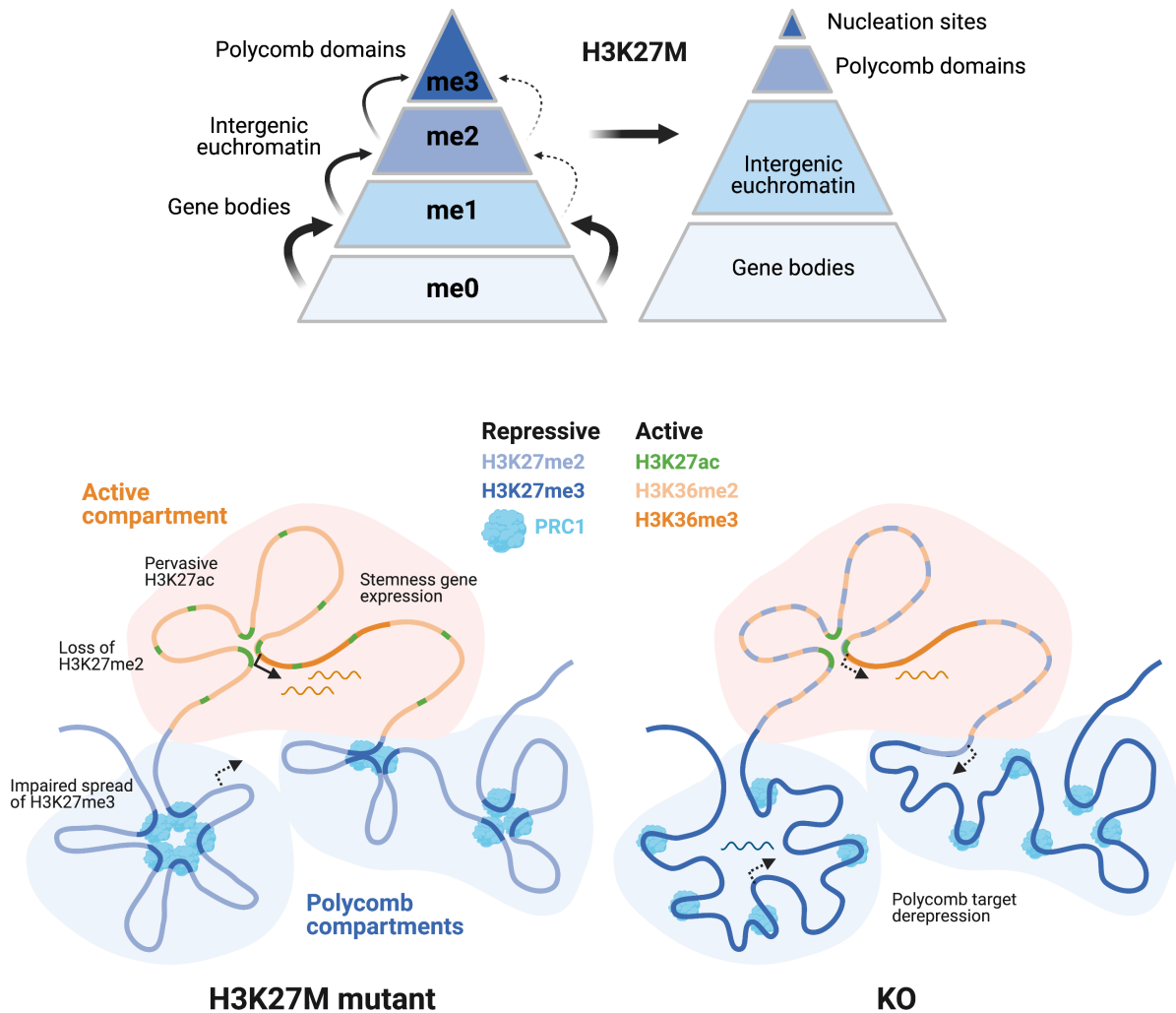


**Figure 1. Summary of H3K27M's chromatin consequences learned from isogenic modeling.**

Top panel: PRC2 normally methylates H3K27 in a sequential, hierarchical manner where higher states becomes more spatially restricted on chromatin of brain tumour cells. The H3K27M mutant histone impairs spread of H3K27me2/3 that results in a step-wise restriction of the higher methylation states to where the methylation state one below it is normally deposited. Lower panel: the distribution of repressive and active chromatin modifications is summarized, along with some of the transcriptional consequences. The figure is created with Biorender.com.

### **The role of H3K27ac in H3K27M HGGs**

Since the publication of Chapter 3, more recent papers have described the phenomena of pervasive acetylation without an increase in enhancer features in H3K27M neural stem cell culture models (Brien et al., 2021), confirming our observations in tumour-derived cell lines. This model also confirmed a sensitivity of H3K27M mutants to EZH2 inhibitors, while no change in sensitivity to bromodomain inhibitors matches our observations. I have also generated more ChIP-seq data in carefully controlled experiments with libraries sequenced to a high read depth, and performed Cleavage Under Target and Release Under Nuclease (CUT&RUN) experiments, that both represent H3K27M-specific pervasive H3K27ac distributions through read-depth normalized genome coverage, independent of ChIP-Rx ratios (unpublished data). These findings build confidence in our model put forth in Chapter 3, which is the first report describing that a quantitative elevation of H3K27ac distribution can be pervasively deposited across the vast majority of chromatin. This implicates non-specific localization of acetyltransferase activity of p300-CBP on chromatin substrates. In the Cancer Cell Line Encyclopedia, histone mass spectrometry was used to quantify PTM abundance changes and cluster cell lines based on their mutation status of epigenetic modifiers. This work discovered recurrent truncating variants in p300-CBP displaying gain of function in cell lines with increased H3K27ac abundance (Ghandi et al., 2019). The physiological consequences of pervasive histone acetylation and the effects leading to these states remain unexplored and warrant further investigation.

The work of Roulois et al. and Chiapinelli et al. (2015) describe tumour cell contexts that activate a viral mimicry state in response to DNA demethylating agents. Chapter 3 shows that a cancer context carries a specific epigenetic state that renders cells vulnerable to induction of viral mimicry by epigenetic therapies. These findings are relevant for treating numerous cancers that exhibit genome-wide loss of 5mC and/or impaired PRC2 activity, including many leukemias. The link between TE derepression and triggering of associated stress responses could help understand the mechanism of action of epigenetic therapies in clinical use. Using a *Drosophila* model system, recent work identifies derepression of transposable elements by both H3K27M and H3K36M oncohistone mutations (Chaouch et al., 2021), demonstrating the broad applicability of the effect Chapter 3 describes in human and mouse tumour models.

## **Dependencies on brain tumour driver mutations and their therapeutic targeting**

Chapter 2 shows the H3K27M mutation is required for maintenance of impaired H3K27me<sub>2/3</sub> spread and the tumorigenic potential of cells. This was corroborated by work around the same time showing shRNA knockdown of the H3K27M allele can slow the development of xenograft tumours, linked with characteristics of glial differentiation (Silveira et al., 2019). In later work, I contributed to experiments that showed that the application of differentiation media conditions reveals that H3K27M impairs potential to acquire protein markers and transcriptomic signatures of mature glial states (Figure 2) (Jessa et al., 2019). In contrast to H3K27M, H3.3G34R/V mutations are weakly tumour-promoting in mice on their own and require association to *Tp53* loss and further enhanced by *Pdgfra* overexpression (Chen et al., 2020). Removal of the mutation allows cells to further mature across the interneuron lineage even if, unlike H3K27M, this does not impact tumorigenic potential. Together, these histone mutations converge on impaired differentiation, yet rely on different partnering effects throughout the evolution of lineages to high grade tumours. Beyond pediatric HGGs, IDH mutations also appear to sustain tumour progression. The unique catalytic activity of *IHD1*-R132H renders it targetable by small molecule inhibition as blocking 2-HG production promotes glial differentiation (Rohle et al., 2013). Numerous small molecule inhibitors of mutant IDH are currently under clinical investigation for IDH-mutant tumours, and their clinical value for glioma patients is becoming better established. Overall, epigenomic changes are reversible in a number of brain tumours, and in-depth understanding of altered chromatin states may provide rationales for the development of new therapeutic strategies.

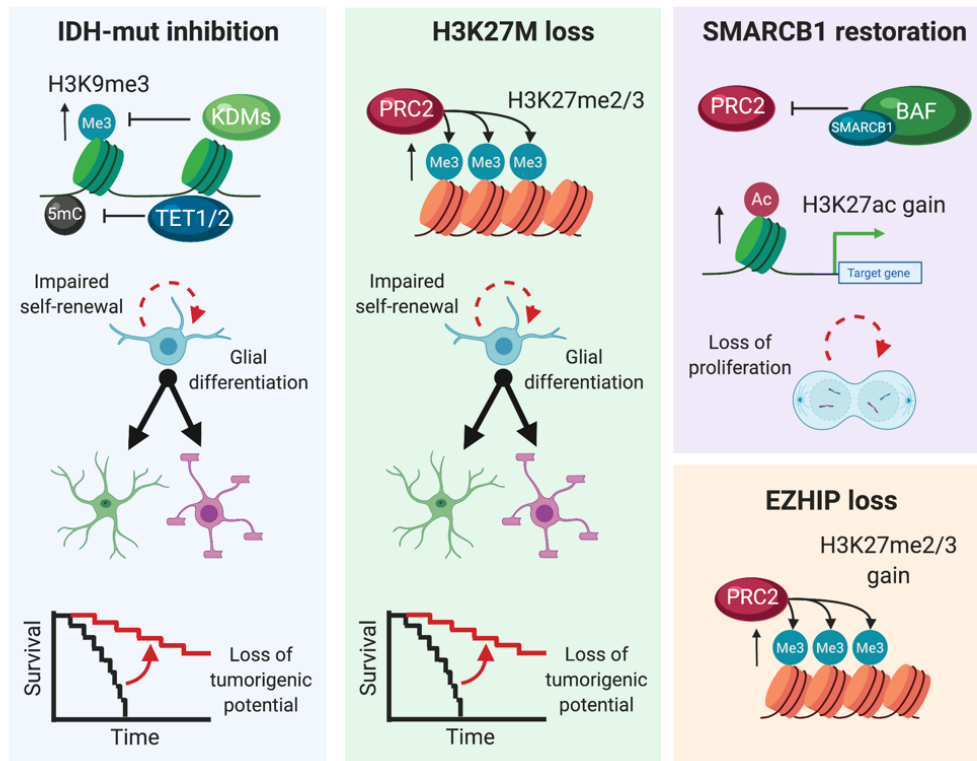


**Figure 2. Manipulation of driver events determines reversibility of tumour epigenomes**

The manipulation of driver events remodeling the epigenome serves to characterize the reversibility of their effects, and the dependence of transformed cells on their function to proliferate, self-renew, and form tumours. The inhibition of 2-HG production by *IDH1*-R132H using a small molecule drug elevates 5-hydroxymethylcytosine, diminishes histone methylation and promotes glial differentiation *in vitro*, while delaying tumour burden in xenografts. The knockout or knockdown of the *H3F3A*-K27M mutant allele in tumour-derived cell lines restores PRC2 activity and H3K27me2/3 deposition, renders the cells capable of enhanced glial differentiation and delays or abolishes the potential to form xenograft tumours. Similar trends are observed upon knockout of *EZH1*, variably diminishing cell proliferation in some contexts. The restoration of *SMARCB1* expression in ATRT lines reversed the loss of H3K27ac to reactivate silenced genes and decrease proliferation. The figure is reproduced from Krug et al. (2021) and created with Biorender.com.

### **H3K27M as a driver among a mosaic of tumour alterations to PRC2**

The scope of brain tumour epigenomes illustrates diverse paths to remodeling of chromatin landscapes. While different routes can be associated with specific lineages of origin across space and time, the silencing of developmental genes by PRC2 emerges as a recurrent pattern. Restraining PRC2 spread can both derepress targets covered by H3K27me3 and repress promoters at nucleation sites in H3K27M tumours (Chapter 2). This likely resembles effects of endogenous EZHIP in specific tissues of early development, and in PFA-EPN that abnormally co-opt this protein. In H3.3G34R/V HGGs, focal H3K27me3 gain can arise from selective loss of H3.3K36me3. Loss of DNA demethylase activity in IDH mutants, or abnormal DNA methylation in the context of ETMR associates with promoter silencing, while the loss of the BAF complexes and H3K27 demethylases in several BT entities plausibly results in failure to activate PRC2 targets. Improved understanding of the interplay between PRC2/1, H3K36 and 5mC, histone and DNA demethylases, BAF and COMPASS complexes during development and cellular differentiation will help illuminate the role played by these mutations and their ultimate consequences. These investigations will be crucial in establishing hierarchies and kinetics of chromatin modifications during lineage commitment and cellular differentiation. Rare cancer drivers may relate to broader trends, as the CGI hypermethylation of developmental PRC2 targets are frequent in numerous cancers, and a CIMP acquisition in aging IDH-WT cells can be a requirement for transformation (Tao et al., 2019). Preserving epigenome integrity must therefore consider selective forces acting to maintain or remodel chromatin over development, from conception to old age. Strong associations between driver events and tumour subgroups imply that select chromatin landscapes are vulnerable to transformation, yet also reversible. Further progress in carefully charting the interplay of these epigenetic marks, their writers and readers will be fruitful paths in taking basic science to clinical application. The generation of brain-penetrant epigenetic modulators, especially for PRC2 subunits, will enable testing of their achievable therapeutic benefits.

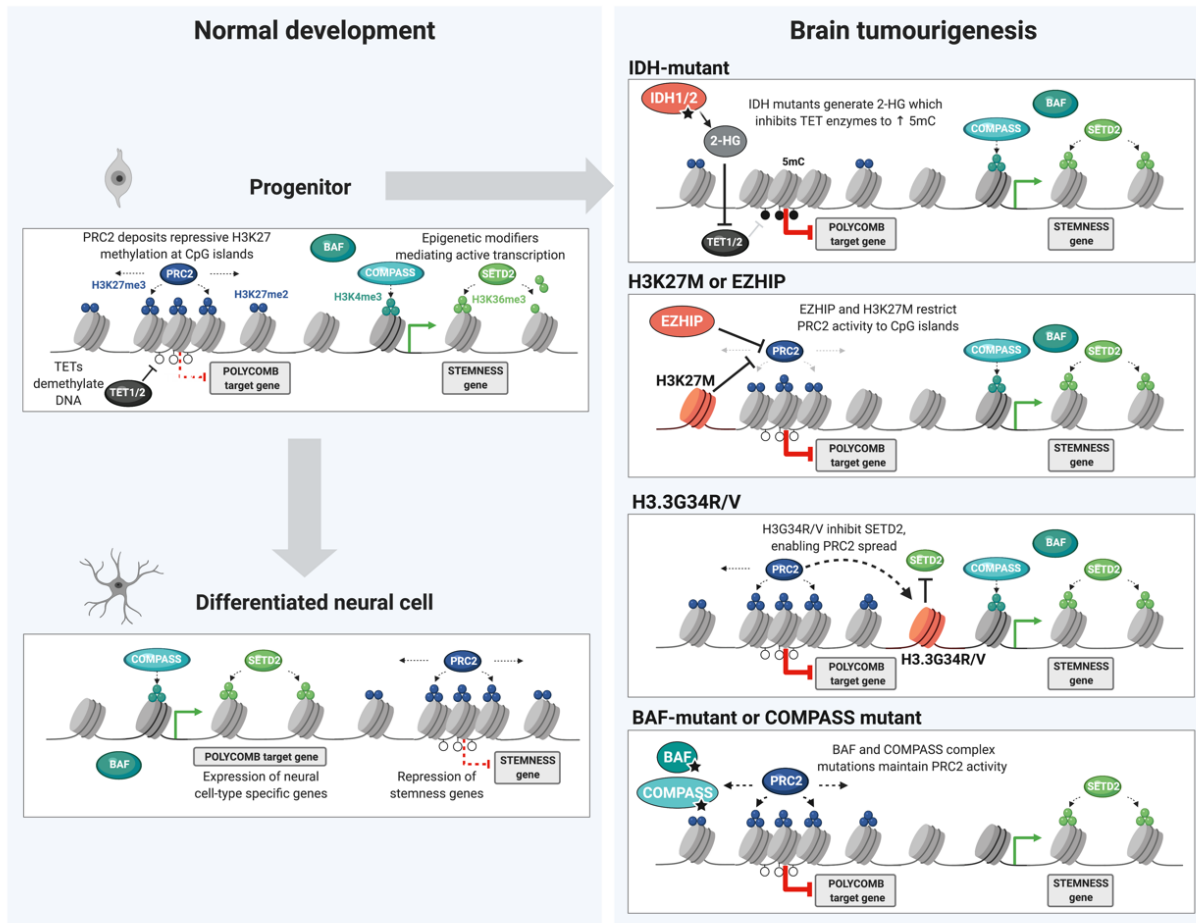


**Figure 3. Chromatin modifiers in normal and altered development among brain tumours.**

Appropriate differentiation of neural lineages requires remodeling of chromatin landscapes through the interplay of polycomb repressive complex 2 (PRC2), acting in opposition to BRG1/BRM associated factors (BAF) complexes and Complex Proteins associated with Set1 (COMPASS). Abnormal PRC2 occupancy at genomic loci involved in fate specification, and expression of stemness associated genes, can stall differentiation and promote tumorigenesis linked to enhanced self-renewal. In stem cells, polycomb targets are prone to acquisition of repressive 5 methyl-cytosine through the inhibition of histone and DNA demethylases. Restraining the spread of PRC2 through H3K27M or Enhancer of Zeste Homologs Inhibitory Protein (EZHIP) aberrant expression maintains repression of specific polycomb targets and an active chromatin at stemness-associated genes. Deposition of H3.3G34R/V mutant histone prevents SET Domain containing 2 (SETD2) deposition of H3K36me3, thereby facilitating PRC2 redistribution to genic regions. The loss of BAF and COMPASS functions further prevents the conversion from repressed

PRC2 targets to an active state, and is associated with stalled neural differentiation. The figure is reproduced from Krug et al. (2021) and created with Biorender.com.

## Chapter 5: Conclusions and Future Directions

I summarize the findings from this thesis and integrate with the published literature to present a unified model of H3K27M-mutants' chromatin states in Figure 1. The mutant histone limits PRC2's catalytic activity to spread H3K27me2 and H3K27me3 in distinct areas of chromatin, thus confining H3K27me3 deposition largely to nucleation sites and H3K27me2 to chromatin normally marked by H3K27me3 in the absence of H3K27M. A substantial quantitative loss of H3K27me2/3 results in pervasive deposition of H3K27ac and a rise in its abundance, however this phenomenon does not largely alter the genome-wide number of enhancer and promoter peaks. From available data, this work proposes that redistribution of H3K27me3 is the strongest predictor of transcriptional consequences; namely derepression of genes losing H3K27me3 and repression of genes retaining H3K27me3 at promoters. The effect of H3K27M is required to preserve tumourigenic competence of cells that we link to enhanced self-renewal potential and impaired differentiation.

The observation of residual H3K27me3 peaks associated with genes downregulated by H3K27M raises interest in understanding the chromatin architecture contributing to this repressive effect. Our observations of RING1B peaks overlapping many H3K27me3 peaks implicates PRC1 localization as a likely consequence (Chapter 2). Since canonical PRC1 contains CBX subunits that read the global H3K27me3 distribution and localize cPRC1 at these sites, future work aims to study the consequence of H3K27M on cPRC1's function. Long range spread of H3K27me3 is found in contexts of development and cellular differentiation, from nucleation sites that can contact each other in 3D space (Zheng & Xie, 2019). Therefore, integration of ChIP-seq datasets with chromatin conformation capture technologies (Hi-C) will serve to describe the potential for H3K27M to shape configurations of distal interactions, linked with both repressive and activating effects on transcription.

After the publication of Chapter 2, further work by Ashot Harutyunyan and others described how enrichment of H3K36me2 marks euchromatin domains that delineate boundaries with the spread of H3K27me2 in H3K27M mutant cells, and H3K27me3 in isogenic KO cells (Harutyunyan et al., 2020). This matches previously described roles of H3K36me2 in restraining the spread of PRC2

activity (Streubel et al., 2018). However, the physiological effects of H3K36me2-defined euchromatin are not completely understood, as well as the relative contribution of H3K27me3 loss versus H3K27me2 loss on the mechanism of H3K27M's phenotype. A more recent paper describes a dependence of H3K27M gliomas on H3K36me2 and a reader protein of this PTM, Lens Epithelium-Derived Growth Factor (LEDGF) (Yu et al., 2021). Future work thus aims to study the functional roles H3K36me2 in our tumour models and how this is influenced by impaired spread of H3K27me2/3. While Chapter 3 describes the absence of changes to numbers of active enhancers caused by H3K27M, further work warrants comparing enhancer activity during differentiation *in vivo* and at single cell resolution, such as through use of recently developed CUT&TAG-based multi-omics profiling of chromatin epitopes and transcriptomes.

Active research continues to investigate numerous epigenetic and immune-based therapies against H3K27M HGGs, in preclinical models and clinical trials. Advancement of the field's potential will rely on creating reliable and faithful syngeneic animal models to study the interaction of host immune systems with H3K27M tumour cells, and their modulation by therapeutic interventions. High-dimensional profiling of tumours and their microenvironments will be facilitated through emerging technologies, including single-cell RNA-sequencing and mass cytometry.

Strong regulatory feedback exists between chromatin modifications and metabolic states of cells. Histone methylation, demethylation, acetylation and deacetylation are some of the reactions regulated by abundance of metabolites within the nucleus, that can change within ranges of normal cellular physiology (Intlekofer & Finley, 2019). The ability to pharmacologically target metabolic pathways and alter metabolite abundance through the diet has invigorated interest in devising cancer therapies using these means. The foundation of knowledge from this work on cancer cells' chromatin states and their dependencies will be valuable to inform the direction of future work aiming to treat H3K27M HGGs and parallel cancer contexts.

## Chapter 6 : Master Reference List

- Akhtar-Zaidi, B., Cowper-Sal-lari, R., Corradin, O., Saiakhova, A., Bartels, C. F., Balasubramanian, D., Myeroff, L., Lutterbaugh, J., Jarrar, A., Kalady, M. F., Willis, J., Moore, J. H., Tesar, P. J., Laframboise, T., Markowitz, S., Lupien, M., & Scacheri, P. C. (2012). Epigenomic enhancer profiling defines a signature of colon cancer. *Science (New York, N.Y.)*, 336(6082), 736–739. <https://doi.org/10.1126/science.1217277>
- Albert, M., & Huttner, W. B. (2018). Epigenetic and Transcriptional Pre-patterning-An Emerging Theme in Cortical Neurogenesis. *Frontiers in Neuroscience*, 12, 359. <https://doi.org/10.3389/fnins.2018.00359>
- Almeida, M. V., Vernaz, G., Putman, A. L. K., & Miska, E. A. (2022). Taming transposable elements in vertebrates: from epigenetic silencing to domestication. *Trends in Genetics : TIG*. <https://doi.org/10.1016/j.tig.2022.02.009>
- Alves dos Santos, M. T. M., & Smidt, M. P. (2011). En1 and Wnt signaling in midbrain dopaminergic neuronal development. *Neural Development*, 6, 23. <https://doi.org/10.1186/1749-8104-6-23>
- An integrated encyclopedia of DNA elements in the human genome. (2012). *Nature*, 489(7414), 57–74. <https://doi.org/10.1038/nature11247>
- Balakrishnan, I., Danis, E., Pierce, A., Madhavan, K., Wang, D., Dahl, N., Sanford, B., Birks, D. K., Davidson, N., Metselaar, D. S., Meel, M. H., Lemma, R., Donson, A., Vijmasi, T., Katagi, H., Sola, I., Fosmire, S., Alimova, I., Steiner, J., ... Venkataraman, S. (2020). Senescence Induced by BMI1 Inhibition Is a Therapeutic Vulnerability in H3K27M-Mutant DIPG. *Cell Reports*, 33(3), 108286. <https://doi.org/10.1016/j.celrep.2020.108286>
- Bao, W., Kojima, K. K., & Kohany, O. (2015). Repbase Update, a database of repetitive elements in eukaryotic genomes. *Mobile DNA*, 6, 11. <https://doi.org/10.1186/s13100-015-0041-9>
- Bardella, C., Al-Dalahmah, O., Krell, D., Brazauskas, P., Al-Qahtani, K., Tomkova, M., Adam, J., Serres, S., Lockstone, H., Freeman-Mills, L., Pfeffer, I., Sibson, N., Goldin, R., Schuster-Böeckler, B., Pollard, P. J., Soga, T., McCullagh, J. S., Schofield, C. J., Mulholland, P., ... Tomlinson, I. (2016). Expression of Idh1R132H in the Murine Subventricular Zone Stem

- Cell Niche Recapitulates Features of Early Gliomagenesis. *Cancer Cell*, 30(4), 578–594. <https://doi.org/10.1016/j.ccell.2016.08.017>
- Baubec, T., Colombo, D. F., Wirbelauer, C., Schmidt, J., Burger, L., Krebs, A. R., Akalin, A., & Schübeler, D. (2015). Genomic profiling of DNA methyltransferases reveals a role for DNMT3B in genic methylation. *Nature*, 520(7546), 243–247. <https://doi.org/10.1038/nature14176>
- Baylin, S. B., & Jones, P. A. (2016). Epigenetic Determinants of Cancer. *Cold Spring Harbor Perspectives in Biology*, 8(9). <https://doi.org/10.1101/cshperspect.a019505>
- Bayliss, J., Mukherjee, P., Lu, C., Jain, S. U., Chung, C., Martinez, D., Sabari, B., Margol, A. S., Panwalkar, P., Parolia, A., Pekmezci, M., McEachin, R. C., Cieslik, M., Tamrazi, B., Garcia, B. A., La Rocca, G., Santi, M., Lewis, P. W., Hawkins, C., ... Venneti, S. (2016). Lowered H3K27me3 and DNA hypomethylation define poorly prognostic pediatric posterior fossa ependymomas. *Science Translational Medicine*, 8(366), 1–14. <https://doi.org/10.1126/scitranslmed.aah6904>
- Bechet, D., Gielen, G. G. H., Korshunov, A., Pfister, S. M., Rousso, C., Faury, D., Fiset, P.-O., Benlimane, N., Lewis, P. W., Lu, C., David Allis, C., Kieran, M. W., Ligon, K. L., Pietsch, T., Ellezam, B., Albrecht, S., & Jabado, N. (2014). Specific detection of methionine 27 mutation in histone 3 variants (H3K27M) in fixed tissue from high-grade astrocytomas. *Acta Neuropathologica*, 128(5), 733–741. <https://doi.org/10.1007/s00401-014-1337-4>
- Behesti, H., Bhagat, H., Dubuc, A. M., Taylor, M. D., & Marino, S. (2013). Bmi1 overexpression in the cerebellar granule cell lineage of mice affects cell proliferation and survival without initiating medulloblastoma formation. *DMM Disease Models and Mechanisms*, 6(1), 49–63. <https://doi.org/10.1242/dmm.009506>
- Behjati, S., Tarpey, P. S., Presneau, N., Scheipl, S., Pillay, N., Van Loo, P., Wedge, D. C., Cooke, S. L., Gundem, G., Davies, H., Nik-Zainal, S., Martin, S., McLaren, S., Goodie, V., Robinson, B., Butler, A., Teague, J. W., Halai, D., Khatri, B., ... Flanagan, A. M. (2013). Distinct H3F3A and H3F3B driver mutations define chondroblastoma and giant cell tumor of bone. *Nature Genetics*, 45(12), 1479–1482. <https://doi.org/10.1038/ng.2814>
- Belgnaoui, S. M., Paz, S., & Hiscott, J. (2011). Orchestrating the interferon antiviral response through the mitochondrial antiviral signaling (MAVS) adapter. *Current Opinion in Immunology*, 23(5), 564–572. <https://doi.org/10.1016/j.coi.2011.08.001>

- Bender, S., Tang, Y., Lindroth, A. M., Hovestadt, V., Jones, D. T. W., Kool, M., Zapatka, M., Northcott, P. A., Sturm, D., Wang, W., Radlwimmer, B., Højfeldt, J. W., Truffaux, N., Castel, D., Schubert, S., Ryzhova, M., Keker-Cin, H., Gronych, J., Johann, P. D., ... Pfister, S. M. (2013). Reduced H3K27me3 and DNA Hypomethylation Are Major Drivers of Gene Expression in K27M Mutant Pediatric High-Grade Gliomas. *Cancer Cell*, *24*(5), 660–672. <https://doi.org/10.1016/j.ccr.2013.10.006>
- Bernstein, B. E., Mikkelsen, T. S., Xie, X., Kamal, M., Huebert, D. J., Cuff, J., Fry, B., Meissner, A., Wernig, M., Plath, K., Jaenisch, R., Wagschal, A., Feil, R., Schreiber, S. L., & Lander, E. S. (2006). A bivalent chromatin structure marks key developmental genes in embryonic stem cells. *Cell*, *125*(2), 315–326. <https://doi.org/10.1016/j.cell.2006.02.041>
- Bestor, T. H., & Bourc'his, D. (2004). Transposon silencing and imprint establishment in mammalian germ cells. *Cold Spring Harbor Symposia on Quantitative Biology*, *69*, 381–387. <https://doi.org/10.1101/sqb.2004.69.381>
- Bickel, P. J., Boley, N., Brown, J. B., Huang, H., & Zhang, N. R. (2010). Subsampling methods for genomic inference. *Annals of Applied Statistics*, *4*(4), 1660–1697. <https://doi.org/10.1214/10-AOAS363>
- Blobel, G. A., Higgs, D. R., Mitchell, J. A., Notani, D., & Young, R. A. (2021). Testing the super-enhancer concept. *Nature Reviews. Genetics*, *22*(12), 749–755. <https://doi.org/10.1038/s41576-021-00398-w>
- Bolger, A. M., Lohse, M., & Usadel, B. (2014). Trimmomatic: a flexible trimmer for Illumina sequence data. *Bioinformatics (Oxford, England)*, *30*(15), 2114–2120. <https://doi.org/10.1093/bioinformatics/btu170>
- Borodovsky, A., Salmasi, V., Turcan, S., Fabius, A. W. M., Baia, G. S., Eberhart, C. G., Weingart, J. D., Gallia, G. L., Baylin, S. B., Chan, T. A., & Riggins, G. J. (2013). 5-azacytidine reduces methylation, promotes differentiation and induces tumor regression in a patient-derived IDH1 mutant glioma xenograft. *Oncotarget*, *4*(10), 1737–1747. <https://doi.org/10.18632/oncotarget.1408>
- Bourc'his, D., & Bestor, T. H. (2004). Meiotic catastrophe and retrotransposon reactivation in male germ cells lacking Dnmt3L. *Nature*, *431*(7004), 96–99. <https://doi.org/10.1038/nature02886>
- Bressan, R. B., Southgate, B., Ferguson, K. M., Blin, C., Grant, V., Alfazema, N., Wills, J. C.,

- Marques-Torrejón, M. A., Morrison, G. M., Ashmore, J., Robertson, F., Williams, C. A. C., Bradley, L., von Kriegsheim, A., Anderson, R. A., Tomlinson, S. R., & Pollard, S. M. (2021). Regional identity of human neural stem cells determines oncogenic responses to histone H3.3 mutants. *Cell Stem Cell*, *28*(5), 877-893.e9. <https://doi.org/10.1016/j.stem.2021.01.016>
- Brien, G. L., Bressan, R. B., Monger, C., Gannon, D., Lagan, E., Doherty, A. M., Healy, E., Neikes, H., Fitzpatrick, D. J., Deevy, O., Grant, V., Marqués-Torrejón, M.-A., Alfazema, N., Pollard, S. M., & Bracken, A. P. (2021). Simultaneous disruption of PRC2 and enhancer function underlies histone H3.3-K27M oncogenic activity in human hindbrain neural stem cells. *Nature Genetics*, *53*(8), 1221–1232. <https://doi.org/10.1038/s41588-021-00897-w>
- Buczkwicz, P., Hoeman, C., Rakopoulos, P., Pajovic, S., Letourneau, L., Dzamba, M., Morrison, A., Lewis, P., Bouffet, E., Bartels, U., Zuccaro, J., Agnihotri, S., Ryall, S., Barszczyk, M., Chornenky, Y., Bourgey, M., Bourque, G., Montpetit, A., Cordero, F., ... Hawkins, C. (2014). Genomic analysis of diffuse intrinsic pontine gliomas identifies three molecular subgroups and recurrent activating ACVR1 mutations. *Nature Genetics*, *46*(5), 451–456. <https://doi.org/10.1038/ng.2936>
- Capper, D., Jones, D. T. W., Sill, M., Hovestadt, V., Schrimpf, D., Sturm, D., Koelsche, C., Sahm, F., Chavez, L., Reuss, D. E., Kratz, A., Wefers, A. K., Huang, K., Pajtler, K. W., Schweizer, L., Stichel, D., Olar, A., Engel, N. W., Lindenberg, K., ... Pfister, S. M. (2018). DNA methylation-based classification of central nervous system tumours. *Nature*, *555*(7697), 469–474. <https://doi.org/10.1038/nature26000>
- Carroll, T. S., Liang, Z., Salama, R., Stark, R., & de Santiago, I. (2014). Impact of artifact removal on ChIP quality metrics in ChIP-seq and ChIP-exo data. *Frontiers in Genetics*, *5*, 75. <https://doi.org/10.3389/fgene.2014.00075>
- Chan, H. L., & Morey, L. (2019). Emerging Roles for Polycomb-Group Proteins in Stem Cells and Cancer. *Trends in Biochemical Sciences*, *44*(8), 688–700. <https://doi.org/10.1016/j.tibs.2019.04.005>
- Chan, K., Fang, D., Gan, H., Dev, G., Chan, K., Fang, D., Gan, H., Hashizume, R., Yu, C., Schroeder, M., Gupta, N., Mueller, S., James, C. D., Jenkins, R., Sarkaria, J., & Zhang, Z. (2013). The histone H3.3K27M mutation in pediatric glioma reprograms H3K27 methylation and gene expression. *Genes & Development*, 985–990.

<https://doi.org/10.1101/gad.217778.113>

- Chang, L., & Takada, S. (2016). Histone acetylation dependent energy landscapes in trinucleosome revealed by residue-resolved molecular simulations. *Scientific Reports*, 6, 34441. <https://doi.org/10.1038/srep34441>
- Chaouch, A., Berlandi, J., Chen, C. C. L., Frey, F., Badini, S., Harutyunyan, A. S., Chen, X., Krug, B., Hébert, S., Jeibmann, A., Lu, C., Kleinman, C. L., Hasselblatt, M., Lasko, P., Shirinian, M., & Jabado, N. (2021). Histone H3.3 K27M and K36M mutations de-repress transposable elements through perturbation of antagonistic chromatin marks. *Molecular Cell*, 81(23), 4876-4890.e7. <https://doi.org/10.1016/j.molcel.2021.10.008>
- Chen, C. C. L., Deshmukh, S., Jessa, S., Hadjadj, D., Lisi, V., Andrade, A. F., Faury, D., Jawhar, W., Dali, R., Suzuki, H., Pathania, M., A, D., Dubois, F., Woodward, E., Hébert, S., Coutelier, M., Karamchandani, J., Albrecht, S., Brandner, S., ... Jabado, N. (2020). Histone H3.3G34-Mutant Interneuron Progenitors Co-opt PDGFRA for Gliomagenesis. *Cell*, 183(6), 1617-1633.e22. <https://doi.org/10.1016/j.cell.2020.11.012>
- Chiappinelli, K. B., Strissel, P. L., Desrichard, A., Li, H., Henke, C., Akman, B., Hein, A., Rote, N. S., Cope, L. M., Snyder, A., Makarov, V., Budhu, S., Slamon, D. J., Wolchok, J. D., Pardoll, D. M., Beckmann, M. W., Zahnow, C. A., Merghoub, T., Chan, T. A., ... Strick, R. (2015). Inhibiting DNA Methylation Causes an Interferon Response in Cancer via dsRNA Including Endogenous Retroviruses. *Cell*, 162(5), 974–986. <https://doi.org/10.1016/j.cell.2015.07.011>
- Cordero, F. J., Huang, Z., Grenier, C., He, X., Hu, G., McLendon, R. E., Murphy, S. K., Hashizume, R., & Becher, O. J. (2017). Histone H3.3K27M represses p16 to accelerate gliomagenesis in a murine model of DIPG. *Molecular Cancer Research*, 15(9), 1243–1254. <https://doi.org/10.1158/1541-7786.MCR-16-0389>
- Court, F., Boiteux, E. Le, Fogli, A., Müller-Barthélémy, M., Vaurs-Barrière, C., Chautard, E., Pereira, B., Biau, J., Kemeny, J. L., Khalil, T., Karayan-Tapon, L., Verrelle, P., & Arnaud, P. (2019). Transcriptional alterations in glioma result primarily from DNA methylation-independent mechanisms. *Genome Research*, 29, 1605–1621. <https://doi.org/10.1101/516997>
- Creyghton, M. P., Cheng, A. W., Welstead, G. G., Kooistra, T., Carey, B. W., Steine, E. J., Hanna, J., Lodato, M. A., Frampton, G. M., Sharp, P. A., Boyer, L. A., Young, R. A., &

- Jaenisch, R. (2010). Histone H3K27ac separates active from poised enhancers and predicts developmental state. *Proceedings of the National Academy of Sciences of the United States of America*, *107*(50), 21931–21936. <https://doi.org/10.1073/pnas.1016071107>
- de Koning, A. P. J., Gu, W., Castoe, T. A., Batzer, M. A., & Pollock, D. D. (2011). Repetitive elements may comprise over two-thirds of the human genome. *PLoS Genetics*, *7*(12), e1002384. <https://doi.org/10.1371/journal.pgen.1002384>
- Delaney, K., Strobino, M., Wenda, J. M., Pankowski, A., & Steiner, F. A. (2019). H3.3K27M-induced chromatin changes drive ectopic replication through misregulation of the JNK pathway in *C. elegans*. *Nature Communications*, *10*(1), 1–15. <https://doi.org/10.1038/s41467-019-10404-9>
- Dhar, S. S., Zhao, D., Lin, T., Gu, B., Pal, K., Wu, S. J., Alam, H., Lv, J., Yun, K., Gopalakrishnan, V., Flores, E. R., Northcott, P. A., Rajaram, V., Li, W., Shilatifard, A., Sillitoe, R. V., Chen, K., & Lee, M. G. (2018). MLL4 Is Required to Maintain Broad H3K4me3 Peaks and Super-Enhancers at Tumor Suppressor Genes. *Molecular Cell*, *70*(5), 825-841.e6. <https://doi.org/10.1016/j.molcel.2018.04.028>
- Dobin, A., Davis, C. A., Schlesinger, F., Drenkow, J., Zaleski, C., Jha, S., Batut, P., Chaisson, M., & Gingeras, T. R. (2013). STAR: ultrafast universal RNA-seq aligner. *Bioinformatics (Oxford, England)*, *29*(1), 15–21. <https://doi.org/10.1093/bioinformatics/bts635>
- Elsässer, S. J., Noh, K.-M., Diaz, N., Allis, C. D., & Banaszynski, L. A. (2015). Histone H3.3 is required for endogenous retroviral element silencing in embryonic stem cells. *Nature*, *522*(7555), 240–244. <https://doi.org/10.1038/nature14345>
- Erkek, S., Johann, P. D., Finetti, M. A., Drosos, Y., Chou, H. C., Zapatka, M., Sturm, D., Jones, D. T. W., Korshunov, A., Rhyzova, M., Wolf, S., Mallm, J. P., Beck, K., Witt, O., Kulozik, A. E., Frühwald, M. C., Northcott, P. A., Korbel, J. O., Lichter, P., ... Kool, M. (2019). Comprehensive Analysis of Chromatin States in Atypical Teratoid/Rhabdoid Tumor Identifies Diverging Roles for SWI/SNF and Polycomb in Gene Regulation. *Cancer Cell*, *35*(1), 95-110.e8. <https://doi.org/10.1016/j.ccell.2018.11.014>
- Fang, D., Gan, H., Cheng, L., Lee, J.-H., Zhou, H., Sarkaria, J., Daniels, D., & Zhang, Z. (2018). H3.3K27M mutant proteins reprogram epigenome by sequestering the PRC2 complex to poised enhancers. *ELife*, *7*, 1–23. <https://doi.org/10.7554/eLife.36696> LK - <http://sfx.library.uu.nl/utrecht?sid=EMBASE&issn=2050084X&id=doi:10.7554%2FeLife.3>

6696&atitle=H3.3K27M+mutant+proteins+reprogram+epigenome+by+sequestering+the+P  
RC2+complex+to+poised+enhancers&stitle=eLife&title=eLife&volume=7&issue=&spage  
=&epage=&aulast=Fang&aufirst=Dong&aunit=D.&aufull=Fang+D.&coden=&isbn=&pag  
es=-&date=2018&aunit1=D&aunitm=

- Fang, J., Huang, Y., Mao, G., Yang, S., Rennert, G., Gu, L., Li, H., & Li, G. M. (2018). Cancer-driving H3G34V/R/D mutations block H3K36 methylation and H3K36me3-MutSa interaction. *Proceedings of the National Academy of Sciences of the United States of America*, *115*(38), 9598–9603. <https://doi.org/10.1073/pnas.1806355115>
- Faury, D., Nantel, A., Dunn, S. E., Guiot, M.-C., Haque, T., Hauser, P., Garami, M., Bognár, L., Hanzély, Z., Liberski, P. P., Lopez-Aguilar, E., Valera, E. T., Tone, L. G., Carret, A.-S., Del Maestro, R. F., Gleave, M., Montes, J.-L., Pietsch, T., Albrecht, S., & Jabado, N. (2007). Molecular profiling identifies prognostic subgroups of pediatric glioblastoma and shows increased YB-1 expression in tumors. *Journal of Clinical Oncology : Official Journal of the American Society of Clinical Oncology*, *25*(10), 1196–1208. <https://doi.org/10.1200/JCO.2006.07.8626>
- Feng, J., Liu, T., Qin, B., Zhang, Y., & Liu, X. S. (2012). Identifying ChIP-seq enrichment using MACS. *Nature Protocols*, *7*(9), 1728–1740. <https://doi.org/10.1038/nprot.2012.101>
- Ferrari, K. J., Scelfo, A., Jammula, S., Cuomo, A., Barozzi, I., Stützer, A., Fischle, W., Bonaldi, T., & Pasini, D. (2014). Polycomb-dependent H3K27me1 and H3K27me2 regulate active transcription and enhancer fidelity. *Molecular Cell*, *53*(1), 49–62. <https://doi.org/10.1016/j.molcel.2013.10.030>
- Filbin, M. G., Hovestadt, V., Shaw, M. L., Escalante, L. E., Nefel, C., Hebert, C. M., Egervari, K., Van Galen, P., Beck, A., Mylvaganam, R., Luo, C. C., Frosch, M. P., Martinez-Lage, M., Getz, G., Louis, D. N., Bernstein, B. E., Suvà, M. L., Sinai, C., Goumnerova, L., ... Batchelor, T. T. (2018). Developmental and oncogenic programs in H3K27M gliomas dissected by single-cell RNA-seq. *Science*, *360*(6386), 331–335. <https://doi.org/10.1126/science.aao4750>
- Fontebasso, A. M., Gayden, T., Nikbakht, H., Neirinck, M., Papillon-Cavanagh, S., Majewski, J., & Jabado, N. (2014). Epigenetic dysregulation: a novel pathway of oncogenesis in pediatric brain tumors. *Acta Neuropathologica*, *128*(5), 615–627. <https://doi.org/10.1007/s00401-014-1325-8>

- Fontebasso, A. M., Liu, X.-Y., Sturm, D., & Jabado, N. (2013). Chromatin remodeling defects in pediatric and young adult glioblastoma: a tale of a variant histone 3 tail. *Brain Pathology (Zurich, Switzerland)*, *23*(2), 210–216. <https://doi.org/10.1111/bpa.12023>
- Fontebasso, A. M., Papillon-Cavanagh, S., Schwartzenruber, J., Nikbakht, H., Gerges, N., Fiset, P. O., Bechet, D., Faury, D., De Jay, N., Ramkissoon, L. A., Corcoran, A., Jones, D. T. W., Sturm, D., Johann, P., Tomita, T., Goldman, S., Nagib, M., Bendel, A., Goumnerova, L., ... Kieran, M. W. (2014). Recurrent somatic mutations in ACVR1 in pediatric midline high-grade astrocytoma. *Nature Genetics*, *46*(5), 462–466. <https://doi.org/10.1038/ng.2950>
- Fontebasso, A. M., Schwartzenruber, J., Khuong-Quang, D. A., Liu, X. Y., Sturm, D., Korshunov, A., Jones, D. T. W., Witt, H., Kool, M., Albrecht, S., Fleming, A., Hadjadj, D., Busche, S., Lepage, P., Montpetit, A., Staffa, A., Gerges, N., Zakrzewska, M., Zakrzewski, K., ... Majewski, J. (2013). Mutations in SETD2 and genes affecting histone H3K36 methylation target hemispheric high-grade gliomas. *Acta Neuropathologica*, *125*(5), 659–669. <https://doi.org/10.1007/s00401-013-1095-8>
- Fortin, J., Tian, R., Zarrabi, I., Hill, G., Williams, E., Sanchez-Duffhues, G., Thorikay, M., Ramachandran, P., Siddaway, R., Wong, J. F., Wu, A., Apuzzo, L. N., Haight, J., You-Ten, A., Snow, B. E., Wakeham, A., Goldhamer, D. J., Schramek, D., Bullock, A. N., ... Mak, T. W. (2020). Mutant ACVR1 Arrests Glial Cell Differentiation to Drive Tumorigenesis in Pediatric Gliomas. *Cancer Cell*, *37*(3), 308–323. <https://doi.org/10.1016/j.ccell.2020.02.002>
- Funato, K., Major, T., Lewis, P. W., Allis, C. D., & Tabar, V. (2014). Use of human embryonic stem cells to model pediatric gliomas with H3.3K27M histone mutation. *Science*, *346*(6216), 1529–1533. <https://doi.org/10.1126/science.1253799>
- Funato, Kosuke, Smith, R. C., Saito, Y., & Tabar, V. (2021). Dissecting the impact of regional identity and the oncogenic role of human-specific NOTCH2NL in an hESC model of H3.3G34R-mutant glioma. *Cell Stem Cell*, *28*(5), 894-905.e7. <https://doi.org/10.1016/j.stem.2021.02.003>
- Ghandi, M., Huang, F. W., Jané-Valbuena, J., Kryukov, G. V., Lo, C. C., McDonald, E. R. 3rd, Barretina, J., Gelfand, E. T., Bielski, C. M., Li, H., Hu, K., Andreev-Drakhlin, A. Y., Kim, J., Hess, J. M., Haas, B. J., Aguet, F., Weir, B. A., Rothberg, M. V., Paoletta, B. R., ... Sellers, W. R. (2019). Next-generation characterization of the Cancer Cell Line Encyclopedia. *Nature*, *569*(7757), 503–508. <https://doi.org/10.1038/s41586-019-1186-3>

- Göke, J., Lu, X., Chan, Y.-S., Ng, H.-H., Ly, L.-H., Sachs, F., & Szczerbinska, I. (2015). Dynamic transcription of distinct classes of endogenous retroviral elements marks specific populations of early human embryonic cells. *Cell Stem Cell*, *16*(2), 135–141. <https://doi.org/10.1016/j.stem.2015.01.005>
- Grasso, C. S., Tang, Y., Truffaux, N., Berlow, N. E., Liu, L., Debily, M.-A., Quist, M. J., Davis, L. E., Huang, E. C., Woo, P. J., Ponnuswami, A., Chen, S., Johung, T. B., Sun, W., Kogiso, M., Du, Y., Qi, L., Huang, Y., Hütt-Cabezas, M., ... Monje, M. (2015). Functionally defined therapeutic targets in diffuse intrinsic pontine glioma. In *Nature medicine* (Vol. 21, Issue 7, p. 827). <https://doi.org/10.1038/nm0715-827a>
- Hammond, C. M., Strømme, C. B., Huang, H., Patel, D. J., & Groth, A. (2017). Histone chaperone networks shaping chromatin function. *Nature Reviews. Molecular Cell Biology*, *18*(3), 141–158. <https://doi.org/10.1038/nrm.2016.159>
- Han, Z. Y., Richer, W., Fréneaux, P., Chauvin, C., Lucchesi, C., Guillemot, D., Grison, C., Lequin, D., Pierron, G., Masliah-Planchon, J., Nicolas, A., Ranchère-Vince, D., Varlet, P., Puget, S., Janoueix-Lerosey, I., Ayrault, O., Surdez, D., Delattre, O., & Bourdeaut, F. (2016). The occurrence of intracranial rhabdoid tumours in mice depends on temporal control of Smarcb1 inactivation. *Nature Communications*, *7*. <https://doi.org/10.1038/ncomms10421>
- Haque, T., Faury, D., Albrecht, S., Lopez-Aguilar, E., Hauser, P., Garami, M., Hanzély, Z., Bognár, L., Del Maestro, R. F., Atkinson, J., Nantel, A., & Jabado, N. (2007). Gene expression profiling from formalin-fixed paraffin-embedded tumors of pediatric glioblastoma. *Clinical Cancer Research : An Official Journal of the American Association for Cancer Research*, *13*(21), 6284–6292. <https://doi.org/10.1158/1078-0432.CCR-07-0525>
- Harutyunyan, A. S., Chen, H., Lu, T., Horth, C., Nikbakht, H., Krug, B., Russo, C., Bareke, E., Marchione, D. M., Coradin, M., Garcia, B. A., Jabado, N., & Majewski, J. (2020). H3K27M in Gliomas Causes a One-Step Decrease in H3K27 Methylation and Reduced Spreading within the Constraints of H3K36 Methylation. *Cell Reports*, *33*(7), 108390. <https://doi.org/10.1016/j.celrep.2020.108390>
- Hashizume, R., Andor, N., Ihara, Y., Lerner, R., Gan, H., Chen, X., Fang, D., Huang, X., Tom, M. W., Ngo, V., Solomon, D., Mueller, S., Paris, P. L., Zhang, Z., Petritsch, C., Gupta, N., Waldman, T. A., & James, C. D. (2014). Pharmacologic inhibition of histone demethylation

- as a therapy for pediatric brainstem glioma. *Nature Medicine*, 20(12), 1394–1396.  
<https://doi.org/10.1038/nm.3716>
- Heinz, S., Benner, C., Spann, N., Bertolino, E., Lin, Y. C., Laslo, P., Cheng, J. X., Murre, C., Singh, H., & Glass, C. K. (2010). Simple combinations of lineage-determining transcription factors prime cis-regulatory elements required for macrophage and B cell identities. *Molecular Cell*, 38(4), 576–589. <https://doi.org/10.1016/j.molcel.2010.05.004>
- Herz, H.-M., Morgan, M., Gao, X., Jackson, J., Rickels, R., Swanson, S. K., Florens, L., Washburn, M. P., Eissenberg, J. C., & Shilatifard, A. (2014). Histone H3 lysine-to-methionine mutants as a paradigm to study chromatin signaling. *Science (New York, N.Y.)*, 345(6200), 1065–1070. <https://doi.org/10.1126/science.1255104>
- Højfeldt, J. W., Laugesen, A., Willumsen, B. M., Damhofer, H., Hedehus, L., Tvardovskiy, A., Mohammad, F., Jensen, O. N., & Helin, K. (2018). Accurate H3K27 methylation can be established de novo by SUZ12-directed PRC2. *Nature Structural & Molecular Biology*, 25(3), 225–232. <https://doi.org/10.1038/s41594-018-0036-6>
- Huang, T. Y.-T., Piunti, A., Qi, J., Morgan, M., Bartom, E., Shilatifard, A., & Saratsis, A. M. (2020). Effects of H3.3G34V mutation on genomic H3K36 and H3K27 methylation patterns in isogenic pediatric glioma cells. *Acta Neuropathologica Communications*, 8(1), 219. <https://doi.org/10.1186/s40478-020-01092-4>
- Hübner, J.-M., Müller, T., Papageorgiou, D. N., Mauermann, M., Krijgsveld, J., Russell, R. B., Ellison, D. W., Pfister, S. M., Pajtler, K. W., & Kool, M. (2019). EZHIP/CXorf67 mimics K27M mutated oncohistones and functions as an intrinsic inhibitor of PRC2 function in aggressive posterior fossa ependymoma. *Neuro-Oncology*, 21(7), 878–889.  
<https://doi.org/10.1093/neuonc/noz058>
- Intlekofer, A. M., & Finley, L. W. S. (2019). Metabolic signatures of cancer cells and stem cells. *Nature Metabolism*, 1(2), 177–188. <https://doi.org/10.1038/s42255-019-0032-0>
- Jain, S. U., Do, T. J., Lund, P. J., Rashoff, A. Q., Diehl, K. L., Cieslik, M., Bajic, A., Juretic, N., Deshmukh, S., Venneti, S., Muir, T. W., Garcia, B. A., Jandolo, N., & Lewis, P. W. (2019). PFA ependymoma-associated protein EZHIP inhibits PRC2 activity through a H3 K27M-like mechanism. *Nature Communications*, 10(1). <https://doi.org/10.1038/s41467-019-09981-6>
- Jain, S. U., Khazaei, S., Marchione, D. M., Lundgren, S. M., Wang, X., Weinberg, D. N.,

- Deshmukh, S., Juretic, N., Lu, C., David Allis, C., Garcia, B. A., Jabado, N., & Lewis, P. W. (2020). Histone H3.3 G34 mutations promote aberrant PRC2 activity and drive tumor progression. *Proceedings of the National Academy of Sciences of the United States of America*, *117*(44), 27354–27364. <https://doi.org/10.1073/pnas.2006076117>
- Jain, S. U., Rashoff, A. Q., Krabbenhoft, S. D., Hoelper, D., Do, T. J., Gibson, T. J., Lundgren, S. M., Bondra, E. R., Deshmukh, S., Harutyunyan, A. S., Juretic, N., Jabado, N., Harrison, M. M., & Lewis, P. W. (2020). H3 K27M and EZHIP Impede H3K27-Methylation Spreading by Inhibiting Allosterically Stimulated PRC2. *Molecular Cell*, *80*(4), 726-735.e7. <https://doi.org/10.1016/j.molcel.2020.09.028>
- Jansz, N. (2019). DNA methylation dynamics at transposable elements in mammals. *Essays in Biochemistry*, *63*(6), 677–689. <https://doi.org/10.1042/EBC20190039>
- Jenuwein, T., & Allis, C. D. (2001). Translating the histone code. *Science (New York, N.Y.)*, *293*(5532), 1074–1080. <https://doi.org/10.1126/science.1063127>
- Jessa, S., Blanchet-Cohen, A., Krug, B., Vladoiu, M., Coutelier, M., Faury, D., Poreau, B., De Jay, N., Hébert, S., Monlong, J., Farmer, W. T., Donovan, L. K., Hu, Y., McConechy, M. K., Cavalli, F. M. G., Mikael, L. G., Ellezam, B., Richer, M., Allaire, A., ... Kleinman, C. L. (2019). Stalled developmental programs at the root of pediatric brain tumors. *Nature Genetics*, *51*(12), 1702–1713. <https://doi.org/10.1038/s41588-019-0531-7>
- Jiao, L., & Liu, X. (2015). Structural basis of histone H3K27 trimethylation by an active polycomb repressive complex 2. *Science (New York, N.Y.)*, *350*(6258), aac4383. <https://doi.org/10.1126/science.aac4383>
- Jih, G., Iglesias, N., Currie, M. A., Bhanu, N. V, Paulo, J. A., Gygi, S. P., Garcia, B. A., & Moazed, D. (2017). Unique roles for histone H3K9me states in RNAi and heritable silencing of transcription. *Nature*, *547*(7664), 463–467. <https://doi.org/10.1038/nature23267>
- Jo, H., & Koh, G. (2015). Faster single-end alignment generation utilizing multi-thread for BWA. *Bio-Medical Materials and Engineering*, *26 Suppl 1*, S1791-6. <https://doi.org/10.3233/BME-151480>
- Johann, P. D., Erkek, S., Zapatka, M., Kerl, K., Buchhalter, I., Hovestadt, V., Jones, D. T. W., Sturm, D., Hermann, C., Segura Wang, M., Korshunov, A., Rhyzova, M., Gröbner, S., Brabetz, S., Chavez, L., Bens, S., Gröschel, S., Kratochwil, F., Wittmann, A., ... Kool, M.

- (2016). Atypical Teratoid/Rhabdoid Tumors Are Comprised of Three Epigenetic Subgroups with Distinct Enhancer Landscapes. *Cancer Cell*, 29(3), 379–393.  
<https://doi.org/10.1016/j.ccell.2016.02.001>
- Jones, P. A., Ohtani, H., Chakravarthy, A., & De Carvalho, D. D. (2019). Epigenetic therapy in immune-oncology. *Nature Reviews. Cancer*, 19(3), 151–161.  
<https://doi.org/10.1038/s41568-019-0109-9>
- Joyon, N., Tauziède-Espariat, A., Alentorn, A., Giry, M., Castel, D., Capelle, L., Zanello, M., Varlet, P., & Bielle, F. (2017). K27M mutation in H3F3A in ganglioglioma grade I with spontaneous malignant transformation extends the histopathological spectrum of the histone H3 oncogenic pathway. In *Neuropathology and applied neurobiology* (Vol. 43, Issue 3, pp. 271–276). <https://doi.org/10.1111/nan.12329>
- Juratli, T. A., Kirsch, M., Robel, K., Soucek, S., Geiger, K., Von Kummer, R., Schackert, G., & Krex, D. (2012). IDH mutations as an early and consistent marker in low-grade astrocytomas WHO grade II and their consecutive secondary high-grade gliomas. *Journal of Neuro-Oncology*, 108(3), 403–410. <https://doi.org/10.1007/s11060-012-0844-1>
- Justin, N., Zhang, Y., Tarricone, C., Martin, S. R., Chen, S., Underwood, E., De Marco, V., Haire, L. F., Walker, P. A., Reinberg, D., Wilson, J. R., & Gamblin, S. J. (2016). Structural basis of oncogenic histone H3K27M inhibition of human polycomb repressive complex 2. *Nature Communications*, 7, 11316. <https://doi.org/10.1038/ncomms11316>
- Kang, P., Lee, H. K., Glasgow, S. M., Finley, M., Donti, T., Gaber, Z. B., Graham, B. H., Foster, A. E., Novitch, B. G., Gronostajski, R. M., & Deneen, B. (2012). Sox9 and NFIA coordinate a transcriptional regulatory cascade during the initiation of gliogenesis. *Neuron*, 74(1), 79–94. <https://doi.org/10.1016/j.neuron.2012.01.024>
- Karch, K. R., Sidoli, S., & Garcia, B. A. (2016). Identification and Quantification of Histone PTMs Using High-Resolution Mass Spectrometry. *Methods in Enzymology*, 574, 3–29.  
<https://doi.org/10.1016/bs.mie.2015.12.007>
- Khazaei, S., De Jay, N., Deshmukh, S., Hendrikse, L. D., Jawhar, W., Chen, C. C. L., Mikael, L. G., Faury, D., Marchione, D. M., Lanoix, J., Bonneil, É., Ishii, T., Jain, S. U., Rossokhata, K., Sihota, T. S., Eveleigh, R., Lisi, V., Harutyunyan, A. S., Jung, S., ... Jabado, N. (2020). H3.3 G34W Promotes Growth and Impedes Differentiation of Osteoblast-Like Mesenchymal Progenitors in Giant Cell Tumor of Bone. *Cancer Discovery*, 10(12), 1968–

1987. <https://doi.org/10.1158/2159-8290.cd-20-0461>

- Khuong-Quang, D. A., Buczkowicz, P., Rakopoulos, P., Liu, X. Y., Fontebasso, A. M., Bouffet, E., Bartels, U., Albrecht, S., Schwartzentruber, J., Letourneau, L., Bourgey, M., Bourque, G., Montpetit, A., Bourret, G., Lepage, P., Fleming, A., Lichter, P., Kool, M., Von Deimling, A., ... Hawkins, C. (2012). K27M mutation in histone H3.3 defines clinically and biologically distinct subgroups of pediatric diffuse intrinsic pontine gliomas. *Acta Neuropathologica*, *124*(3), 439–447. <https://doi.org/10.1007/s00401-012-0998-0>
- Kleinman, C. L., Gerges, N., Papillon-Cavanagh, S., Sin-Chan, P., Pramatarova, A., Quang, D.-A. K., Adoue, V., Busche, S., Caron, M., Djambazian, H., Bemmo, A., Fontebasso, A. M., Spence, T., Schwartzentruber, J., Albrecht, S., Hauser, P., Garami, M., Klekner, A., Bogнар, L., ... Jabado, N. (2014). Fusion of TTYH1 with the C19MC microRNA cluster drives expression of a brain-specific DNMT3B isoform in the embryonal brain tumor ETMR. *Nature Genetics*, *46*(1), 39–44. <https://doi.org/10.1038/ng.2849>
- Langmead, B., & Salzberg, S. L. (2012). Fast gapped-read alignment with Bowtie 2. *Nature Methods*, *9*(4), 357–359. <https://doi.org/10.1038/nmeth.1923>
- Larson, J. D., Kasper, L. H., Paugh, B. S., Jin, H., Wu, G., Kwon, C. H., Fan, Y., Shaw, T. I., Silveira, A. B., Qu, C., Xu, R., Zhu, X., Zhang, J., Russell, H. R., Peters, J. L., Finkelstein, D., Xu, B., Lin, T., Tinkle, C. L., ... Baker, S. J. (2019). Histone H3.3 K27M Accelerates Spontaneous Brainstem Glioma and Drives Restricted Changes in Bivalent Gene Expression. *Cancer Cell*, *35*(1), 140-155.e7. <https://doi.org/10.1016/j.ccell.2018.11.015>
- Laugesen, A., Højfeldt, J. W., & Helin, K. (2019). Molecular Mechanisms Directing PRC2 Recruitment and H3K27 Methylation. *Molecular Cell*, *74*(1), 8–18. <https://doi.org/10.1016/j.molcel.2019.03.011>
- Lee, C.-H., Yu, J.-R., Granat, J., Saldaña-Meyer, R., Andrade, J., LeRoy, G., Jin, Y., Lund, P., Stafford, J. M., Garcia, B. A., Ueberheide, B., & Reinberg, D. (2019). Automethylation of PRC2 promotes H3K27 methylation and is impaired in H3K27M pediatric glioma. *Genes & Development*, *33*, 1–13. <https://doi.org/10.1101/gad.328773.119>
- Lee, W., Teckie, S., Wiesner, T., Ran, L., Prieto Granada, C. N., Lin, M., Zhu, S., Cao, Z., Liang, Y., Sboner, A., Tap, W. D., Fletcher, J. A., Huberman, K. H., Qin, L.-X., Viale, A., Singer, S., Zheng, D., Berger, M. F., Chen, Y., ... Chi, P. (2014). PRC2 is recurrently inactivated through EED or SUZ12 loss in malignant peripheral nerve sheath tumors.

- Nature Genetics*, 46(11), 1227–1232. <https://doi.org/10.1038/ng.3095>
- Lewis, P. W., Muller, M. M., Koletsky, M. S., Cordero, F., Lin, S., Banaszynski, L. a, Garcia, B. a, Muir, T. W., Becher, O. J., & Allis, C. D. (2013). Inhibition of PRC2 Activity by a Gain-of-Function H3 Mutation Found in Pediatric Glioblastoma. *Science*, 340(May), 857–861. <https://doi.org/10.1126/science.1232245>
- Li, H., & Durbin, R. (2009). Fast and accurate short read alignment with Burrows-Wheeler transform. *Bioinformatics (Oxford, England)*, 25(14), 1754–1760. <https://doi.org/10.1093/bioinformatics/btp324>
- Li, H., Handsaker, B., Wysoker, A., Fennell, T., Ruan, J., Homer, N., Marth, G., Abecasis, G., & Durbin, R. (2009). The Sequence Alignment/Map format and SAMtools. *Bioinformatics (Oxford, England)*, 25(16), 2078–2079. <https://doi.org/10.1093/bioinformatics/btp352>
- Liao, Y., Smyth, G. K., & Shi, W. (2014). featureCounts: an efficient general purpose program for assigning sequence reads to genomic features. *Bioinformatics (Oxford, England)*, 30(7), 923–930. <https://doi.org/10.1093/bioinformatics/btt656>
- Lin, C. Y., Erkek, S., Tong, Y., Yin, L., Federation, A. J., Zapatka, M., Haldipur, P., Kawauchi, D., Risch, T., Warnatz, H. J., Worst, B. C., Ju, B., Orr, B. A., Zeid, R., Polaski, D. R., Segura-Wang, M., Waszak, S. M., Jones, D. T. W., Kool, M., ... Northcott, P. A. (2016). Active medulloblastoma enhancers reveal subgroup-specific cellular origins. *Nature*, 530(7588), 57–62. <https://doi.org/10.1038/nature16546>
- Lin, G. L., Wilson, K. M., Ceribelli, M., Stanton, B. Z., Woo, P. J., Kreimer, S., Qin, E. Y., Zhang, X., Lennon, J., Nagaraja, S., Morris, P. J., Quezada, M., Gillespie, S. M., Duveau, D. Y., Michalowski, A. M., Shinn, P., Guha, R., Ferrer, M., Klumpp-Thomas, C., ... Monje, M. (2019). Therapeutic strategies for diffuse midline glioma from high-throughput combination drug screening. *Science Translational Medicine*, 11(519). <https://doi.org/10.1126/scitranslmed.aaw0064>
- Liu, X. Y., Gerges, N., Korshunov, A., Sabha, N., Khuong-Quang, D. A., Fontebasso, A. M., Fleming, A., Hadjadj, D., Schwartzentruber, J., Majewski, J., Dong, Z., Siegel, P., Albrecht, S., Croul, S., Jones, D. T. W., Kool, M., Tonjes, M., Reifenberger, G., Faury, D., ... Jabado, N. (2012). Frequent ATRX mutations and loss of expression in adult diffuse astrocytic tumors carrying IDH1/IDH2 and TP53 mutations. *Acta Neuropathologica*, 124(5), 615–625. <https://doi.org/10.1007/s00401-012-1031-3>

- Louis, D. N., Perry, A., Reifenberger, G., von Deimling, A., Figarella-Branger, D., Cavenee, W. K., Ohgaki, H., Wiestler, O. D., Kleihues, P., & Ellison, D. W. (2016). The 2016 World Health Organization Classification of Tumors of the Central Nervous System: a summary. *Acta Neuropathologica*, *131*(6), 803–820. <https://doi.org/10.1007/s00401-016-1545-1>
- Louis, D. N., Perry, A., Wesseling, P., Brat, D. J., Cree, I. A., Figarella-Branger, D., Hawkins, C., Ng, H. K., Pfister, S. M., Reifenberger, G., Soffietti, R., von Deimling, A., & Ellison, D. W. (2021). The 2021 WHO Classification of Tumors of the Central Nervous System: a summary. *Neuro-Oncology*, *23*(8), 1231–1251. <https://doi.org/10.1093/neuonc/noab106>
- Lovén, J., Hoke, H. A., Lin, C. Y., Lau, A., Orlando, D. A., Vakoc, C. R., Bradner, J. E., Lee, T. I., & Young, R. A. (2013). Selective inhibition of tumor oncogenes by disruption of super-enhancers. *Cell*, *153*(2), 320–334. <https://doi.org/10.1016/j.cell.2013.03.036>
- Lu, C., Jain, S. U., Hoelper, D., Bechet, D., Molden, R. C., Ran, L., Murphy, D., Venneti, S., Hameed, M., Pawel, B. R., Wunder, J. S., Dickson, B. C., Lundgren, S. M., Jani, K. S., De Jay, N., Papillon-Cavanagh, S., Andrulis, I. L., Sawyer, S. L., Grynspan, D., ... Lewis, P. W. (2016). Histone H3K36 mutations promote sarcomagenesis through altered histone methylation landscape. *Science (New York, N.Y.)*, *352*(6287), 844–849. <https://doi.org/10.1126/science.aac7272>
- Lu, C., Ward, P. S., Kapoor, G. S., Rohle, D., Turcan, S., Abdel-Wahab, O., Edwards, C. R., Khanin, R., Figueroa, M. E., Melnick, A., Wellen, K. E., Oğrourke, D. M., Berger, S. L., Chan, T. A., Levine, R. L., Mellinghoff, I. K., & Thompson, C. B. (2012). IDH mutation impairs histone demethylation and results in a block to cell differentiation. *Nature*, *483*(7390), 474–478. <https://doi.org/10.1038/nature10860>
- M. Gagné, L., Boulay, K., Topisirovic, I., Huot, M. É., & Mallette, F. A. (2017). Oncogenic Activities of IDH1/2 Mutations: From Epigenetics to Cellular Signaling. *Trends in Cell Biology*, *27*(10), 738–752. <https://doi.org/10.1016/j.tcb.2017.06.002>
- Machold, R., Klein, C., & Fishell, G. (2011). Genes expressed in Atoh1 neuronal lineages arising from the r1/isthmus rhombic lip. *Gene Expression Patterns : GEP*, *11*(5–6), 349–359. <https://doi.org/10.1016/j.gep.2011.03.007>
- Mack, S. C., Witt, H., Piro, R. M., Gu, L., Zuyderduyn, S., Stütz, A. M., Wang, X., Gallo, M., Garzia, L., Zayne, K., Zhang, X., Ramaswamy, V., Jäger, N., Jones, D. T. W., Sill, M., Pugh, T. J., Ryzhova, M., Wani, K. M., Shih, D. J. H., ... Taylor, M. D. (2014). Epigenomic

- alterations define lethal CIMP-positive ependymomas of infancy. *Nature*, 506(7489), 445–450. <https://doi.org/10.1038/nature13108>
- Mack, Stephen C., Pajtlér, K. W., Chavez, L., Okonechnikov, K., Bertrand, K. C., Wang, X., Erkek, S., Federation, A., Song, A., Lee, C., Wang, X., McDonald, L., Morrow, J. J., Saiakhova, A., Sin-Chan, P., Wu, Q., Michaelraj, K. A., Miller, T. E., Hubert, C. G., ... Rich, J. N. (2018). Therapeutic targeting of ependymoma as informed by oncogenic enhancer profiling. *Nature*, 553(7686), 101–105. <https://doi.org/10.1038/nature25169>
- Mackay, A., Burford, A., Carvalho, D., Izquierdo, E., Fazal-Salom, J., Taylor, K. R., Bjerke, L., Clarke, M., Vinci, M., Nandhabalan, M., Temelso, S., Popov, S., Molinari, V., Raman, P., Waanders, A. J., Han, H. J., Gupta, S., Marshall, L., Zacharoulis, S., ... Jones, C. (2017). Integrated Molecular Meta-Analysis of 1,000 Pediatric High-Grade and Diffuse Intrinsic Pontine Glioma. *Cancer Cell*, 32(4), 520-537.e5. <https://doi.org/10.1016/j.ccell.2017.08.017>
- Margueron, Raphael, Justin, N., Ohno, K., Sharpe, M. L., Son, J., Drury, W. J. 3rd, Voigt, P., Martin, S. R., Taylor, W. R., De Marco, V., Pirrotta, V., Reinberg, D., & Gambin, S. J. (2009). Role of the polycomb protein EED in the propagation of repressive histone marks. *Nature*, 461(7265), 762–767. <https://doi.org/10.1038/nature08398>
- Margueron, Raphaël, & Reinberg, D. (2011). The Polycomb complex PRC2 and its mark in life. *Nature*, 469(7330), 343–349. <https://doi.org/10.1038/nature09784>
- Marmorstein, R., & Zhou, M.-M. (2014). Writers and readers of histone acetylation: structure, mechanism, and inhibition. *Cold Spring Harbor Perspectives in Biology*, 6(7), a018762. <https://doi.org/10.1101/cshperspect.a018762>
- Matys, V., Kel-Margoulis, O. V, Fricke, E., Liebich, I., Land, S., Barre-Dirrie, A., Reuter, I., Chekmenev, D., Krull, M., Hornischer, K., Voss, N., Stegmaier, P., Lewicki-Potapov, B., Saxel, H., Kel, A. E., & Wingender, E. (2006). TRANSFAC and its module TRANSCompel: transcriptional gene regulation in eukaryotes. *Nucleic Acids Research*, 34(Database issue), D108-10. <https://doi.org/10.1093/nar/gkj143>
- McCabe, M. T., Graves, A. P., Ganji, G., Diaz, E., Halsey, W. S., Jiang, Y., Smitheman, K. N., Ott, H. M., Pappalardi, M. B., Allen, K. E., Chen, S. B., Della Pietra, A. 3rd, Dul, E., Hughes, A. M., Gilbert, S. A., Thrall, S. H., Tummino, P. J., Kruger, R. G., Brandt, M., ... Creasy, C. L. (2012). Mutation of A677 in histone methyltransferase EZH2 in human B-cell lymphoma promotes hypertrimethylation of histone H3 on lysine 27 (H3K27). *Proceedings*

- of the National Academy of Sciences of the United States of America*, 109(8), 2989–2994.  
<https://doi.org/10.1073/pnas.1116418109>
- Michealraj, K. A., Kumar, S. A., Kim, L. J. Y., Cavalli, F. M. G., Przelicki, D., Wojcik, J. B., Delaidelli, A., Bajic, A., Saulnier, O., MacLeod, G., Vellanki, R. N., Vladoiu, M. C., Guilhamon, P., Ong, W., Lee, J. J. Y., Jiang, Y., Holgado, B. L., Rasnitsyn, A., Malik, A. A., ... Taylor, M. D. (2020). Metabolic Regulation of the Epigenome Drives Lethal Infantile Ependymoma. *Cell*, 181(6), 1329-1345.e24.  
<https://doi.org/10.1016/j.cell.2020.04.047>
- Mikkelsen, T. S., Ku, M., Jaffe, D. B., Issac, B., Lieberman, E., Giannoukos, G., Alvarez, P., Brockman, W., Kim, T.-K., Koche, R. P., Lee, W., Mendenhall, E., O'Donovan, A., Presser, A., Russ, C., Xie, X., Meissner, A., Wernig, M., Jaenisch, R., ... Bernstein, B. E. (2007). Genome-wide maps of chromatin state in pluripotent and lineage-committed cells. *Nature*, 448(7153), 553–560. <https://doi.org/10.1038/nature06008>
- Mohammad, F., Weissmann, S., Leblanc, B., Pandey, D. P., H, J. W., Comet, I., Zheng, C., Vilstrup Johansen, J., Rapin, N., Porse, B. T., Tvardovskiy, A., Jensen, O. N., Olaciregui, N. G., Lavarino, C., Su, M., de Torres, C., Mora, J., Carcaboso, A. M., & Helin, K. (2017). EZH2 is a potential therapeutic target for H3K27M-mutant pediatric gliomas. *Nature Medicine*, November 2016. <https://doi.org/10.1038/nm.4293>
- Mohn, F., Weber, M., Rebhan, M., Roloff, T. C., Richter, J., Stadler, M. B., Bibel, M., & Schübeler, D. (2008). Lineage-specific polycomb targets and de novo DNA methylation define restriction and potential of neuronal progenitors. *Molecular Cell*, 30(6), 755–766.  
<https://doi.org/10.1016/j.molcel.2008.05.007>
- Monje, M., Mitra, S. S., Freret, M. E., Raveh, T. B., Kim, J., Masek, M., Attema, J. L., Li, G., Haddix, T., Edwards, M. S. B., Fisher, P. G., Weissman, I. L., Rowitch, D. H., Vogel, H., Wong, A. J., & Beachy, P. A. (2011). Hedgehog-responsive candidate cell of origin for diffuse intrinsic pontine glioma. *Proceedings of the National Academy of Sciences*, 108(11), 4453–4458. <https://doi.org/10.1073/pnas.1101657108>
- Mootha, V. K., Lindgren, C. M., Eriksson, K.-F., Subramanian, A., Sihag, S., Lehar, J., Puigserver, P., Carlsson, E., Ridderstråle, M., Laurila, E., Houstis, N., Daly, M. J., Patterson, N., Mesirov, J. P., Golub, T. R., Tamayo, P., Spiegelman, B., Lander, E. S., Hirschhorn, J. N., ... Groop, L. C. (2003). PGC-1alpha-responsive genes involved in

- oxidative phosphorylation are coordinately downregulated in human diabetes. *Nature Genetics*, 34(3), 267–273. <https://doi.org/10.1038/ng1180>
- Nagaraja, S., Vitanza, N. A., Woo, P. J., Taylor, K. R., Liu, F., Zhang, L., Li, M., Meng, W., Ponnuswami, A., Sun, W., Ma, J., Hulleman, E., Swigut, T., Wysocka, J., Tang, Y., & Monje, M. (2017). Transcriptional Dependencies in Diffuse Intrinsic Pontine Glioma. *Cancer Cell*, 31(5), 635–652.e6. <https://doi.org/10.1016/j.ccell.2017.03.011>
- Narayanan, R., Pirouz, M., Kerimoglu, C., Pham, L., Wagener, R. J., Kiszka, K. A., Rosenbusch, J., Seong, R. H., Kessel, M., Fischer, A., Stoykova, A., Staiger, J. F., & Tuoc, T. (2015). Loss of BAF (mSWI/SNF) Complexes Causes Global Transcriptional and Chromatin State Changes in Forebrain Development. *Cell Reports*, 13(9), 1842–1854. <https://doi.org/10.1016/j.celrep.2015.10.046>
- Ng, J. M. Y., Martinez, D., Marsh, E. D., Zhang, Z., Rappaport, E., Santi, M., & Curran, T. (2015). Generation of a Mouse Model of Atypical Teratoid / Rhabdoid Tumor of the Central Nervous System through Combined Deletion of Snf5 and p53. *Cancer Research*, 4629–4640. <https://doi.org/10.1158/0008-5472.CAN-15-0874>
- Niessen, H. E. C., Demmers, J. A., & Voncken, J. W. (2009). Talking to chromatin: post-translational modulation of polycomb group function. *Epigenetics & Chromatin*, 2(1), 10. <https://doi.org/10.1186/1756-8935-2-10>
- Nikbakht, H., Panditharatna, E., Mikael, L. G., Li, R., Gayden, T., Osmond, M., Ho, C. Y., Kambhampati, M., Hwang, E. I., Faury, D., Siu, A., Papillon-Cavanagh, S., Bechet, D., Ligon, K. L., Ellezam, B., Ingram, W. J., Stinson, C., Moore, A. S., Warren, K. E., ... Nazarian, J. (2016). Spatial and temporal homogeneity of driver mutations in diffuse intrinsic pontine glioma. *Nature Communications*, 7. <https://doi.org/10.1038/ncomms11185>
- Northcott, P. A., Buchhalter, I., Morrissy, A. S., Hovestadt, V., Weischenfeldt, J., Ehrenberger, T., Gröbner, S., Segura-Wang, M., Zichner, T., Rudneva, V. A., Warnatz, H. J., Sidiropoulos, N., Phillips, A. H., Schumacher, S., Kleinheinz, K., Waszak, S. M., Erkek, S., Jones, D. T. W., Worst, B. C., ... Lichter, P. (2017). The whole-genome landscape of medulloblastoma subtypes. *Nature*, 547(7663), 311–317. <https://doi.org/10.1038/nature22973>
- Noushmehr, H., Weisenberger, D. J., Diefes, K., Phillips, H. S., Pujara, K., Berman, B. P., Pan, F., Pelloski, C. E., Sulman, E. P., Bhat, K. P., Verhaak, R. G. W., Hoadley, K. A., Hayes, D.

- N., Perou, C. M., Schmidt, H. K., Ding, L., Wilson, R. K., Van Den Berg, D., Shen, H., ... Aldape, K. (2010). Identification of a CpG Island Methylator Phenotype that Defines a Distinct Subgroup of Glioma. *Cancer Cell*, *17*(5), 510–522.  
<https://doi.org/10.1016/j.ccr.2010.03.017>
- Oksuz, O., Narendra, V., Lee, C.-H., Descostes, N., LeRoy, G., Raviram, R., Blumenberg, L., Karch, K., Rocha, P. P., Garcia, B. A., Skok, J. A., & Reinberg, D. (2018). Capturing the Onset of PRC2-Mediated Repressive Domain Formation. *Molecular Cell*, *70*(6), 1149–1162.e5. <https://doi.org/10.1016/j.molcel.2018.05.023>
- Orlando, D. A., Chen, M. W., Brown, V. E., Solanki, S., Choi, Y. J., Olson, E. R., Fritz, C. C., Bradner, J. E., & Guenther, M. G. (2014). Quantitative ChIP-Seq normalization reveals global modulation of the epigenome. *Cell Reports*, *9*(3), 1163–1170.  
<https://doi.org/10.1016/j.celrep.2014.10.018>
- Pajtler, K. W., Wen, J., Sill, M., Lin, T., Orisme, W., Tang, B., Hübner, J. M., Ramaswamy, V., Jia, S., Dalton, J. D., Hauptfear, K., Rogers, H. A., Punchihewa, C., Lee, R., Easton, J., Wu, G., Ritzmann, T. A., Chapman, R., Chavez, L., ... Ellison, D. W. (2018). Molecular heterogeneity and CXorf67 alterations in posterior fossa group A (PFA) ependymomas. *Acta Neuropathologica*, *136*(2), 211–226. <https://doi.org/10.1007/s00401-018-1877-0>
- Pajtler, K. W., Witt, H., Sill, M., Jones, D. T. W., Hovestadt, V., Kratochwil, F., Wani, K., Tatevossian, R., Punchihewa, C., Johann, P., Reimand, J., Warnatz, H. J., Ryzhova, M., Mack, S., Ramaswamy, V., Capper, D., Schweizer, L., Sieber, L., Wittmann, A., ... Pfister, S. M. (2015). Molecular Classification of Ependymal Tumors across All CNS Compartments, Histopathological Grades, and Age Groups. *Cancer Cell*, *27*(5), 728–743.  
<https://doi.org/10.1016/j.ccell.2015.04.002>
- Pathania, M., De Jay, N., Maestro, N., Harutyunyan, A. S., Nitarska, J., Pahlavan, P., Henderson, S., Mikael, L. G., Richard-Londt, A., Zhang, Y., Costa, J. R., Hébert, S., Khazaei, S., Ibrahim, N. S., Herrero, J., Riccio, A., Albrecht, S., Ketteler, R., Brandner, S., ... Salomoni, P. (2017). H3.3K27M Cooperates with Trp53 Loss and PDGFRA Gain in Mouse Embryonic Neural Progenitor Cells to Induce Invasive High-Grade Gliomas. *Cancer Cell*, *32*(5), 684–700.e9. <https://doi.org/10.1016/j.ccell.2017.09.014>
- Piunti, A., Hashizume, R., Morgan, M. A., Bartom, E. T., Horbinski, C. M., Marshall, S. A., Rendleman, E. J., Ma, Q., Takahashi, Y. H., Woodfin, A. R., Misharin, A. V., Abshiru, N.

- A., Lulla, R. R., Saratsis, A. M., Kelleher, N. L., James, C. D., & Shilatifard, A. (2017). Therapeutic targeting of polycomb and BET bromodomain proteins in diffuse intrinsic pontine gliomas. *Nature Medicine*, 23(4), 493–500. <https://doi.org/10.1038/nm.4296>
- Piunti, A., & Shilatifard, A. (2021). The roles of Polycomb repressive complexes in mammalian development and cancer. *Nature Reviews. Molecular Cell Biology*, 22(5), 326–345. <https://doi.org/10.1038/s41580-021-00341-1>
- Piunti, A., Smith, E. R., Morgan, M. A. J., Ugarenko, M., Khaltyan, N., Helmin, K. A., Ryan, C. A., Murray, D. C., Rickels, R. A., Yilmaz, B. D., Rendleman, E. J., Savas, J. N., Singer, B. D., Bulun, S. E., & Shilatifard, A. (2019). Catacomb: An endogenous inducible gene that antagonizes H3K27 methylation activity of Polycomb repressive complex 2 via an H3K27M-like mechanism. *Science Advances*, 5(7). <https://doi.org/10.1126/sciadv.aax2887>
- Qu, H.-Q., Jacob, K., Fatet, S., Ge, B., Barnett, D., Delattre, O., Faury, D., Montpetit, A., Solomon, L., Hauser, P., Garami, M., Bognar, L., Hansely, Z., Mio, R., Farmer, J.-P., Albrecht, S., Polychronakos, C., Hawkins, C., & Jabado, N. (2010). Genome-wide profiling using single-nucleotide polymorphism arrays identifies novel chromosomal imbalances in pediatric glioblastomas. *Neuro-Oncology*, 12(2), 153–163. <https://doi.org/10.1093/neuonc/nop001>
- Quinlan, A. R., & Hall, I. M. (2010). BEDTools: a flexible suite of utilities for comparing genomic features. *Bioinformatics (Oxford, England)*, 26(6), 841–842. <https://doi.org/10.1093/bioinformatics/btq033>
- Ragazzini, R., Hi, B., Diop, S., Ancelin, K., Zielinski, D., Givelet, M., Borsos, M., Aflaki, S., Legoix, P., Pwtc, J., Servant, N., Me, P., Bourc, D., Fouchet, P., Vermeulen, M., & Margueron, R. (2019). EZHIP constrains Polycomb Repressive Complex 2 activity in germ cells. *BiorXiv*, 33(0), 1–18. <https://doi.org/10.1038/s41467-019-11800-x>
- Ramírez, F., Dünder, F., Diehl, S., Grüning, B. A., & Manke, T. (2014). deepTools: a flexible platform for exploring deep-sequencing data. *Nucleic Acids Research*, 42(Web Server issue), W187-91. <https://doi.org/10.1093/nar/gku365>
- Ramírez, F., Ryan, D. P., Grüning, B., Bhardwaj, V., Kilpert, F., Richter, A. S., Heyne, S., Dünder, F., & Manke, T. (2016). deepTools2: a next generation web server for deep-sequencing data analysis. *Nucleic Acids Research*, 44(W1), W160-5. <https://doi.org/10.1093/nar/gkw257>

- Ramsey, S. A., Knijnenburg, T. A., Kennedy, K. A., Zak, D. E., Gilchrist, M., Gold, E. S., Johnson, C. D., Lampano, A. E., Litvak, V., Navarro, G., Stolyar, T., Aderem, A., & Shmulevich, I. (2010). Genome-wide histone acetylation data improve prediction of mammalian transcription factor binding sites. *Bioinformatics (Oxford, England)*, *26*(17), 2071–2075. <https://doi.org/10.1093/bioinformatics/btq405>
- Ran, F. A., Hsu, P. D., Wright, J., Agarwala, V., Scott, D. A., & Zhang, F. (2013). Genome engineering using the CRISPR-Cas9 system. *Nature Protocols*, *8*(11), 2281–2308. <https://doi.org/10.1038/nprot.2013.143>
- Robinson, J. T., Thorvaldsdóttir, H., Winckler, W., Guttman, M., Lander, E. S., Getz, G., & Mesirov, J. P. (2011). Integrative genomics viewer. In *Nature biotechnology* (Vol. 29, Issue 1, pp. 24–26). <https://doi.org/10.1038/nbt.1754>
- Rohle, D., Popovici-Muller, J., Palaskas, N., Turcan, S., Grommes, C., Campos, C., Tsoi, J., Clark, O., Oldrini, B., Komisopoulou, E., Kunii, K., Pedraza, A., Schalm, S., Silverman, L., Miller, A., Wang, F., Yang, H., Chen, Y., Kernysky, A., ... Mellinghoff, I. K. (2013). An inhibitor of mutant IDH1 delays growth and promotes differentiation of glioma cells. *Science*, *340*(6132), 626–630. <https://doi.org/10.1126/science.1236062>
- Roulois, D., Loo Yau, H., Singhanian, R., Wang, Y., Danesh, A., Shen, S. Y., Han, H., Liang, G., Jones, P. A., Pugh, T. J., O'Brien, C., & De Carvalho, D. D. (2015). DNA-Demethylating Agents Target Colorectal Cancer Cells by Inducing Viral Mimicry by Endogenous Transcripts. *Cell*, *162*(5), 961–973. <https://doi.org/10.1016/j.cell.2015.07.056>
- Ryall, S., Guzman, M., Elbabaa, S. K., Luu, B., Mack, S. C., Zapotocky, M., Taylor, M. D., Hawkins, C., & Ramaswamy, V. (2017). H3 K27M mutations are extremely rare in posterior fossa group A ependymoma. *Child's Nervous System*, *33*(7), 1047–1051. <https://doi.org/10.1007/s00381-017-3481-3>
- Saint-André, V., Federation, A. J., Lin, C. Y., Abraham, B. J., Reddy, J., Lee, T. I., Bradner, J. E., & Young, R. A. (2016). Models of human core transcriptional regulatory circuitries. *Genome Research*, *26*(3), 385–396. <https://doi.org/10.1101/gr.197590.115>
- Salloum, R., McConechy, M. K., Mikael, L. G., Fuller, C., Drissi, R., DeWire, M., Nikbakht, H., De Jay, N., Yang, X., Boue, D., Chow, L. M. L., Finlay, J. L., Gayden, T., Karamchandani, J., Hummel, T. R., Olshefski, R., Osorio, D. S., Stevenson, C., Kleinman, C. L., ... Jabado, N. (2017). Characterizing temporal genomic heterogeneity in pediatric high-grade gliomas.

*Acta Neuropathologica Communications*, 5(1), 78. <https://doi.org/10.1186/s40478-017-0479-8>

- Sandberg, D. I., Yu, B., Patel, R., Hagan, J., Miesner, E., Sabin, J., Smith, S., Fletcher, S., Shah, M. N., Sirianni, R. W., & Taylor, M. D. (2019). Infusion of 5-Azacytidine (5-AZA) into the fourth ventricle or resection cavity in children with recurrent posterior Fossa Ependymoma: a pilot clinical trial. *Journal of Neuro-Oncology*, 141(2), 449–457. <https://doi.org/10.1007/s11060-018-03055-1>
- Sasaki, M., Knobbe, C. B., Itsumi, M., Elia, A. J., Harris, I. S., In, I., Chio, C., Cairns, R. A., Mccracken, S., Wakeham, A., Haight, J., Ten, A. Y., Snow, B., Ueda, T., Inoue, S., Yamamoto, K., Ko, M., Rao, A., Yen, K. E., ... Mak, T. W. (2012). D-2-hydroxyglutarate produced by mutant IDH1 perturbs collagen maturation and basement membrane function. *Genes & Development*, 26, 2038–2049. <https://doi.org/10.1101/gad.198200.112.a>
- Sasaki, T., Katagi, H., Goldman, S., Becher, O. J., & Hashizume, R. (2020). Convection-Enhanced Delivery of Enhancer of Zeste Homolog-2 (EZH2) Inhibitor for the Treatment of Diffuse Intrinsic Pontine Glioma. *Neurosurgery*, 87(6), E680–E688. <https://doi.org/10.1093/neuros/nyaa301>
- Schlee, M., Schuhmacher, M., Hölzel, M., Laux, G., & Bornkamm, G. W. (2007). c-MYC impairs immunogenicity of human B cells. *Advances in Cancer Research*, 97, 167–188. [https://doi.org/10.1016/S0065-230X\(06\)97007-9](https://doi.org/10.1016/S0065-230X(06)97007-9)
- Schuettengruber, B., Bourbon, H. M., Di Croce, L., & Cavalli, G. (2017). Genome Regulation by Polycomb and Trithorax: 70 Years and Counting. *Cell*, 171(1), 34–57. <https://doi.org/10.1016/j.cell.2017.08.002>
- Schwartzentruber, J., Korshunov, A., Liu, X.-Y., Jones, D. T. W., Pfaff, E., Jacob, K., Sturm, D., Fontebasso, A. M., Quang, D.-A. K., Tönjes, M., Hovestadt, V., Albrecht, S., Kool, M., Nantel, A., Konermann, C., Lindroth, A., Jäger, N., Rausch, T., Ryzhova, M., ... Jabado, N. (2012). Driver mutations in histone H3.3 and chromatin remodelling genes in paediatric glioblastoma. *Nature*, 484(7392), 130–130. <https://doi.org/10.1038/nature11026>
- Shen, L., Shao, N., Liu, X., & Nestler, E. (2014). ngs.plot: Quick mining and visualization of next-generation sequencing data by integrating genomic databases. *BMC Genomics*, 15, 284. <https://doi.org/10.1186/1471-2164-15-284>
- Sidoli, S., Bhanu, N. V., Karch, K. R., Wang, X., & Garcia, B. A. (2016). Complete Workflow

- for Analysis of Histone Post-translational Modifications Using Bottom-up Mass Spectrometry: From Histone Extraction to Data Analysis. *Journal of Visualized Experiments : JoVE*, 111. <https://doi.org/10.3791/54112>
- Sievers, P., Sill, M., Schrimpf, D., Stichel, D., Reuss, D. E., Sturm, D., Hench, J., Frank, S., Krskova, L., Vicha, A., Zapotocky, M., Bison, B., Castel, D., Grill, J., Debily, M., Harter, P. N., Snuderl, M., Kramm, C. M., Reifenberger, G., ... Sahm, F. (2020). A subset of pediatric-type thalamic gliomas share a distinct DNA methylation profile, H3K27me3 loss and frequent alteration of EGFR. *Neuro-Oncology*, 23(November 2020), 34–43. <https://doi.org/10.1093/neuonc/noaa251>
- Silveira, A. B., Kasper, L. H., Fan, Y., Jin, H., Wu, G., Shaw, T. I., Zhu, X., Larson, J. D., Easton, J., Shao, Y., Yergeau, D. A., Rosencrance, C., Boggs, K., Rusch, M. C., Ding, L., Zhang, J., Finkelstein, D., Noyes, R. M., Russell, B. L., ... Baker, S. J. (2019). H3.3 K27M depletion increases differentiation and extends latency of diffuse intrinsic pontine glioma growth in vivo. *Acta Neuropathologica*, 137(4), 637–655. <https://doi.org/10.1007/s00401-019-01975-4>
- Smit, A., Hubley, R., & Green, P. (n.d.). RepeatMasker Open-4.0. <Http://Www.Repeatmasker.Org>.
- Sneeringer, C. J., Scott, M. P., Kuntz, K. W., Knutson, S. K., Pollock, R. M., Richon, V. M., & Copeland, R. A. (2010). Coordinated activities of wild-type plus mutant EZH2 drive tumor-associated hypertrimethylation of lysine 27 on histone H3 (H3K27) in human B-cell lymphomas. *Proceedings of the National Academy of Sciences of the United States of America*, 107(49), 20980–20985. <https://doi.org/10.1073/pnas.1012525107>
- Solovyov, A., Vabret, N., Arora, K. S., Snyder, A., Funt, S. A., Bajorin, D. F., Rosenberg, J. E., Bhardwaj, N., Ting, D. T., & Greenbaum, B. D. (2018). Global Cancer Transcriptome Quantifies Repeat Element Polarization between Immunotherapy Responsive and T Cell Suppressive Classes. *Cell Reports*, 23(2), 512–521. <https://doi.org/10.1016/j.celrep.2018.03.042>
- Sonoda, E., Takata, M., Yamashita, Y. M., Morrison, C., & Takeda, S. (2001). Homologous DNA recombination in vertebrate cells. *Proceedings of the National Academy of Sciences of the United States of America*, 98(15), 8388–8394. <https://doi.org/10.1073/pnas.1111006398>
- Stafford, J. M., Lee, C. H., Voigt, P., Descostes, N., Saldana-Meyer, R., Yu, J. R., Leroy, G.,

- Oksuz, O., Chapman, J. R., Suarez, F., Modrek, A. S., Bayin, N. S., Placantonakis, D. G., Karajannis, M. A., Snuderl, M., Ueberheide, B., & Reinberg, D. (2018). Multiple modes of PRC2 inhibition elicit global chromatin alterations in H3K27M pediatric glioma. *Science Advances*, 4(10). <https://doi.org/10.1126/sciadv.aau5935>
- Streubel, G., Watson, A., Jammula, S. G., Scelfo, A., Fitzpatrick, D. J., Oliviero, G., McCole, R., Conway, E., Glancy, E., Negri, G. L., Dillon, E., Wynne, K., Pasini, D., Krogan, N. J., Bracken, A. P., & Cagney, G. (2018). The H3K36me2 Methyltransferase Nsd1 Demarcates PRC2-Mediated H3K27me2 and H3K27me3 Domains in Embryonic Stem Cells. *Molecular Cell*, 70(2), 371-379.e5. <https://doi.org/10.1016/j.molcel.2018.02.027>
- Sturm, D., Bender, S., Jones, D. T. W., Lichter, P., Grill, J., Becher, O., Hawkins, C., Majewski, J., Jones, C., Costello, J. F., Iavarone, A., Aldape, K., Brennan, C. W., Jabado, N., & Pfister, S. M. (2014a). Paediatric and adult glioblastoma: multiform (epi)genomic culprits emerge. *Nature Reviews. Cancer*, 14(2), 92–107. <https://doi.org/10.1038/nrc3655>
- Sturm, D., Bender, S., Jones, D. T. W., Lichter, P., Grill, J., Becher, O., Hawkins, C., Majewski, J., Jones, C., Costello, J. F., Iavarone, A., Aldape, K., Brennan, C. W., Jabado, N., & Pfister, S. M. (2014b). Paediatric and adult glioblastoma: Multiform (epi)genomic culprits emerge. *Nature Reviews Cancer*, 14(2), 92–107. <https://doi.org/10.1038/nrc3655>
- Sturm, D., Witt, H., Hovestadt, V., Khuong-Quang, D. A., Jones, D. T. W., Konermann, C., Pfaff, E., Tönjes, M., Sill, M., Bender, S., Kool, M., Zapatka, M., Becker, N., Zucknick, M., Hielscher, T., Liu, X. Y., Fontebasso, A. M., Ryzhova, M., Albrecht, S., ... Pfister, S. M. (2012). Hotspot Mutations in H3F3A and IDH1 Define Distinct Epigenetic and Biological Subgroups of Glioblastoma. *Cancer Cell*, 22(4), 425–437. <https://doi.org/10.1016/j.ccr.2012.08.024>
- Sturm, D., Witt, H., Hovestadt, V., Khuong-Quang, D. A., Jones, D. T. W. W., Konermann, C., Pfaff, E., Tönjes, M., Sill, M., Bender, S., Kool, M., Zapatka, M., Becker, N., Zucknick, M., Hielscher, T., Liu, X. Y., Fontebasso, A. M., Ryzhova, M., Albrecht, S., ... Pfister, S. M. (2018). Epidemiology and molecular pathology of glioma. *Cancer Cell*, 2017(3), 11. <https://doi.org/10.1016/j.ccr.2006.02.019>
- Subramanian, A., Tamayo, P., Mootha, V. K., Mukherjee, S., Ebert, B. L., Gillette, M. A., Paulovich, A., Pomeroy, S. L., Golub, T. R., Lander, E. S., & Mesirov, J. P. (2005). Gene set enrichment analysis: a knowledge-based approach for interpreting genome-wide

- expression profiles. *Proceedings of the National Academy of Sciences of the United States of America*, 102(43), 15545–15550. <https://doi.org/10.1073/pnas.0506580102>
- Tao, Y., Kang, B., Petkovich, D. A., Bhandari, Y. R., In, J., Stein-O'Brien, G., Kong, X., Xie, W., Zachos, N., Maegawa, S., Vaidya, H., Brown, S., Chiu Yen, R. W., Shao, X., Thakor, J., Lu, Z., Cai, Y., Zhang, Y., Mallona, I., ... Easwaran, H. (2019). Aging-like Spontaneous Epigenetic Silencing Facilitates Wnt Activation, Stemness, and Braf V600E -Induced Tumorigenesis. *Cancer Cell*, 35(2), 315–328. <https://doi.org/10.1016/j.ccell.2019.01.005>
- Taylor, K. R., Mackay, A., Truffaux, N., Butterfield, Y., Morozova, O., Philippe, C., Castel, D., Grasso, C. S., Vinci, M., Carvalho, D., Carcaboso, A. M., de Torres, C., Cruz, O., Mora, J., Entz-Werle, N., Ingram, W. J., Monje, M., Hargrave, D., Bullock, A. N., ... Grill, J. (2014). Recurrent activating ACVR1 mutations in diffuse intrinsic pontine glioma. *Nature Genetics*, 46(5), 457–461. <https://doi.org/10.1038/ng.2925>
- Thorvaldsdóttir, H., Robinson, J. T., & Mesirov, J. P. (2013). Integrative Genomics Viewer (IGV): high-performance genomics data visualization and exploration. *Briefings in Bioinformatics*, 14(2), 178–192. <https://doi.org/10.1093/bib/bbs017>
- Topper, M. J., Vaz, M., Chiappinelli, K. B., DeStefano Shields, C. E., Niknafs, N., Yen, R.-W. C., Wenzel, A., Hicks, J., Ballew, M., Stone, M., Tran, P. T., Zahnow, C. A., Hellmann, M. D., Anagnostou, V., Strissel, P. L., Strick, R., Velculescu, V. E., & Baylin, S. B. (2017). Epigenetic Therapy Ties MYC Depletion to Reversing Immune Evasion and Treating Lung Cancer. *Cell*, 171(6), 1284-1300.e21. <https://doi.org/10.1016/j.cell.2017.10.022>
- Torchia, J., Golbourn, B., Feng, S., Ho, K. C., Sin-Chan, P., Vasiljevic, A., Norman, J. D., Guilhamon, P., Garzia, L., Agamez, N. R., Lu, M., Chan, T. S., Picard, D., de Antonellis, P., Khuong-Quang, D. A., Planello, A. C., Zeller, C., Barsyte-Lovejoy, D., Lafay-Cousin, L., ... Huang, A. (2016). Integrated (epi)-Genomic Analyses Identify Subgroup-Specific Therapeutic Targets in CNS Rhabdoid Tumors. *Cancer Cell*, 30(6), 891–908. <https://doi.org/10.1016/j.ccell.2016.11.003>
- Turcan, S., Makarov, V., Taranda, J., Wang, Y., Fabius, A. W. M., Wu, W., Zheng, Y., El-Amine, N., Haddock, S., Nanjangud, G., Lekaye, H. C., Brennan, C., Cross, J., Huse, J. T., Kelleher, N. L., Osten, P., Thompson, C. B., & Chan, T. A. (2018). Mutant-IDH1-dependent chromatin state reprogramming, reversibility, and persistence. *Nature Genetics*, 50(1), 62–72. <https://doi.org/10.1038/s41588-017-0001-z>

- van den Boom, V., Maat, H., Geugien, M., Rodríguez López, A., Sotoca, A. M., Jaques, J., Brouwers-Vos, A. Z., Fusetti, F., Groen, R. W. J., Yuan, H., Martens, A. C. M., Stunnenberg, H. G., Vellenga, E., Martens, J. H. A., & Schuringa, J. J. (2016). Non-canonical PRC1.1 Targets Active Genes Independent of H3K27me3 and Is Essential for Leukemogenesis. *Cell Reports*, *14*(2), 332–346. <https://doi.org/10.1016/j.celrep.2015.12.034>
- van der Maaten, L., & Hinton, G. (2008). Visualizing Data using t-SNE. *Journal of Machine Learning Research*, *9*, 2579–2605. <https://doi.org/10.1007/s10479-011-0841-3>
- Vitte, J., Gao, F., Coppola, G., Judkins, A. R., & Giovannini, M. (2017). Timing of Smarcb1 and Nf2 inactivation determines schwannoma versus rhabdoid tumor development. *Nature Communications*, *8*(1), 1–12. <https://doi.org/10.1038/s41467-017-00346-5>
- Vladoiu, M. C., El-Hamamy, I., Donovan, L. K., Farooq, H., Holgado, B. L., Sundaravadanam, Y., Ramaswamy, V., Hendrikse, L. D., Kumar, S., Mack, S. C., Lee, J. J. Y., Fong, V., Juraschka, K., Przelicki, D., Michealraj, A., Skowron, P., Luu, B., Suzuki, H., Morrissy, A. S., ... Taylor, M. D. (2019). Childhood cerebellar tumours mirror conserved fetal transcriptional programs. *Nature*. <https://doi.org/10.1038/s41586-019-1158-7>
- Voon, H. P. J., Udugama, M., Lin, W., Hii, L., Law, R. H. P., Steer, D. L., Das, P. P., Mann, J. R., & Wong, L. H. (2018). Inhibition of a K9/K36 demethylase by an H3.3 point mutation found in paediatric glioblastoma. *Nature Communications*, *9*(1), 1–10. <https://doi.org/10.1038/s41467-018-05607-5>
- Walsh, C. P., Chaillet, J. R., & Bestor, T. H. (1998). Transcription of IAP endogenous retroviruses is constrained by cytosine methylation. In *Nature genetics* (Vol. 20, Issue 2, pp. 116–117). <https://doi.org/10.1038/2413>
- Wang, X., Paucek, R. D., Gooding, A. R., Brown, Z. Z., Ge, E. J., Muir, T. W., & Cech, T. R. (2017). Molecular analysis of PRC2 recruitment to DNA in chromatin and its inhibition by RNA. *Nature Structural & Molecular Biology*, *24*(12), 1028–1038. <https://doi.org/10.1038/nsmb.3487>
- Watanabe, T., Nobusawa, S., Kleihues, P., & Ohgaki, H. (2009). IDH1 mutations are early events in the development of astrocytomas and oligodendrogliomas. *American Journal of Pathology*, *174*(4), 1149–1153. <https://doi.org/10.2353/ajpath.2009.080958>
- Weinberg, D. N., Papillon-Cavanagh, S., Chen, H., Yue, Y., Chen, X., Rajagopalan, K. N.,

- Horth, C., McGuire, J. T., Xu, X., Nikbakht, H., Lemiesz, A. E., Marchione, D. M., Marunde, M. R., Meiners, M. J., Cheek, M. A., Keogh, M.-C., Bareke, E., Djedid, A., Harutyunyan, A. S., ... Lu, C. (2019). The histone mark H3K36me2 recruits DNMT3A and shapes the intergenic DNA methylation landscape. *Nature*, *573*(7773), 281–286. <https://doi.org/10.1038/s41586-019-1534-3>
- Wells, J. N., & Feschotte, C. (2020). A Field Guide to Eukaryotic Transposable Elements. *Annual Review of Genetics*, *54*, 539–561. <https://doi.org/10.1146/annurev-genet-040620-022145>
- Wen, H., Li, Y., Xi, Y., Jiang, S., Stratton, S., Peng, D., Tanaka, K., Ren, Y., Xia, Z., Wu, J., Li, B., Barton, M. C., Li, W., Li, H., & Shi, X. (2014). ZMYND11 links histone H3.3K36me3 to transcription elongation and tumour suppression. *Nature*, *508*(7495), 263–268. <https://doi.org/10.1038/nature13045>
- Whyte, W. A., Orlando, D. A., Hnisz, D., Abraham, B. J., Lin, C. Y., Kagey, M. H., Rahl, P. B., Lee, T. I., & Young, R. A. (2013). Master transcription factors and mediator establish super-enhancers at key cell identity genes. *Cell*, *153*(2), 307–319. <https://doi.org/10.1016/j.cell.2013.03.035>
- Wilson, B. G., Wang, X., Shen, X., McKenna, E. S., Lemieux, M. E., Cho, Y. J., Koellhoffer, E. C., Pomeroy, S. L., Orkin, S. H., & Roberts, C. W. M. (2010). Epigenetic antagonism between polycomb and SWI/SNF complexes during oncogenic transformation. *Cancer Cell*, *18*(4), 316–328. <https://doi.org/10.1016/j.ccr.2010.09.006>
- Wu, G., Broniscer, A., McEachron, T. A., Lu, C., Paugh, B. S., Becksfort, J., Qu, C., Ding, L., Huether, R., Parker, M., Zhang, J., Gajjar, A., Dyer, M. A., Mullighan, C. G., Gilbertson, R. J., Mardis, E. R., Wilson, R. K., Downing, J. R., Ellison, D. W., ... Baker, S. J. (2012). Somatic histone H3 alterations in pediatric diffuse intrinsic pontine gliomas and non-brainstem glioblastomas. *Nature Genetics*, *44*(3), 251–253. <https://doi.org/10.1038/ng.1102>
- Wu, G., Diaz, A. K., Paugh, B. S., Rankin, S. L., Ju, B., Li, Y., Zhu, X., Qu, C., Chen, X., Zhang, J., Easton, J., Edmonson, M., Ma, X., Lu, C., Nagahawatte, P., Hedlund, E., Rusch, M., Pounds, S., Lin, T., ... Baker, S. J. (2014). The genomic landscape of diffuse intrinsic pontine glioma and pediatric non-brainstem high-grade glioma. *Nature Genetics*, *46*(5), 444–450. <https://doi.org/10.1038/ng.2938>
- Yadav, R. K., Jablonowski, C. M., Fernandez, A. G., Lowe, B. R., Henry, R. A., Finkelstein, D.,

- Barnum, K. J., Pidoux, A. L., Kuo, Y. M., Huang, J., O'Connell, M. J., Andrews, A. J., Onar-Thomas, A., Allshire, R. C., & Partridge, J. F. (2017). Histone H3G34R mutation causes replication stress, homologous recombination defects and genomic instability in *S. Pombe*. *ELife*, *6*, 1–28. <https://doi.org/10.7554/eLife.27406>
- Yamashita, A. S., da Costa Rosa, M., Borodovsky, A., Festuccia, W. T., Chan, T., & Riggins, G. J. (2019). Demethylation and epigenetic modification with 5-azacytidine reduces IDH1 mutant glioma growth in combination with temozolomide. *Neuro-Oncology*, *21*(2), 189–200. <https://doi.org/10.1093/neuonc/noy146>
- Younesy, H., Nielsen, C. B., Lorincz, M. C., Jones, S. J. M., Karimi, M. M., & Möller, T. (2016). ChAsE: chromatin analysis and exploration tool. *Bioinformatics (Oxford, England)*, *32*(21), 3324–3326. <https://doi.org/10.1093/bioinformatics/btw382>
- Yu, J.-R., LeRoy, G., Bready, D., Frenster, J. D., Saldaña-Meyer, R., Jin, Y., Descostes, N., Stafford, J. M., Placantonakis, D. G., & Reinberg, D. (2021). The H3K36me2 writer-reader dependency in H3K27M-DIPG. *Science Advances*, *7*(29). <https://doi.org/10.1126/sciadv.abg7444>
- Yu, J. R., Lee, C. H., Oksuz, O., Stafford, J. M., & Reinberg, D. (2019). PRC2 is high maintenance. *Genes and Development*, *33*(15–16), 903–935. <https://doi.org/10.1101/gad.325050.119>
- Zhang, L., Chen, L. H., Wan, H., Yang, R., Wang, Z., Feng, J., Yang, S., Jones, S., Wang, S., Zhou, W., Zhu, H., Killela, P. J., Zhang, J., Wu, Z., Li, G., Hao, S., Wang, Y., Webb, J. B., Friedman, H. S., ... Yan, H. (2014). Exome sequencing identifies somatic gain-of-function PPM1D mutations in brainstem gliomas. *Nature Genetics*, *46*(7), 726–730. <https://doi.org/10.1038/ng.2995>
- Zhang, Y., Liu, T., Meyer, C. A., Eeckhoute, J., Johnson, D. S., Bernstein, B. E., Nusbaum, C., Myers, R. M., Brown, M., Li, W., & Liu, X. S. (2008). Model-based analysis of ChIP-Seq (MACS). *Genome Biology*, *9*(9), R137. <https://doi.org/10.1186/gb-2008-9-9-r137>
- Zheng, H., & Xie, W. (2019). The role of 3D genome organization in development and cell differentiation. *Nature Reviews Molecular Cell Biology*, *20*(9), 535–550. <https://doi.org/10.1038/s41580-019-0132-4>
- Zhu, W., Krishna, S., Garcia, C., Lin, C.-C. J., Mitchell, B. D., Scott, K. L., Mohila, C. A., Creighton, C. J., Yoo, S.-H., Lee, H. K., & Deneen, B. (2017). Daam2 driven degradation of

VHL promotes gliomagenesis. *ELife*, 6. <https://doi.org/10.7554/eLife.31926>

# Appendices

## Copyright permissions

**SPRINGER NATURE**

**H3K27M induces defective chromatin spread of PRC2-mediated repressive H3K27me2/me3 and is essential for glioma tumorigenesis**

**Author:** Ashot S. Harutyunyan et al  
**Publication:** Nature Communications  
**Publisher:** Springer Nature  
**Date:** Mar 19, 2019

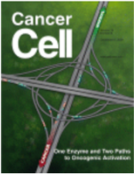
*Copyright © 2019, The Author(s)*

**Creative Commons**

This is an open access article distributed under the terms of the [Creative Commons CC BY](#) license, which permits unrestricted use, distribution, and reproduction in any medium, provided the original work is properly cited.

You are not required to obtain permission to reuse this article.

To request permission for a type of use not listed, please contact [Springer Nature](#)



**Pervasive H3K27 Acetylation Leads to ERV Expression and a Therapeutic Vulnerability in H3K27M Gliomas**

**Author:** Brian Krug, Nicolas De Jay, Ashot S. Harutyunyan, Shriya Deshmukh, Dylan M. Marchione, Paul Guilhamon, Kelsey C. Bertrand, Leonie G. Mikael, Melissa K. McConechy, Carol C.L. Chen, Sima Khazaei, Robert F. Koncar, Sameer Agnihotri, Damien Faury, Benjamin Ellezam et al.  
**Publication:** Cancer Cell  
**Publisher:** Elsevier  
**Date:** 13 May 2019

*© 2019 Elsevier Inc.*

**Journal Author Rights**

Please note that, as the author of this Elsevier article, you retain the right to include it in a thesis or dissertation, provided it is not published commercially. Permission is not required, but please ensure that you reference the journal as the original source. For more information on this and on your other retained rights, please visit: <https://www.elsevier.com/about/our-business/policies/copyright#Author-rights>

[BACK](#) [CLOSE WINDOW](#)



**Polycomb repressive complex 2 in the driver's seat of childhood and young adult brain tumours**

**Author:** Brian Krug, Ashot S. Harutyunyan, Shriya Deshmukh, Nada Jabado  
**Publication:** Trends in Cell Biology  
**Publisher:** Elsevier  
**Date:** October 2021

*© 2021 Elsevier Ltd. All rights reserved.*

**Journal Author Rights**

Please note that, as the author of this Elsevier article, you retain the right to include it in a thesis or dissertation, provided it is not published commercially. Permission is not required, but please ensure that you reference the journal as the original source. For more information on this and on your other retained rights, please visit: <https://www.elsevier.com/about/our-business/policies/copyright#Author-rights>

[BACK](#) [CLOSE WINDOW](#)

## Ethics certificate



August 5, 2021

### Animal Certificate

This is to certify that **Dr. Nada Jabado, RI-MUHC Glen site**, currently holds an approved **Animal Use Protocol # 2010-5684** with McGill University and its Affiliated Hospital's Research Institutes for the following project:

**Animal Use Protocol Title:** Oncohistones in Cancer; Tackling Childhood Brain Cancer at the root to Improve survival and quality of life; Signature; Oncohistones: Role of Histone H3 Mutations in the Oncogenesis of Pediatric Cancers; Immuno-modulation to treat poor prognosis pediatric brain tumours

**Start date:** July 1, 2021

**Expiration date:** June 30, 2022

McGill University and Affiliated Hospitals Research Institutes recognize the importance of animal research in our efforts to further our knowledge of natural processes, diseases and conservation. Research, educational and testing projects are conducted with full commitment to the wellbeing of the animal subjects. In order to limit animal use to meritorious research or educational projects, the institution relies on stringent peer review processes, along with assessment of ethical issues by the Animal Care Committee. McGill University recognizes that the use of animals in research, teaching and testing carries significant responsibilities. The institution will continue to develop and maintain guidelines and regulations, following the high standards established by the Canadian Council on Animal Care. It is committed to conducting the highest-quality research and to providing animals with the best care.

A handwritten signature in blue ink that reads "Cynthia Lavoie".

**Cynthia Lavoie**

Animal Ethics and Compliance Administrator  
Animal Compliance Office  
Office of Vice-Principal (Research and Innovation)  
Suite 325, James Administration Building, McGill University  
845 Sherbrooke Street West, Montreal, Quebec, Canada H3A 0G4  
[animal.approvals@mcgill.ca](mailto:animal.approvals@mcgill.ca)